Computer Aided Medical Procedures
(CAMP)
Prof. Dr. Nassir Navab

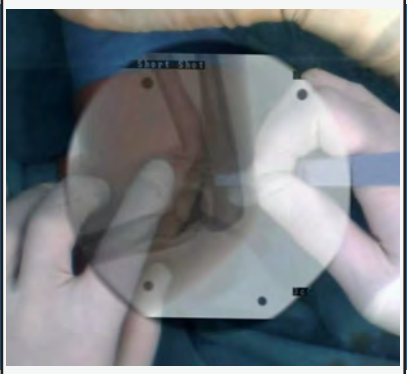

Dissertation

# Novel Techniques for Integrating Video Augmented X-ray Imaging into Orthopedic and Trauma Surgery

Lejing Wang

Fakultät für Informatik
Technische Universität München

TECHNISCHE UNIVERSITÄT MÜNCHEN

Chair for Computer Aided Medical Procedures & Augmented Reality

# Novel Techniques for Integrating Video Augmented X-ray Imaging into Orthopedic and Trauma Surgery

Lejing Wang

Vollständiger Abdruck der von der Fakultät für Informatik der Technischen Universität München zur Erlangung des akademischen Grades eines

Doktors der Naturwissenschaften (Dr. rer. nat.)

genehmigten Dissertation.

Vorsitzende: Univ.-Prof. Dr. Darius Burschka

Prüfer der Dissertation:

1. Univ.-Prof. Dr. Nassir Navab
2. apl. Prof. Dr. Ekkehard Euler, Ludwig-Maximilians-Universität München
3. Prof. Russell H. Taylor, Ph.D., Johns Hopkins University, USA

Die Dissertation wurde am 20.03.2012 bei der Technischen Universität München eingereicht und durch die Fakultät für Informatik am 26.09.2012 angenommen.

**Abstract**

The standard mobile C-arm fluoroscope, found in nearly every hospital worldwide, is the primary technology used in guiding orthopedic and trauma surgeries. It produces a real-time X-ray image that provides surgeons with live visual information of the anatomy to be treated. However, there are several distinct limitations to X-ray guidance: radiation exposure, limited field of view of the anatomy and the difficulties in maneuvering to achieve a desired X-ray viewpoint. The aim of this thesis is to propose novel image guided solutions enabling optimal X-ray guidance by taking into account these limitations.

Surgical workflow analysis has become a new paradigm for developing novel interventional imaging solutions. The first major contribution to this thesis is investigating the surgical workflow in several orthopedic and trauma surgeries which would allow for the effective use of the Camera Augmented Mobile C-arm (CamC) at specific points in the procedure. The CamC augments a standard mobile C-arm with a video camera and mirror construction thereby providing a co-registered overlay between the X-ray and the video images. The workflow based analysis demonstrates that several surgical tasks benefit from the overlay, namely: skin incision, entry point localization, instrument axis alignment, K-wire guidance and X-ray positioning.

The second contribution is the development and evaluation of parallax-free panoramic X-ray imaging. Existing methods in literature cannot avoid parallax effects in the creation of panoramic X-ray images when imaging non-planar bone structures. We resolve this limitation with our solution that stitches multiple X-ray images together by rotating a C-arm around its X-ray source. However, rotating the mobile C-arm around its source center is impractical and sometimes impossible due to the mechanical design of mobile C-arms. Thus, to ensure that the C-arm motion is a relative pure rotation we propose to reposition the patient table to compensate for the translational part of the motion.

Finally, we propose a solution to optimally acquire X-ray images by modeling the C-arm and table setup as an integrated 6 degrees of freedom (DOF) kinematics chain. The closed-form solutions for the inverse kinematics problem are derived in order to obtain the required values for all C-arm joint and table movements to position the X-ray source at a desired pose. The modeling method and the closed-form solutions can be applied to general isocentric or non-isocentric mobile C-arms.

The proposed novel image guided solutions are validated through pre-clinical experiments, including animal cadaver and dry bone phantoms, as well as clinical trials involving 43 patients.

**Keywords:**
Image Guided Surgery, Camera Augmented Mobile C-arm, Parallax-Free Panoramic X-ray image, C-arm Kinematics

**Zusammenfassung**

Mobile C-Bogen Röntgengeräte sind in fast jedem Krankenhaus weltweit vorhanden und sind die primäre bildgebende Technologie in der Orthopädie und Unfallchirurgie. Sie erzeugen Röntgenbilder welche den Chirurgen während des Eingriffs visuelle Informationen über die zu behandelnde Anatomie liefern. Allerdings haben Röntgenbilder einige schwerwiegende Nachteile: Strahlenbelastung, ein eingeschränktes Blickfeld auf die Anatomie und Probleme das mobile Röntgengerät an die korrekte Stelle zu manövrieren. Das Ziel dieser Arbeit ist es, unter Berücksichtigung dieser Probleme, neue bildgestützte Verfahren zu entwickeln, welche die optimale Nutzung von Röntgenbildern erlauben.

Bei der Entwicklung neuer bildgestützter Methoden ist die Analyse chirurgischer Arbeitsabläufe von wachsender Bedeutung. Der erste wissenschaftliche Beitrag dieser Arbeit ist eine Analyse chirurgischer Arbeitsabläufe verschiedener orthopädischer und unfallchirurgischer Eingriffe, welche von einem Einsatz des Camera Augmented Mobile C-arm (CamC) profitieren können. Das CamC System erweitert ein mobiles C-Bogen Röntgengerät um eine Videokamera und eine Spiegelkonstruktion, welche eine korrekte Überlagerung zwischen Röntgen- und Videobild erlaubt. Die Analyse der Arbeitsabläufe zeigt, dass mehrere chirurgische Eingriffe und Arbeitsschritte von der Überlagerung profitieren können. Dies sind: Hautschnitt, Lokalisieren des Eingriffspunktes, axiales Ausrichten eines Instrumentes, Platzierung eines Kirschner-Drahts und Positionierung des Röntgengeräts.

Der zweite wissenschaftliche Beitrag ist die Entwicklung und Evaluierung einer Methode zur Erzeugung parallaxefreier Röntgen-Panoramabilder. Bisherige Methoden erzeugen einen Parallaxeeffekt bei Röntgen-Panoramabildern von nicht-planaren Knochenstrukturen. Wir lösen dieses Problem indem wir den C-Bogen bei der Aufnahme der Bilder um die Strahlenquelle rotieren. Ein Problem hierbei ist, dass eine Rotation um die Strahlenquelle in der Praxis schwierig und aufgrund der mechanischen Konstruktion mobiler C-Bögen manchmal unmöglich ist. Um sicherzustellen, dass die Bewegung des C-Bogen eine relative reine Rotation ist, führen wir eine Bewegung des Lagerungstischs durch um Translationsbewegungen des Röntgengeräts auszugleichen.

Ausserdem stellen wir eine Methode zur optimalen Aufnahme von Röntgenbildern vor, bei der C-Bogen und Lagerungstisch als integrierte kinematische Kette mit sechs Freiheitsgraden modelliert werden. Um es zu ermöglichen die Röntgenquelle an eine bestimmte Position zu bewegen wurde eine geschlossene analytische Lösung der inversen Kinematik abgeleitet, welche Werte für alle Gelenke des C-Bogens und des Tischs liefern kann. Die Modellierung und die geschlossene Lösung kann für alle isozentrischen oder nicht isozentrischen C-Bögen verwendet werden.

Die vorgestellten bildgestützten Methoden wurden durch präklinische Studien validiert, darunter Studien mit Tierkadavern und Knochenmodellen, sowie durch eine klinische Studie an 43 Patienten.

**Schlagwörter:**
Bildgestütze Chirurgie, Camera Augmented Mobile C-arm, Parallaxenfreie Röntgen-Panoramabilder, C-Bogen Kinematik

# ACKNOWLEDGMENTS

First of all, I would like to express my great gratitude to my PhD adviser Prof. Dr. Nassir Navab for accepting me as one of his PhD students and making my dissertation possible. I deeply appreciate his helpful advice, guidance and support during the last four years. The philosophy that I learned from him on research, teaching and project management not only made my work successful, but will also be a precious reference for my future work. I would also like to thank Prof. Dr. med. Ekkehard Euler for guiding me as my medical mentor through the complex medical domain. Many thanks also to him for initiating, arranging and conducting the many clinical experiments we performed. I would also like to thank Prof. Russell H. Taylor, PhD, for reviewing my PhD thesis. Thanks also go to Prof. Dr. Darius Burschka who was the chairman of my thesis.

I owe a lot to Dr. Jörg Traub, who brought me into the field of image guided surgery and shared his senior PhD experience with me, as well as to Pascal Fallavollita, PhD, who guided me in scientific research work and proofread my PhD thesis. This work would not have been complete without the support of these two senior scientific researchers.

I would like to express special thanks to our medical collaboration partners, in particular Dr. med. Simon Weidert for his active collaboration, insightful medical advice and invaluable contribution, resulting in many joint publications throughout my entire PhD work; Dr. med. Sandro M. Heining for initiating and planning the CamC clinical study; Dr. med. Jürgen Landes for designing and organizing interlocking study on cow cadavers; and Dr. med. Peter H. Thaller for insightful discussions on the clinical applications for X-ray image stitching. I also owe a great deal to Anna von der Heide and Alexander Brand who contributed greatly to the CamC clinical study and the X-ray image stitching experiments. I wish to thank Prof. Dr. med. Wolf Mutschler for providing me and my colleagues with the ideal working space at the Narvis Lab for the interdisciplinary research of computer assisted surgery and medical augmented reality.

I would also like to thank my colleagues Tobias Blum, Ahmad Ahmadi, Stuart Holdstock, Martin Horn, Tassilo Klein, Dr. Christoph Bichlmeier, Dr. Hauke Heibel, Ali Bigdelou, Dr. Stefanie Demirci, Dr. Selim Benhimane, Dr. Philipp Sandner, as well as students Rui Zou, Maximilian Springer, Xin Chen, Oleg Simin, Florian Pichlmeier, Benoit Diotte, Matthias Wieczorek, and Andre Aichert, for the great support, joint work, joint publications, suggestive feedbacks and creative ideas on research. Furthermore, many thanks go to many people at the CAMP chair, namely Dr. Oliver Kutter, Dr. Pierre Georgel, Dr. Alexander Ladikos, Dr. Martin Groher, Andreas Hofhauser, Tobias Reichl,

Jose Gardiazabal, Dr. Daniel Pustka, Athanasios Karamalis, Dr. Olivier Pauly, Mehmet Yigitsoy, Nicolas Brieu, Dr. Stefan Hinterstoisser, and many more, for our discussions and making it possible to work in the most collaborative and also fun environment. Special thanks go to the medability team at the Narvis lab, Patrick Wucherer, Philipp Stefan, and Dr. Stefan Taing, for a lot of support on managing the lab and organizing parties.

I would like to acknowledge Dr. Rainer Graumann from Siemens Healthcares for the continuous support and valuable feedback to the Camera Augmented Mobile C-arm project. I wish to thank Martina Hilla for her support on organizational and administrative issues.

I owe a lot of thanks to my parents Changrong Hu and Yi Wang for encouraging and supporting me to study abroad and also for their endless patience and love. Lastly, I must say I also owe a very deep and warm appreciation to Ya Chen who has given so so so much support to my PhD work.

# CONTENTS

CHAPTER

# ONE

# IMAGE GUIDED ORTHOPEDIC SURGERY (IGOS)

## 1.1 Introduction

The word "orthopédie" introduced by 18th-centry french physician Nicholas Andry is derived from two Greek words "orthos" meaning straight and free from deformity, and "paidios" meaning a child. Later, it was translated into English as "orthopedia". Modern orthopedic surgery (also spelled orthopaedic surgery in British English) mainly treats trauma, injuries, diseases and congenital disorders of the musculoskeletal system [1]. Approximately one in six Americans is affected with orthopedic disorders, whereas in Germany alone, roughly 12 million patients undergo some type of orthopedic procedure [2]. Furthermore, two new studies show that the number of patients requiring orthopedic surgery is expected to outpace the number of surgeons to perform such procedures [3].

Technology for intra-operative imaging and visualization of patient's anatomy has evolved over the past decades in the field of orthopedics. Medical imaging technologies play a vital role for a successful treatment, especially in minimally invasive procedures. As internal structures of the patient's body are invisible to the human naked eye, natural openings and incisions on the patient are often needed to enable surgeons to have a direct visual feedback on the anatomical structure under operation. However, this could result in the risk of infection and damaging the sensitive tissue or anatomy and thus could cause pain and a long recovery time for patients. The technology of X-ray imaging was invented by Konrad Röntgen in Würzburg, Germany in 1895 [4]. The famous X-ray photograph he took with his wife's hand, which revealed her wedding ring and her bones, has transcended time and continues to electrify the general public and arouse great scientific interest. The first clinical operation performed under the help of X-ray was removing a needle from the hand of a woman in early 1896 [5]. It can be regarded as the advent of modern intra-operative imaging and image guided surgery. X-ray images today are still the most frequently used form of medical imaging in trauma and orthopedic surgery, where bone structures are the major concerns. Additionally, other advanced imaging devices are developed based on the principle of X-ray imaging. Computed tomography (CT) can provide 3D X-ray image data of patient's body, which is mainly used for diagnostics and a traditional source of information for image guided surgery. Due to

the bulky system, cost, and relative high radiation dose, CT scanner is not often used during surgery. Mobile X-ray C-arms, however, are ubiquitous in today's operating rooms and play a vital role intra-operatively for the success of different orthopedic and trauma surgeries. They are compact and versatile, and can provide real-time 2D projection X-ray images. Some advanced mobile C-arms are capable of intra-operative 3D X-ray cone-beam reconstruction, but increases the radiation exposure to both patients and surgical team. Other medical imaging like magnetic resonance, ultrasound, and molecular techniques are available. However, none of them can replace the role of X-ray imaging for trauma and orthopedic surgery because of the image quality of bone structures.

Image guided surgery (IGS) has been introduced to offer surgeons improved visual perception and guidance. IGS augments and complements the physician's ability to quickly and clearly perceive the structure or function of anatomies and the spatial relation between the anatomies, implants and surgical instruments. It is achieved by fusing relevant surgical information in real time, e.g. medical images, patient and the location of the instruments, in a common coordinate system thanks to computer based registration and tracking techniques. Image guided surgery is also called computer assisted (or aided) surgery (CAS) as various computer technologies are employed.

Image guided surgery was initially employed in neurosurgery in the 1980s for supporting intracranial needle biopsies, isotope implantation and tumor resection [6, 7, 8, 9, 10]. Neurosurgery has played a leading role in the early development of IGS, most probably since accurate positioning of medical instruments and minimizing the damage of the sensitive intracranial anatomy is critical for a successful surgery. However, the continuous change of anatomy during surgery caused by manipulation of the surgeon or patient's breathing introduces challenge to IGS. Through the years, IGS rapidly evolved for orthopedic and trauma surgery, since bones are typically non-deformable during surgery. The first clinical application of image guided orthopedic surgery (IGOS) was for placement of lumbar pedicle screws as reported by Nolte LP et al. in 1995 [11]. These IGS technologies are reviewed in [12, 13, 14, 15, 16]. Various approaches and clinical applications of IGOS are outlined in [17, 18, 19, 20, 21, 22, 23, 24, 25]. Image guided orthopedic surgery is also knwon as computer assisted (or aided) orthopedic surgery (CAOS) in many literatures.

IGOS solutions can be generally divided into four based categories: preop-CT, 2D C-arm fluoroscopy, 3D C-arm fluoroscopy and image-free. IGOS solutions have been employed in many different clinical applications in orthopedics, e.g. spinal surgery, pelvic surgery, total hip arthroplasty, total knee arthroplasty, anterior-cruciate ligament reconstruction, reconstruction and trauma surgery. Potential clinical benefits and challenges of using IGS solutions have been discussed in the review articles [12, 13, 14, 15, 16, 17, 18, 19, 20, 21, 22, 23, 24, 25]. Employing IGS solutions for orthopedic surgery could reduce the invasiveness of procedures, decrease the variability of surgical outcomes, increase the reproducibility of surgeons' performance, narrow the gap between exceptional and standard clinical cases, and reduce radiation exposures to both surgical team and patients. IGS could enable new minimally invasive solutions, allowing surgeons to perform operations that were previously considered too dangerous. It also allows quantification of surgical procedure and thus a quantitative comparison between plan and execution. Potential problems of employing IGS solutions include complex system

setup, e.g. calibration procedure before each surgery and additional equipment within the crowded operating room. For many IGS solutions, surgeons and even surgical teams need to be trained to understand the underlying concept in order to make use of the IGS solutions and be aware of potential pitfalls. More detail on the challenges of using IGS solutions for orthopedics will be discussed in section 1.4.

## 1.2 Building Components of IGOS

The essential component of IGOS is the visual data of treated anatomy inside the patient's body. Established medical imaging is the main and direct way to obtain information of the treated anatomy without serious invasive procedures. The treated anatomy, medical images, and surgical instruments locate separately in different coordinate systems. Fusion of relevant surgical information that provide surgeons enhanced visual feedbacks and guidance becomes an indispensable component of IGOS. For this, computer based registration and tracking methods are applied to build mathematical spatial relationship between different information modalities. User-system interaction is another necessary component, since an intuitive way of presenting information on a friendly user interface play an important role for users to take full advantage of IGOS.

### 1.2.1 Imaging Techniques

Image guided interventional procedures are in some way assisted by the interactive use of medical images, which are acquired before or during surgery. Since the advent of X-ray imaging, various medical image technologies have greatly evolved in the past centuries. Surgeons could now see inside the patient's body and be guided to perform operation by what they observe in the image. The employment of medical images enables the minimally invasive procedure by offering indirect image based feedback instead of direct eye based feedback. It reduces the risk of infection and damaging the sensitive tissue or anatomy and thus could eventually improve the quality and lower the overall cost of surgery. Modern image guided surgical solutions further improve the surgeons visual perception and offer guidance by tracking the movements of the anatomy and instruments, and by fusing different images.

The physical principles of various medical imaging are well explained in [5]. Wolbarst and Hendee [26] have reviewed the medical imaging technologies including some of recently inventions, such as molecular imaging. Other review articles [17, 18, 19, 20, 21, 22, 23, 24] discuss different medical image modalities and imaging devices for image guided orthopedic and trauma surgery. In the following section we briefly discuss the common modalities used during orthopedic and trauma surgery.

#### 1.2.1.1 X-ray Imaging

The physical principle of X-ray imaging is measuring attenuation of X-ray photons passed through the human body on the detector. X-ray imaging is best suited for imaging bony structures among all modern medical image modalities, since bones have a high X-ray

attenuation compared to the surrounding tissue. Thus, it is the most used image modality for IGOS. X-ray imaging can be classified into two categories: 1) projection approaches, such as standard radiography and fluoroscopy, and 2) computed tomography approaches, such as CT. One common and major drawback of X-ray imaging techniques is inevitable ionizing radiation. Radiation exposure has been reported to increase the risk of fatal cancer [27, 28] and genetic defects [29]. Necessary protection against radiation should be adopted.

C-arms are interventional devices capturing projection X-ray images. One C-arm consists of a tube that emits X-ray photons and a photon detector mounted on two ends of a C-shape arm (see figure 1.1). C-arms are commonly categorized into stationary and mobile solutions. Stationary C-arms are mainly used for angiography, while mobile C-arms are commonly used during orthopedic and trauma surgeries, because they are compact, versatile, portable and providing real time imaging. For image guided surgery, standard mobile C-arm X-ray imaging suffers from two problems. The first is geometrical distortion mainly due to the curved surface of the detector as well as mechanical C-arm sagging from gravity. C-arm X-ray distortion correction is presented in section 2.2.1.2. The second is that it provides two dimensional projections of the three dimensional anatomy; thus the information along the X-ray beam is lost. However, some modern mobile C-arms are capable of reconstructing 3D volume from a set of 2D projection images intra-operatively, which is named cone-beam CT. Stuebig et al. [30] have performed a study to compare the performance of C-arm 3D imaging of Siemens Iso-C 3D and Ziehm Vario 3D. Kendoff et al. [31] have evaluated the utility of 3D imaging in articular fracture reconstruction. Kendoff et al.[32] compared the accuracy of 3D C-arm imaging with 2D C-arm imaging and CT imaging in evaluating acetabular fracture displacement and implant placement.

(a) (b)

Figure 1.1: (a) A typical mobile C-arm fluoroscope used during orthopedic surgery; (b) Acquired projection X-ray images displayed on monitors. The images are taken from a surgery performed by Dr.med. Peter-Helmut Thaller at Klinikum Innenstadat, LMU, München

X-ray computed tomography (CT) imaging provides three dimensional data by stack-

ing a series of 2D slices that are created by tomography method using computer processing. A typical CT scanner has X-ray source and detector (array) rotating around the interested anatomy in order to acquire the X-ray attenuation profiles, from which the slices of the anatomy can be computed. CT images are almost the ideal image modality for orthopedic surgery. It is regarded to be geometrically accurate [33], but suffers from intensity artifacts when metallic objects are presented in the imaging field due to strong attenuation of the metal. Many works have been done to reduce such artifacts in CT, e.g. higher energy X-ray beams [34], interpolating the missing projection data [35, 36, 37, 38, 39], and in cone-beam CT e.g. tracking the position of the metal [40]. Due to their size, a larger amount of radiation when compared to X-ray C-arms, and significant cost, CT scanners are rarely deployed in operating rooms. Thus, CT images are mainly acquired pre-operatively for diagnosis and surgery planning, and also for representing the bony strutures in computer aided surgery. Figure 1.2 shows a CT scanner and a generated CT image.

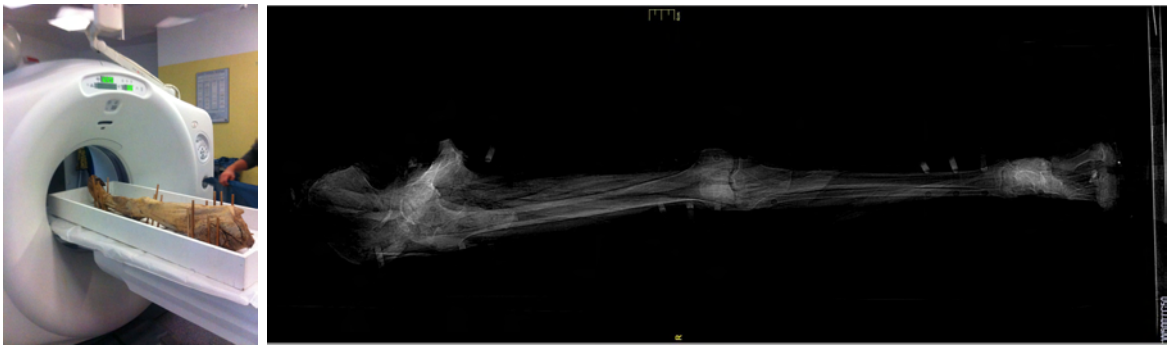

(a) (b)

Figure 1.2: (a) A CT scanner (Siemens SOMATOM Sensation 64-slice configuration) used for taking the CT image of a human corpus leg; (b) A CT image slice of the human corpus leg on the frontal plane .

#### 1.2.1.2 Magnetic Resonance Imaging

Magnetic resonance imaging (MRI) is a powerful imaging technique for visualizing soft tissues. It is especially useful in imaging the brain, muscles, the heart, and cancers compared to X-ray imaging. Therefore, MRIs are mainly used for diagnosis in neurological, musculoskeletal, cardiovascular, and oncological diseases, but not widely used for orthopedic surgery. 3D MRI images (see figure 1.3(a)) can be generated by MRI scanners. Compared to CT using ionizing radiation to generate images, MRI use non-ionizing radio frequency (RF) signals to acquire its images, which is based on the excitement of nucleis within a strong magnetic field. MRI images could suffer from both geometric and intensity distortions. Geometric distortions, which are mainly caused by inhomogeneity of the magnetic field and non-linearity of the magnetic field gradients, have been studied in [33, 41]. Some modern MRI scanners integrated the geometric distortion correction.

Phantom based distortion correction schemes can be applied to further improve the correction [42, 43, 44]. Recent developments in intensity inhomogeneity correction are reviewed in [45, 46]. Intra-operative MRI is not widely available, mostly because it requires the specialized interventional suites as well as its image quality being low.

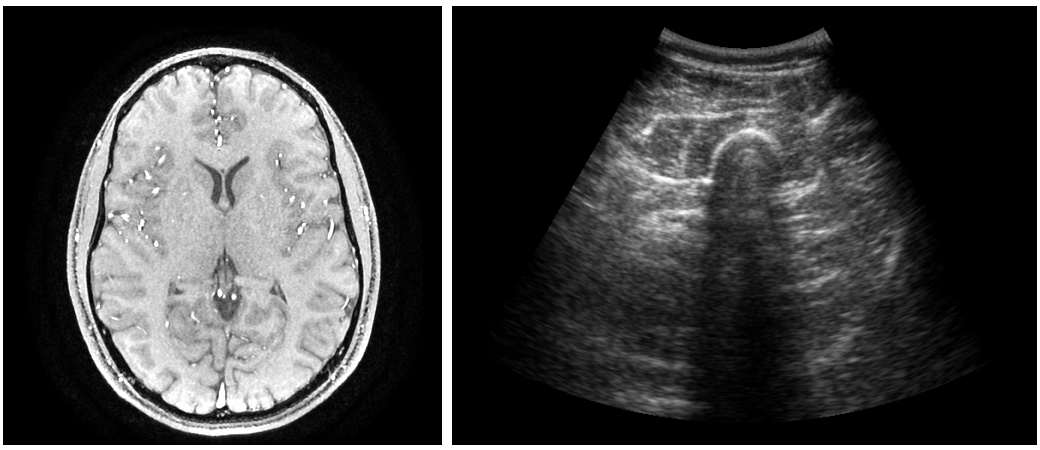

(a) (b)

Figure 1.3: (a) A MRI image slice of human brain on the axial plane; (b) A 2D Ultrasound slice of human leg on the axial plane.

#### 1.2.1.3 Ultrasound Imaging

Ultrasound (US) imaging (also referred to as ultrasonography) is mainly used to capture the shape, structure and pathological lesions of muscle, tendons, and many internal organs. The physical theory of US imaging is using a US probe to generate sound waves passing through the body and measure the echo. A physical gas contact between the probe and the anatomy is required because the nature of ultrasound waves in gas. The US probe is generally connected to a computer that processes the measured echo and visualizes the data as an image. Ultrasound images (see figure 1.3(b)) are hard to interpret due to the images suffering from variable contrast, speckle, and shadowing artifacts. It increases the difficulties for an operator to interpret the 2D slices because they do not know the exact direction where the slices are taken. Therefore, a comprehensive interpretation of the 2D slice images depends on the experience of the operator. 3D ultrasound images can be generated by either tracking a 1D US probe to construct 3D from a stack of 2D images with known acquisition positions, or using a 2D US probe to directly acquire a 3D volume. The US imaging machines are relative cheaper and portable compared to CT scanners, MRI scanners or C-arm machines. US imaging has primarily been used as real time examination to evaluate soft tissue structures, fracture union and reunion, infection, ligamentous injury, and nerve compression for trauma and orthopedic treatments. For IGOS, US imaging has been used as a non-invasive method to generate a 3D surface of a patient bone by tracking the US probe and a dynamic reference object (DRO) which is rigidly attached to the bone in one coordinate system [47, 48]. The registration of

the generated bone surface and the CT volume of the bone will allow tracked surgical instruments to be aligned with the CT image or a pre-operative plan.

#### 1.2.1.4 Optical Video Imaging (Visible Light)

Optical video imaging (visible light) is well employed in endoscopic surgery, e.g. bronchoscopy, laparoscopy and arthroscopy. They aim to obtain a normal vision within the patient's body without serious trauma of the patient by inserting an optical instrument with video cameras at the proximal end through small incision (port) or natural opening (e.g. bronchoscope introduced trough nose and trachea into the airways). Optical video images alone are not commonly used in orthopedic surgery to obtain the anatomical information, since it cannot penetrate the skin surface to image the underlying bone structures. Navab et al. [49, 50] propose a novel intra-operative video augmented X-ray imaging system by attaching a standard mobile C-arm with a video camera and mirror construction near to the X-ray source (see figure 2.2). The combination of the X-ray and optical images that visualize the bone and live video in a common image frame opens a new direction for medical imaging in orthopedic surgery.

#### 1.2.1.5 Other Imaging Techniques

Positron emission tomography (PET) and SPECT (Single Photon Emission Computed Tomography) are nuclear medicine imaging techniques using gamma rays. Both provide 3D information of functions or metabolism of the body compared to 2D X-ray images, CTs and MRIs. PET is mainly used in the medical fields of cardiology, neurology, and oncology. SPECT is capable of providing information about blood flowing to tissue therefore can be used as a diagnostic tool to detect stress fracture, spondylosis, infection, and tumor. The fusion of SPECT or PET images with CT or MRI images [51, 52] allows visual physiologic information to be registered with detailed anatomic map so that tissue function can be correlated directly with tissue structure. The fusion can be achieved by using a composited machine, e.g. CT/PET scanner [51], or by employing image registration methods to align obtained images [52].

In addition, some other recently developed medical image modalities, e.g. near-infrared imaging, terahertz imaging, and microwave imaging, have been reviewed in [26].

### 1.2.2 Fusion of Relevant Surgical Information

It is definitely necessary for a successful surgery to register the medical images to the corresponding anatomy and to locate surgical instruments, and it is a challenge for surgeons to mentally establish the spatial relation between them. Therefore, a key component in modern image guided surgery is to fuse these informations by aligning them into one common spatial coordinate system.

#### 1.2.2.1 Segmentation

Image segmentation is primordial in delineating the anatomy under surgery for usual assessment or for subsequent registration between imaging modalities. There are various segmentation algorithms being developed, such as simple threshold and region growing methods and more complex algorithms like graph cuts [53]. Some recent works on segemntation are based on active contour models [54], level sets [55, 56], or atlas registration [57]. However, there does not exist a fully automatic segmentation solution that can be applied across different imaging modalities and anatomical structures. To obtain accurate results, segmentation procedures often involve some form of interaction from users, e.g. specifying suitable parameters or roughly selecting an initial segmentation region.

#### 1.2.2.2 Registration

Aligning multiple data sets into a common coordinate system such that the locations of corresponding points coincide is defined as registration, which has been studied extensively both for medical and non medical applications [58, 59, 60, 61, 62, 63]. One major challenge in medical registration is accounting for deformable anatomical structure, which is still a very active area of research. For image guided orthopedic surgery, rigid registration methods are commonly employed, as bones are assumed to be non-deformable. The main purpose of registration for IGOS is aligning pre-/intra-operative medical images and patient's bones.

The most robust and mature registration used in IGOS is 3D/3D paired point based methods. In order to obtain the point correspondences, the most obvious way is to identifying corresponding anatomical landmarks in two different modalities, which could be error-prone due to poor localization of the landmarks. Fiducial based solutions have been proposed to improve the accuracy of point localization. The fiducial markers can be implantable, i.e. fixed to the treated anatomy. This requires additional surgical procedure and usually yield more accurate registration. Skin adhesive fiducials can be attached on skin surface without additional invasive surgical procedures, but skin movement between data acquisitions could compromise the accuracy of registration. Thus, procedures that can tolerate larger registration errors may be best suited for these markers. Intra-operative identification of the location of fiducial markers attached to patients is generally performed by using a tracked calibrated probe to touch the fiducial markers.

The limited points and their spatial arrangement could alter the registration accuracy. Surfaces represented by a points cloud can be used for robust and stable registration. In this case, the point correspondences are generally not available. The iterative closest point (ICP) method is used to find the transformation between two point sets without known correspondences. Several ICP methods have been developed [64, 65, 66, 67, 68]. ICP requires an initial guess, which can be computed form paired point registration using the anatomical landmarks. For pre-operative images, the points cloud of the surface can be obtained as the result of segmentation. Intra-operative acquisition of the point cloud of the surface is mainly achieved by touching the anatomical structures using a tracked probe. Alternatively, surface can be generated non-invasively by using ultrasound imaging. Surface based registration has been employed and evaluated in different image

guided orthopedic surgical procedures, e.g. CT-based image-guided spine surgery [69, 70], tumor resection in pelvis [71], hip surgery [72], and total knee arthroplasty [73]. Talib et al. [48] compare the use of a tracked pointer and ultrasound for obtaining surface points of two cast proximal femurs.

Maurer et al. [52] proposed to combine the surface and implanted fiducial markers to register CT images of the head to physical space. They demonstrated that using few bone implanted markers can improve the accuracy of the surface based registration.

2D/3D registration is employed to register the pre-operative images into C-arm X-ray projection geometry. Algorithms can be roughly classified into geometric feature-based [74], intensity-based [75, 76], and hybrid approaches [77, 78]. All 2D/3D registration algorithms are iterative and need an initial coarse registration, which can be obtained from the clinical setup according to the patient's position and the intra-operative imaging view, or using paired point registration based on skin adhesive markers (or anatomical landmarks).

If the imaging devices, e.g. C-arms, is tracked during image acquisition, the position of the acquired image is known relative to the tracking coordinate system. Thus the acquired intra-operative 2D or 3D images can be inherently aligned into the common tracking coordinate system.

#### 1.2.2.3 Tracking

In order to locate the surgical instruments with respect to the treated anatomy or implants in real time, computer aided tracking technology is employed to determine the positions and orientations of the instruments, anatomy, and implants in a common tracking coordinate system. Several tracking solutions are proposed for image guided surgery, such as encoded mechanical arms, optical ego-motion (self-motion) tracking, fiber optic based devices (ShapeTapeTM), optical tracking, electromagnetic tracking, ultrasonic based tracking. A brief comparison between these tracking solutions is presented in [12]. As discussed in [12, 79], an ideal tracking system for image guided surgery should have the following properties: small in physical size; complete (estimates all six degrees of freedom); accurate (error less than 1mm and $0.1^o$); fast (refresh rate of 1,000Hz with a latency of less than 1ms, regardless of the number of deployed sensors); concurrent (tracks multiple objects concurrently); line of sight (does not require line of sight); robust (not affected by the environment, e.g. light, sound, magnetic fields); large working volume; wireless (sensors are wireless and can function for several hours; inexpensive.

For modern image guided orthopedic surgery, the optical tracking method is mostly used. It employs at least two optical cameras to track at least three fiducial markers in a rigid arrangement construction that is fixed onto the tracked object. Compared to other solutions, optical tracking is robust to the operation environment, has enough working volumes for most orthopedic surgeries, provides a sufficient real time update rate, and can track multiple targets concurrently. The major drawback is the requirement of line of sight, i.e. requiring no occlusion between the tracking camera and tracked fiducial markers. The fiducial markers attached to the instrument or anatomy can be categorized into active markers, i.e. light-emitting diodes (LED), and passive marker, i.e. light-reflecting spheres. The active markers need to be powered using cables or wireless

with battery. The passive markers do not need power supply. The wireless solutions require a unique configuration of fiducial markers for each tracked target in order to distinguish among the tracked targets. Many works have been conducted to evaluate the positional accuracy of the optical tracking systems employed for image guided surgery [80, 81, 82, 83, 84].

### 1.2.3 User-System Interface

Modern image guided surgery systems provide rich surgical information but require interaction from the surgeons to adjust system settings for an optimal performance. It is necessary for an IGOS system to present to surgeons the visual information in an intuitive and understandable way and to enable the surgeons to manage the system efficiently. The user-system interface can be divided into two categories, information presentation that includes visualization methods and display solutions, and user interaction that is the way the user interacts with the system.

#### 1.2.3.1 Information Presentation

**Visualization** Image guided surgery systems present surgeons with visual data about the surgical procedure, which is generally shown in display devices. Modern display devices are two dimensional screens, which introduces challenges to display 3D data. 3D visualization solutions have been developed to concisely and intuitively convey the relevant information of 3D volumetric data as 2D images. The most common way of visualizing 3D data is volume re-slicing that displays an image created by placing a 2D plane through the 3D volume. In most cases, the images are generated from the standard axial, sagittal and coronal planes, with which surgeons are familiar.

Surface rendering is an indirect way of visualizing the anatomical structure of 3D data, which is mainly used in computer graphics. For visualizing medical 3D images of anatomies, this method requires a pre-segmentation of the surface, and visualization accuracy depends on the segmentation accuracy. Direct volume rendering (DVR) methods do not require explicit segmentation of anatomical structures from 3D data. However, a suitable transfer function, a mapping from volume data to color and opacity values, must be defined to render a desired 2D image. Kutter [85] discusses the basic theory of DVR, reviews DVR using GPU ray casting, and proposes an efficient GPU-accelerated volume rendering method. Maximum intensity projection (MIP) is a traditional volume rendering method. It projects the voxels with maximum intensity along the parallel rays traced from the viewpoint to the plane of projection. However, the resulted 2D images do not provide an accurate depth perception of the visualized volume data. Surface rendering and volume rendering techniques for 3D CT images have been evaluated in [86, 87, 88].

Visual data stems from different modalities, e.g. CT images, X-ray fluoroscopy images, optical images, or virtual model images. Merging and fusing different modalities enhances intra-operative visual feedback for many image guided interventions. Navab et al. [49, 50] introduce a system to overlay C-arm X-ray images onto co-registered optical video images. They have used a simple alpha blending (or alpha compositing) method to merge the X-ray images over the optical video images. Gao et al. [89] propose a registration method to

align (3D) transesophageal echocardiography (TEE) and fluoroscopy for the guidance of cardiac interventions. For image visualization, they also use the alpha blending method.

Intensities in 2D X-ray images are computed by accumulating absorption from the complete ray traversal through the body and do not correspond to a specific depth along the ray. For fusion of visual data with 2D X-ray images, the alpha blending method could result in misleading depth cues from the fused view. Wieczorek et al. [90] develop a novel interactive X-ray perceptual visualization (IXPV) method to improve the depth perception of a single 2D X-ray image by retrieving a priori knowledge which has absorptive properties from pre-operative CT. Figure 1.4 shows the fusion of an X-ray image and ultrasound slice for animal cadaver cow leg using alpha blending and IXPV respectively. Visual composition of real and virtual anatomy of the patient is an important factor for medical augmented reality (AR) applications. Kutter [85] develops a GPU-accelerated medical AR visualization solution for head mounted display devices to optimize perception, performance and quality of medical AR visualization. Bichlmeier [91] proposes a contextual in-situ visualization method to generate artificial depth cues for support a correct and intuitive perception of depth, pose, and shape of all involved objects in an AR scene (see figure 1.5(b)).

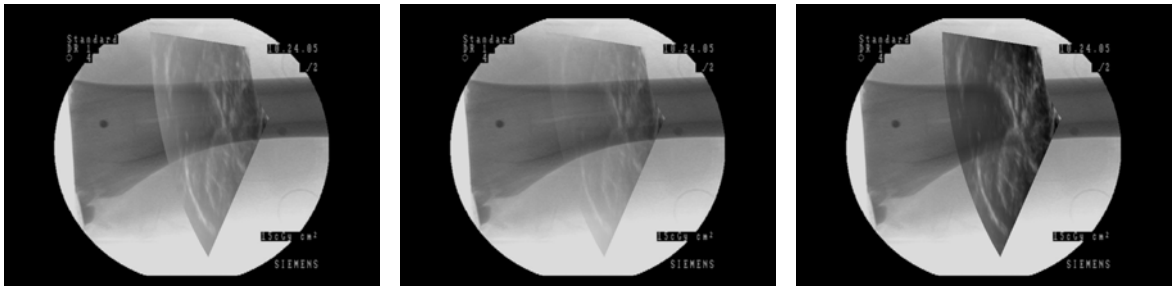

(a) (b) (c)

Figure 1.4: Animal cadaver cow leg visual assessment. (a) Fusion using 2D blending of ultrasound and X-ray; (b) The depth of field technique. (c) When applying the IXPV technique the tibia is now displayed correctly in front of the ultrasound plane. Image courtesy of Matthias Wieczorek [90]

**Information Display** Currently, the majority of image guided orthopedic surgical systems use standard 2D monitors for displaying images. The screen is commonly divided into four sections that display axial, sagittal, coronal views, and 3D rendering of the anatomy. The main drawbacks of 2D monitors are 1) they are usually placed away from the operation site, which leads surgeons to switch their focus between the patient and display; 2) one dimensional information of 3D volumetric data could be lost.

Head mounted display (HMD) devices have been proposed for medical in-situ to avoid complex mental mapping from 2D monitor images onto the 3D patient. Bajura et al. first proposed the usage of augmented reality technology based on a HMD device that visualizes the acquired ultrasound image of a pregnant woman's abdomen [92]. Fuchs et al. [93] present an optical-see-through HMD system to assist understanding of 3D

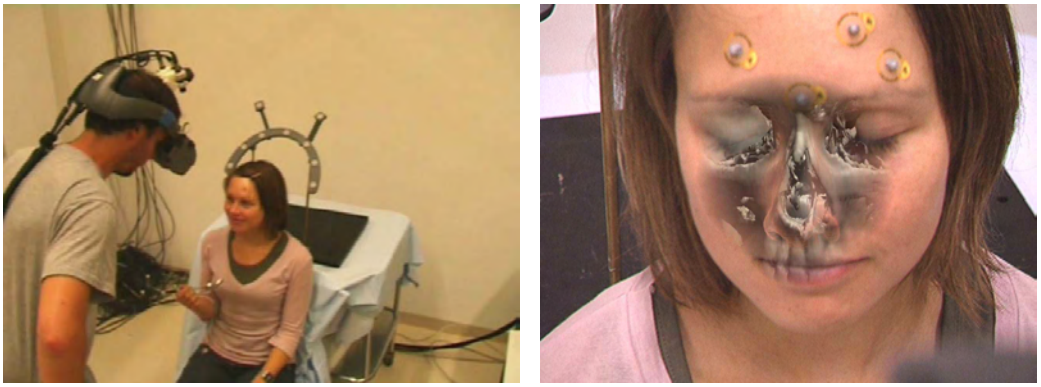

(a) (b)

Figure 1.5: Augmenting video images of a human head by the virtual anatomy of brain using video-see-through head mounted display (HMD). (a) HMD system setup; (b) Contextual in-situ visualization of the video image and related virtual anatomy, which is displayed on the HMD. Image courtesy of Christoph Bichlmeier [91].

anatomical structures during laparoscopic surgical procedures. Sauer at al. [94] report a video-see-through HMD solution to display a stereo video view of patient augmented by a graphical representation of anatomical structures that are segmented from image images. They have performed pre-clinical evaluation for neurosurgery. Traub et al. [95] introduce a hybrid intra-operative visualization solution based on combing HMD display and 2D slice rendering for orthopedic and trauma surgery, and the solution has been evaluated based on phantom study of drilling. Bichlmeier demonstrates several intra-operative visualization techniques based on HMD devices for supporting orthopedic and trauma surgery, e.g. virtual mirror [96, 97, 98] and contextual anatomic mimesis (see figure 1.5) [99].

Alternative to 2D monitor and HMD solutions, a display solution of combining a monitor and a semi-transparent mirror has been proposed for image guided surgery. Several systems have been developed to enable surgeons to view patients directly through the mirror with the reflection of images from the monitor [100, 101, 102].

However, HMD and semi-transparent mirror based display solutions are still the subject of research. The major challenges for their clinical translation is: (i)complex system setup that needs additional cables, (ii)system calibration, (iii)poor comfortability due to wearing the HMD or placing the mirror between the surgeons and the treated patients, and (iv)unacceptable overlay accuracy of virtual and real objects caused by a poor registration or tracking performance.

#### 1.2.3.2 User Interaction

Modern image guided surgical systems (or solutions) often require user interactivity. The general challenges for user interaction are optimized space organization, intuitive and user friendly to use during stressed operation, and the sterilization within the space of the surgical field.

It is impractical to employ the traditional keyboard-mouse solution, since they cannot be sterilized and are too cumbersome for use in the crowded environment close to the patient. Several strategies have been proposed for the user interaction including touch screens, foot switches, tracked virtual keypads, speech recognition, visual marker detection, and gesture recognition. Tracked virtual keypads and voice recognition solutions have been evaluated over 40 image guided spine surgical procedures [103]. Bichlmeier [91] develops and evaluates three user interaction solutions for HMD based medical augmented reality applications, which are voice recognition, computer vision based gesture recognition, and foot pedal. Graetzel et al. [104] present a computer vision based hand gesture recognition for user interaction. Samset et al. [105] propose to detect the event of the occlusion of a visual marker using a video camera and use this event as an user input for computer assisted surgery. Schwarz et al. [106] introduce a gesture-based interaction solution that surgeons can customize to personal gestures by training the required gestures based on low-dimensional manifold learning. Wireless body-worn inertial sensors are used in their solution in order to avoid issues of camera-based systems, such as sensitivity to illumination and occlusions.

## 1.3 Verification, Validation and Evaluation

Many IGS systems have been introduced in the last decades, e.g. systems using external camera tracking for navigation or augmented reality visualization. All of them provide various promising solutions to simplify surgery and/or improve patient treatment. However, very few IGS systems have succeeded to become clinically accepted and even a small number of them were integrated into daily clinical routine. Development of novel IGS solutions involves a long and complicated process from the initial idea until their acceptance and use for clinical applications. This process includes the phases of clinical problem investigation and analysis, problem modeling, system and algorithm design, implementation, system verification and validation, and finally evaluating the system in terms of its clinical outcome. The practicability, efficiency and clinical suitability of a system are mostly confirmed within the clinical evaluation phase.

The terms verification, validation, and evaluation describe different parts of the assessment in an image guided surgery system. Verification refers to the process of ensuring that the system was built according to the specified requirements. Validation refers to the activity of ensuring that the system fulfills the purpose it was designed for [107]. Evaluation refers to the action of analyzing merit, worth, and significance of a system in various dimensions.

### 1.3.1 Multi-Stage based Evaluation Strategy

Evaluation of the image guided surgery solutions definitely involves different aspects ranging from technical system properties, towards the clinical impact on surgical performance and patient outcome, and further towards social and legal impacts. The focused evaluation aspect depends on the system development phase.

Different methodologies of multi-phase based evaluation have been proposed for health care technology. A six-level strategy was proposed for evaluating the efficacy of diagnostic imaging [108]. These six levels are 1) technical quality; 2) diagnostic accuracy and sensitivity; 3) impact on physician's diagnostic thinking; 4) efficacy on the patient management plan; 5) efficacy on patient outcomes; 6) societal costs and benefits of a diagnostic imaging technology. Verbeeck et al. [109] present a two-phase protocol, which are the functional specification phase and the clinical acceptability phase, for the technical and clinical evaluation of a system for the planning of stereotactic neurosurgical interventions. Goodman [110] proposes a ten-steps for health care technology assessment: 1) identify assessment topics; 2) clearly specify assessment problem or question (i.e. assessment objective); 3) determine locus of assessment (e.g., who will perform the assessment?); 4) retrieve available evidence; 5) collect new primary data; 6) interpret evidence; 7) synthesize evidence; 8) formulate findings and recommendations; 9) disseminate findings and recommendations; and 10) monitor impact. The assessment of IGS systems has been discussed in detail by Jannin and Korb [111]. They propose an assessment framework with six levels classified according to the progress of the clinical acceptance, 1) technical system properties; 2) diagnostic reliability (indirect) and therapeutic reliability (direct); 3) surgical strategy (indirect) and surgical performance (direct); 4) patient outcome; 5) economic aspects; 6) social, legal, and ethical aspects.

### 1.3.2 Validation of Technical Accuracy

Image guided orthopedic surgery systems are generally built based on several different components, e.g. medical imaging, image registration, and tracking, to provide intra-operative visualization or guidance for surgical tasks. Technical and functional aspects of an IGOS system must be validated for the employed individual components separately, as well as the overall system. Simon et al. [112] present a study to validate the accuracy of a CT based navigation solution for total hip replacement. They have first indentified and evaluated potential error sources from different system components, e.g. registration, tracking, etc. For validation of the overall system, they have evaluated how well a cavity cut in a femur match the planned cavity location. It is recommended to first conduct a clinical bench test using highly accurate phantom in a well controlled laboratory environment followed by a clinical outcome study in a simulated operating room setting utilizing cadavers [113]. Medical image processing is one of the most critical components for an IGOS system. Jannin et al. [114] discuss criteria for the validation of medical image processing, which are accuracy, precise and reproducibility (or reliability), robustness, consistency or close loop, fault detection, functional complexity, and computation time. They also present the principal technical requirements for validation, including standardization of validation methodology, design of validation data sets, and validation metrics. Complete validation data sets for the validation as suggested in [114] should include numerical simulations; realistic simulations from clinical data sets; physical phantoms; and clinical data sets distinguished from absolute ground truth to lack of ground truth.

### 1.3.3 Evaluation of Clinical Relevance and Impacts

It becomes a critical point to evaluate the practicability, efficiency and clinical suitability of an IGOS system. Compared to the validation of technical accuracy, it requires a more tight collaboration between scientists, medical experts, and engineers to define evaluation protocols and to conduct evaluation experiments. Moreover, evaluation criteria could vary depending on clinical applications and IGOS systems, and involved factors could be various, e.g. human factors and system user interface. It is difficult to define an absolute ground truth. Questionnaires are often employed as an efficient tool to measure quality factors such as clinical relevance or the confidence of the surgeon. Questionnaire based evaluation was employed to assess the surgical impression and clinical functionality of IGS systems for neurosurgery [109, 115]. Image guided surgical procedures involve various sophisticated technologies, delicate instruments, complex setups, and modified surgical workflow. These can offer space for human errors. Jiang et al. [116] introduce "Failure modes & effects analysis" to systematically study human factors and human errors in image guided surgery. As it is difficult to build the absolute ground truth, clinical impact of a newly developed IGS solution is often evaluated by comparing it with a conventional solution. Traub et al. [117] propose a surgical workflow based evaluation to investigate the clinical performance of vertebroplasty using the Camera Augmented Mobile C-arm(CamC) system compared to using intra-CT based solution. This interesting initial study involved only one surgeon and a very small number of samples, and could therefore not show significant results. In this work, the concept of surgical workflow based evaluation is extended and applied to assess the clinical impact of the CamC system, which will be presented in sections 2.4 and 2.5.

### 1.3.4 Cost Evaluation

Image guided solutions provide several advantages compared to traditional surgical techniques. However, the expense of employing new IGOS solutions is a hurdle for their clinical acceptance, and thus it should be analyzed in order to justify the clinical benefits.

The cost can be divided into direct costs and indirect costs. The direct costs include the investment of purchasing or leasing of hardware and software and service associated with use the systems, e.g. tracking devices, instrument tray, navigation computer with the software modules, and tracking camera. The indirect costs include the loss of productivity associated with learning the technique as well as the extra time in the operating room utilizing the technique, e.g. hourly cost for an operating room and anesthesia professional fees [113].

Jolesz et al. [118] discuss the expenses of deploying an open-architecture intra-operative MR imaging system. Lavernia et al. [113] analyze the cost for total knee and hip arthroplasty using commercial IGOS systems. They define cost effectiveness as a percentage number, one hundred percent as the point at which the volume of yearly cases performed yields the reduction in revision and dislocation rates that compensates for the expenses. They show that IGOS in total hip arthroplasty is cost effective (cost effectiveness $> 100\%$) after low surgical volumes while in total knee arthroplasty does not become cost effective (cost effectiveness $< 100\%$). Watkins IV et al. [119] study the cost

effectiveness of thoracolumbar pedicle screw instrumentation using a commercial image guidance system consisting of NaviVision (Vector Vision-BrainLAB) and Arcadis Orbic C-arm (Siemens Healthcare SP). They show that employing the image guided solution may be cost effective compared to traditional techniques without image guidance in spine practices with heavy volume, that perform surgery in difficult cases, and that require long surgical times for the placement of pedicle screws. The cost saving of using IGS solutions compared to traditional solutions could potentially come from the reduced rate of revision surgery, reduced operation time, and the reduced hospital stay [119, 118].

## 1.4 Problem and Challenge

Image guided surgery solutions have been widely employed for a variety of clinical situations of orthopedics. Their clinical benefits have been proven, which include increase of accuracy, reduction of variability of surgical interventions, less invasive operations, reduction of radiation exposure to both surgeons and patients, and potential decrease of operation time. Although initial experiences appear promising, there are considerable potential pitfalls for using IGOS systems, which could lead to prolonged operation time, unacceptable clinical outcomes, and eventually overhead costs. Some of the major pitfalls that may occur during navigated orthopedic surgery have been summarized in [120, 121].

For IGOS, medical images are always required to be registered to the patients. Systems must provide false information if the registration is not fulfilled or the registration result is not valid. Unfortunately, failure is not always obvious, because the transition between exact matching and inexact matching is smooth. Potential error sources for a failed and inaccurate registration using pre-operative images could come from surgeons failing to exactly identify the predefined anatomical landmarks, or an inaccurate measurement of the position of the skin attached markers due to the movement of the skin relative to the bone. Bone implanted markers provide a high and reproducible accuracy, but require an additional intervention. Furthermore, the correct segmentation of the CT scan is a prerequisite for reliable registration, and the bone configuration between the acquisition of pre-operative images and intra-operative registration should be consist for a valid matching process. For C-arm based solutions, registration is achieved inherently by the calibration of the C-arm. However, the surgical operation may considerably change the bone structure. The registration is only valid when the current situation in situ still corresponds to the previously acquired images. In the case of an invalid registration, surgeons must be informed to update the image.

Tracking is an indispensable component for many IGOS systems to locate the surgical instruments and anatomical structures. The most used solution is optical tracking based on active infra-red light emitting diodes (LEDs) or passive infra-red light reflecting spheres. A direct line of sight is needed between the tracking camera and the tracked markers. The arrangement of the tracking camera should be carefully considered and evaluated depending on available space within the OR, the position of the staff around the operating table, the position of the treated anatomy, preferences of the surgeon, the cable length of the tracking system, and the working volume of the tracking camera. Light sources such as operating lights may interfere with the optical tracking. Letting the cam-

era face these intensive light sources directly should be avoided. Current well established registration and tracking methods for image guided orthopedic surgery rely on the rigid body principle. However, some slim tools, like drill bits or K-wires, can bend easily, which should be taken care.

Surgeons must understand the underling concept of the IGOS solutions, the complexity of usage of the IGOS systems, and their weaknesses. For this, the surgeons and even the whole surgical team should be intensively trained in order to maximize the benefits resulting from optimal operating of the system and minimize the negative effects resulting from wrong handling of the system or the technical insufficiency. Only the optimal performance of a navigation system will probably justify its significant investment costs.

## 1.5 C-arm X-ray Imaging for IGOS

The mobile C-arm is the primary X-ray imaging device in today's operating rooms and plays a vital role intra-operatively for guiding orthopedic and trauma surgeries, because it is compact, versatile, portable and providing real time imaging, as discussed in the previous sections. However, there are several distinct limitations to C-arm X-ray guidance: radiation exposure to patients and surgical teams, limited field of view of the anatomy and the difficulties in maneuvering to achieve a desired X-ray viewpoint. The aim of this dissertation is to propose novel image guided solutions enabling optimal X-ray guidance by taking into account the limitations of the C-arm.

In order to reduce radiation exposure, decrease the invasiveness of surgical procedures, and increase the reproducibility of surgeons' performance, navigation systems are often employed together with the C-arm in order to facilitate various surgical procedures. The basic concept of surgical navigation is the coupling of medical images and surgical actions such that surgeons could see instruments displayed in the same coordinate system as treated anatomy in real time. For achieving this, as shown in section 1.2.2, optical tracking systems are developed to detect and track the fiducial markers attached to the treated anatomy, the C-arm and surgical instruments, by using external optical cameras. Zheng et al. [122] employ an optoelectronic tracking system for their proposed augmented virtual fluoroscopy technique. This technique has a potential to reduce radiation for repositioning of bone fragments during close fracture reduction and osteosynthesis. Leloup et al. [123] use an optical tracking system to localize a C-arm, implants, and drilling devices in order to support distal locking of intramedullary nail. Particularly, many commercial IGOS solutions are implemented based on using the mobile C-arm and optical navigation system, such as FluoroNav (Medtronic Surgical Navigation Technologies, Broomfield, CO, USA) employed in [124], SurgiGATE system (Medivision, Oberdorf, Switzerland) used in [125] and NaviVision (BrainLAB AG, Feldkirchen, Germany) employed in [119]. One significant advantage of using such navigation is to reduce radiation exposure to the patient and surgical team by eliminating the need to obtain multiple images to update instrument for example. However, the common problems of the navigation solutions include considerable investment, calibration during surgery, cable spaghetti, and the requirement of line of sight.

The previously introduced CamC system [49, 50] that is built by attaching a video

camera and mirror construction to the C-arm provides a video augmented X-ray. Due to the mirror construction and an offline calibration, the video camera has the same geometrical view on the patient as the X-ray device. Therefore, the video augmented X-ray shows bone anatomy or implants co-registered with the live video displaying skin, surgeon's hands, and instruments. This has a potential to minimize radiation exposure for orthopedic and trauma surgery. Compared to the optical navigation solutions, the CamC technology is attractive from both clinical and economical points of view, as no additional separated devices and calibration are required during surgery. This dissertation investigates the surgical workflow in orthopedic surgery which would allow the effective use of the CamC system in terms of minimizing radiation exposure. X-ray images acquired by mobile C-arms have a narrow field of view and cannot visualize the entire bone structure of a lower leg within one single X-ray image. Acquiring several individual X-ray images to visualize the entire bone structure only gives a vague impression of the relative position and orientation of bone segments. This often compromises the correct alignment of fragments and placement of the implants in long bone reduction surgery. X-ray image stitching methods were proposed to enable the standard mobile C-arm to have exceptionally wide fields of view. Yaniv and Joskowicz [126] employ a radiolucent X-ray ruler and stitch X-ray images based on the segmented ruler features. This method requires sufficient overlapping areas between two consecutive X-ray images to estimate the planar transformation and thus introduces additional radiation exposure. Another method [127] employs a radio-opaque absolute reference panel and registers X-ray images into one common image coordinate system based on the known geometry of this panel. In our own previous work [128], we propose an X-ray image stitching method based on the CamC system. It uses the video images of the CamC system in combination with a visual marker pattern to estimate the planar transformation for creating panoramic X-ray images. However, all of the previously proposed methods suffer from parallax errors, which could introduce misalignment or ghosting to the generated panoramic X-ray images. In this dissertation, a method of parallax-free X-ray image stitching using minimum radiation exposure is proposed.

For trauma and orthopedic surgery, moving the mobile C-arm into the best viewing projection in regard to the anatomy is a routine surgical task, which requires time, skill and a lot of X-ray shots. This is because that, the complex kinematic chain of the mobile C-arms could lead to the acquisition of X-ray images from additional "gantry positions" that have no bearing on the treatment until the desired projection image is achieved. Many solutions and systems have been developed to facilitate C-arm positioning for acquiring a correct projection X-ray image. Matthews et al. [129] develop a solution for repositioning the C-arm by using an optical tracking based navigation system. Matthaeus et al. [130] present a complete robotized mobile C-arm developed by equipping all the C-arm joints with motors and encoders and closed-form solutions for the inverse kinematics have been found for automated C-arm positioning. Grezda et al. [131] use tilt sensing accelerometers for C-arm rotation encoding in order to track the C-arm angular and orbital rotations during the surgery. Lastly, several medical groups [132, 133, 134] have investigated the C-arm system equipped with laser aiming device for C-arm positioning and also for instrument placement. However, these previously developed methods are

based on standard mobile C-arms that only have five joints (five DOF), three of which are rotational joints and two are translation joints. This restricts the X-ray source in terms of reaching an arbitrary position and orientation, which in turns creates difficulties for a precise positioning of the C-arm. To address this issue, this dissertation introduces a solution for optimally and precisely positioning the C-arm to a desired view point by modeling the C-arm and table setup as an integrated 6 degrees of freedom (DOF) kinematic chain.

## 1.6 Contribution

This dissertation includes three major contributions to the field of interventional medical imaging for orthopedic and trauma surgery.

The first contribution is a surgical workflow based methodology for evaluating the clinical relevance and impact of novel IGS systems. Analyzing single workflow steps not only reveals individual strengths and weaknesses related to each step, but also allows surgeons and developers to be involved intuitively to evaluate and have an insight into the clinical impact of the IGS systems. Using a workflow based assessment is easier to generalize results for single workflow steps that are common to several procedures. The proposed surgical workflow based evaluation methodology is applied to assess the clinical performance of the Camera Augmented Mobile C-arm (CamC) system on 42 cow cadavers and 43 real patients in a close collaboration with medical doctors at Klinikum Innenstadt, München, Germany (see section 2.4 and 2.5).

The second contribution is an intra-operative parallax-free X-ray image stitching method based on enabling the mobile C-arm to rotate around its X-ray source center, relative to the patient's table (see chapter 3). Rotating the mobile C-arm around its X-ray source center is impractical and sometimes impossible due to the mechanical design of mobile C-arm systems. In order to ensure that the C-arm motion is a relative pure rotation around its X-ray source center, we propose to move the table to compensate for the translational part of the motion based on C-arm pose estimation. For this we employ a visual marker pattern and the CamC system. Unlike existing methods that cannot avoid parallax effects in the creation of panoramic X-ray images when imaging non-planar bone structures, we are able to produce a parallax-free panoramic X-ray image independent of the geometric configuration of imaged anatomical structures. Our method does not require a fronto-parallel setup or any overlap between the acquired X-ray images. The generated parallax-free panoramic X-ray image preserves the linear perspective projection property. This true panoramic X-ray image now can be treated as a single image obtained by a C-arm having an exceptional wide imaging field of view and also can be further processed by various computer vision or image processing algorithms that assume linear perspective projection, e.g. 2D-3D rigid registration of X-ray fluoroscopy and CT images. Taking into account that the economical issues in healthcare are of high importance for computer aided intervention solutions, the proposed approach of using a CamC system and a visual planar marker pattern for intra-operative parallax-free X-ray image stitching is also attractive from an economical point of view, since no additional calibration and no external tracking systems are required during surgery.

The third contribution is a method to model both the mobile C-arm and patient's table as an integrated kinematic chain having six DOF without constraining table position (see chapter 4). The closed-form solutions for the inverse kinematics problem are derived in order to obtain the required values for all C-arm joint and table movements to position the fluoroscope at a desired pose. The modeling method and the closed-form solutions can be applied to general isocentric or non-isocentric mobile C-arms. Having the 6-DOF C-arm model with the closed-form inverse kinematics solutions enables novel solutions for many advanced applications in the fields of surgical navigation and advanced X-ray imaging that require C-arms to be precisely positioned or repositioned relative to the patient's table, and also in other clinical fields such as cardiology or prostate brachytherapy imaging to name a few. Particularly, we present a novel approach for parallax-free panoramic X-ray imaging based on the inverse kinematics of the 6-DOF C-arm model. This allows surgeons to intuitively specify the position of an X-ray image in the panorama, and be automatically guided by the system on how much to move the C-arm joints and the table for a desired result.

Additionally, publications I authored or co-authored during this dissertation are listed in appendix B.

CHAPTER

# TWO

# CAMERA AUGMENTED MOBILE C-ARM (CAMC): VIDEO AUGMENTED X-RAY IMAGING

Orthopedic and trauma surgeries rely heavily on intra-operative X-ray images to visualize bone configuration and guide treatments, especially in minimally invasive surgery. Within the last two decades, mobile X-ray C-arms have become an everyday tool to acquire X-ray images during surgeries. However, the X-ray images of bone structures and implants are not directly aligned the real scene seen by surgeons. It is essential for surgeons to understand spatial relations between anatomy, implants, and surgical tools for a successful treatment. This often requires considerable mental effort, time, and radiation exposure, and thus introduces additional difficulties and potential human mistakes that can impair the quality of surgeries.

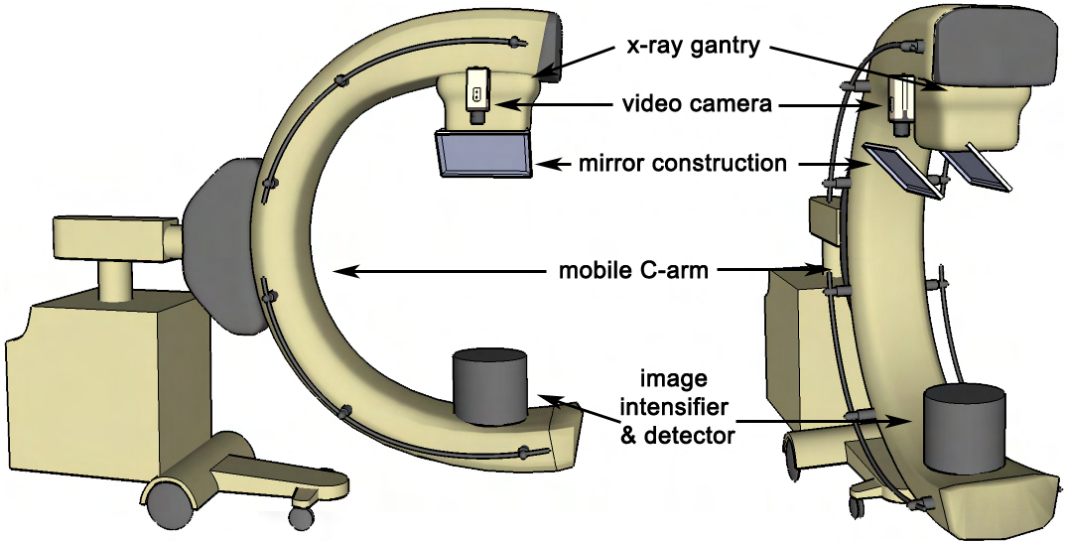


Figure 2.1: The Camera Augmented Mobile C-arm system setup. The mobile C-arm is extended by an optical camera. Image courtesy of Nassir Navab [50].

The Camera Augmented Mobile C-arm (CamC) system that extends a standard mobile C-arm by a video camera and mirror construction was introduced by Navab et al. [49, 50]

(see figure 2.1). By placing the video camera and mirror in such a way that the camera optical center and the X-ray source virtually coincide, the camera can have the same view of the patient as the C-arm X-ray. This allows the CamC system to provide an intuitive real-time intra-operative visualization of X-ray images co-registered with a live video (see figure 2.2). This technology is coined as video augmented X-ray imaging (VAX), meaning the overlay of X-ray and video images. As the spatial relations between bone strcutures, implants, tools and skin surface can be quickly and intuitively perceived in the overlay of X-ray and video images, surgeons could perform operations more confidently with less radiation exposure, reduced rate of potential surgical mistakes, and increased reproducibility. The CamC technology is attractive from both clinical and economical points of view, as no additional separated devices and calibration are required during surgery. Over forty patients were treated successfully with CamC support between July 2009 and March 2010. This is the first time that a medical Augmented Reality (AR) technology is used consistently in real orthopedic surgeries worldwide.

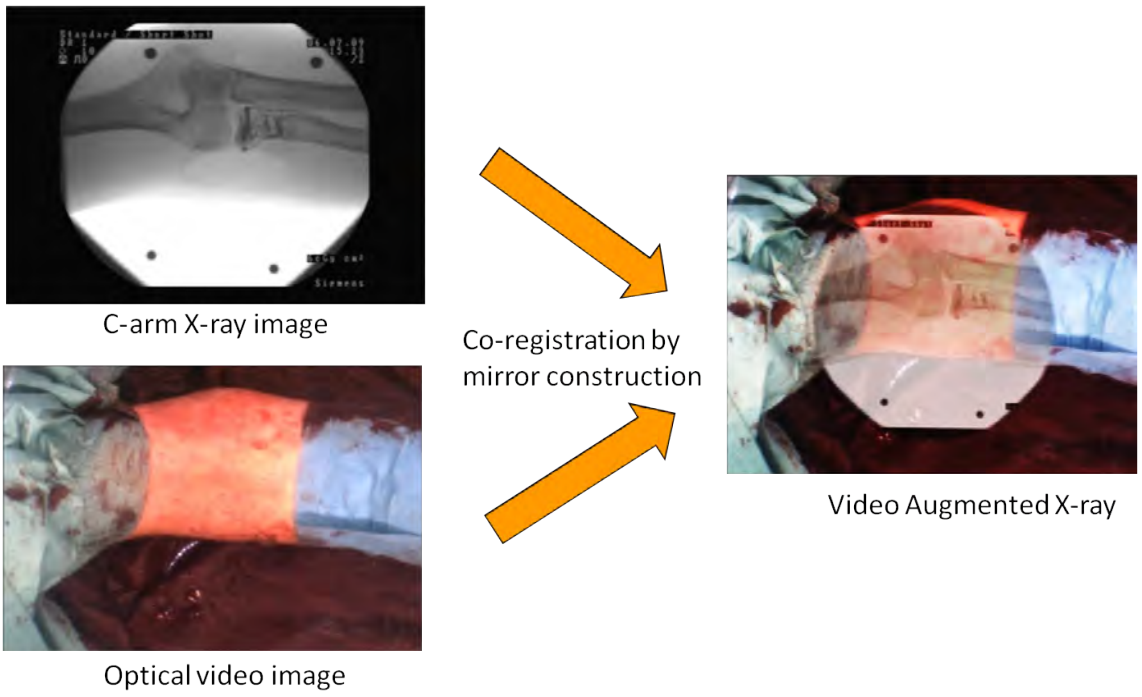


Figure 2.2: Thanks to a joint construction and calibration, the CamC system implicitly registers X-ray (upper-left) and video images (lower-left) to provide video augmented X-ray imaging (right). The pictures are from an elbow fracture reduction surgery under CamC support.

This chapter first presents the previous work related to the CamC technology in section 2.1. A practical and robust method for an accurate intra-operative video augmented X-ray imaging is explained in section 2.2. The construction of the first clinically used CamC system is described in section 2.3. A surgical workflow based evaluation methodology and a pre-clinical study of the CamC system based on 42 animal cadavers are discussed in section 2.4. Furthermore, a clinical study of the CamC system on 43 patients is presented

in section 2.5.

## 2.1 CamC: state of the art

### 2.1.1 Augmenting Intra-operative Medical Images

Augmented Reality (AR) supplements the real scene with a virtual scene. It has been widely used in areas such as manufacturing and repair, annotation and visualization, robot path planning, entertainment, and military aircraft guidance [135]. Lately, the operating rooms have welcomed AR technology for specific workflow tasks, and the technology has aided surgeons with surgical planning. Further, medical AR technology that enhances the surgeon's view of the patient with computer generated images of anatomy and tools in real time has been successfully applied in various disciplines of surgery, such as neurosurgery, orthopedic surgery, and maxillofacial surgery [136, 137]. It was shown that AR is a promising solution to improve the accuracy of surgical procedures, decrease the variability of surgical outcomes, reduce trauma to the critical structures, increase the reproducibility of surgeons' performance, and reduce radiation exposure [136, 137].

Most in-situ AR visualization systems augment the view of a surgeon or an optical video camera with pre-operative data based on various image registration techniques. Pre-operative data however cannot always represent the latest anatomical information. For this, intra-operative imageing has been employed for surgical AR, since the images can be updated during surgery. Stetten et al. [138] present a Real Time Tomographic Reflection (RTTR) system to augment one slice of 3D ultrasound images of the anatomy with its surface based on a half silvered mirror and a flat panel miniature monitor mounted in a specific arrangement. Fichtinger et al. [101] propose an intra-operative CT based medical AR system for visualizing one CT slice onto the patient in-situ thanks to a specific arrangement of a half transparent mirror and a monitor rigidly attached to a CT scanner. A similar technique was proposed for the in-situ visualization of a single MRI slice [102]. Feuerstein et al. [139] augment laparoscope video images with intra-operative 3D cone-beam CT by tracking C-arm and laparoscope using the same external optical tracking system. Wendler et al. [140] fuse the real time ultrasound image with synchronized real time functional nuclear information from a gamma probe based on optical tracking the ultrasound and nuclear probes in a common coordinate system. Wendler et al. [140] also propose freehand SPECT to augment the 3D reconstruction of radioactive distributions by a live video by using a calibrated optical tracking and video camera system [141]. A clinical study of the freehand SPECT system for sentinel lymph node biopsy over 50 patients is reported in [142]. Zheng et al. [122] introduce an augmented fluoroscopy by tracked bones and implants for minimally invasive diaphyseal long bone fracture reduction. All these systems require either tracking techniques or a specific arrangement of the imaging devices in order to align the different images or viewing geometries. However, AR has not been widely accepted, mainly because of its cumbersome system setup which includes a line of sight for tracking and on-site calibration and registration procedures. Furthermore, non-rigid registration, intra-operative image updates, display techniques, and user interface must be addressed for both reliability and ease of use required by the medical community.

### 2.1.2 Construction Concept

The CamC technology first emerged in 1999. It was developed by Navab et al. for online estimation of C-arm X-ray projection geometry for 3D cone-beam reconstruction [143]. In its infancy, the technology involved attaching a video camera near the C-arm X-ray source such that they have almost the same viewing direction, i.e. both optical axes are almost parallel. This system has further been employed for augmenting the live video images with the pre-reconstructed cone-beam CT image [49].

Later, Navab et al. [49, 50] introduced a mirror reflection concept to enable the attached video camera and the C-arm X-ray to have the exact same virtual view point (see figure 2.3). Thanks to an offline calibration, the acquired X-ray images are co-registered with the video images without any further calibration or registration during the intervention. Providing a correct overlay of the X-ray and video images is known as the CamC technology, and it is valid for the entire X-ray cone-beam projection geometry.

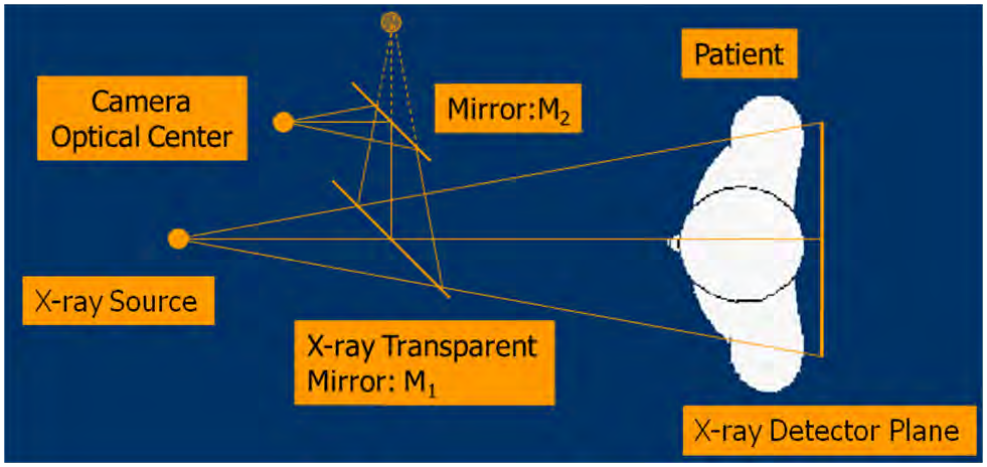


Figure 2.3: Video camera and mirror construction concept of the CamC system.

The calibration concept for the CamC system proposed in [49, 50] includes three steps:

1. **Distortion correction**: Both the optical video camera and the X-ray images have distortions. They must first be corrected for their distortion such that they preserve the linear projection property. Furthermore, the X-ray geometric distortion depends on the orientation of the mobile C-arm with regard to the earth's magnetic field. For precise distortion correction, the C-arm has to be calibrated for every orientation. Look up tables provided by the vendor can correct for the geometrical X-ray distortion for most common poses of the C-arm. For C-arms with flat panel detectors instead of X-ray image intensifiers, distortion is a minor problem and is often taken into account by system providers.

2. **Alignment of X-ray source and camera optical center**: Having a geometrical correct overlay of the video and X-ray image requires both images be acquired from the exact same view point. The second step of the calibration is to position the

camera and the mirrors such that the camera optical center coincides with the X-ray source center. This is the most critical step. The projection center is determined by the intersection of at least two distinct linear rays, each of which is defined by two distinct points. The alignment of two projection centers is thus guaranteed by the alignment of at least two pairs of the linear rays (see figure 2.4).

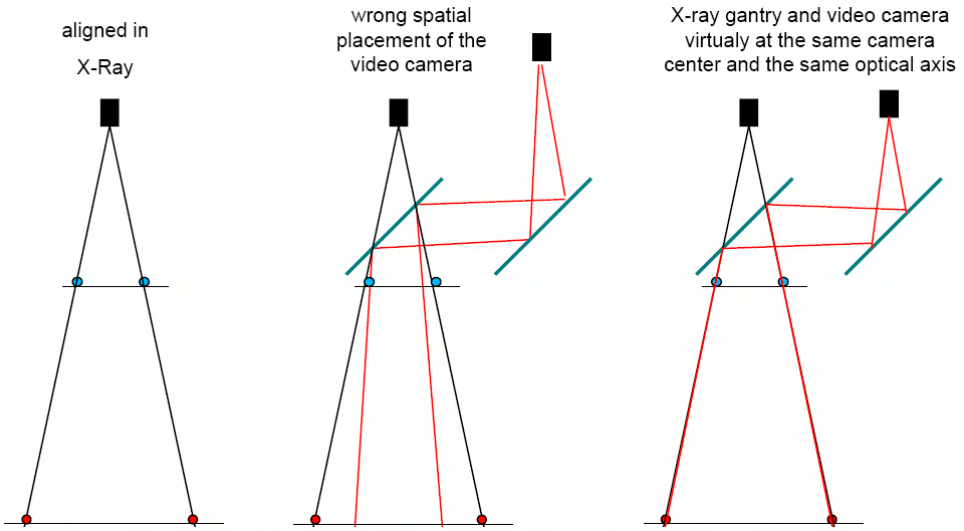


Figure 2.4: The camera optical center virtually coincides with the X-ray source center when at least two rays from both projection centers pass through two pairs of markers. Image courtesy of Joerg Traub [144].

3. **Homography estimation for image overlay**: Even after successful alignment of X-ray source and camera optical center, X-ray and optical camera have different intrinsic parameters and they differ in orientation. A homograph $H \in \mathbb{R}^{3\times3}$ must be estimated to compensate for the difference in intrinsic parameters and imaging orientation in order to warp the X-ray image onto video images correctly. Direct linear transformation (DLT) can be employed to compute $H$ with at least four corresponding points in the X-ray and video images.

### 2.1.3 Potential Clinical Applications

Mitschke et al. [145] present a protocol for needle placement procedures under guidance of the X-ray and video image overlay. They require minimum two X-ray images acquired from different unknown C-arm pose and the exact placement of the needle can be achieved under the video guidance assisted by a special designed placement device having two orthogonal rotation planes. Heining et al. present the interlocking of intramedullary nails [146] and pedicle screw placement [147] under the guidance of video augmented X-ray images. Traub et al. [117] propose to use the CamC system for vertebroplasty procedures, and compare the surgical performance of these procedures using the CamC system and fluoro-CT guidance. In this work, more clinical applications are identified,

which include X-ray positioning, incision, entry point location, instrument axis alignment, K-wire guidance, and surgery documentation (see section 2.5).

### 2.1.4 Extensions to CamC platform

Having aligned projection geometries of the C-arm X-ray and the attached video camera enables various computer aided surgery solutions. Navab et al. [148] develop a visual servoing solution for intra-operative positioning and repositioning of mobile C-arms. Additional visual markers on patients' skin allow the optical camera to compute the C-arm's pose and its required displacement for positioning. In the absence of electronically controlled mobile C-arms, the visual servoing solution provides step-by-step guidance on how much to move each of C-arm joints until a desired position is achieved.

The CamC system provides visualization and guidance in a two dimensional space. However, no depth control was possible. Thus, the system was limited to applications where depth did not matter, such as interlocking. As an extension to the CamC system, Traub et al. [149] develop a multi-view opto-xray imaging system (see figure 2.5(a)) that is capable of depth control during surgery by attaching a second video camera to the C-arm. Furthermore, they apply cross ratio to estimate the tip of a linear surgical instrument in 2D images. After one time calibration of the newly attached second video camera, they are able to show the instrument tip in the orthogonal view to the C-arm X-ray (see figure 2.5(b)). The feasibility of the system has been validated trough cadaver studies.

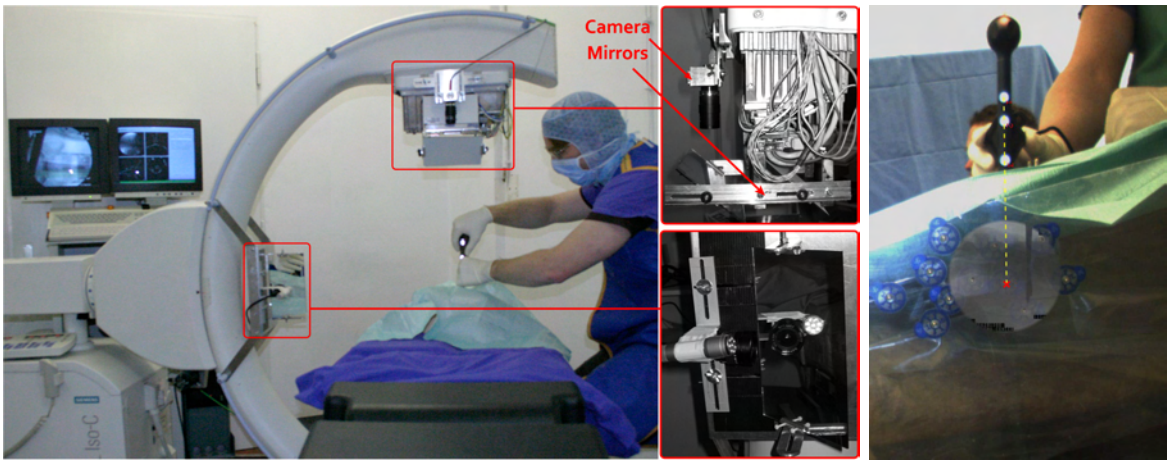


(a) (b)

Figure 2.5: (a) The C-arm with two attached optical cameras. The first camera is attached to the gantry with a double mirror construction. The second camera is attached in an orthogonal direction with a single mirror construction. (b) The second camera is used for depth control. Image courtesy of Joerg Traub [149].

Dressel et al. [150] propose to guide intra-operative C-arm positioning using artificial fluoroscopy. This is achieved by computing digitally reconstructed radiographs (DRRs) from pre- or intra-operative CT data. An initial pose between the patient (the CT image)

and the C-arm is computed by rigid 2D/3D registration. After the initial pose estimation, a spatial transformation between the patient and the C-arm is obtained from C-arm motion estimation, for which the CamC system is employed (see figure 2.6). Using this information, it is able to generate DRRs and simulate fluoroscopic images (see figure 2.7). For positioning tasks, this system appears to match conventional fluoroscopy; however simulating the images from the CT data in real time as the C-arm is moved without the application of ionizing radiation.

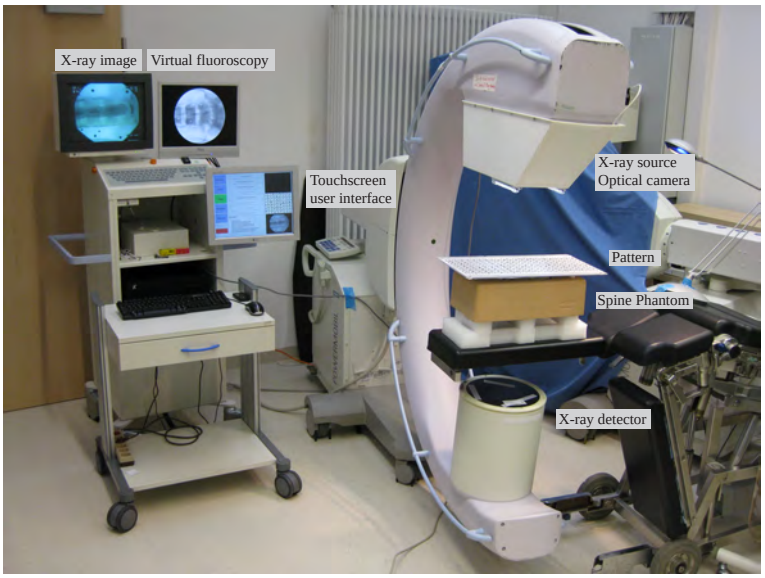


Figure 2.6: The system setup for artificial fluoroscopy generation using the CamC system. Image courtesy of Philipp Dressel [150].

An X-ray image stitching method was implemented based on the CamC platform [128]. The CamC system acquires registered X-ray and optical images by construction, which facilitates the generation of panoramic X-ray images. This is achieved by first stitching, then embedding the X-ray images (see figure 2.8). Visual marker tracking is employed to automatically stitch the sequence of the optical video images and to rectify images. The proposed method is suitable for intra-operative usage, generating panoramic X-ray images with less exposure and without the requirement of fronto-parallel setup and overlapping X-ray images.

The CamC technology paves the way for developing various novel computer aided surgery solutions. In this dissertation, I propose two computer aided intra-operative X-ray imaging solutions: parallax-free panoramic X-ray imaging (see chapter 3) and closed-form inverse kinematics for C-arm X-ray imaging with six degrees of freedom (DOF) (see chapter 4). These two novel imaging solutions are implemented using the CamC system that allows for real-time, radiation-free C-arm motion estimation using visual markers and the attached video camera, thereby improving the surgical workflow integration and reducing radiation exposure in the majority of today's orthopedic and trauma interventions.

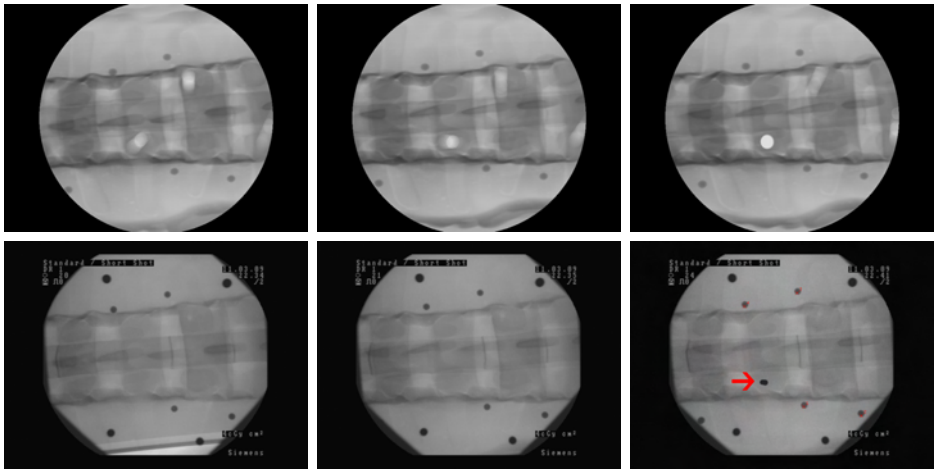

Figure 2.7: The upper row shows generated DRRs, the lower row shows corresponding X-ray images; The first column shows the starting position after registration, followed by an intermediate shot during positioning. The right column shows the final position. Note that the righmost X-ray was taken after the actual drilling, with a metal pin inserted into the drill hole for better contrast. Image courtesy of Philipp Dressel [150].

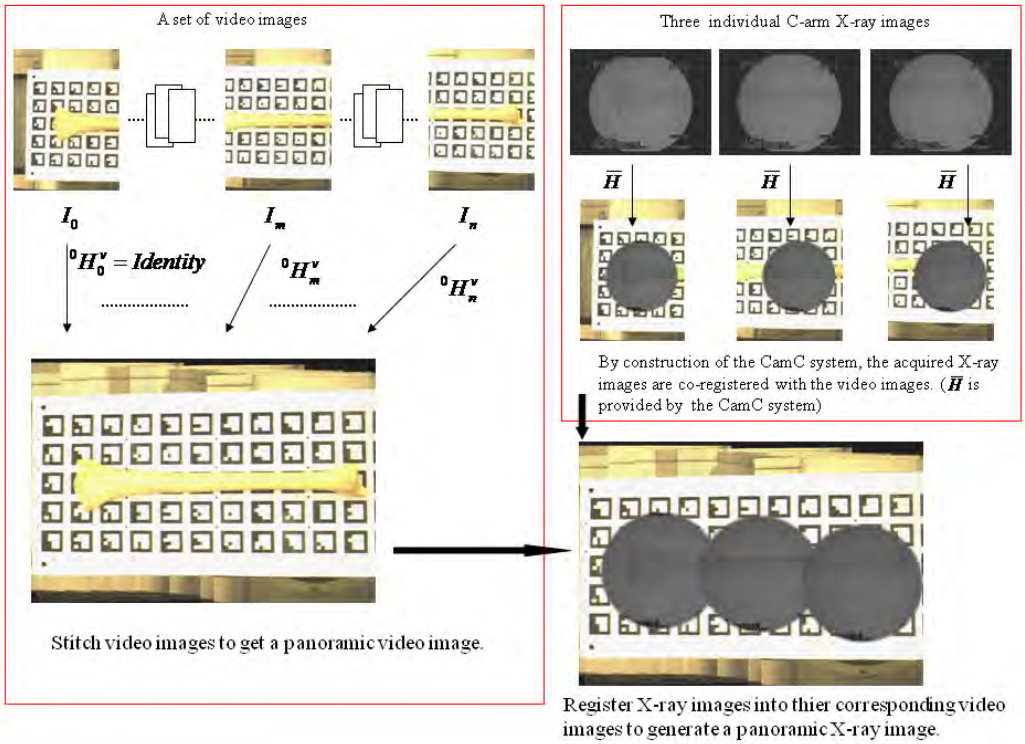


Figure 2.8: The concept of X-ray image stitching using the camera augmented mobile C-arm system and a square marker pattern.

## 2.2 System Calibration

The accurate overlay between the images is crucial to high quality surgical outcomes. This cahpter presents a practical and robust solution that improves the overlay accuracy for any C-arm orientation by: (i) improving the existing CamC calibration, (ii) reducing X-ray distortion effects, and (iii) accounting for the mechanical sagging of the C-arm gantry due to gravity. Zhang's method used for optical cameras and a traditional C-arm method based on equidistant grid model are implemented for X-ray distortion correction (see section 2.2.1). The concept of Virtual Detector Plane (VDP) is adapted to reduce errors due to the mechanical sagging of the C-arm gantry. A planar phantom is placed at different distances to the image intensifier in order to obtain an optimal homography that co-registers X-ray and video images with a minimum overall error for all image points. Section 2.2.2 shows that applying the optimal homography and the traditional distortion correction of a calibrated C-arm pose together with VDP dramatically improves the overlay accuracy for all C-arm poses when using the CamC technology.

### 2.2.1 Calibration of C-arm X-ray

Accurate C-arm X-ray projection geometry is critical for optimizing subsequent reconstruction of anatomy and tool tracking. In the previous work [50], the CamC system is calibrated in such a way that the X-ray images are warped onto distortion free optical images in order to enable the C-arm X-ray to have the same projection geometry as the calibrated camera. This calibration method is hypothesized not optimal for estimating the X-ray projection geometry of the CamC system. Three methods: (i) the existing CamC method of [50] (ii) Zhang's method used for optical cameras [151], and (iii) a traditional C-arm method, are investigated and compared for distortion correction and calibration accuracy of the X-ray projection geometry. In this study, the mobile C-arm is a Siremobile Iso-C 3D with the X-ray image resolution of $640 \times 480$ pixels, from Siemens Healthcare. The optical video camera attached to the C-arm is a Flea with the image resolution of $800 \times 600$ pixels, from Point Grey Research Inc.

**Zhang's Optical Camera Calibration:** The intrinsic parameters and distortion coefficients of the optical camera are commonly calculated using the classical Zhang's method [151]. The technique only requires the camera to observe a planar pattern shown at least two different orientations. The proposed procedure consists of a closed-form solution, followed by a nonlinear refinement based on the maximum likelihood criterion. For employing Zhang's method to calibrate the C-arm X-ray, 15 images are acquired and the calibration procedure is performed according to [151].

**Traditional C-arm Calibration:** Only a few works, such as [152], use the Zhang's method to calibrate the X-ray fluoroscope. Traditionally the intrinsic parameters of the X-ray fluoroscope are calculated based on multi-plane phantoms after distortion correction. In [153] a phantom with points on three planes is designed to do off-line calibration. The projection matrix can be computed using the corresponding 3D coordinates of the phantom and the 2D coordinates of X-ray images. Then the projection matrix is decomposed by the methods such as Tsai's method [154]. Another phantom [155], which can provide more points on two parallel planes to do the on-line calibration, was developed by

Livyatan. In contrast with the numerical method described above, intrinsic parameters are calculated directly from the geometric relationship of the pinhole camera model in the geometric calibration method [156]. The design and imlpemetation of a traditional C-arm calibration procedure is described in section 2.2.1.1.

#### 2.2.1.1 Implementation of C-arm X-ray Calibration

A traditional C-arm calibration procedure that first corrects the image distortion and then computes the intrinsic parameters is designed and implemented.

**Distortion Correction Procedure:** A calibration board with X-ray opaque beads (3mm diameter) arranged in a grid pattern with 10mm spacing is constructed and used to calculate the distortion correction coefficients of the traditional method (see figure 2.9(a)). Three larger X-ray opaque markers (4mm diameter) are attached on the calibration board to define the local coordinate of the board. The calibration board is closely attached to the face of the intensifier while images are taken. The 3D coordinates of the points on the board are then correlated to its coordinates in the 2D image. The predicted distortion free points are calculated by building an equidistant grid according to [157]. The predicted distortion free points can then be related to the distorted points detected in the image. Lastly, distortion coefficients of each image are calculated based on the model of high-order polynomial [158].

**Intrinsic parameters computation:** The intrinsic parameters of the C-arm X-ray are calculated using Forsyth's method [159]. The calibration board with three markers is again used to acquire sets of images. As it is shown in figure 2.9(c), four screws with wooden bases are affixed onto the board and the distance between the nuts under the board and the top of the screw is set to 50mm. Then, the four wooden bases are fixed to the intensifier of the C-arm. Parallel constraint is ensured between the five planes by fixing the nuts above and below the board, making the screws perpendicular to the board. Then five C-arm images are acquired at different depths to the image intensifier in the increments of 10mm [10-50 mm]. Any two planes are chosen and six points from the markers are used to provide 2D/3D correspondence using Direct Linear Transform (DLT) estimation. Non-linear optimization method using all the other points is performed to optimize the projection matrix calculated by DLT. As the normalization of the data can affect the final solution [160], the data is normalized beforehand. Then the points of the other three planes are projected onto the corresponding images respectively to calculate the RMS re-projection errors. Since five images are acquired, this process is repeated ten times to examine all the possible combinations. The combination with the minimum average RMS error is recognized to be the best pair and the projection matrix is calculated using the points on these two planes. The above methodology is used for intrinsic parameter estimation using the traditional method.

#### 2.2.1.2 Error Analysis Study

Accuracy of the distortion correction for each of the three methods is compared by analyzing the error based on a synthetic model and the linearity and cross-ratio properties. Also, the accuracy of calibrated X-ray projection geometry is evaluated by performing

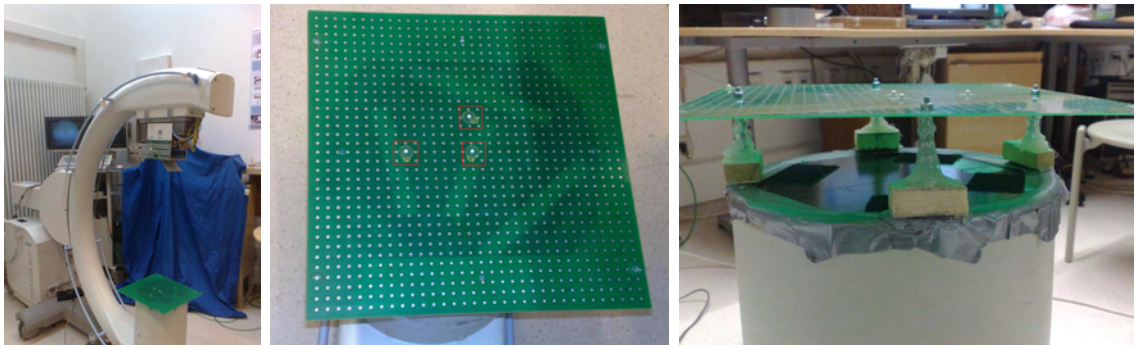

(a) (b) (c)

Figure 2.9: Setup of the traditional C-arm calibration procedure. (a)The setup for distortion correction; (b) Calibration board with the three large X-ray opaque markers (marked within red squares); (c) Phantom used in intrinsic parameters computation. Image courtesy of Xin Chen [161].

C-arm pose estimation using a planar pattern with known geometry. Table 2.1 shows the errors of the three C-arm X-ray calibration methods.

Distortion correction accuracy is compared using the existing CamC method, Zhang's method, and the traditional C-arm calibration method described above. After the distortion correction using the three methods, the 2D/3D correspondence is again detected. The 2D redetected points and the predicted distortion free points are used to evaluate the residual mean square (RMS) error, which is labeled as the predict/redetect error. Since an undistorted projection image should preserve linearity and the cross ratio of imaged objects, these two properties are evaluated in the study as well. In the linearity comparison, the points on the two ends of each line in the corrected image are used to define a line and the average distance between this line and other points that should be on this line is calculated. In the cross-ratio comparison, the ground truth of the cross-ratio of each four points on a line can be known from the 3D points, and the difference between the cross-ratio of the four corresponding points on the same line in the image and the ground truth is divided by the ground truth to show how severe the difference truly is (i.e. the ratio error is in %). Suppose a line has $N$ points, a number of $\binom{N}{4}$ combinations of each line are used to evaluate the error in terms of the cross-ratio.

Calibration of X-ray projection geometry using the traditional method is again compared to Zhang and the existing CamC methods. Here, 15 images of the calibration board with different pose relative to X-ray fluoroscope are taken. In the reprojection error comparison, half of the points were randomly chosen from the board and used for pose estimation using different intrinsic parameters. The remaining unused points are reprojected onto the image to evaluate the error. In the relative pose estimation comparison, the five planes used to perform calibration are used again and the relative pose between each of the two planes are known (i.e the RMS reprojection error of unused three planes used to calculate the projection matrix is very small (i.e. 0.59 pixel)).

The calibration accuracy of X-ray projection geometry for the CamC technology is

| | Traditional method | Zhang's method | CamC method |
|---|---|---|---|
| Evaluation of Distortion Correction | | | |
| Predict/Redetect RMS error (pixels) | 0.39 ± 0.069 | 0.68 ± 0.095 | 1.07 ± 0.114 |
| Linearity (pixels) | 0.20 ± 0.014 | 0.35 ± 0.015 | 0.66 ± 0.031 |
| Cross-ratio (%) | 0.93 ± 0.05 | 0.93 ± 0.04 | 1.48 ± 0.04 |
| Evaluation of X-ray Projection Calibration | | | |
| Reprojection error (pixels) | 0.33 ± 0.038 | 0.48 ± 0.037 | 1.02 ± 0.083 |
| Translational error (mm) | 0.25 | 0.41 | 1.13 |

Table 2.1: Results of error analysis of the three C-arm X-ray calibration methods.

studied by comparing the existing method [50] to classical Zhang's and X-ray traditional methods. The results show that when the distortion coefficients and intrinsic parameters obtained from the implemented traditional method are used to do distortion correction and pose estimation, the error is relatively smaller than the other two techniques.

### 2.2.2 A Practical and Robust Method for an Accurate Intra-operative Video Augmented X-ray

The CamC system can be operated like a standard C-arm that is familiar to medical staff, which enables it to be smoothly integrated into clinical routine. Recent pre-clinical studies and clinical trials show that using the overlay of X-ray and video remarkably avoids unnecessary radiation for several clinical applications [147, 146, 50, 162]. Furthermore, the co-registration of X-ray and video images enables many CAOS solutions such as parallax-free X-ray image stitching [163, 164] and visual servoing based C-arm down-the-beam positioning [165]. An accurate overlay becomes not only crucial for the precise guidance of interventional procedures, but also important for any advanced CAOS techniques based on the CamC technology. The overlay errors after co-registration of X-ray and video are mainly introduced from CamC calibration, X-ray distortion and the mechanical sagging of the C-arm gantry due to gravity [50, 164]. In this section, we bridge an important gap in literature and analyze the influence of these error sources on the overlay accuracy and propose a clinically practical solution that increases CamC precision. Figure 2.10 shows the experimental setup for this study. The employed mobile C-arm is a Powermobile with the X-ray image resolution of 768 × 576 pixels, from Siemens Healthcare. The optical video camera attached to the C-arm is a Flea2 with the image resolution of 1024 × 768 pixels, from Point Grey Research Inc.

The proposed CamC calibration method first aligns the camera optical center with X-ray source and then estimates a homography for image overlay [50]. The alignment of the two centers can be guaranteed by at least two rays from both projection centers passing through two pairs of markers, one pair including one marker on one plane and another marker on the different plane. Then, a homograph must be estimated in order to warp the X-ray image onto video images correctly. The C-arm pose, at which the calibration is performed, is called calibrated pose. In the previous work [50], the overlay error of the X-ray and video image is evaluated based on the images of a planar grid board attached on the image intensifier at the calibrated pose. Hence, the estimated

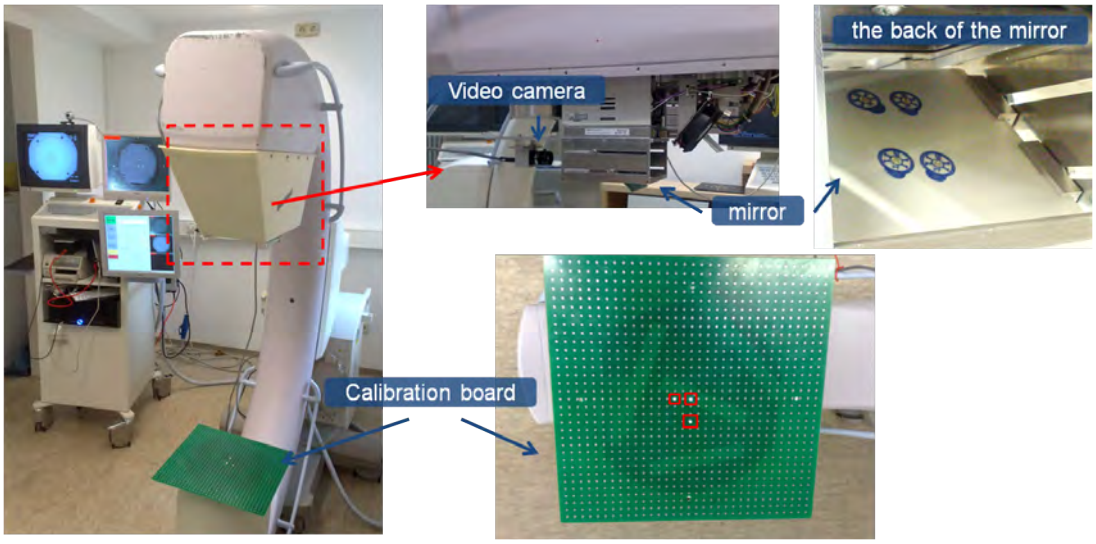


Figure 2.10: The experimental setup for analyzing the overlay accuracy of the CamC technology: The left image shows the CamC system. The top middle image shows the camera and mirror construction. The top right shows the four X-ray markers attached on the back of mirror for the virtual detector plane method. The left bottom image shows the employed calibration board with grid.

error is only valid for the plane of the image intensifier. However, patients are located in any area between the X-ray source and image intensifier. Furthermore, authors in [50] conducted experiments using the same evaluation, for overlay error, with different C-arm angular and orbital rotations around the calibrated pose. Results showed an increase in alignment error between X-ray and video when the C-arm was rotated at increasing rotational angles. This was observed when the homography estimated at the calibrated pose is applied for different C-arm positions. In the event where a re-estimation of the homography is performed at a specific C-arm position, the error is roughly constant during orbital and angular rotation of the C-arm. In this work, the overlay accuracy is assessed for the entire volume, or C-arm cone angle, between the image intensifier and X-ray gantry. Moreover, we take the inaccurate alignment between the optical center of camera and X-ray source into consideration when calculating the optimal homography that minimizes errors for all image points thereby guaranteeing an optimal overlay.

#### 2.2.2.1 Methods

**X-ray Distortion Correction** Zhang's method and the traditional C-arm method are implemented for X-ray distortion correction according to section 2.2.1.1. The analysis in section 2.2.1.2 shows that the traditional C-arm distortion correction method is superior to Zhang's method in terms of the linearity and cross-ratio properties. Here, their contributions to the overlay accuracy are analyzed and compared.

**CamC Calibration** Unlike most medical AR systems that require on-site calibration and registration procedures to align computer generated images with the surgeon's view

of the real world [136, 137], the CamC system relies solely on a one-time offline calibration enabling a geometrically correct overlay of the X-ray and video images [50]. In our study, the CamC calibration is performed when all five C-arm joints are set to zero. Hereafter, we refer to this scenario as the calibrated pose or reference pose. In our experiments, the focus of the attached video camera has been adjusted such that the object located around 40 cm away from the intensifier results in a sharpest video image (i.e. the approximate distance of the patient-table location). For calibration, we built a calibration phantom with two parallel visual transparent planes, where five markers that are visible in both X-ray and optical images are arranged on each plane. The phantom is then placed on the image intensifier of the C-arm. It is necessary to first position the five pairs of markers such that the positions of the two markers from one pair coincide in the X-ray image frame. Following this, the positions of all the markers on both planes are fixed. The camera and the mirror should be mounted to the C-arm such that the two markers for each pair are aligned in the video image. After successful alignment of X-ray source and camera optical center, X-ray and video have different intrinsic parameters and differ in orientation. A homograph $H$ must be estimated to compensate for the difference in intrinsic parameters and imaging orientation in order to warp the X-ray onto video images accurately.

The homography $H$ between X-ray and video images can be expressed according to [126] as,

$$H = K_v R K_x^{-1} + \frac{1}{d} K_v t n^T K_x^{-1} \tag{2.1}$$

where $K_x$ and $K_v$ are the intrinsic parameters of the video camera and X-ray respectively. $R$ and $t$ are the rotation and translation from the X-ray to the camera. In the case that the camera center and X-ray source are correctly aligned, $t$ is equal to zero. Then the homography is valid for all image points. For the co-registration of X-ray and video images during the CamC calibration, the calibration board visible in both X-ray and video is used to calculate the homography based on point correspondences between the video and X-ray image. However, in practice the inaccurate alignment of both projection centers leads to a non-zero $t$. Therefore, the homography is valid only for all image points for which corresponding space points are on the same plane defined by the normal vector $n$ and distance $d$ in the X-ray coordinate system. Any anatomical structure that is not on this plane in 3D space will result in misaligned image points. Thus, the estimated homography for the CamC overlay is only valid for the plane where the calibration board is placed. The position of the plane where the homography is estimated could influence the overlay accuracy. We design a study to look for an optimal homography that results in a minimum overlay error for all image points no matter where their corresponding space points are located. Within this experiment, we also evaluate the contribution of the two X-ray distortion strategies, i.e. Zhang's method and the traditional method, to the overlay accuracy.

**Experiments:** The distance between the image intensifier and the mirrors is 70 cm. The calibration grid board is placed on seven different planes parallel to the image intensifier from 0 cm to 60 cm with incremental 10 cm steps. On each plane, two pairs of X-ray and video images are acquired; one pair is used to estimate the homography and one is used to compute the overlay accuracy for that plane (i.e. hereafter overlay-plane-errors).

The points in one X-ray and video pair are correlated. These point correspondences are used to estimate the homography or to compute the overlay error. The overlay-plane-errors are calculated as RMS deviation between the corresponding points in the X-ray and video image in mm. From this, we first obtain the seven homographies, $H_0$, $H_1$, $H_2$, $H_3$, $H_4$, $H_5$, and $H_6$, estimated at the seven planes 0 cm, 10 cm, 20 cm, 30 cm, 40 cm, 50 cm, and 60 cm away from the intensifier respectively. For one estimated homography, we apply it to align the X-ray and video image for each of the seven evaluation pairs and then evaluate the overlay-plane-errors. The overlay-overall-error resulted by one homography is computed as the mean of the overlay-plane-errors of the seven planes. We define the optimal homography as the one having the least overall-overlay-error among all of the estimated homographies. We perform the evaluation three times using the same X-ray images with no distortion correction, and distortion correction using Zhang's method and by the traditional method.

**Model of C-arm X-ray Imaging with Fixed Projection Parameters** The X-ray source and the detector plane are loosely coupled and mounted on opposite sides of the C-arm. Due to gravity, it is difficult to suppose a fixed relation between the X-ray source and the detector plane, i.e. intrinsic parameters change in different C-arm orientations. Therefore in theory, C-arm X-ray distortion correction is required at each orientation. In [153], a phantom with points on three planes attached to the intensifier is designed to perform X-ray calibration for different C-arm poses. The previous evaluation of the CamC overlay accuracy [50] shows that the overlay error increases as the rotation of the C-arm device increases. In order to compensate for the overlay error caused by the changes of the C-arm orientation, we adapted the idea of the Virtual Detector Plane (VDP) proposed in [166, 143]. In our implementation, four spherical X-ray markers (1.5 mm diameter) attached on the back of the mirror, are considered fixed references to the X-ray source in all C-arm orientations (see figure 2.10). Warping image points of the X-ray markers to the fixed positions defined by a reference image acquired in the calibrated pose guarantees fixed intrinsic parameters. In order to investigate the influence of the VDP method on the overlay accuracy, we conduct another experiment to evaluate the overlay error with and without applying the VDP method and distortion correction at different angular and orbital rotations.

**Experiments:** In this experiment, we employ an optimal homography obtained at the calibrated pose for the co-registration of the X-ray and video images. The calibration grid board is placed 30 cm away from the intensifier to simulate one of most common source-to-object distances of the C-arm (i.e. the patient-table position). Then, the C-arm is rotated in angular and orbital directions respectively. The employed angular rotations are 0°, ±5°, ±10°, ±15°, ±20°, ±25°, ±30°, ±60°, ±90°, and 180°, and orbital rotations are 0°, ±5°, ±10°, ±15°, ±20°, ±25°, ±30°, ±60°, and ±90°. For all angular and orbital poses, we analyzed the overlay-plane-errors with and without applying the VDP method. The traditional method is employed to compute distortion coefficients for all of the angular and orbital poses. In order to determine whether the online distortion correction for all C-arm poses is necessary in obtaining the most accurate overlay, we perform the experiments three times using the same X-ray images: with no distortion correction, using distortion

coefficients of each pose (i.e. online distortion correction), and finally, using the distortion coefficients of the calibrated pose.

#### 2.2.2.2 Results

**Overlay Error at the Calibrated Pose** Figure 2.11 (a-g) shows the overlay-plane-errors for the X-ray and video images aligned by $H_0$, $H_1$, ... $H_6$ respectively. When applying each of the estimated homographies, the overlay-plane-errors can have variations. Our experimental results suggest that it is crucial to look for an optimal homography that will ultimately lead to a more accurate co-registration between X-ray and video images for all image points, regardless of where their corresponding space points are located. Figure 2.11 (h) shows the overall-overlay-errors when applying the seven different homographies in our experiments. The results of the overall-overlay-errors demonstrate that the traditional X-ray distortion correction method always outperforms the other two techniques. The analysis in section 2.2.1.1 shows a similar comparison result that the traditional distortion correction method is superior to Zhang's method in terms of the linearity and cross-ratio properties. For each group of the three distortion correction strategies, all minimum overall-overlay-errors are achieved by employing homography $H_3$. The minimum overall-overlay-errors are $0.375 \pm 0.061$ mm, $0.272 \pm 0.064$ mm and $0.269 \pm 0.056$ mm when using no distortion correction, Zhang's method, and traditional method respectively. Here, we choose the homography calculated by traditional distortion correction method $H_3$ as the optimal homography and its overall-overlay-error is in fact the minimum among all of the estimated homographies. This homography is also used to correct images during subsequent C-arm rotations.

**VDP Evaluation** Figure 2.12 shows that without the VDP, the overlay error is considerably increased if the C-arm is rotated. By applying the VDP, the overlay accuracy is remarkably improved and the errors are almost constant for all rotations of the C-arm gantry. Furthermore, with the VDP method, applying the distortion coefficients of the calibrated pose could result in comparable overlay accuracy as applying online distortion corrections. Consequently, without X-ray distortion corrections, the overlay is less reliable. Thus, using the VDP method combined with the distortion coefficients of the calibrated pose is sufficient to reduce the overlay error introduced by the mechanical sagging of the C-arm due to gravity. In this experiment, a total of 34 different C-arm poses are employed for the evaluation. For all of the tested C-arm rotations, with and without using the VDP method, the mean overlay-plane-errors are $0.53 \pm 0.24$ mm and $1.67 \pm 1.25$ mm when applying the distortion coefficients of the calibrated pose and are $0.52 \pm 0.24$ mm and $2.09 \pm 1.30$ mm when applying online distortion correction.

**The Overlay Images of a Dry Bone** Experiments on a dry femur bone placed in the middle area between the X-ray source and intensifier are performed to demonstrate the improved overlay accuracy when applying the VDP method. Qualitative inspection of the image overlay at 60° angular orientation shows a clear misalignment of video and X-ray images without applying the VDP and a significant improvement of the alignment when applying the VDP (see Figure 2.13).

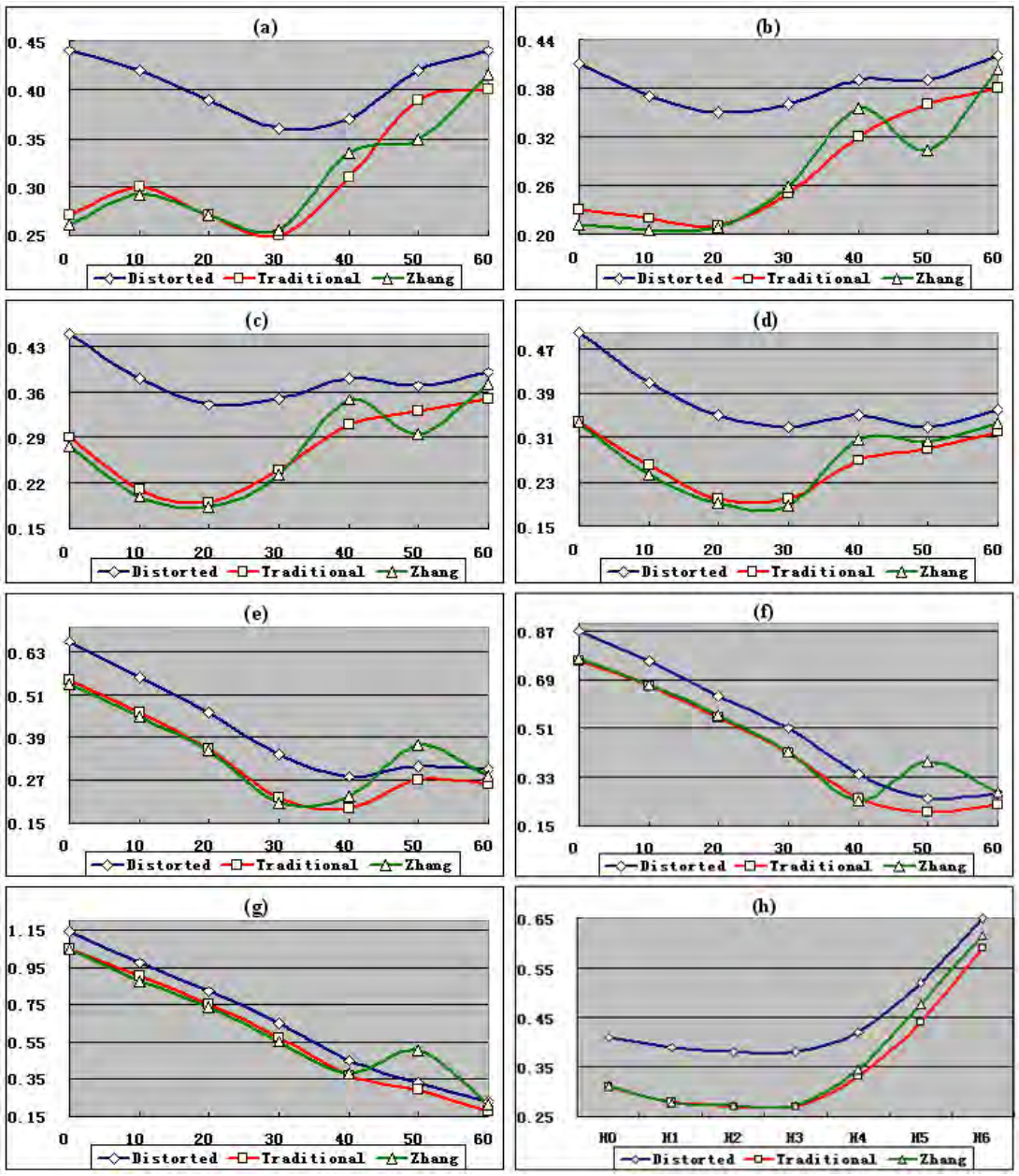


Figure 2.11: (a-g) shows the overlay-plane-errors for the X-ray and video images aligned by $H_0$, $H_1$, $H_2$, $H_3$, $H_4$, $H_5$, and $H_6$ respectively. The horizontal axis of (a-g) demonstrates the distance between the intensifier and the plane where the overlay errors have been estimated. (h) shows the overall-overlay-errors when applying the seven different homographies in our experiments. The horizontal axis in (h) represents the seven homographies. The vertical axis in all of the sub-figures shows the error in millimeter. The errors resulted by no distortion correction, traditional and Zhang's method are drawn by diamond, square and triangle separately in each image.

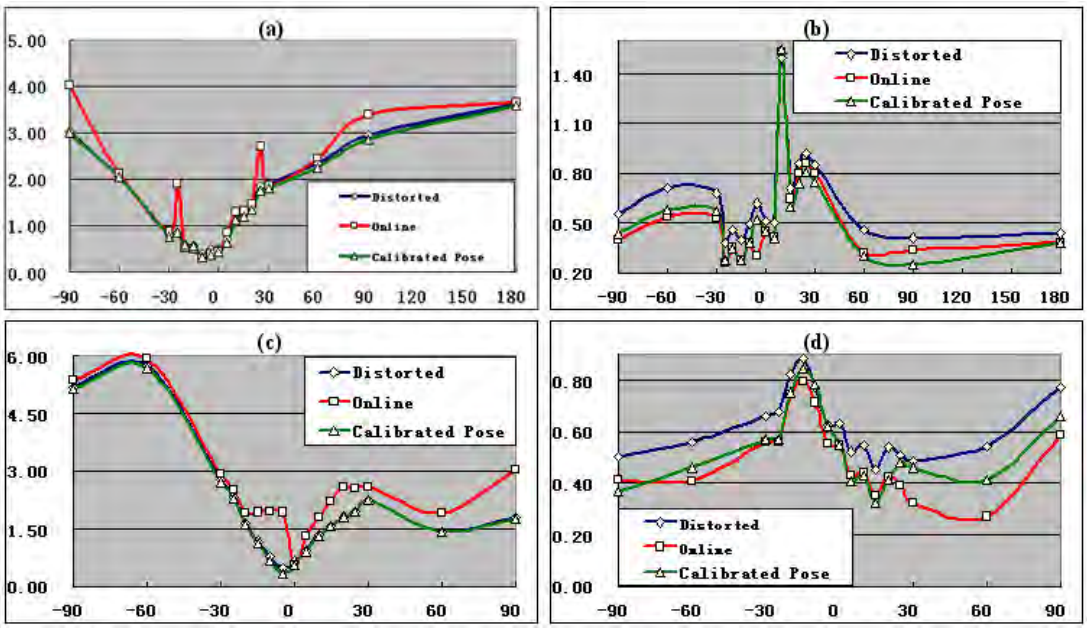


Figure 2.12: (a) and (c) are the overlay error of images that are aligned without VDP during angular (a) and orbital (c) rotations. (b) and (d) are the corresponding error compared with (a) and (c) if the VDP is used to compensate for the mechanical sagging during the rotation. The errors resulted by using distorted images, online distortion correction, and distortion coefficients of calibrated pose are drawn by diamond, square and triangle separately in each image. The horizontal axis is the angle rotated and the vertical axis is the error measured in millimeter.

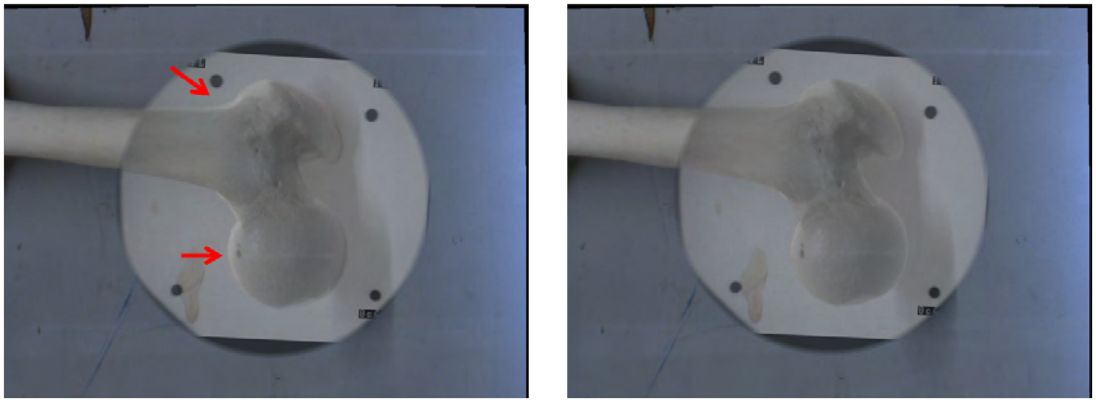

Figure 2.13: The left image shows the X-ray and video image overlay of the dry femur bone without applying the VDP method in the C-arm orientation of angular 60°. The right image shows the same bone with the VDP method used in the same C-arm orientation. The arrows indicate clear misalignments between X-ray and video images in the left image.

## 2.3 Clinical System Setup: CamC in Operating Room

This section describes various critical aspects of building the first clinical CamC system, including estimation of radiation dose generated by the CamC system to air (see section 2.3.1), online detection of overlay misalignment (see section 2.3.2), and hardware and software components of the clinical system (see section 2.3.3).

### 2.3.1 Applied Dose of CamC System

#### 2.3.1.1 Dose-Area Product (DAP)

Effective dose is a common used quantity to estimate the stochastic risk of radiation applied to patients in interventional procedures. It is the sum of the weighted radiation absorbed in the tissues and organs depending on tissue weighting factors [167, 168, 169].

Every clinically used mobile C-arm has a dose-area product (DAP) meter permanently built into the X-ray tube housing to measure the radiation dose. The overall measured DAP values must be recorded for each patient, and these DAP values allow to determine the patient exposition and eventually the effective dose which is related to the cancer risk of the procedure [168, 169, 170, 171]. Perisinakis et al. [171] present a way to compute normalized data for the estimation of patient effective dose and associated radiogenic risks from measured DAP values for fluoroscopically guided surgical reconstruction of femoral fractures. A similar study of computing effective dose for fluoroscopically guided pedicle screw insertion has been performed [170]. In the literatures [168, 169], dose conversion coefficients that convert DAP to effective dose can be found for different interventional procedures and different organs and tissues. Schultz and Zoetelief [169] report that the dose conversion coefficients mainly depend on surgical protocol and imaging equipment parameters, e.g. X-ray tube voltage, the position of the X-ray unit with respect to the patient, patient age, and exposed organ.

One mirror of the CamC system is however placed between the DAP meter and the patient (see figure 2.14). Thus, it is partially absorbing and scattering radiation, and the patient will receive less dose than the reading from the built-in DAP meter. The correct applied dose to the patient by using the CamC system is one of clinically important parameters. Therefore, the percentage of absorbed and scattered radiation of the mirror must be evaluated for the clinical study. This value can then be used to estimate the correct applied dose to the patient. For this, a protocol for estimating the correct applied dose by using an independent dose measurement device is developed [172].

#### 2.3.1.2 Estimation of Applied Dose

The mobile C-arm is Siremobile Iso-C 3D from Siemens Healthcare. One standard mirror of the CamC system is placed between the built-in DAP meter and the image intensifier. For evaluation of the applied radiation dose for the patient, an independent dose measurement device (see figure 2.14)is employed, which consists of the Unfors Xi R/F Detector and the Unfors Xi Base Unit, from Unfors Instruments GmbH, Germany. The Unfors


Figure 2.14: The left shows the CamC system, the right top is the built-in DAP meter, and the right bottom shows our dose measurement device (Unfors Xi).

Xi R/F Detector can measure the X-ray radiation dose in the range from 10 nGy - 9999 Gy with the uncertainty of 5%. This detector is connected to the Unfors Xi Base Unit which displays and records the measured results. It is used to evaluate the percentage of absorbed and scattered radiation by the mirror.

Figure 2.15: The positions of the Unfors Xi R/F Detector in our experiments. From the left to the right, they are position A, position B and position C.

Since the Unfors Xi R/F Detector cannot intercept the entire area of the X-ray beam on any plane perpendicular to the beam central axis between the X-ray housing and the image intensifier, it is not possible to directly measure the total dose. Thus, the property of the dose distribution on the plane has to be known to derive the total dose in our case. Generally, the dose distribution of the C-arm Cone-Beam on the plane perpendicular to the beam central axis is equivalent. For this, an experiment was conducted to check the dose distribution in both cases of with mirror and without mirror. The dosimeter, Unfors Xi R/F Detector, is placed on the image intensifier in three different positions. For each of the three positions (see figure 2.15), we took 3 shots with the mirror and another 3 shots without the mirror. Throughout the whole experiment, we used the single shot mode (DR-mode) with fixed radiation time and tube voltage (64kv) in order to produce constant

radiation doses for each shot on the level of the x-ray tube. The dose values measured by the unfors dosimeter are shown in table 2.2. For each case, the standard deviation is relatively small. This means dose distribution on the detector level is equivalent with and without the mirror. Therefore, the percentage of the absorbed and scattered radiation estimated for the partial area of the X-ray beam corresponds to the entire X-ray beam. In order to investigate the influence of the tube voltage on the percentage of absorbed and scattered radiation, we performed another experiment. In this experiment, we used the DR-mode of the C-arm and a fixed dosimeter position (Position B) for all shots. In each of the three different tube voltage settings, 64 kv, 70 kv and 77 kv, we took 5 shots with mirror and another 5 shots without mirror. Table 2.3 shows the average dose values for each case. The percentage of absorbed and scattered radiation by the mirror was found to be almost constant for the different tube voltage settings. Knowing the total applied dose (DAP) from the C-arm's built-in DAP meter, we can apply 39% as the percentage of the absorbed and scattered radiation by the mirror to estimate the correct applied dose for the patient according to our experiments.

| | position A | | | position B | | | position C | | | Mean±std |
|---|---|---|---|---|---|---|---|---|---|---|
| Without Mirror | 27.04 | 25.82 | 25.85 | 26.00 | 26.00 | 26.25 | 26.54 | 26.05 | 26.17 | 26.1911 ± 0.3862 |
| With Mirror | 15.36 | 14.41 | 15.71 | 14.93 | 16.06 | 16.00 | 15.46 | 15.62 | 15.08 | 15.4033 ± 0.5302 |

Table 2.2: The measured dose($\mu$Gy) of each shot by the Unfors Xi R/F Detector with the fixed tube voltage(64 kv).

| | 64kv (Mean±std) | 70kv (Mean±std) | 77kv (Mean±std) |
|---|---|---|---|
| Without Mirror | 26.0833 ± 0.1443 | 33.6200 ± 0.1572 | 96.6167 ± 0.5369 |
| With Mirror | 15.6633 ± 0.6358 | 20.5467 ± 0.3656 | 60.1967 ± 1.7923 |
| Percentage of absorbed and scattered radiation | 39.95% | 38.89% | 37.70% |

Table 2.3: The average measured dose ($\mu$Gy) for three different tube voltage settings, 64 kv, 70 kv and 77 kv.

### 2.3.2 Visual Marker Based Online Detection of Overlay Misalignment

If a treated anatomical structure moves away from the position where the X-ray image was acquired, the static X-ray image and the live video image are misaligned, which may lead to misinterpretation. For this reason, a tracking method [173] is adopted to track visual square markers that are rigidly attached to the skin of the treated anatomical structure.

#### 2.3.2.1 Design of Visual Square Markers

A square marker is divided into $6 \times 6$ square tiles of equal size. The inner $4 \times 4$ tiles that are colored by white or black can provide a 16-bit binary code for marker recognition. The markers that can have four different codes by incremental 90° rotation are used (see

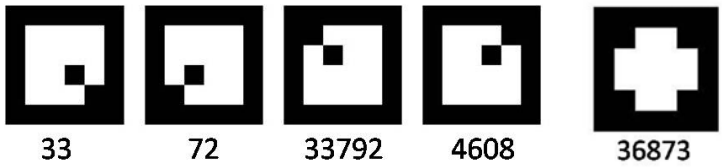


(a) (b)

Figure 2.16: (a) A marker with four times incremental 90° rotation, their respective code written in decimal numbers below. The smallest number, 33, is the code of this marker; (b) A marker that has the same code after incremental 90° rotation.

figure 2.16(a)), since it makes the orientation detection possible. The smallest code of these four codes is defined as the code of the marker. The corners of the square marker that can be extracted as the intersection of the two adjacent edges of the marker in the image is used as feature points.

#### 2.3.2.2 Online Information of Overlay Misalignment

To visually inform surgeons about misalignments, the initial positions of markers that are recorded when the acquisition of the X-ray image are drawn as green quadrilaterals and their positions in the current video image are drawn as red quadrilaterals. Moreover, a gradient color bar is shown on the right side of the video images, whose length indicates the pixel-difference between the marker's initial and current positions (see figure 2.17). Square markers that are sterilizable and used in animal cadaver and real patient studies are produced by Adolf BAUSCH GmbH [1].

Figure 2.17: Visual square marker tracking for informing surgeons about a misalignment of X-ray and video image.

[1] www.adolfbausch.de

### 2.3.3 The First Clinical CamC System

The first clinical CamC system (see figure 2.19) was built by attaching a video camera (Flea2, from Point Grey Research Inc., Vancouver, BC, Canada) and mirror construction, integrated into an X-ray source housing, to a mobile C-arm (Powermobile, isocentric C-arm, from Siemens Healthcare, Erlangen, Germany). The proposed one time calibration [50] was used to construct the system. The system comprises three monitors: the common C-arm monitor showing the conventional fluoroscopic image, the CamC monitor displaying the video image augmented by fluoroscopy and a touch screen display providing the user interface. A simple alpha blending method is used to visualize the co-registered X-ray and video images. The surgical crew can operate the CamC system like any standard mobile C-arm. This enables smooth integration of this novel AR modality into clinical practice. Until now over 40 orthopedic and trauma procedures have been performed under CamC's AR imaging by different surgeons within the operating rooms (OR) of the Trauma Surgery Department of LMU university hospital in München, Germany.

A visualization and navigation software (CamC software) running in the CamC PC is developed in C++ based on our medical augmented reality framework (CAMPAR) [174] that is capable of temporal calibration and synchronization of various input signals (e.g. image and tracking data). The CamC PC connects two displays, an LCD monitor and a touch screen. The LCD monitor mounted on the top of the C-arm cart displays the live video overlaid by the X-ray image (see figure 2.18(a)), and the touch screen monitor mounted on the side of the C-arm cart provides a user interface (see figure 2.18(a)).

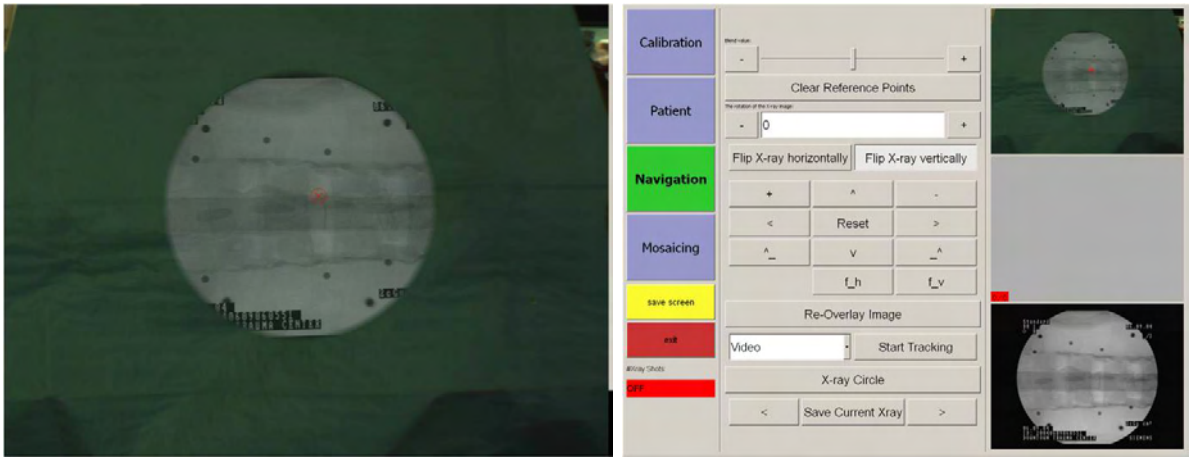


(a) (b)

Figure 2.18: (a) The live video overlaid by the X-ray image shown on the LCD monitor; (b) The control interface of the CamC software shown on the touch screen .

Radiation warning LEDs located on the C-arm cart will flash when X-ray acquisition is activated. A light sensor is attached on one warning LED in order to obtain the signal of X-ray acquisition. There are three components for detecting X-ray acquisition.

1. A light sensor with a little hardware board to detect and process the light changes.

The light sensor converts the amplified resistance change of the light resistor to an analog sigmoid signal. This hardware was built by Ahmad Ahmadi [2] .

2. A USB box, to which the light sensor is connected, communicates with a PC directly. It reads the processed analogue electrical signal and converts it to a digital signal, sending it over USB to the PC. This one is a National Instrument NI USB-6009 [3].

3. In the CamC PC, LabView (v3.6 with a student license) reads the digitized sigmoid function (detecting changes at a rate of 1kHz), thresholds it and writes it to a TXT file. CamC software consistently checks the TXT file to obtain the signal of X-ray acquisition.

For documentation and postoperative analysis of the surgeries, the CamC video stream is transferred via a VGA splitter to a dedicated recoding PC equipped with an UFG-05 frame grabber card [4].

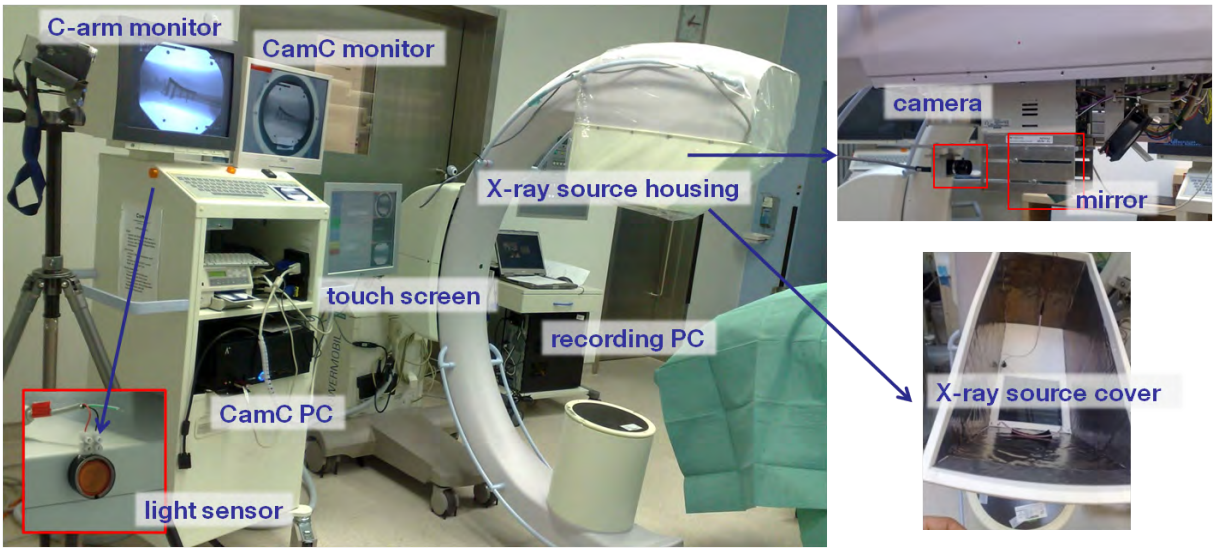


Figure 2.19: The hardware components of the CamC system used within the operating room of Chirurgische Klinik und Poliklinik Innenstadt, LMU, München.

## 2.4 A Surgical Workflow Based Evaluation on Animal Cadaver

The CamC system provides an overlay visualization of X-ray and video images, i.e. video augmented X-ray (VAX). In order to evaluate and predict the clinical impact of VAX, an animal cadaver study was performed to compare surgical performance using VAX from the CamC system versus conventional fluoroscopy (CF) from a standard C-arm [162].

[2] mangotee@gmail.com
[3] http://sine.ni.com/nips/cds/view/p/lang/en/nid/201987
[4] http://www.unigraf.fi/?page=170

Interlocking of intramedullary nails in cow metacarpals was chosen for evaluating applied radiation exposure, operation time and quality of drilling. Analyzing single workflow steps reveals individual strengths and weaknesses related to each step. The study involves three surgeons with different skill levels, each performing seven pairs of experiments. Each pair of experiments consists of one interlocking procedure using VAX, and the other using CF.

### 2.4.1 Study Motivation

The CamC technology is expected to reduce radiation exposure during surgery without introducing major changes to the standard surgical workflow. Whereas many experiments were conducted to evaluate the technical characteristics of the CamC system, its clinical performance has not been investigated in detail. Traub et al. [117] performed a reference based assessment, comparing the workflow of the standard CT to the CamC system for a simulated procedure of vertebroplasty using five spine phantoms. This interesting initial study involved only one surgeon and a very small number of samples, and could therefore not show significant results. It did, however, show that one way of estimating clinical impacts of the CamC system on trauma and orthopedic surgery is to evaluate it in a simulated clinical scenario. A workflow based method is proposed and applied to predict the clinical impact of the CamC system by comparing its performance to a conventional system, i.e. standard mobile C-arm.

### 2.4.2 Surgical Workflow Based Evaluation for Image Guided Surgery Systems

In order to evaluate the clinical performance of a new IGS system and easily identify its advantages and disadvantages, we propose a workflow based comparison of the new system to a conventional method which will be used as a reference. Assessment criteria, like patient outcome and radiation dose, are defined to compare the new method to the reference method. Instead of using only criteria for the whole procedure, our workflow based method differentiates between single workflow steps. This has several advantages. Novel systems may introduce changes to the overall workflow or change the strategy within a single workflow step. While a system might show advantageous results for one step of a procedure, it may indicate disadvantages in another. Therefore, sometimes we may need to combine the functions of the novel solution and the traditional solution for the best result. A workflow based evaluation allows analyzing these aspects in more detail. Also the advantages and problems can be identified more clearly when estimating the impact on single steps instead of only investigating the impact on the whole procedure. For systems that can be used in different procedures it is usually not possible to deduce the possible impact on other procedures from the results of one procedure. Using a workflow based assessment it is easier to generalize results for single workflow steps that are common to several procedures. Moreover, workflow analysis allows technical researchers and surgeons to work together in order to evaluate and make improvements on the system.

The workflow based assessment evaluation consists of the following steps:

a. **Initial formulation of assessment objective.** It includes a description of the

motivation, the system, surgical context, assessment level and a hypothesis of the anticipated result [111].

b. **Modeling the workflows of the reference and the IGS based procedure.** First the workflow of the conventional method is modeled. Depending on the assessment objective and level a suitable workflow model has to be chosen. This can range from simple models, consisting only of few workflow steps, to more detailed methods [175]. Based on the reference workflow and the anticipated use of the IGS, the new workflow is designed. This is done jointly by surgeons and technical researchers which facilitates a common understanding of technical and medical advantages and challenges. In this step, the hypothesis might be refined for each workflow step.

c. **Definition of evaluation criteria for each workflow step.** Based on the assessment objective, evaluation criteria for comparing the new system to the conventional one are first defined for each workflow step. In order to quantify the comparison, measurement parameters must be chosen, such that they represent the evaluation criteria. Then, measures of statistics are defined, e.g. mean value or standard deviation, and hypotheses for these measures are made.

d. **Experiments and acquisition of measurement parameters.** A protocol for recording the measurement parameters must be established. This can be data obtained from video or live observations [176] or it can be data that is captured from medical devices. Upon the introduction of any novel medical system, it is often not possible to use human patients immediately. Rather, the system must be first employed in a simulated setup. In order to avoid a bias analysis, a comparison of a conventional method in the same simulated setup must be used.

e. **Comparison of values from reference and IGS based procedure.** A statistical comparison of the measured parameters is performed for each workflow step in order to obtain quantitative results.

### 2.4.3 Animal Cadaver Study of Interlocking of Intramedullary Nails: CamC vs. C-arm

Intramedullary nailing is a common surgical procedure, mostly used in diaphysal fracture stabilization of long bones. After successful insertion of the nail into the medullary canal, the nail has to be fixed in its position by inserting screws perpendicular to the nail through the provided proximal and distal holes inside the nail's shaft. This is done to prevent rotation or dislocation of the nail within the canal. This procedure is called interlocking of intramedullary nails and is usually performed in a minimally invasive way. The insertion of the screws near the entrance point of the nail is done using the aiming bow attached to the nail. In the distal part of the nail, interlocking is commonly performed free-hand with an AO radiolucent drill attachment or similar aiming device. Various techniques and devices developed for supporting interlocking procedures are reviewed in [177]. This is a challenging surgical procedure, which requires much skill and involves significant levels of radiation to patients and surgical staff in particular [178, 179]. Much

experimental work was done to evaluate the amount of radiation exposure to surgeons during interlocking procedures [178, 179, 180, 181]. Müller et al. [181] showed that the average fluoroscopy time per procedure, mainly spent with interlocking, was 4.63 min. and the primary surgeon received a 2.02 mSv mean radiation exposure to his hand. Levin et al. even showed a total fluoroscopy time of 8 min. while the exposition of the surgeons hand was 0.12 mSV.

Several ingenious methods and devices were developed to facilitate interlocking procedures, e.g. miniature robot based guide positioning [182] and optical tracking with using two non-constrained X-ray images [123]. Suhm et al. [125] employed a commercial navigation system (SurgiGATE system, Medivision, Oberdorf, Switzerland) for interlocking. They showed that the navigation system reduces radiation exposure, but requires significantly longer operation time when compared to the standard C-arm system because of the complexity of the navigation system. These developed solutions have not yet gained worldwide acceptance in clinical practice due to the complex system setup, considerable investment or additional cumbersome hardware involved in the operating room. In contrast, the CamC technology is attractive from both clinical and economical points of view, as no additional separated devices and calibration are required during surgery. In this work, our objective is not to compare the robotics or external tracking based interlocking solution to that of using the CamC system for guidance. Here we focus on the evaluation of the CamC system versus conventional C-arm solutions.

#### 2.4.3.1 Assessment Objective

Our objective was to evaluate VAX versus CF. Interlocking was chosen because it contains various surgical workflow steps that require fluoroscopy guidance using a fair amount of radiation exposure. Also, these workflow steps are structured sequentially, which facilitates the analysis of the procedure. Furthermore, several workflow tasks involved with Interlocking are also necessary in other surgical procedures. Thus, the results of the workflow-based evaluation for each single step can be used to predict the clinical impact of VAX beyond this particular study. By comparing operation time, radiation exposure and outcome quality, we can evaluate VAX and predict its clinical impact.

#### 2.4.3.2 Surgical Workflow for Free Hand Interlocking

The experiments were carried out with bovine forelimb cadavers after approval of the study design by the veterinary public health office. In this study, a single interlocking procedure began with successful implanting of the long nail into the medullary canal of the bovine metacarpal, and ended after successfully inserting one locking screw. The interlocking workflow was divided into seven steps:

i. **X-ray positioning.** Moving the C-arm from outside of the operation field over the cow specimen. It ends after the fluoroscopy image shows the site of interest (in this experiment the distal part of the nail inside the bone).

ii. **Adjustment of hole.** Turning the nail until the hole is perfectly round in order to allow for orthogonal drilling. Due to the setup, it is not possible to turn the

specimen as would be the patients' leg in reality.

iii. **Skin incision.** Finding the incision position and cutting the skin. The correct incision position is confirmed by images showing the scalpel tip located inside the locking hole on the fluoroscopy image when using the standard mobile C-arm, or on VAX when using the CamC system.

iv. **Center punch.** Alignment of a Steinmann pin with the target hole. Then, with the help of a hammer, a small dimple is formed on the bone surface in which the tip of the drill will fit. This step is required only to prevent slipping of the drill bit within the next step, as the cow bone is harder than human bone.

v. **Alignment of the tip of the drill.** Alignment of the drill bit with the target hole. It ends when fluoroscopy shows that the projection of the tip is located inside the circle of the target hole.

vi. **Drilling.** Drilling the bone until the drill bit passes through the locking hole of the nail and the bone cortex on the other side. It ends after confirmation by fluoroscopy.

vii. **Locking screw insertion.** Inserting a locking screw into the hole. Fluoroscopy is required to confirm the success of the insertion, which indicates the end of the procedure.

#### 2.4.3.3 Evaluation Criteria

The first evaluation criterion is to measure the amount of applied radiation exposure using the CamC system compared to the standard mobile C-arm. Through the whole comparison study, we used the pulsed fluoroscopic mode by fixing the tube voltage and radiation time to a setting that was empirically found to be ideal for imaging the bovine bone structures. This produced constant radiation doses for each shot on the level of the x-ray tube. The number of X-ray shots can therefore be used to compare the radiation exposure. It has been claimed that employing the CamC system for interventional procedures does not complicate the surgical procedure compared to using the standard mobile C-arm [50]. This will be further evaluated by comparing operation time and quality of drilling in our study.

The author makes the null hypothesis that it takes a similar number of X-ray shots and a similar operation time when using VAX compared to CF for the whole procedure and for each single step. For both systems, we expect similar results with regard to drilling quality.

#### 2.4.3.4 Materials and Experiments

In this pre-clinical study, we used bovine cadaver forelimbs having similar shape and size, and common surgical instruments, including an AO radiolucent drill attachment, and a 10 mm solid Titanium Femoral Nail (Synthes, Oberdorf, Switzerland). This kind of cadaver was chosen because it has similar dimensions as a human long bone. The cow legs were placed on a carbon table for minimal X-ray absorption. In order to simulate the

rigidity of a normal leg, they were roughly fixed to a wooden board by a strap. So, minor movements of the cadaver were inevitable, providing near-real conditions. Each bone was drilled open from the proximal joint and the nail was inserted in the medullary cavity of the metacarpal bone prior to the beginning of the experiment.

The clinical CamC system described in section 2.3.3 was employed in the study (see figure 2.20). For the interlocking procedure using CF, we used the same C-arm but turned off the monitor showing the overlay images. This reduces variability of using several C-arm systems with differing handling and image quality.

In order to remove skill level of the surgeon as a possible variable for the anticipated results using the CamC system, three surgeons each with varying experience were employed in the study: a young surgeon (below 5 nailing procedures), one experienced surgeon (80 to 120 recorded nailing procedures) and one expert surgeon (more than 200 recorded nailing procedures). The study covered 21 pair experiments (i.e. 42 procedures), 7 pairs performed by each surgeon. Each pair consists of one interlocking using VAX and one using CF. The sequence of two procedures within one pair was randomized by coin flipping and the two procedures were performed consecutively. The inserted nail has two distal locking holes, both of which were used for one pair experiment.

The number of X-ray shots and operation time were recorded by medical and technical staff observing the experiments and then verified by video recording. The quality of drilling through the holes of the nail was assessed by the surgeon as "successful without interference with the nail" giving 1 point, "successful with slight interference with the nail" giving 2 points, "successful with severe interference with the nail" (in this case the drill gets jammed and a correction of drilling angle has to be performed) giving 3 points and "failure" giving 5 points. The drilling quality level was determined as a consensus reached by participating surgeons directly after each drilling. In [15], the authors have employed a similar criterion to assess the quality of drilling in interlocking of intramedullary nails.

#### 2.4.3.5 Results and Comparison

All 21 pair experiments were carried out and their results were statistically evaluated, providing mean values and standard deviation regarding the number of X-ray shots, procedure time and drilling quality. In addition, we applied a paired t-test to determine the statistical significance on all three evaluation parameters between VAX and CF. Table 2.4 shows the mean, standard deviation (SD), and p-value of the number of X-ray shots and the operation time for the whole interlocking procedure as well as for each surgical step in both groups. The results of drilling quality were $1.80 \pm \textit{0.70}$ for the VAX group and $2.20 \pm \textit{0.77}$ for the CF group.

For the whole interlocking procedure, significantly less X-ray shots were needed in the VAX group compared to the CF group ($P < 0.05$). The two groups showed similar overall operation time ($P = 0.958$). Although the VAX group demonstrates better drilling quality ($P = 0.12$) in our study, this difference was not statistically significant.

In the step of X-ray positioning, the VAX group performed better with significantly less X-ray shots ($P < 0.05$) due to the exact aiming of the X-ray area shown as overlay to the live video. The VAX group took significantly less X-ray shots ($P < 0.05$) and significantly less operation time ($P < 0.05$) than the CF group in the step of skin incision, since

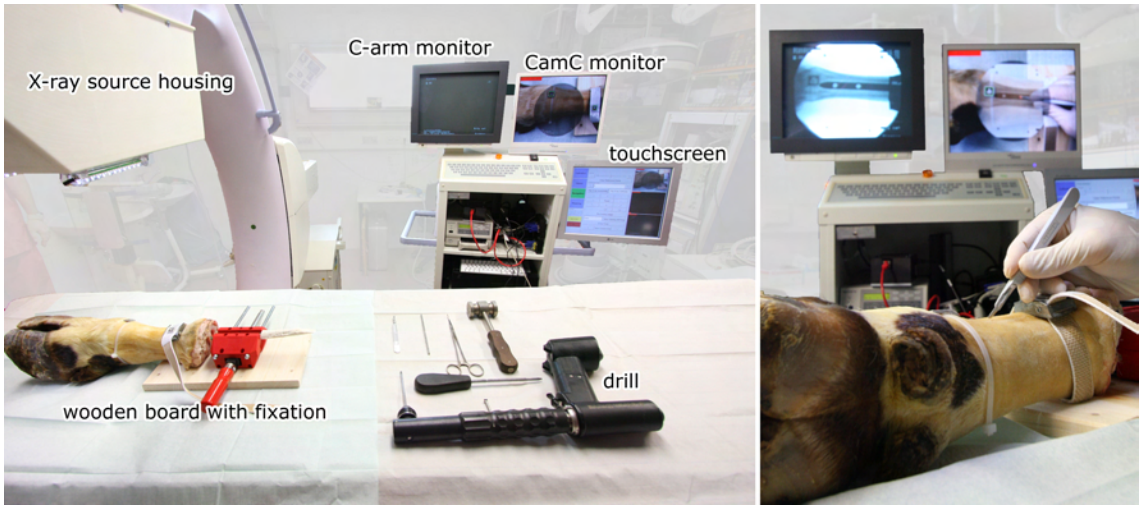


Figure 2.20: The experimental setup for interlocking of intramedullary nails on a cow bone is shown in the left image. The right image demonstrates the system configuration for the procedure using the CamC system. In the system configuration for the procedure using the standard mobile C-arm, the CamC monitor is turned off.

surgeons can quickly find the target place for skin incision using the guidance of the video with the aligned fluoroscopy image (see figure 2.21(a)). Aligning the tip of the Steinmann pin for center punching, the number of required X-ray shots is significantly smaller in the VAX group than in the CF group ($P < 0.05$) (see figure 2.21(b)). Consequently, aligning the tip of the drill bit also requires less X-ray shots; however, the comparison is not statistically significant ($P = 0.14$). In the step of drilling, the VAX can support the control of the drilling axis (see figure 2.21(c)), and thus the VAX group needs significantly less X-ray shots ($P < 0.05$) than the CF group. Overall operation time did not show significant differences ($P = 0.96$). The steps of hole adjustment and screw insertion do not provide any signs of significant differences between the two groups.

We also evaluate the relationship of the surgical performance (in terms of the employed number of X-ray shots and operation time) between the three participating surgeons, and further compare such relationships between the VAX and CF groups. For this, we performed multiple regression analyses with straightforward ordinary least square estimation by defining the number of X-ray shots and operation time as dependent variables and the surgeons' experience level as an independent variable for each workflow step as well as the overall procedure. The experience levels of the three surgeons are modeled as linear increments thereby assuming equidistant experience differences between the surgeons. Table 2.5 shows the results for the number of X-ray shots and operation time. The row experience describes the difference of performance between a specific experience level and next higher level when using CF. The row imaging system shows the difference of performance between using VAX in comparison to CF. The row interaction expresses the change in experience-related difference in performance when using VAX. Note that the coefficient of this interaction variable appears to be insignificant if the experience of the surgeon or using VAX are independent sources of better performance. Conversely, if the coefficient

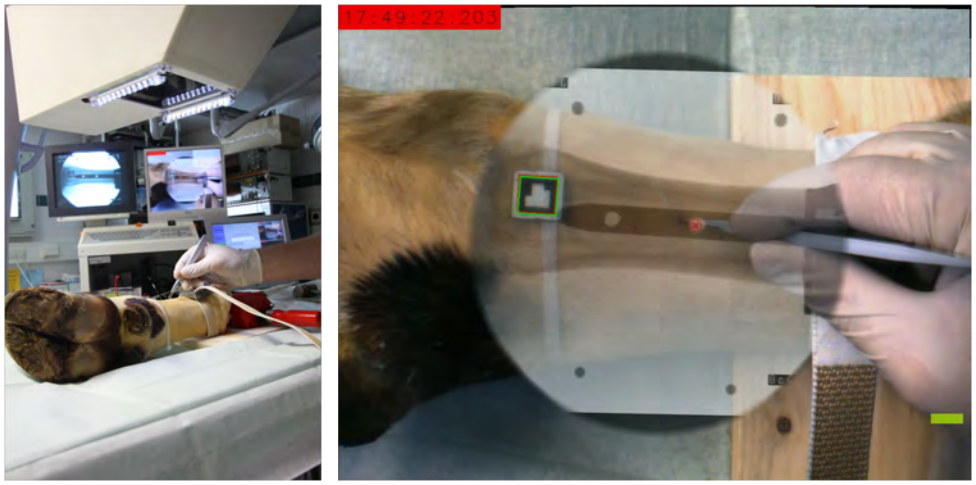


(a)

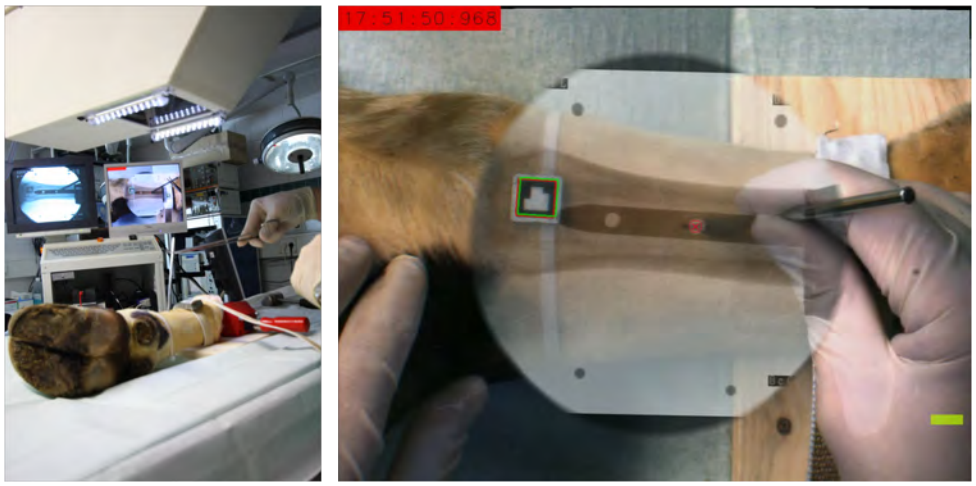


(b)

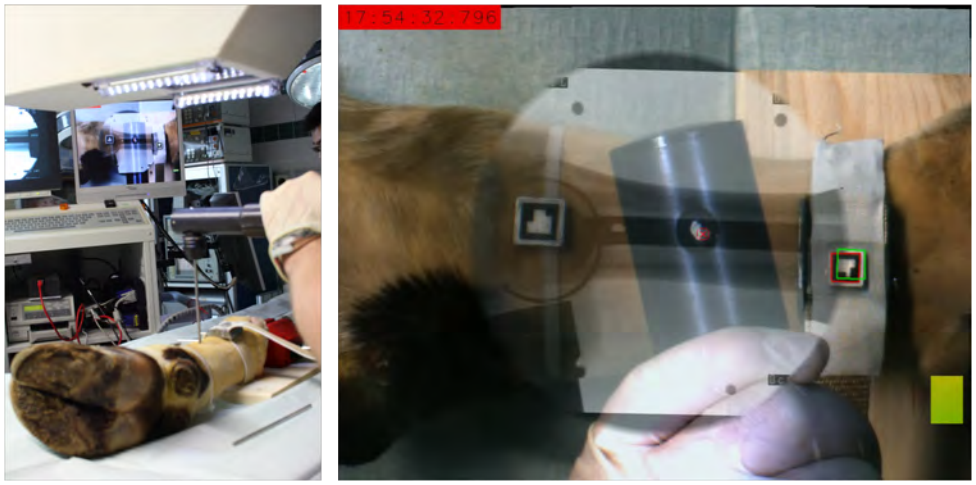


(c)

Figure 2.21: Skin incision (a), center punch (b) and drilling (c) tasks using video augmented X-ray images. The left images show the working scenario and the right images shows video augmented X-ray images seen in the monitor .

| | X-ray positioning | Adjustment of hole | Skin incision | Center punch | Alignment of the tip of the drill | Drilling | Locking screw insertion | Overall |
|---|---|---|---|---|---|---|---|---|
| **The number of X-ray shots** (**mean**±*STD*) | | | | | | | | |
| VAX Group | **1.05** ±*0.22* | **2.81** ±*1.157* | **0.00** ±*0.00* | **2.67** ±*2.56* | **1.38** ±*0.97* | **1.10** ±*0.30* | **1.00** ±*0.00* | **10.00** ±*3.36* |
| CF Group | **1.57** ±*0.75* | **3.10** ±*1.58* | **2.67** ±*0.86* | **4.67** ±*2.99* | **1.81** ±*1.33* | **3.29** ±*2.80* | **1.05** ±*0.22* | **18.14** ±*5.48* |
| p-value | **<0.05*** | 0.34 | **<0.05*** | **<0.05*** | 0.14 | **<0.05*** | 0.33 | **<0.05*** |
| **Operation time** (**mean**±*STD*) | | | | | | | | |
| VAX Group (seconds) | **23.81** ±*9.24* | **25.57** ±*21.87* | **20.00** ±*7.56* | **65.95** ±*55.18* | **26.43** ±*16.86* | **161.71** ±*110.13* | **56.91** ±*52.11* | **380.38** ±*165.11* |
| CF Group (seconds) | **27.05** ±*10.77* | **24.10** ±*16.34* | **29.48** ±*9.69* | **64.00** ±*36.34* | **28.00** ±*26.79* | **163.67** ±*91.08* | **42.48** ±*22.61* | **378.76** ±*101.10* |
| p-value | 0.16 | 0.75 | **<0.05*** | 0.86 | 0.80 | 0.94 | 0.13 | 0.96 |

Table 2.4: The mean, standard deviation (STD), and p-value of the number of X-ray shots and operation time (seconds) for the whole interlocking procedure, as well as for each surgical step, in VAX group and CF group. Note: * $p <= 0.05$

is significant, there is a combined effect of the experience of the surgeon and using VAX.

As the results from the multiple regression analysis shows, whether using VAX or CF, less experienced surgeons require significantly more X-ray shots in the steps of 3, 4, 5, and 6, and for the overall procedure. They also need significantly more operation time in the steps of 3 and 5. It is noteworthy that with drilling, less experienced surgeons show a significantly higher reduction of the number of X-ray shots when using VAX than experienced ones.

| | X-ray positioning | Adjustment of hole | Skin incision | Center punch | Alignment of the tip of the drill | Drilling | Locking screw insertion | Overall |
|---|---|---|---|---|---|---|---|---|
| **The number of X-ray shots** (p-value) | | | | | | | | |
| Imaging system | -0.38 (0.16) | 0.29 (0.71) | -3.02 (<0.05*) | -2.36 (0.08) | -0.79 (0.15) | -3.76 (<0.05*) | -0.12 (0.12) | -10.14 (<0.05*) |
| Experience | 0.21 (0.15) | -0.07 (0.87) | -0.36 (<0.05*) | -1.43 (<0.05*) | -0.71 (<0.05*) | -1.64 (<0.05*) | -0.07 (0.09) | -4.07 (<0.05*) |
| Interact | -0.14 (0.49) | -0.57 (0.34) | 0.36 (0.11) | 0.36 (0.72) | 0.36 (0.39) | 1.57 (<0.05*) | 0.07 (0.22) | 2.00 (0.17) |
| Constant | 1.36 <0.05*) | 3.17 (<0.05*) | 3.02 (<0.05*) | 6.10 (<0.05*) | 2.52 (<0.05*) | 4.93 (<0.05*) | 1.12 (<0.05*) | 22.21 (<0.05*) |
| F | 4.0 | 0.9 | 75.2 | 4.1 | 3.0 | 9.3 | 1.4 | 23.4 |
| $R^2$ | 0.240 | 0.067 | 0.856 | 0.247 | 0.193 | 0.423 | 0.098 | 0.649 |
| **Operation time** (p-value) | | | | | | | | |
| Imaging system | -0.31 (0.95) | 10.48 (0.24) | -11.69 (<0.05*) | 3.38 (0.88) | -2.29 (0.82) | 3.33 (0.95) | 12.57 (0.54) | 15.48 (0.82) |
| Experience | 0.64 (0.82) | -4.14 (0.39) | -4.93 (<0.05*) | -15.93 (0.20) | -13.79 (<0.05*) | 3.50 (0.90) | -2.86 (0.80) | -37.50 (0.31) |
| Interact | -2.93 (0.45) | -9.00 (0.19) | 2.21 (0.48) | -1.43 (0.94) | 0.71 (0.93) | -5.29 (0.89) | 1.86 (0.91) | -13.86 (0.79) |
| Constant | 26.40 <0.05*) | 28.24 (<0.05*) | 34.40 (<0.05*) | 79.93 (<0.05*) | 41.79 (<0.05*) | 160.17 (<0.05*) | 45.33 (<0.05*) | 416.26 (<0.05*) |
| F | 0.6 | 2.8 | 6.8 | 1.2 | 4.3 | 0.0 | 0.5 | 1.0 |
| $R^2$ | 0.046 | 0.180 | 0.349 | 0.089 | 0.253 | 0.001 | 0.035 | 0.076 |

Table 2.5: The results for regression analyses with straightforward ordinary least square estimation by defining the number of X-ray shots and operation time (seconds) as dependent variables and the surgeons' experience level as an independent variable for each workflow step as well as the overall procedure. Note: p-values in parentheses and * $p <= 0.05$.

## 2.5 Patient Study: First Clinical Cases of CamC

The first patient was successfully treated for bunion under CamC navigation (see figure 2.22) in the OR of Chirurgische Klinik und Poliklinik Innenstadt, LMU Müchen on July 02, 2009. A clinical study of the CamC system had been conducted between July 2009 and March 2010 at Chirurgische Klinik und Poliklinik Innenstadt, LMU. The study was approved by the hospital's ethics committee and all patients enrolled into the study have given their consents. This study aims at discovering potential clinical applications of the CamC technology and evaluating its clinical performance.

Figure 2.22: The images of the first surgery performed using the CamC system on July 02, 2009. The left image shows the CamC system setup in the OR. The last two images demonstrate that the primary surgeon uses the overlay image as a guidance to position the C-arm to acquire a desired X-ray image showing exactly the bone deformity of the toe.

### 2.5.1 Study Overview

During the clinical study, 43 orthopedic and trauma surgeries were successfully performed using the clinical CamC system developed at our lab(see section 2.3.3). Eight surgeons participated as primary surgeons, performing 32 plate osteosyntheses, 3 intramedullary nails, 8 metal removals, 1 wire cerclage, 1 tension wiring and 1 ventral stabilization of the lumbar spine (one surgery may contain more than one procedure). One of the participating surgeons has performed phantom and cadaver experiments using the CamC technology prior to the clinical study. All the participating surgeons have received a one-hour presentation of the CamC technology and a practical introduction before the study.

The CamC system is operated like a standard C-arm, not requiring additional devices or calibration during surgery. However, before each surgery, the overlay accuracy of the CamC system has to be verified. For this, the CamC system is positioned in the calibration orientation (i.e. orbital and wigwag rotations are zero, and angular rotation is $\pi$) and a radio-opaque planar marker pattern (see figure 2.23) is placed on the detector. The corners of the square markers in the pattern are extracted in both X-ray and video images with subpixel accuracy and used to compute the overlay error, which is defined

as the pixel distance between corresponding corner points (see figure 2.23). If the mean of the pixel distances between the extracted corner points is larger than 2 pixels, the CamC system must be re-calibrated. Throughout our study however, no re-calibration was required.

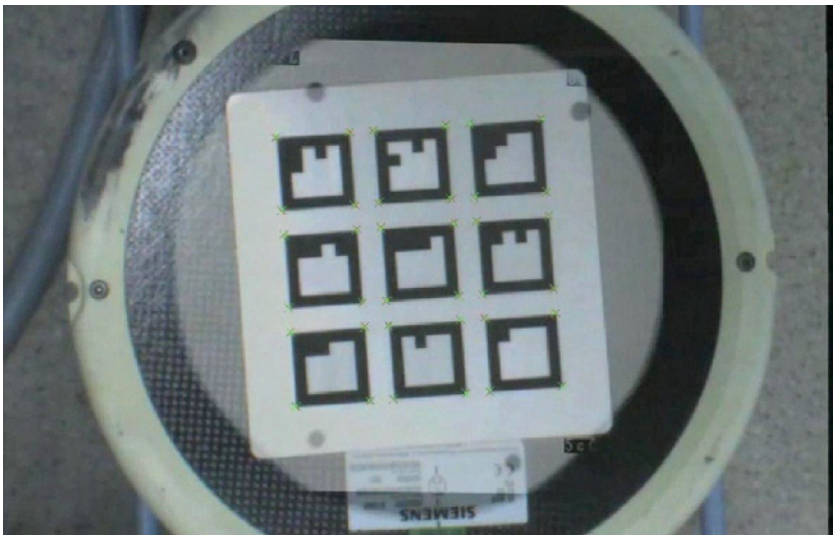


Figure 2.23: The corners of each square marker in the pattern are extracted in both X-ray and video image of the overlay. Red and Green crosses indicate the detected corners in the X-ray and video image respectively.

### 2.5.2 Discovered Clinical Applications

Augmenting X-ray images by co-registered live video images allows surgeons to quickly and intuitively perceive the spatial relations between patients and medical images. Once an X-ray image is acquired, the surgical procedure may be continued under visualization of the live video co-registered with the X-ray image. This allows surgeons to place a surgical tool or to locate an internal target under video imaging in regard to patient's anatomy. The clinical study on 43 patients allowed us to identify the following surgical tasks which directly benefit from the medical AR imaging of CamC:

#### 2.5.2.1 X-ray Positioning

During the intervention, the C-arm machine is often moved over the patient to visualize the anatomical site of interest in X-ray images. This is called X-ray positioning and the task is completed once the X-ray C-arm is correctly positioned to show a particular anatomical structure or implant. The overlay of the X-ray and live video shows an exact X-ray imaging area as a semi-transparent grey circle within the video image frame. This augmentation allows medical staff to intuitively and efficiently position the C-arm instead of the usual acquisition of multiple X-ray images for achieving an optimal view for the X-ray imaging system. Figure 2.24 demonstrates X-ray positioning for visualizing distal radius in one orthopedic and trauma surgery. The left image shows that the projection

area of the X-ray image in the overlay can play the role of an aiming circle. The right image shows the acquired X-ray images overlaid onto the video image.

Figure 2.24: Position the C-arm to visualize the structure of distal radius in an X-ray image. The left image shows that the projection area of the X-ray image in the overlay can play the role of an aiming circle for C-arm positioning; The right image shows the acquired X-ray images overlaid onto the video images after the C-arm is positioned.

#### 2.5.2.2 Incision

After acquiring an X-ray image showing internal bone structures or implants, it is often required to open the skin in order to access bone anatomies or implants. The X-ray augmented by the co-registered live video can be used to plan the correct incision, placing it exactly above the fracture or implant with what the surgeon considers as the optimal length, minimizing the wound. Figure 2.25(a) demonstrates that the incision line is being marked in its optimal length and position relative to the underlying distal radius fracture line, and figure 2.25(b) shows skin cut above an elbow fracture under the guidance of the X-ray and live video image overlay. Internal fixation by a plate is often employed for stabilization of a fracture. For this, a plate can be inserted percutaneously along the bone and across the fracture zone. It then needs to be fixed to the bone by screws that go through the holes of the plate, which can be done by small incisions, avoiding a long wound and soft tissue trauma. Figure 2.25(c) shows the skin incision which is needed to fit the screws to the plate using the overlay of the X-ray and video image.

The same procedure can be used to fulfill an even more precise task which is the incision placement for interlocking of a medullary nail. As the distal locking holes can only be located in X-ray, the Video augmented X-ray view can help. Using a classic C-arm and using the common down-the-beam technique, several X-rays are needed to find the exact incision point, i.e. entry point. This is needed to safely hit the hole inside the nail with the drill in the adjacent step. We call this task as entry point localization. Routinely, a scalpel is placed on the skin and X-rays are taken until the tip of the scalpel is aligned with the hole. With the help of the X-ray Video Overlay, once the nail is visualized in the desired position, only one X-ray is needed, as the incision can be made by watching the video monitor and cutting the skin exactly where the X-ray and video overlay shows the hole.

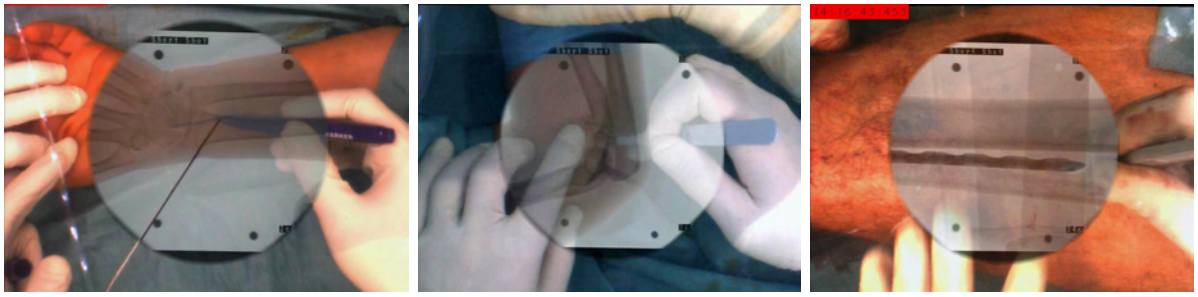

(a) (b) (c)

Figure 2.25: Incision path planning at a distal radius fracture (a), skin cut above a elbow fracture (b), and skin incision above the locking hole of the plate for its internal fixation (c), under the overlay of the X-ray and video images.

Figure 2.26 demonstrates entry point localization in interlockig procedure. After down-the-beam positioning, the locking hole on the nail appears as a round circle in the X-ray image. The entry point, which is defined by the round circle, can be quickly identified on the skin using the live video co-registered by the X-ray image.

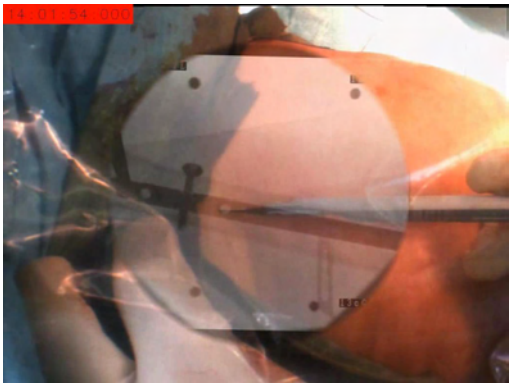

Figure 2.26: The entry point on the skin for the locking hole is identified using the live video co-registered by the X-ray image.

#### 2.5.2.3 Instrument Axis Alignment

Insertion of a linear surgical instrument through internal bone along a preferred axis is a common surgical task in many orthopedic and trauma procedures, e.g. interlocking of intramedullary nails and percutaneous spinal interventions. It requires the positioning of the C-arm in the so called down-the-beam position. More specifically, the axis of insertion coincides with the direction of the radiation beam and is projected as a single point (entry point) onto the acquired X-ray image. The precise alignment of the instrument with the correct axis is usually achieved by first aligning the tip of the instrument with the entry point and then orienting the instrument to be aligned with the axis. Many X-ray images are always required to guide the instrument placement. As the video camera and

radiation beam share the same projection geometry for CamC, the process of instrument axis alignment and insertion can be guided under the live video co-registered with one X-ray image taken at the C-arm down-beam position.

Figure 2.27 and 2.28 demonstrate the instrument axis alignment using the overlay of X-ray and video image in interlocking of intramedullary nails, where a hole has to be drilled through the bone, passing through the preformed hole in the intramedullary nail. In order to achieve the drilling perfectly, the position of the drilling and the axis of the drill itself have to be exact. Figure 2.27 shows aligning the tip of the drill within the locking hole using VAX. The instrument is generally inserted through a small skin incision to reach the internal bone surface (see paragraph above). Thus, the tip of the instrument that is under the skin becomes invisible to the video camera and X-ray images are taken to confirm the alignment. Since the live video can offer visual information about the orientation of the drill, orienting the drilling axis such that it is aligned with the down-the-beam axis can also be accomplished using VAX (see figure 2.28(a)). The employed drill machine is designed for using X-ray images, thus the correct drilling axis is confirmed by the X-ray image showing embedded radiolucent cylinder structures inside the drill machine imaged as two co-centric round circles (see figure 2.28(b)).

(a) (b)

Figure 2.27: (a) Aligning the tip of the drill within the locking hole using the X-ray and video image overlay; (b) Alignment is confirmed by the X-ray image showing that the tip is within the hole.

#### 2.5.2.4 K-wire Guidance

K-wires are often used for temporary fixation of bone fragments or for temporary immobilization of a joint during surgeries. They can also be used for definitive fixation if the fracture fragments are small, e.g. for wrist or hand fracture reduction. Great care must be taken not to injure the sensory branch of the radial nerve during insertion of K-wires for wrist fracture reductions. The insertion direction of the K-wire relative to the bone is commonly viewed using C-arm X-ray images. With the CamC system, the direction of a linear K-wire relative to the bone can be intuitively anticipated from the overlay image showing the projected direction of the K-wire and bone in a common image frame.

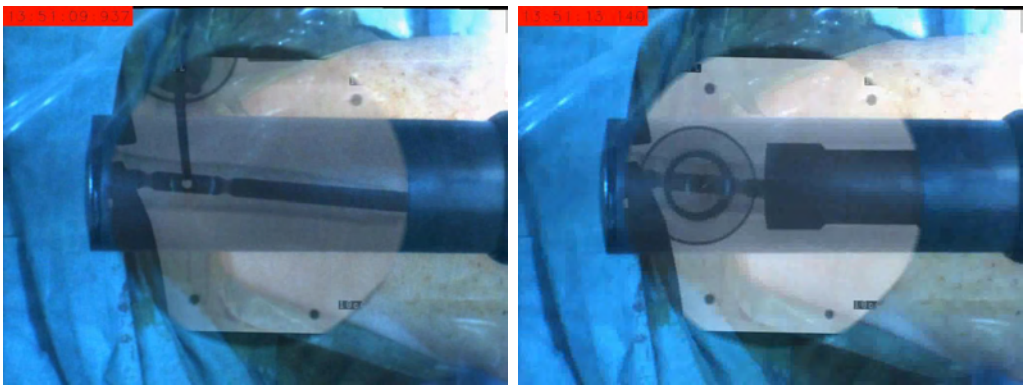

(a) (b)

Figure 2.28: (a) Orienting the drilling axis to be aligned with the down-the-beam axis using the X-ray and video image overlay; (b) Alignment is confirmed by the X-ray image showing embedded radiolucent cylinder structures inside the drill machine imaged as two co-centric round circles.

Figure 2.29(a) shows the placement of a linear K-wire for fractures of the distal radius using the X-ray and video image overlay. Figure 2.29(b) shows that the final placement of the K-wire is confirmed by one X-ray image.

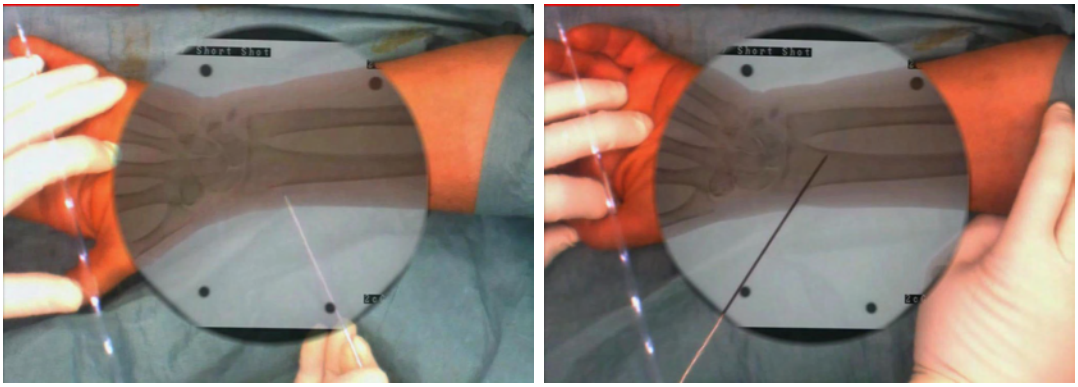

(a) (b)

Figure 2.29: (a) Placing a K-wire relative to fractures of the distal radius using the X-ray and video image overlay; (b) Confirmation of the K-wire placement.

#### 2.5.2.5 Others

The overlay of X-ray and video image has the potential to help surgeons choose a suitable implant size, since the bone structure and the implant will be visible in a common image frame. In distal radius fracture reduction surgery, surgeons have used the overlay image to check if the length of a bridge plate is suitable before inserting the plate under the skin (see figure 2.30(a)). However, the bone structure and implant are not often at the

same depth, which introduces magnification error and leads to difficulties for choosing the correct size of implant. Projection geometry was not a problem in this case because the distance between the internal bone and the plate is short.

With the CamC system, the surgeons can easily see in the overlay if their hands are directly inside the X-ray image area (see figure 2.30(b)). By moving their hands out of the X-ray image area, they can drastically reduce the direct radiation exposure, especially in situations when the surgeon is holding the patient's extremity in a special position in order to acquire a fluoroscopy image of a certain perspective.

Moreover, the video images with co-registered X-ray images from the CamC system can be used for automatic documentation of an operation, to allow to retrospectively analyze surgical procedures or to create educational videos from real surgeries.

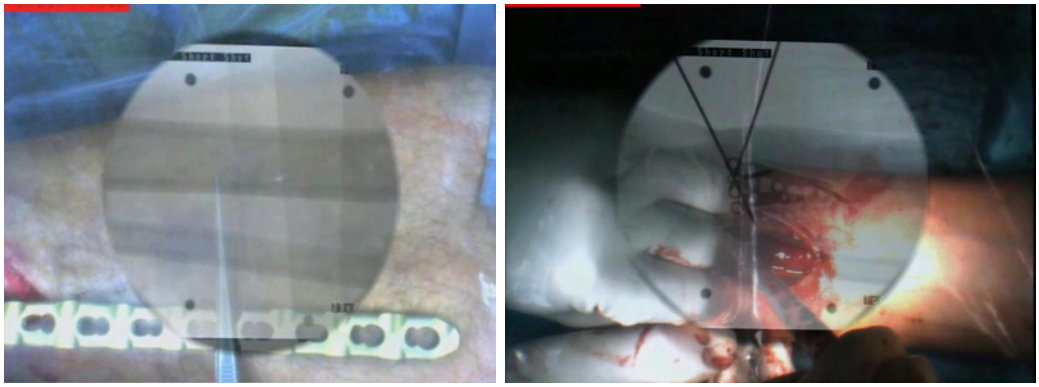

(a) (b)

Figure 2.30: (a) The X-ray and video image overlay is used to check if the length of a bridge plate is suitable; (b) The hand of a surgeon is within the X-ray beam, as it is visualized within the X-ray image area of the overlay.

### 2.5.3 Clinical Performance: CamC VS. C-arm

Clinical performance of the CamC system is quantified by the number of X-ray shots required to perform a surgical procedure. We compare the required number of X-ray shots using the CamC system and using standard C-arm systems. The quantification study includes 29 surgical procedures using the CamC system and 44 surgical procedures using the C-arm systems. The number of X-ray shots are recorded by the same medical staff within the OR for both CamC and C-arm groups. The recording of the C-arm group is conducted after the CamC clinical study. The CamC and C-arm groups include the same types of procedures, but may have different number of cases for the same type procedure. $27.28 \pm 23.16$ X-ray shots are required for each surgery in CamC group. C-arm group needs $37.70 \pm 44.24$ for one surgery.

## 2.6 Discussion and Conclusion

The CamC system that extends a standard mobile C-arm by a video camera and mirror construction was introduced by Navab et al. [49, 50]. One key feature of the CamC system is that it can be operated as a conventional C-arm system, with the additional feature of offering X-ray images co-registered with a live video anytime without online calibtation or registration and additional devices during intervention. Augmenting X-ray images by a live video can benefit many surgical procedures: needle placement [145], interlocking of intramedullary nails [146], pedicle screw placement [147], and vertebroplasty [117] to name a few. Furthermore, having aligned projection geometries of the C-arm X-ray and the attached video camera enables new computer aided surgery solutions, such as visual servoing based C-arm positioning [148], artificial fluoroscopy [150], and parallax-free X-ray image stitching [164]. The solutions based on CamC platform are attractive from both clinical and economical points of view, as no additional separate tracking devices and calibration are required during surgery.

The accurate overlay between the images is crucial for the guidance of high quality surgical outcomes. We evaluated the influence of CamC calibration, X-ray distortion, and the mechanical sagging of the C-arm gantry on the overlay accuracy. The inaccurate alignment of the camera optical center and X-ray source causes the estimated homography for the co-registration only to be valid for image points for which corresponding space points are on the same plane defined by the homography. For this, we developed an experimental protocol that searches for an optimal homography resulting in a minimum overlay error for all image points no matter where their corresponding space points are located. When applying any of the estimated homographies, the minimum overlay-plane-error should happen for the plane where the homography is estimated in theory according to equation 2.1. IIn all our experiments we had one exception. This occurred at the image intensifier for which the overlay-plane-error is not minimum on that plane among all the planes. This exception could be caused by a poor focus of the video camera for the plane of the intensifier. The poor focus will introduce errors to the blob point detections and thus influences the accuracy of the homography estimation. The influence of the camera's focus on the overlay accuracy will be investigated in the future.

In current literature, online X-ray distortion correction strategies require a longer execution time and a more complex system setup, i.e. the calibration board must be attached to the intensifier for all C-arm orientations. The VDP method that relies on much less image points than the traditional X-ray distortion correction strategies is adapted in order to compensate for perspective distortion correction caused by the changes of the C-arm orientation. In section 2.2.2.2, we have shown that using the VDP method combined with the distortion coefficients at the calibrated pose can dramatically improve the overlay accuracy for any C-arm rotation. Future work will involve attaching additional markers behind the mirror in order to have at least 4 points visible at all time during surgery for the VDP calculation (i.e. to avoid occlusion of markers in the images due to anatomy or surgical tool obstructions).

The clinical performance and impact of the CamC technology is assessed and quantified on 42 animal cadavers and 43 patients. A surgical workflow based method is proposed

and applied to compare surgical performance using VAX versus CF in the animal cadaver study. Interlocking of intramedullary nails in cow metacarpals is chosen for evaluating applied radiation exposure, operation time and quality of drilling. Overall, the results of the evaluation study show that the VAX group required significantly less radiation exposure, achieved a similar drilling quality for the whole interlocking procedure but required similar operation time compared to the CF group. VAX has its main positive impact in C-arm positioning, entry targeting for skin incision or center punch, and axis control in drilling, needing significantly less X-ray shots to fulfill the tasks. Due to the fact that X-ray positioning and skin incision are necessary steps in many other surgical procedures, our results are also valuable for predicting the clinical impact of VAX beyond this particular application. The standard deviations of the number of X-ray shots are smaller for VAX. We see this as a sign of increased reproducibility for the surgeons. Using the VAX did not save operation time. The mean of the whole procedure time is even slightly higher when using VAX. In combination with a higher overall standard deviation, we see this as the effect of a learning curve with the users still exploring the abilities of the system and taking their time for the apprenticeship. This becomes particularly clear in the last step of screw insertion which took much longer in the VAX group than in the C-arm group. After video analysis and confirmation with the surgeons we found out that the participants tended to make use of the VAX to find the hole to put the screw in, although they could definitely find it even quicker without any image based guidance, since the hole is easy to feel. We expect these effects to disappear with further use of the system, most likely allowing a reduced operation time in the future. Furthermore, less skilled surgeons may benefit even more from VAX, as the regression analyses show a significantly higher reduction of the number of X-ray shots for less experienced surgeons when using VAX while drilling the interlocking hole.

Different clinical applications of the CamC system are discovered in the patient study, such as C-arm X-ray positioning, incision, entry point localization, instrument axis alignment, K-wire guidance, and surgery documentation. The patient study shows that the surgical procedures require less X-ray shots when using the CamC system compared to the standard C-arm systems. However, we cannot show a statistically significant difference from the results of this initial clinical study due to the limited number of patient data sets.

Surgeons' feedback on the first CamC guided operations indicates that the new device can be smoothly integrated into the surgical workflow. The video guided X-ray C-arm positioning works intuitively and reduces radiation exposure as there is no more need for iterative acquisition of X-ray images in order to reach the desired image. After acquiring one X-ray image which includes the fractured anatomy or implant, the X-ray and video overlay can further be used to plan the correct incision, guide the K-wire insertion, or locate the entry point on the skin. The power and importance of CamC's image guided C-arm positioning is especially demonstrated when imaging small parts. In these cases, the anatomy of interest is often placed near the X-ray source and the desired image area is small, making it hard to position the C-arm correctly and get the right image. Some commercial C-arms provide laser guidance but unlike our solution they only point at the center of imaging area and do not visualize the total area to be imaged by the X-ray

system.

In our experience, apart from saving radiation dose in standard orthopedic and trauma surgeries, the CamC system provides additional information to the surgeon that helps him or her carry out many tasks not only more intuitively but also more confidently. The participating surgeons claim that the decision-making process becomes easier with the CamC system and that they feel more secure when they observe their tool, their hand as well as the deep-seated anatomical target within live video augmentation. The CamC system provides more information which eventually enables surgeons to optimize their performance of tasks, but if so desired, the device can still be operated like a classic C-arm.

In the animal cadaver study, the accidental movements of the cow cadavers were most often observed during center punching and drilling. In the patient study, the accidental movements of the treated anatomies were mainly introduced by placing implants or instruments with strong force. We also notice that the surgeons often moved the patients in order to have better access to the anatomies during the real surgeries. These movements would result in an unanticipated misalignment of X-ray and video image. Using that misaligned VAX image for invasive actions could be a threat to the patient and the success of the surgery. For that reason, consequently informing surgeons about such a misalignment is compulsory. Through visual marker tracking and display of the deviation on the main VAX monitor, this issue was solved in our experiments. Accordingly, the participating surgeons were responsible for acquiring a new X-ray image when misalignment occurred. However, we saw that in many cases the surgeons did not take a new X-ray as he either reversed the movement, reaching the original position indicated on the screen, or he did not require an exact overlay at that point of the procedure. As the visual markers were attached on the skin surface that tends to have minor movements relative to the underlying bone, the visual marker tracking method could misinterpret the image alignment. Likely because the distance between the skin and the bone in our cow specimens was short, and movement was very small, we did not experience any problems in the animal cadaver study. However, serious skin movements relative to the internal bone were noticed when drilling through femur in the human surgeries. Thus skin adhesive marker based tracking could mislead the surgeons in this case. In the current implementation for informing about misalignment, the color bar is displayed close to the border of the VAX image and out side of the X-ray image area. Thus, surgeons need to actively switch their attention between the X-ray image area and the color bar. In a highly stressful environment, surgeons prefer to be notified about misalignment in order to concentrate on the X-ray image area showing the most relevant surgical visual data. Possible ideas for showing the misalignment without deterring the attention of the surgeon are adding special effects (such as blurring or fuzzy effects) to the video images within the X-ray area, directly turning off the video images, or generating alarming sound. We note that the treated anatomy can be positioned firmly with the help of an extension C-arm fluoroscopy table. This minimizes the potential risks of injuring the anatomy and accidental movements.

Surgeons are generally exposed to scattered radiation during fluoroscopy. Scattered radiation in various C-arm positions and orientations used in surgical procedures are well

studied [183]. The recommended standard position of mobile C-arms is having the X-ray tube below the patient and the image intensifier above, reducing the scattering towards the surgeons head. In order to visualize the patient in video augmented X-ray, the X-ray source must be placed above the patient, potentially increasing the scattering dose to the surgeon's head per X-ray shot. In [184] however, the authors show that for surgeries at the periphery of the limbs, the inverted C-arm position required by VAX reduces the scattering dose to the head of the surgeon compared to the standard position. Additionally, we found that the surgeons can easily see in VAX if their hands are directly inside the X-ray beam. By moving their hands out of the X-ray area, they can drastically reduce their exposure, especially in situations when the surgeon is holding the patients extremity in a special position in order to acquire a fluoroscopy image of a certain perspective.

Within OR, surgical lamps are used to illuminate operation areas, causing a large dynamic range (luminance range from the largest brightness value to the smallest brightness value). Human eye has high dynamic range and can perceive all brightness levels, while the current video camera of the CamC system has a low dynamic range. Thus, the captured images may suffer from overexpourse or underexpourse and can lose image data (see figure 2.31(a)). In the patient study, the surgical lamps were moved out of operation field in order to have an ideal video image quality when the surgeons were watching VAX. High dynamic range (HDR) video cameras that have a great dynamic range are commercially available. In the future work, HDR cameras will be adpated in the CamC system and its performance should be assessed in a real clinical setup. Figure 2.31(b) shows the scene of the OR captured by the digital camera of Iphone 4 without and with HDR function. The captured HDR image can reveal more details of the scene compared to the non-HDR image.

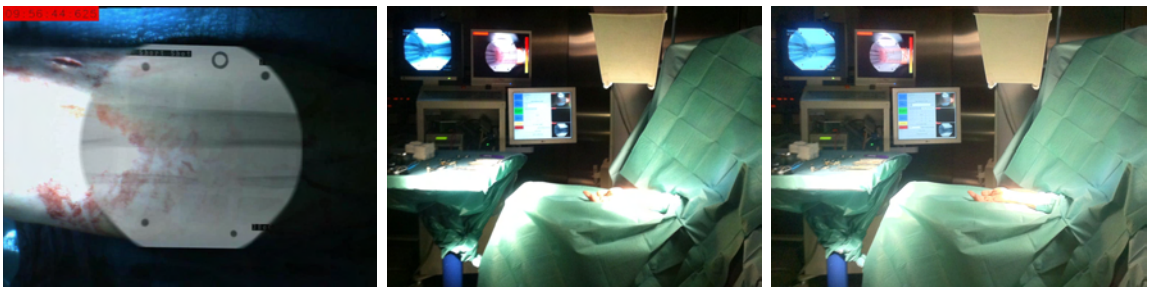

(a) (b)

Figure 2.31: (a) The video image of the VAX suffers from overexpourse, which is caused by the limited dynamic range of the video camera; (b) The left and right imags show the scene of the OR captured by the digital camera of Iphone 4 without and with HDR function.

For the CamC system, the space between the X-ray gantry and image intensifier is reduced by the optic system, i.e. mirrors, placed between them. The limited space sometimes makes it difficult to perform operations on an entire body. Employing optical lenses instead of using only the planar mirrors may reduce the size of the entire optic system while the video camera can remain the size of the field of view. This should be

researched in the future. Furthermore, whether optical lenses introduce further distortion to the X-ray images has to be investigated and taken care.

A simple alpha blending method is used to visualize the co-registered X-ray images and video images. The alpha value must be adjusted manually to help surgeons better perceive surgical related information, e.g. bone structures, skin, and instruments, from the X-ray and video image overlay. However, X-ray images typically suffer from high noise, non-uniform intensities, as well as weak and spurious edges between bone structures, soft tissues, and background. The video images could have bad contrast and overexposed or underexposed areas due to noise and high illumination range. Thus, simply superimposing the X-ray and video images with alpha blending method sometimes introduces challenges for the surgeons to quickly recognize and differentiate important structures in the overlay image. In the future work, visualization solutions and image feature enhancement methods need to be explored in order to improve the visualization of the image overlay. The contextual in-situ visualization proposed by Bichlmeier et al. [185] allows for improved depth perception when displaying the visual medical data of internal anatomies with co-registered video images.

The X-ray image area does not always contain pertinent anatomical information, as in foot and hand surgeries. In order to preserve more visual data from video images, one possibility is to remove the X-ray background that has no anatomical information from the overlay (see a mimic sample in figure 2.32). This requires the segmentation of anatomical strctures in X-ray images, which may be difficult. Alternatively, the segmentation may be achieved based on the skin of the anatomy in the video images, and the segmented area can be directly applied to the co-registered X-ray image.

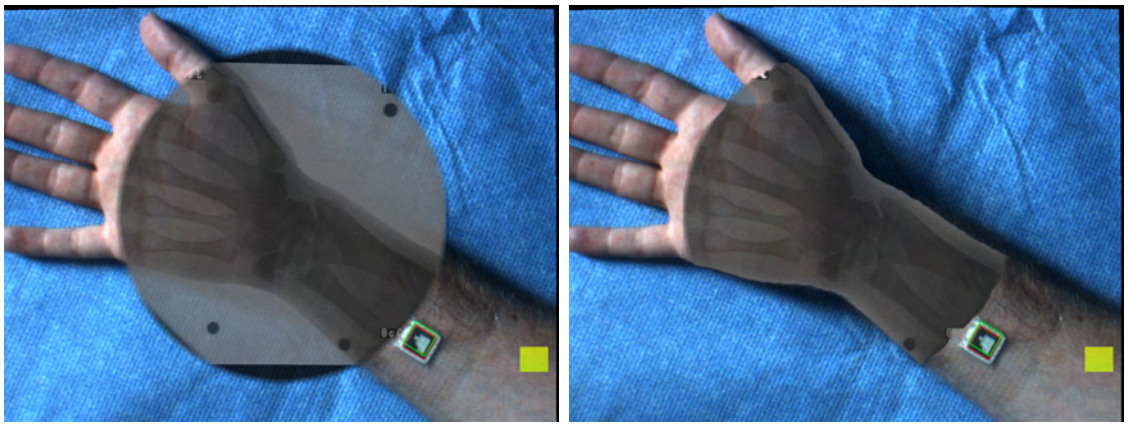

(a) (b)

Figure 2.32: A mimic sample of removing the X-ray background that has no anatomical information from the overlay of a human hand: (a) The overlay of original X-ray and video image; (b) The overlay of the segmented X-ray and video image. The X-ray image is manually segmented.

As in many cases where a new image guided surgery system is being introduced to the OR, surgeons need to explore the system and take advantage of the full potential of

its functionalities. At this stage close collaboration between surgeons and engineers is extremely crucial, since joint design of the system, its functionalities and user interface could play an important role in its further development and its future clinical impact. Many new applications could emerge from this first set of surgeries. Full video documentations of the current procedures need to be analyzed closely in order not only to identify and describe advantages and shortcomings of the system, but also to allow surgeons to eventually modify single workflow steps, optimize the way that surgeries are performed, or even invent new procedures taking full advantage of the simple and intuitive augmented reality imaging and visualization provided by CamC.

In conclusion, VAX shows bone anatomy or implants co-registered with live video displaying skin, surgeon's hands, and instruments. This makes spatial relation between clinically relevant structures more clear and more quickly perceived by the surgeon, potentially reducing stress, radiation and sources of surgical mistakes. This new imaging technology can further be transferred to other orthopedic and trauma applications from needle guidance to minimally invasive orthopedic surgery. Furthermore, the co-registered X-ray and video images pave the way for the implementations of different image guided surgery solutions. The implementation of two novel C-arm X-ray imaging solutions based on the CamC platform are presented in chapters 3 and 4.

This paragraph summarizes the contributions in the chapter. I have designed a practical and robust calibration method for the CamC system in order to achieve an accurate intra-operative video augmented X-ray imaging. In order to complete the first clinical prototype of the CamC system, I have estimated radiation dose generated by the CamC system to air and developed an online detection method of overlay misalignment. The hardware and software components of the clinical system were built in collaboration with my colleagues and students at the chair. Furthermore, I have proposed a surgical workflow based evaluation methodology and applied it for the assessment of clinical relevance and impact of the CamC system based on 42 animal cadavers and 43 patients. The cadaver and patient studies were performed in a close collaboration with our clinical partners of medical doctors and medical students. The workflow based analysis demonstrates that several surgical tasks benefit from the overlay, namely: skin incision, entry point localization, instrument axis alignment, K-wire guidance and X-ray positioning.

CHAPTER

# THREE

# INTRA-OPERATIVE PARALLAX-FREE PANORAMIC X-RAY IMAGING

This chapter presents a novel method to generate parallax-free panoramic X-ray images during surgery by enabling the mobile C-arm to rotate around its X-ray source center, relative to the patient's table. Rotating the mobile C-arm around its X-ray source center is impractical and sometimes impossible due to the mechanical design of mobile C-arm systems. In order to ensure that the C-arm motion is a relative pure rotation around its X-ray source center, I propose to move the table to compensate for the translational part of the motion based on C-arm pose estimation. For this I employ a visual marker pattern and a Camera Augmented Mobile C-arm system. We are able to produce a parallax-free panoramic X-ray image independent of the geometric configuration of imaged anatomical structures. The method does not require a fronto-parallel setup or any overlap between the acquired X-ray images. This generated parallax-free panoramic X-ray image preserves the linear perspective projection property. It also presents a negligible difference (below 2 pixels) in the overlapping area between two consecutive individual X-ray images and has a high visual quality. This promises suitability for intra-operative clinical applications in orthopedic and trauma surgery. The experiments on phantoms and ex-vivo bone structure demonstrate both the functionality and accuracy of the method. The proposed method of parallax-free panoramic X-ray imaging has been presented in [164].

## 3.1 Clinical Motivation

Accurate intra-operative determination of mechanical axis alignment, joint orientation and leg length is crucial for the treatment of knee osteoarthritis, correction of deformities, and long bone shaft fractures. The correct mechanical axis alignment of the lower extremity plays an important role in preventing osteoarthritis, especially of the knee. For this reason, the verification of this axis is critical for reconstructive surgery as well as trauma surgery of long bones of the lower limb. In bone fracture reduction surgery, surgeons need X-ray images to determine the relative position and orientation of bones and implants not only for diagnosis and surgery planning, but also for ensuring and validating the quality of

their treatment during and after surgery. X-ray images acquired by mobile C-arms have a narrow field of view and cannot visualize the entire bone structure of a lower leg within one single X-ray image. Acquiring several individual X-ray images to visualize the entire bone structure only gives a vague impression of the relative position and orientation of bone segments. This often compromises the correct alignment of fragments and placement of the implants in long bone reduction surgery. Axial malalignment in long bone fracture reduction surgery is reported to be up to 28% [186, 187, 188, 189]. Unfortunately, the correct fixation of the bones often only can be confirmed post-operatively using a common X-ray machine with a large field of view that cannot be used in the operating room. Thus, a second surgery for correction and repositioning may be required, which introduces additional costs, pain, radiation, and risk. Panoramic X-ray images with exceptionally wide fields of view could be very helpful during surgery, since they can show the whole bone structure with its entire mechanical axis, in a single image. Furthermore, it can also facilitate measuring the length and determining suitable implants [190, 191]. In addition to their main application, determination of mechanical axis alignment, joint orientation and leg length, panoramic X-ray images are also useful for visualizing the spinal column to determine the positions of vertebrae [192, 193].

Many methods and systems were proposed for the generation of panoramic X-ray images by combining multiple individual X-ray images with limited fields of view [190, 192, 193, 126, 127, 128]. However, all of these proposed methods have their own shortcomings. I propose a novel method to generate true parallax-free panoramic X-ray images during surgery. Unlike existing methods, in which parallax effects, i.e. ghosting and misalignment (see figure 3.1), in the panoramic X-ray image can not be avoided for imaging a non-planar bone structure, the proposed method can create a parallax-free panoramic X-ray image by making the mobile C-arm rotate around its X-ray source, relative to the patient's table.

## 3.2 Related Work

Image stitching, the process of creating panoramas, has been intensively studied in the last decades and many robust algorithms were developed in non-medical areas [194, 195, 196, 197]. However, directly applying these methods for stitching X-ray images will be either impractical or unreliable. It is well known that, one central component of stitching is image registration, i.e. the estimation of a transformation to align two images. Intensity-based registration needs large overlap areas between the consecutive X-ray images, which as a side effect increases the radiation exposure. For feature-based registration, reliably and accurately detecting anatomical features is hard in the X-ray images, especially in long bone X-ray images. On the other hand, all of the methods applied to optical images are based on an implicit assumption, occlusion, i.e. the pixel value in the image is only related to the first imaged object along the ray's path. But, in the X-ray image the pixel value in the original image is related to the attenuation of the imaged object along the ray's path, and the same feature in two different X-ray images could have totally different intensities.

A special purpose digital X-ray machine was introduced to generate panoramic X-ray images by simultaneously translating the X-ray source and the image intensifier over the

patient [190, 192, 193]. This X-ray machine is not versatile enough to replace mobile C-arms within operating rooms. The correct mechanical axis alignment or fracture reduction can only be confirmed post-operatively. Therefore an intra-operative solution based on mobile C-arms is still required. For obtaining a long bone panoramic X-ray image intra-operatively, two methods were proposed using standard mobile C-arms. The first one proposed by Yaniv and Joskowicz [126] introduces an orthopadic radiolucent X-ray ruler placed along the limbs. It first segments the detected graduations of the ruler on the X-ray images, and then uses graduations of the ruler to estimate the planar transformation based on a feature-based alignment method. In this method, the radiolucent X-ray ruler must be placed roughly parallel to the imaged bone and users are required to manually select points on the contour of the reconstruction plane in order to compensate for parallax effects on that plane. The biggest drawback of this method is that sufficient overlapping areas between two consecutive X-ray images are required to estimate the planar transformation and thus additional radiation exposure is inevitable. Another method employs a radio-opaque absolute reference panel with absolute coordinates placed under the bones [127]. This reference panel contains a grid of radio-opaque rigid markers and thus X-ray images can be registered based on the known geometry of this panel. This absolute referencing method is independent from overlapping X-ray regions, but requires an X-ray visible panel, which will occlude fine anatomical structures in the X-ray images. Furthermore, no method was proposed in the paper to solve for the parallax effects, which are introduced by the stitching plane and the target plane not being on the same level. Both methods require a fronto-parallel mobile C-arm setup, i.e. the ruler plane and the reference panel plane must be parallel to the detector plane of mobile C-arm.

In [128], a method is introduced to generate panoramic X-ray images intra-operatively using a CamC system and a planar marker pattern. This method does not require overlapping X-ray images and special X-ray markers. It uses the video images in combination with a visual marker pattern to estimate the planar transformation for creating panoramic X-ray images. In order to reduce the parallax effects on the bone plane, the marker plane and the bone plane need to be parallel to each other and the distance between them has to be manually estimated. The major advantages over the previous C-arm based solutions [126, 127] are the reduction of ionizing radiation and the independence from fronto-parallel C-arm setup.

The parallax effects will cause not only the blurring and ghosting (see figure 3.1), but also the metric measurement errors in the image. Although methods for reducing parallax effects on the bone plane were described in [126, 128], they require the bone segments to be on the same plane and parallel to the plane used for estimating the transformation. In practice, it is unlikely that the plane of the bone is exactly parallel to the plane of the ruler (or marker pattern) due to soft tissue around bones. Bone segments furthermore may be on different plane levels due to fracture or inability to fully extend the joints. For these complex situations, completely removing the parallax effects in the panoramic images is impossible by using the existing methods including [126, 128]. This would restrict the usefulness of stitching approaches within clinical routine to a limited number of cases.

In order to remove parallax effects in the final panoramic images, algorithms from the computer vision and image processing community, e.g. manifold method [196], multi-

perspective plane sweep method [198] and virtual frames method [197] were introduced. However, all of them only ensure a perceptually correct result, but the property of linear perspective projection is not preserved in the images and thus the metric information can not be recovered. Another way of obtaining a parallax-free panorama is making a parallax-free camera motion, in which the camera undergoes a pure rotation around its center [194]. The parallax-free camera motion results in a true panorama without any parallax effect. This true panorama is desirable for two reasons: it is the same as a single image acquired by a pinhole projection camera with a wide viewing angle; it therefore preserves the property of linear perspective projection. However, making the mobile C-arm rotate around its X-ray source is impractical and sometimes impossible, due to the limitation of the mechanical configuration of mobile C-arms.

This chapter introduces a new method for parallax-free X-ray image stitching by making the C-arm rotate around its X-ray source, relative to the patient's table. This is achieved by moving the table to compensate for the translational part of the motion based on C-arm pose estimation, for which a CamC system and a visual planar marker pattern are employed. Finally, the proposed solution is able to generate a true parallax-free panoramic X-ray image, independent of the configuration of bone structures and without the requirement of a fronto-parallel setup or overlapping X-ray regions. This true panoramic X-ray image now can be treated as a single image obtained by a C-arm having an exceptional wide imaging field of view and also can be further processed by various computer vision or image processing algorithms that assume linear perspective projection, e.g. 2D-3D rigid registration of X-ray fluoroscopy and CT images. Taking into account that the economical issues in healthcare are of high importance for computer aided intervention solutions, the proposed approach of using a CamC system and a visual planar marker pattern for intra-operative parallax-free X-ray image stitching is also attractive from an economical point of view, since no additional calibration and no external tracking systems are required during surgery.

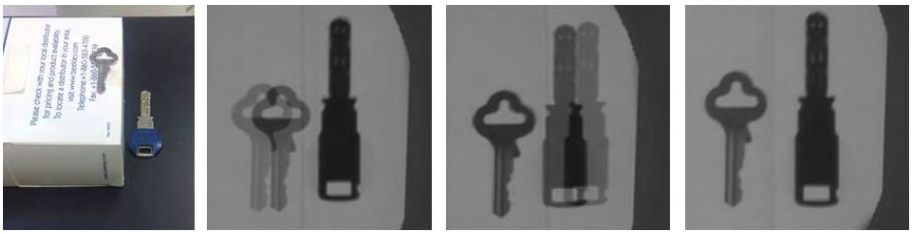

Figure 3.1: Illustration of the parallax effects in the panorama of stitching two X-ray images. From left to right, the first image shows the construction of two metal keys on two different parallel planes. The second image is the panorama generated using the transformation for the plane of the bigger key, and the third image shows the panorama generated using the transformation for the plane of the smaller key. The last image presents a parallax-free panorama generated by the X-ray source undergoing a relative pure rotation.

## 3.3 Method

The key step of image stitching is the estimation of the planar transformation for aligning images. The camera pose of the first image is defined as the world coordinate system, and the second image is obtained after a rotation $R \in \mathbb{R}^{3\times3}$ and a translation $t \in \mathbb{R}^3$ of the camera. The planar homography that aligns the first camera image to the second camera image is defined by

$$H = KRK^{-1} + \frac{1}{d}Ktn^TK^{-1} \tag{3.1}$$

where $K \in \mathbb{R}^{3\times3}$ is the intrinsic matrix of the camera. $H$ is valid for all image points whose corresponding space points are on the same plane, called stitching plane, defined by the normal vector $n \in \mathbb{R}^3$ and distance $d$ to the origin in the world coordinate system. However, any structure that is not on this stitching plane in 3D space will result in ghosting or blurring effects (see figure 3.1) caused by parallax.

$H$ has two parts, $KRK^{-1}$ and $\frac{1}{d}Ktn^TK^{-1}$, in which only the second part depends on the plane parameters $n$ and $d$. In case that the camera motion only contains the rotation $R$ around its center, $\frac{1}{d}Ktn^TK^{-1}$ is equal to zero. Then the homography $H$ is independent from the plane parameters, and thus it is valid for all image points without the coplanar constraint on their corresponding space points. However, making the X-ray source of mobile C-arms rotate around its center is impractical and sometimes impossible, due to the limitation of the mechanical configuration of mobile C-arms.

Note that, the camera motion in equation 3.1 is with respect to the patient's table. Here, we propose a novel method to produce panoramic X-ray images based on computing poses of the X-ray source relative to the table. For parallax-free stitching, the movement of the x-ray source needs to be a pure rotation around its center. As this position is only relevant with respect to the patient's table, translating the table can compensate for the translational part of the x-ray source's motion. Thus, computing each pose relative to the table and translating the table accordingly enables us to maintain the virtual X-ray source's center when aquiring multiple images. By this means, generating true parallax-free x-ray images is possible and practical.

### 3.3.1 C-arm and Operating Table Setup

The proposed parallax-free X-ray image stitching method requires a planar square marker pattern, a translatable operating table and a CamC system consisting of a mobile C-arm and a camera and mirror construction. The camera and mirror are attached to the C-arm such that the optical center of the camera virtually coincides with the X-ray source. A planar homography is estimated for X-ray and video image overlay. A joint construction and calibration make sure that the X-ray source and the video camera have the same intrinsic and extrinsic parameters [49, 50]. Therefore, all the poses and motions estimated using the video camera directly correspond also to that of the X-ray projection geometry.

The origin of the coordinate system of the marker pattern is situated on the corner of the marker pattern, the $X$-axis parallel to the short edge of the pattern, the $Y$-axis parallel to the long edge of the pattern, and the $Z$-axis following the right hand rule (see figure 3.2(b)). The marker pattern was rigidly and flatly attached under the operating

table, the edges of the square markers being roughly parallel to the edges of the table. The table coordinate system is defined in order to support translating the table, its origin located at the same position as the marker coordinate system, the $X$, $Y$ and $Z$ axes being parallel to the left-right, forward-backward, and up-down translations respectively. Figure 3.2 shows the marker coordinate system in red solid color and the table coordinate system in green dash color. For relating the marker coordinate system to the table coordinate system, a proposed calibration is performed, which will be described in section 3.3.3.

The mobile C-arm will be positioned in the common setup, in which the X-ray source is below the operating table (see figure 3.2). In the method [128], the marker pattern was placed above the patient and could occlude the view onto the operation situs. Compared to that solution, this system setup does not only make the marker pattern visible to the camera for pose estimation, but also let the marker pattern be smoothly integrated into the surgical procedure without disturbing the physician's view. In order to reduce the error caused by varying intrinsic parameters of C-arm X-ray imaging, we attach four spherical X-ray markers with 1.5mm diameter on the back of the mirror, near the border of and within the X-ray's field of view (see figure 2.10).

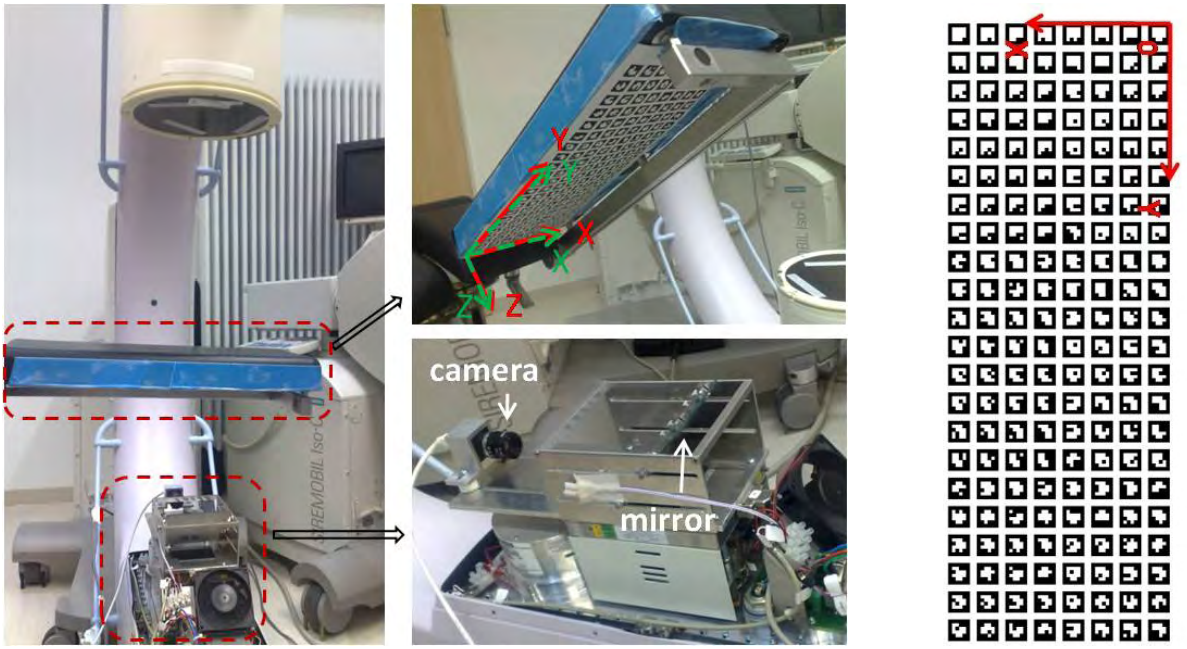


(a) (b)

Figure 3.2: (a) The left image shows the setup for X-ray image stitching, in which the camera can see the marker pattern attached to the back of the operating table. The right top image shows the attachment of the marker pattern under the table and both marker and table coordinate systems. The right bottom image shows our custom made camera and mirror construction; (b) Our planar square marker pattern and its coordinate system. The edge length of a square marker is 16.5mm, the distance between two markers is 5.5mm.

### 3.3.2 Visual-Marker-Pattern based Pose Estimation

Kainz et al. [199] developed a method to do C-arm pose estimation based on an X-ray visible planar marker pattern attached to the operating table. However, their method needs one X-ray shot for each pose estimation and is very impractical, since the proposed solution needs to update pose estimation frequently in order to guide the surgeon moving the table into the correct position.

Thanks to the CamC system, the proposed solution can make use of the video images in combination with a visual square marker tracking system (see section 2.3.2) for C-arm pose estimation without radiation. A planar marker pattern (see figure 3.2) is designed, in which all the square markers can be uniquely detected. The corners of the square marker can be extracted with subpixel accuracy and used as feature points. Having the marker pattern with known geometries, it is able to establish point correspondences between the 2D image points and 3D space points at the marker pattern that is on the plane $Z = 0$ of the table-marker coordinate system (see figure 3.2). Let the camera pose in the table-marker coordinate system consist of $R^p = \begin{bmatrix} r_1 & r_2 & r_3 \end{bmatrix} \in \mathbb{R}^{3\times3}$ the rotation matrix and $t^p \in \mathbb{R}^3$ the translation vector. Let $K$ represent the known matrix of camera intrinsic parameters. The pinhole camera model from [200] describes the relationship between 3D space point $M = \begin{bmatrix} X & Y & 0 & 1 \end{bmatrix}^T$ and its 2D image point $m = \begin{bmatrix} u & v & 1 \end{bmatrix}^T$ as

$$\begin{aligned} sm &= K \begin{bmatrix} R^p & t^p \end{bmatrix} \begin{bmatrix} X & Y & 0 & 1 \end{bmatrix}^T && (3.2) \\ &= K \begin{bmatrix} r_1 & r_2 & t^p \end{bmatrix} \begin{bmatrix} X & Y & 1 \end{bmatrix}^T && (3.3) \\ &= A\hat{M} && (3.4) \end{aligned}$$

with

$$\begin{aligned} A &= K \begin{bmatrix} r_1 & r_2 & t^p \end{bmatrix} \\ \hat{M} &= \begin{bmatrix} X & Y & 1 \end{bmatrix}^T \end{aligned}$$

where $s$ is the unknown scale factor. Based on known point correspondences, matrix $A$ can be computed up to a scaling factor by using the Normalized Direct Linear Transformation (DLT) [200]. In [151], we have

$$\begin{aligned} r_1 &= \lambda K^{-1} a_1 && (3.5) \\ r_2 &= \lambda K^{-1} a_2 && (3.6) \\ r_3 &= r_1 \times r_2 && (3.7) \\ t^p &= \lambda K^{-1} a_3 && (3.8) \end{aligned}$$

where $\lambda = 1/||K^{-1}a_1|| = 1/||K^{-1}a_2||$ and $A = \begin{bmatrix} a_1 & a_2 & a_3 \end{bmatrix}$. Then, the computed matrix $R^p = \begin{bmatrix} r_1 & r_2 & r_3 \end{bmatrix}$ is enforced to satisfy the orthogonality of a rotation matrix by using the method proposed in [151]. However, the pose is solved only through minimizing algebraic distances which are not geometrically meaningful. We use the solution of $R^p$ and $t^p$ as

an initial value for minimizing the geometric distances in the image expressed by the cost function

$$\arg\min_{R^p,t^p} \sum_{i=1}^{n} \parallel m_i - \hat{m}(K, R^p, t^p, \hat{M}_i) \parallel^2 \tag{3.9}$$

where $n$ is the number of corresponding points and $\hat{m}(K, R^p, t^p, \hat{M}_i)$ is the projection of point $\hat{M}_i$ in the image. Finally the optimal solution of the camera pose is computed by using the Levenberg-Marquardt algorithm to solve this nonlinear minimization problem.

### 3.3.3 Table Coordinate System Calibration

The table and the marker coordinate systems are located at the same position, but differ in orientation. In this section, we propose a calibration method to estimate a 3D rotation matrix ${}^tR_m \in \mathbb{R}^{3\times3}$, such that $P_t = {}^t R_m P_m$, in which $P_t$ and $P_m$ are the coordinates of the same point in the table and marker coordinate systems. With known 3D point correspondences in two coordinate systems, a 3D-rotation estimation method based on Singular Value Decomposition (SVD) [201, 202] is employed to compute the relation of the table and the marker coordinate systems.

In order to obtain the point correspondences, the table is moved in the forward-backward direction that is parallel to the $Y$-axis of the table coordinate system, while the marker pattern is visible to the camera. Thus, the camera translates from $C1$ to $C2$ in a direction parallel to the $Y$-axis of the table coordinate system (see figure 3.3(a)). The coordinates of $C1$ and $C2$ in the marker coordinate system are known by pose estimation and the distance $D_t$ between $C1$ and $C2$ is computed. The origins of both coordiante systems are translated to $C1$ (see figure 3.3(b)), which does not have an effect on the ${}^tR_m$. Then, the coordinates of $C2$ in both coordinate systems can be obtained, because $C2$ locates on the $Y$-axis of the table coordinate system and its coordinate in the table coordinate system is $\begin{bmatrix}0 & D_t & 0\end{bmatrix}^T$. The same derivation can be applied to other two directions of the table translation, i.e. up-down and left-right.

The calibration step is the followings, the table is translated in at least two directions in order to avoid degenerate configurations, e.g. forward-backward and up-down, $N(\geqslant 3)$ times with different distances. Therefore, we are able to obtain $N$ point correspondences to compute ${}^tR_m$. The calibration has to be performed only once after attaching the marker pattern to the table.

### 3.3.4 Generation of panoramic X-ray images

#### 3.3.4.1 X-ray image stitching

To generate panoramic images, the first acquired X-ray image is defined as the reference image, and all others will be registered to this reference image frame. The homography that transforms the $i$-th images to the first image coordinate system will be calculated according to equation 3.1. The intrinsic parameter $K$ was obtatined during the calibration of the CamC system. Let $R_i^p \in \mathbb{R}^{3\times3}$ and $t_i^p \in \mathbb{R}^3$ be the pose of the X-ray source in the marker coordinate system for the $i$-th X-ray image. The X-ray source motion, $R_i$ and $t_i$,

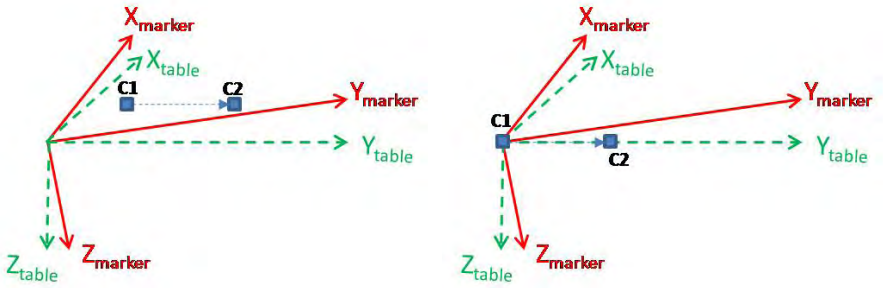


(a) (b)

Figure 3.3: The relation of the marker coordinate system (red solid line) and the table coordinate system (green dash line). The camera translates from $C1$ to $C2$. (a) and (b) are before and after the origins of both coordinate systems are translated to the position of $C1$.

from the pose of the $i$-th image to the pose of the first image can be computed by

$$\begin{bmatrix} R_i & t_i \\ 0 & 1 \end{bmatrix} = \begin{bmatrix} R_1^p & t_1^p \\ 0 & 1 \end{bmatrix} \begin{bmatrix} R_i^p & t_i^p \\ 0 & 1 \end{bmatrix}^{-1} \tag{3.10}$$

To obtain the homography, the plane parameters are still missing. The parameters of the marker plane in the marker coordinate system are known and represented by $\hat{n}$ and $\hat{d}$. Let $n_i$ and $d_i$ be the parameters of this marker plane in the camera coordinate system of acquiring the $i$-th image. In [200], we have

$$\begin{bmatrix} n_i \\ d_i \end{bmatrix} = \begin{bmatrix} R_i^p & t_i^p \\ 0 & 1 \end{bmatrix}^{-T} \begin{bmatrix} \hat{n} \\ \hat{d} \end{bmatrix} \tag{3.11}$$

So far, we are able to establish a homography, transforming the $i$-th image to the first image coordinate system, which is valid only for image points whose corresponding space points are on the exact marker plane. In order to obtain the homography valid for the bone plane (i.e. the tibial plane or the nail plane in the intramedullary tibial fracture reduction surgery), which is used for panoramic X-ray images and metric measurements, we need two constraints: 1) the bone plane is placed roughly parallel to the marker plane; 2)The distance between the marker plane and the bone plane is known or estimated. The first constraint provides us the normal of the bone plane and the second constraint gives the distance of this bone plane to the origin in the world coordinate system. With these two constraints, we have the plane parameters for the bone plane, and thus the homography valid for the bone plane is calculated and parallax effects on this plane are reduced. However, the parallax effects still exist for the image points whose corresponding space points are not on this bone plane. We call this X-ray image stitching method as one-plane X-ray image stitching method or one-plane stitching in short (see figure 3.4), which only aligns the image points whose 3D points within the plane that is defined by the applied planar transformation. The methods described in [126, 127, 128] are one-plane X-ray image stitching methods.

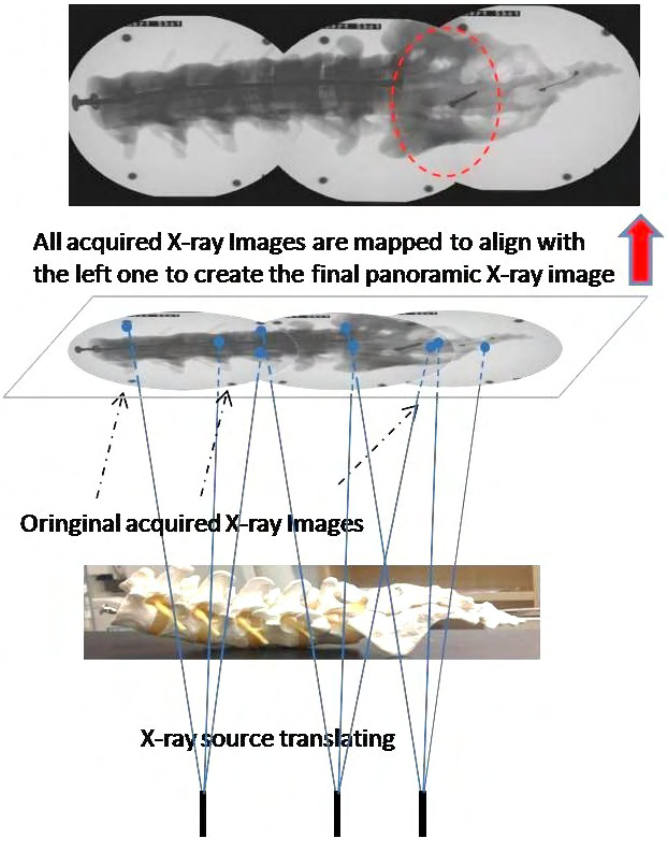


Figure 3.4: One-plane X-ray image stitching method. A panoramic X-ray image of a plastic lumbar and sacrum is generated by stitching three X-ray images acquired by translating the X-ray source. The individual X-ray images are aligned by using the planar transformation computed for the marker pattern plane. The parallax effects (ghosting) are marked by the red dash circle.

#### 3.3.4.2 Parallax-free X-ray image stitching

For most clinical cases, the bone structure is hardly a simple and planar structure. This makes parallax effects inevitable in the panoramas generated by one-plane X-ray image stitching methods. A true parallax-free panoramic image that preserves the property of linear perspective projection is more attractive. Rotating the X-ray source around its center is an indispensable step for this. Therefore, the rotational movements of the C-arm must be involved in order to achieve a parallax-free X-ray stitching of a non planar object.

As discussed before, it is impractical and sometimes impossible to make the C-arm rotate around its X-ray source center by changing the five joints of the C-arm. Therefore, after moving the C-arm by changing its available rotational movements, we translate the patient's table to compensate for the translation of the X-ray source with respect to the table. The guidance is supported by pose estimation using the attached video camera.

The camera position $pos_i \in \mathbb{R}^3$ of the $i$-th X-ray image in the table coordinate system

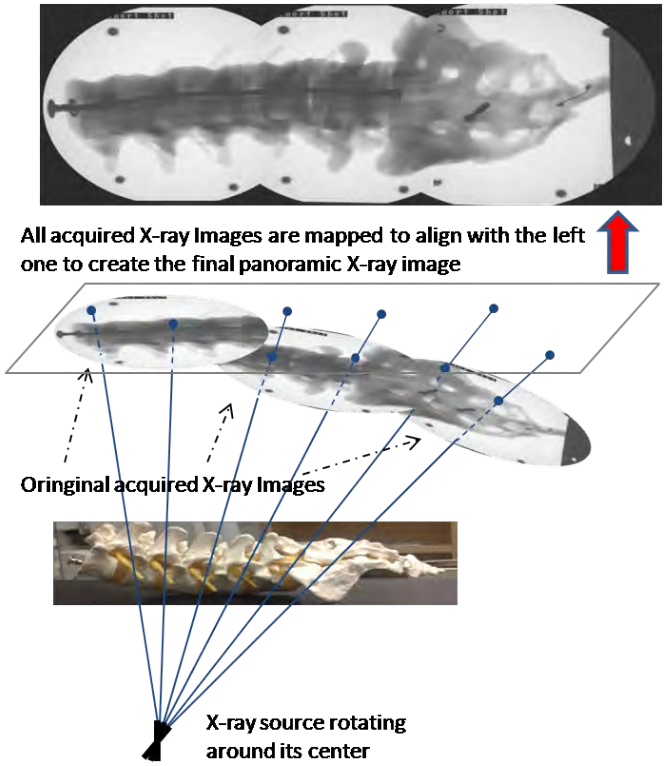


Figure 3.5: Parallax-free X-ray image stitching method. A parallax-free panoramic X-ray image of a plastic lumbar and sacrum is generated by stitching three X-ray images acquired by the X-ray source undergoing pure rotations.

is

$$pos_i = ({}^tR_m)(R_i^p)^T(-t_i^p) \tag{3.12}$$

The translation of the table is the difference between the camera position of acquiring the first image and its current position in the table coordinate system. The estimation of the pose is performed with a frequency of 8-10 Hz in our implementation. This provides a continuous feedback for the translation of the table. Kainz et al. [199] developed a method to do C-arm pose estimation using an X-ray visible planar marker pattern attached to the operating table. It is not suitable as guidance for positioning of the table, since a continuous X-ray exposure and therefore a large amount of radiation is inevitable. After translation compensation, the homography for aligning X-ray images can be computed and it is valid for all image points.

An intuitive image acquisition protocol for guiding the generation of a complete panoramic X-ray image is proposed as following,

1. Position the C-arm to take the first X-ray. The surgeon positions the C-arm such that the X-ray image includes the area of interest. This is a daily task in the operating room.

2. Take the first X-ray image. This fixes the reference panoramic image frame.

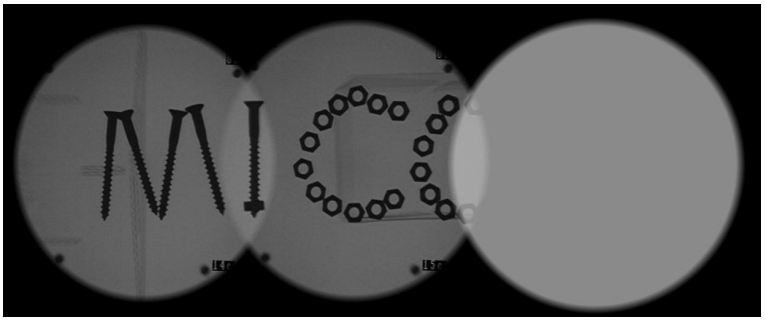

Figure 3.6: During the acquisition of a complete panorama , a predicted virtual X-ray frame is visualized as a grey circle in the reference panoramic image frame for guiding the panoramic X-ray image acquisition and controlling the overlapping regions of X-ray images.

3. Rotate the C-arm into a new viewing position. The rotational movements offered by the C-arm system can be decomposed into a rotation around the X-ray source and a translation. Our system visualizes the border of the predicted X-ray frame in the reference panoramic image frame assuming that the translational component is being compensated for (see figure 3.6). The surgeon, familiar with the bone geometries, knows in which direction he wants to extend the first x-ray by appending the second one. Therefore, the border of the predicted X-ray frame is very helpful for placing the following X-ray images and controlling the overlap regions of X-ray images. Note that, without such visualization, the surgeon may need to take more X-ray images before achieving the desired X-ray position.

4. Translate the patient's table to compensate for the translational component of the X-ray source motion. The system visually guides how much the physician needs to translate the table in three different directions, i.e. forward-backward, left-right, and up-down. In our experiments, the relative X-ray source motion to the table is considered as a pure rotation if the relative translation of the X-ray source is below 1 mm.

5. Acquire a new X-ray image. It is visualized onto the reference panoramic image frame.

6. Stop if the panoramic X-ray image is complete, else repeat step 3-6.

### 3.3.5 Metric Measurements

Metric measurements are possible for the 3D space plane whose plane parameters in the world coordinate system are known. Let $P = \begin{bmatrix} x & y & z \end{bmatrix}^T$ be a 3D space point on the space plane defined by normal $n$ and distance $d$ in the camera coordinate system, and $m$ be its image projection expressed in homogeneous coordinates. In the camera coordinate system, we have

$$P = zK^{-1}m \tag{3.13}$$

$$n^T P = d \tag{3.14}$$

Substituting 3.13 into 3.14 we obtain

$$d = n^T z K^{-1} m \Rightarrow \tag{3.15}$$
$$z = d/(n^T K^{-1} m) \tag{3.16}$$

Substituting 3.16 into 3.13 we obtain

$$P = (dK^{-1}m)/(n^T K^{-1} m) \tag{3.17}$$

With the known plane parameters in the camera coordinate system, we can derive the coordinates of space points within this plane from their projections. Therefore, metric measurements on the image are possible for this plane. In our stitching algorithm, all images are registered into the first image coordinate system. Thus the bone plane parameters in the first camera coordinate system are needed for metric measurements. Currently, obtaining the bone plane parameters also relies on the two constraints: 1) the bone plane is placed roughly parallel to the marker plane; 2) The distance between the marker plane and the bone plane is known or estimated.

## 3.4 Experiments and Results

We performed experiments to quantify and qualify our new method. The difference of the overlapping area of two stitched X-ray images was computed in order to quantify parallax-free stitching. Metric measurements were carried out on the panoramic X-ray images obtained from both parallax-free stitching and one-plane stitching. In order to validate and qualify parallax-free stitching in comparison to one-plane stitching, we conducted an experiment with a cow's ex-vivo femoral bone in a nearly realistic clinical configuration, and the panoramic X-ray images of the bone were generated by using both stitching methods. The image acquisition protocol for parallax-free X-ray image stitching proposed in section 3.3.4.2 is used in our experiments. For one-plane X-ray image stitching, the image acquisition protocol was much simpler, because the surgeon only needs to translate the table with the C-arm orientation remaining the same as its calibrated for during acquiring X-ray images.

In the conducted experiments, the employed planar square marker pattern (see figure 3.2(b)) is printed in A2 size paper by a high definition printer. The clinical CamC system (see section 2.3.3) is employed in the experiments. In order to compensate for perspective distortion caused by the changes of the C-arm orientation in the final panoramas, we adapted the Virtual Detector Plane (VDP) method introduced in section 2.2.2.1.

### 3.4.1 Quantitative Stitching Errors

In order to quantify the accuracy of the panoramic X-ray images generated by our parallax-free X-ray image stitching method, we conducted an experiment to compute the difference of the overlapping area of two stitched X-ray images. One possibility to

compute this difference is using similarity measurements. However, very limited feature information and high noise in the bone X-ray images make similarity measurements unreliable. This is the reason that others have employed the ruler [126], the X-ray pattern [127], or the video images [128] for X-ray image stitching.

We constructed a phantom composed of spherical X-ray markers on three different planes (see figure 3.7(a)) and attached it to the operating table. The phantom has 8cm depth between the top most plane and the lowest plane. We performed parallax-free X-ray image stitching to stitch two X-ray images, in the overlapping area of which at least two X-ray markers on each plane were imaged. The centroids of these markers are extracted with subpixel accuracy in the two X-ray images and used to compute the difference of the overlapping area which is the distance between corresponding centroids pairs (see figure 3.7(b)). This procedure was performed twice. Moreover, we evaluated the influence of applying the VDP method to our parallax-free stitching. Results with and without applying the VDP method show a similar error below 2 pixels (see table 3.1). The improvement of applying the VDP is negligible, since the X-ray source undergoes very limited rotations (around 5°). The VDP method has originally been proposed to compensate for perspective distortion caused by a varying geometric relation between the X-ray source and the detector plane, i.e. intrinsic parameters change, in different C-arm orientation. The overlay error of the CamC system caused by perspective distortion error increases with the increase of the C-arm rotation as shown in section 2.2.2.2. However, a limited rotation introduces minor perspective distortion errors to parallax-free X-ray stitching compared to other sources of inaccuracy. This relatively small distortion error can still be reduced by the VDP method as shown in table 3.1.

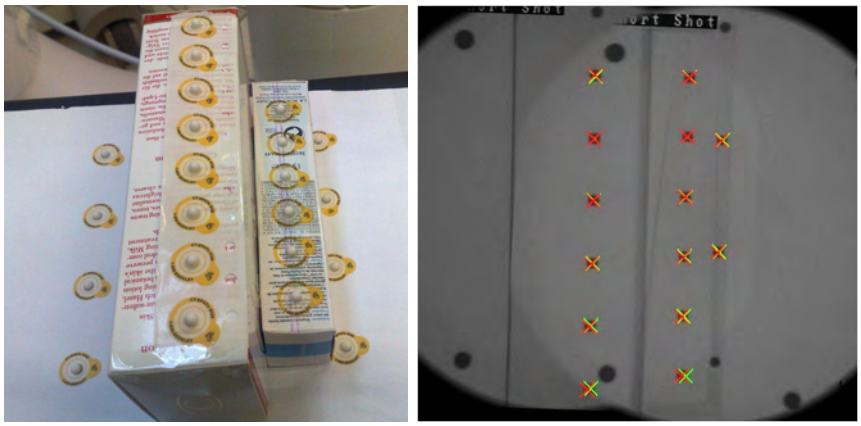

(a) (b)

Figure 3.7: (a) A phantom of spherical X-ray markers on three different planes; (b) The extracted centroids of the X-ray markers are marked by red and green crosses in the two X-ray images stitched by using parallax-free X-ray image stitching.

Besides computing the difference of the overlapping area of two stitched X-ray images, another experiment was carried out to perform metric measurements on the panoramic X-ray images generated by parallax-free stitching and one-plane stitching respectively. The

| Without VDP | | | | With VDP | | | |
|---|---|---|---|---|---|---|---|
| | #1 | #2 | Overall | | #1 | #2 | Overall |
| Mean | 1.85475 | 2.00565 | 1.92741 | Mean | 1.68037 | 1.84381 | 1.75906 |
| STD | 1.34975 | 1.36968 | 1.36417 | STD | 1.30408 | 1.17027 | 1.35613 |
| # X-ray markers | 14 | 13 | 27 | # X-ray markers | 14 | 13 | 27 |

Table 3.1: The distance (pixels) between the corresponding extracted marker centroids in the two X-ray images stitched by using parallax-free X-ray image stitching for two independent experimental procedures. The distance was computed with and without applying the VDP method respectively.

distance is defined by clicking on two points in the image, or three points for an angle. To determine the accuracy of metric measurements, we used spherical X-ray markers. These markers can be extracted with subpixel accuracy. The ground truth of distance measurements is constructed by attaching spherical X-ray markers on a flat pattern with known metric properties. The accuracy of the attachments was controlled by a ruler. The error in the ground truth was confirmed to be below 1mm. This phantom with the X-ray markers was placed on the operating table (see figure 3.8), parallel to the marker pattern attached to the table. The physical distance between the marker pattern plane and the phantom plane was measured manually. This configuration satisfied the two constraints for metric measurements, which are also the constraints for parallax reduction of one-plane stitching. Experimetal results (see table 3.2) show that the errors in the metric measurements are less than 1% for all cases. One-plane stitching and parallax-free stitching have a similar error. The accuracy of metric measurements is improved less than 0.5% with applying the VDP for parallax-free stitching.

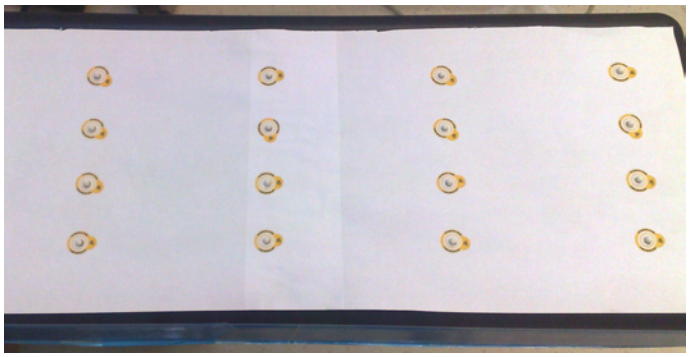

Figure 3.8: The X-ray marker pattern used for metric measurements.

### 3.4.2 Qualitative Analysis of Panoramic X-ray Images

For the evaluation of the quality of the final panoramic X-ray images, we generated the panoramic X-ray images of a cow's femoral bone (see figure 3.9). In the experiment, the cow bone was positioned on the operating table, and two metal tools were placed approximately 6cm below the middle of the bone, parallel to the marker pattern plane. The bone however was not parallel to the marker pattern plane due to the big distal end

| Actual Values | Measured Values | | |
|---|---|---|---|
| | A | B | C |
| 240 mm | 239.80 | 239.25 | 239.55 |
| 120 mm | 119.51 | 119.46 | 119.61 |
| 90 ° | 89.54 | 89.50 | 89.46 |
| 180 ° | 179.84 | 179.72 | 179.36 |

Table 3.2: Measured distances(mm)/angles(°) between the spherical X-ray markers on the panoramic images generated by parallax-free stitching and one-plane stitching respectively. In the second row, A represents parallax-free stitching with VDP; B represents parallax-free stitching without VDP; C represents one-plane stitching.

of the cow femur. This setup is close to the real clinical cases, in which it is hard to assume that the the long bone is placed parallel to the marker pattern plane due to the soft tissue, muscle and fat around the bone.

We conducted both parallax-free stitching and one-plane stitching to create panoramic X-ray images respectively. The resulting panoramic X-ray images have overlapping areas. The pixel values in the overlapping areas can be computed by taking either the median, minimum, maximum or average of the individual pixel values. We created the panoramic X-ray images by using maximum pixel values and average pixel values respectively. The maximum would always match to one of several images, even if the others are wrongly aligned. The average is only correct if all images are correctly aligned. Therefore, the maximum yields the most uniform image but hides the misalignments (parallax effects) in the panoramas, and the average makes the misalignments visible in the panoramas (see figure 3.10).

In the case of one-plane X-ray stitching, it is quite difficult to recover the planar transformation for the bone plane, since the bone plane is not parallel to the marker pattern plane. Thus, we generated panoramic X-ray images first by using the planar transformation computed for the plane (marked by red dash lines approximately in figure 3.9) intersecting the middle of the bone horizontally and parallel to the marker pattern plane. Figure 3.10(b) shows the resulting images, in which less discontinuity occured in the bone boundary. The metal tools are located on a different plane and clearly show parallax effects. More discontinuity occured in the bone boundary and the ghosting disappeared from the metal tools in the panoramic X-ray images (see figure 3.10(b)) created using the planar transformation computed for the plane of the metal tools. In comparison to one-plane stitching, parallax-free stitching produced a true parallax-free panoramic X-ray image (see figure 3.10(a)), in which the cow bone and metal tools are almost perfectly aligned at the same time. This parallax-free panoramic X-ray image can be treated as a single true image obtained from a C-arm having an exceptional wide field of view for X-ray imaging.

Note that, the overlap between the consecutive images is used to illustrate and compare the quality of panoramic X-ray images generated by two stitching methods, and it is not necessarily required since our stitching methods use the co-registered optical images and not the X-ray images.

Figure 3.9: The left image shows a real cow's femoral bone. The right image shows the setup for generating panoramic X-ray images of the real cow bone with two metal tools below.

## 3.5 Discussion and Conclusion

Panoramic X-ray imaging is a promising technology for visualizing fracture configuration and supporting repositioning and osteosynthesis during orthopedic and trauma surgery, especially in minimally invasive surgery. In our work, we presented a novel method to generate parallax-free panoramic X-ray images during surgery by using the CamC system and a planar marker pattern. However, our method does not require the use of the CamC system and can be easily applied to other C-arm setups as long as the pose of the C-arm relative to the patient's table is available, such as using an external tracking system, or a robotic C-arm and electronically controlled bed. In our system setup, the marker pattern was attached under the operating table and is thus invisible to surgical crew during the whole operation. This allows our solution to be smoothly integrated into the surgical procedure. Our method does not rely on overlapping X-ray regions and does not require a fronto-parallel C-arm setup. Unlike existing methods, we are able to generate a true parallax-free panoramic X-ray image that can be treated as a single image obtained from a C-arm having an exceptional wide imaging field of view and also can be further processed by various computer vision algorithms that assume linear perspective projection, e.g. 2D-3D rigid registration of X-ray fluoroscopy and CT images. We additionally implemented a method to reduce the error caused by varying intrinsic parameters of C-arm X-ray imaging.

The results show that the parallax-free panoramic X-ray image generated by our method is accurate enough and has high visual quality. Additionally, metric measurements are possible with known plane parameters. We further validated our parallax-free X-ray image stitching in comparison to one-plane X-ray image stitching of a long bone. The true parallax-free panoramic X-ray images are more attractive to surgeons in the case of complex bone structures. The clinical partners confirmed that, apart from long bone surgery, parallax-free stitching could also support a wide range of potential intra-operative X-ray imaging applications such as pelvic fracture or whole-spine imaging, since this method is independent of the configuration of bone structures and suitable for any part of body. On the other hand, in the X-ray image the pixel value in the original image is related to the attenuation of the imaged object along the path of the ray. Thus, two

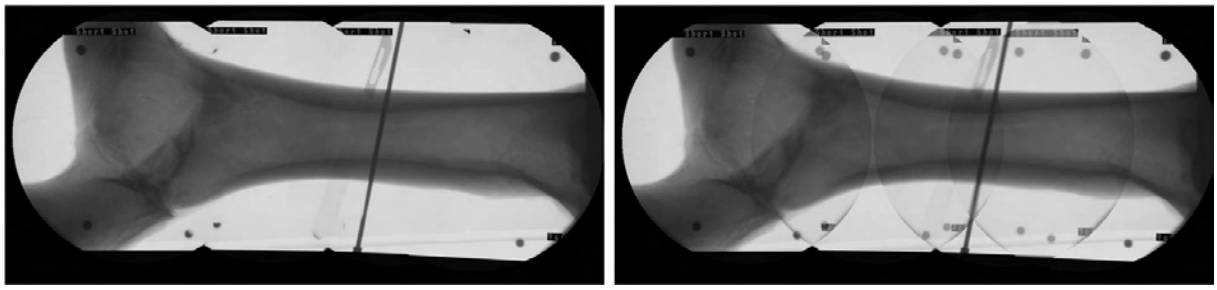

(a) Parallax-free panoramic X-ray images generated by parallax-free stitching with applying the VDP method .

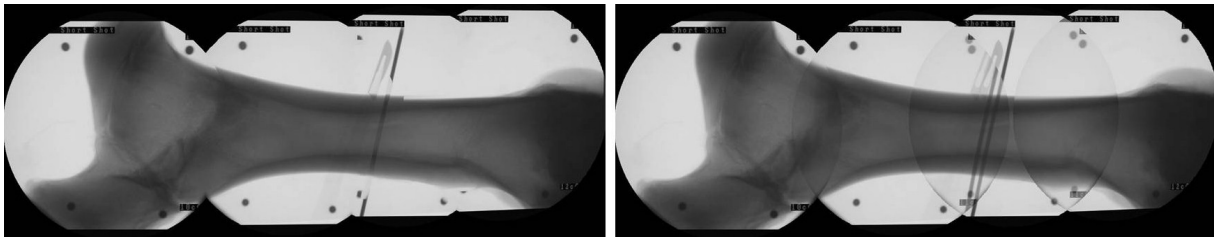

(b) Panoramic X-ray images generated by one-plane stitching using the planar transformation computed for the plane intersecting the middle of the bone horizontally and parallel to the marker pattern plane.

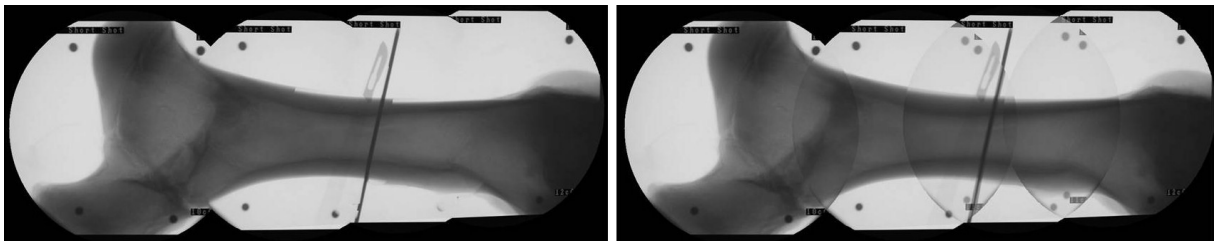

(c) Panoramic X-ray images generated by one-plane stitching using the planar transformation computed for the plane of metal tools.

Figure 3.10: Panoramic X-ray images of a real cow's femoral bone with metal tools below from four individual X-ray images. (a) shows parallax-free panoramic X-ray images. (b) and (c) show panoramic X-ray images generated by one-plane X-ray stitching using different planar transformations. In each row, the left panoramas were created by using the maximum pixel values in the overlapping areas and the right panoramas were created by using the average pixel values in the overlapping areas. The maximum yields the most uniform image but hides the misalignments (parallax effects) in the panoramas, and the average makes the misalignments visible in the panoramas.

X-ray images stitched by one-plane stitching will have different gray values for the aligned pixels. This difference however is negligible if the bone has a very limited depth, as it is the case with long bones. Note that this is not the case for our parallax-free method, since the X-ray's paths are all identical, e.g. no parallax.

In order to guide the generation of a complete panoramic X-ray image and control the overlap regions of the images, we presently display one predicted virtual X-ray image boundary on the screen. However, surgeons prefer to specify a target position of the next

X-ray image in the panorama, and to be guided by the system how to move the C-arm and the table. Hence, in a future development, we will build a 6-DOF C-arm system by integrating the motion of the table into the standard C-arm kinematics, and apply inverse kinematic analysis to obtain the parameters for moving the C-arm and the table. Acquiring X-ray images from two orthogonal views is necessary in most orthopedic and trauma surgeries, i.e. the AP view and the lateral view. As the planar marker pattern is attached underneath the table, only the AP view is currently suitable for X-ray stitching. In order to obtain parallax-free panoramic X-ray images from these two orthogonal views, we will integrate the main idea of Multi-View Opto-Xray Imaging System presented in [149], into our parallax-free stitching solution. In our current system setup, surgeons need to put in additional effort to move the table to the correct position. However, motorized tables that could further support the translation of the table are already available at many clinical sites. In general, the plane parameters for precise metric measurements are not trivial to estimate. Current practical clinical approaches place some references, such as an X-ray ruler, along the measured bones and thus allow surgeons to estimate the length of the bone [191]. In our preclinical phantom setup we set the plane with known plane parameters. Appropriate methods have to be incorporated to define the plane for metric measurements. This is still an open question and requires to offer a pratical, but also precise solution.

The economical issue is also considered as an important factor when developing a new technology in computer aided surgery. One key feature of the CamC system is that it can be operated as a standard mobile C-arm. No additional devices or training on surgical staff are required to deploy the CamC technology in the OR. Our low-cost approach for parallax-free X-ray image stitching based on the CamC platform is valuable from both clinical and economical points of view. Patient studies will be performed in the near future to evaluate the clinical value of panoramic X-ray images produced by our low-cost solution. Figure 2.19 shows the entire CamC system that we designed and constructed for the operating room. We believe that our solution for creating panoramic X-ray images has high potential to be introduced in everyday surgical routine, and will allow surgeons to ensure and validate the quality of their treatment during orthopedic and trauma surgery with less radiation exposure.

This paragraph summarizes the contributions in the chapter. I have proposed the intra-operative parallax-free X-ray image stitching method and further implemented it using the CamC system. The radiation-free C-arm pose estimation was developed by using the visual marker pattern and the video camera of the CamC system. Furthermore, the method of calibrating the table and the visual marker pattern coordinate systems was proposed. Metric measurement on the generated panoramic X-ray image was formulated in this chapter. Finally, the experiments on phantoms and ex-vivo bone structure were performed in a close collaboration with our clinical partners in order to quantify and qualify the developed method and system.

CHAPTER

# FOUR

# CLOSED-FORM INVERSE KINEMATICS FOR C-ARM X-RAY IMAGING WITH SIX DEGREES OF FREEDOM

For trauma and orthopedic surgery, maneuvering a mobile C-arm fluoroscope into a desired position to acquire an X-ray is a routine surgical task. The precision and ease of use of the C-arm becomes even more important for advanced interventional imaging techniques such as parallax-free X-ray image stitching. Today's standard mobile C-arms have been modeled with only five degrees of freedom (DOF), which definitely restricts their motions in 3D Cartesian space. In this chapter, I present a method to model both the mobile C-arm and patient's table as an integrated kinematic chain having six DOF without constraining table position. The closed-form solutions for the inverse kinematics problem are derived in order to obtain the required values for all C-arm joint and table movements to position the fluoroscope at a desired pose. The modeling method and the closed-form solutions can be applied to general isocentric or non-isocentric mobile C-arms. By achieving this I develop an efficient and intuitive inverse kinematics based method for parallax-free panoramic X-ray imaging. In addition, I implement a 6-DOF C-arm system from a low-cost mobile fluoroscope to optimally acquire X-ray images based solely on the computation of the required movement for each joint by solving the inverse kinematics on a continuous basis. Through simulation experimentation, we demonstrate that the 6-DOF C-arm model has a larger working space than the 5-DOF model. C-arm repositioning experiments show the practicality and accuracy of our 6-DOF C-arm system. I also evaluate the novel parallax-free X-ray stitching method on phantom and dry bones. Using five trials, results show that parallax-free panoramas generated by our method are of high visual quality and within clinical tolerances for accurate evaluation of long bone geometry (i.e. image and metric measurement errors are less than 1% compared to ground-truth). This particular work was originally presented in [203].

## 4.1 Clinical Motivation

Modern trauma and orthopedic surgical procedures use X-ray images during surgery for intervention guidance, especially in minimally invasive surgery. Mobile C-arms are the

most used tool for interventional X-ray imaging since they are compact and versatile, and can provide real-time X-ray images. Maneuvering a mobile C-arm device into a desired position in order to acquire the right picture is a routine surgical task especially for the following example orthopedic applications: the interlocking of intramedullary nails for the treatment of long bone fractures [204], the placement of transpedicular screws for spinal surgery [205, 206] and precise needle placement for vertebroplasty procedures. In the above cases, surgeons need to position C-arms such that the axis of perforation is projected into a single point or the interlocking hole appears as a round circle on the X-ray image in order to get a correct viewing direction for insertion. This is known as down-the-beam positioning. During intervention, the C-arm is often required to be repositioned to acquire another X-ray image from the same viewing point as the reference image, e.g. for the confirmation of surgical outcome [129]. Furthermore, the precision and ease of use of the C-arm positioning can become even more important for advanced interventional imaging and navigation techniques, e.g. parallax-free X-ray image stitching [164], intra-operative cone beam CT [130], and artificial fluoroscopy based C-arm navigation [150]. Moving the mobile C-arm into the best viewing projection in regard to the anatomy requires time, skill and additional radiation exposure. This is due to a complex kinematic chain defining mobile C-arms leading to the acquisition of X-ray images from additional "gantry positions" that have no bearing on the treatment until the desired projection image is achieved. Many solutions and systems have been proposed and developed to support acquisition of a desired C-arm X-ray image, e.g. optical tracking based navigation system [129], visual servoing based C-arm positioning [165], robotized C-arm system [130], artificial fluoroscopy [150], and the inverse C-arm positioning using real-time body part detection [207]. However, standard mobile C-arms only have five joints (5-DOF) [208], three of which are rotation joints and two are translation joints. As in 3D Cartesian space six DOF are required to specify a rigid transformation, the C-arm X-ray source is certainly restricted in terms of reaching an arbitrary position and orientation.

In this chapter, we propose a method to model the general C-arm and the operating table as an integrated 6-DOF imaging system, thus enabling the X-ray source to have six DOF with respect to the patient's table. The modeling method and closed-form inverse kinematics solutions do not constrain table position and are valid for general mobile C-arms, i.e. isocentric and non-isocentric C-arms. Having the 6-DOF C-arm model with the closed-form inverse kinematics enables novel solutions for many advanced applications in the fields of surgical navigation and advanced X-ray imaging that require C-arms to be precisely positioned or repositioned relative to the patient's table, i.e. cardiology or prostate brachytherapy imaging, to name a few. Particularly in this work, we present a novel approach for parallax-free panoramic X-ray imaging based on the inverse kinematics of the 6-DOF C-arm model. This allows surgeons to intuitively specify the position of an X-ray image in the panorama and be automatically guided by the system on how much to move the C-arm joints and the table for a desired result.

## 4.2 Related Work

### 4.2.1 C-arm positioning for acquiring a desired X-ray image

Many solutions and systems have been developed to facilitate C-arm positioning for acquiring a correct projection X-ray image with minimized radiation and operation time. Matthews et al. [129] developed a solution for repositioning the C-arm by using an optical tracking based navigation system. They attach optical reference markers to the patient and the C-arm, and the optical navigation system guides the repositioning of C-arm. Navab et al. [165] employ the Camera Augmented Mobile C-arm (CamC) system for the down-the-beam positioning and C-arm repositioning based on a visual servoing method. Additionally, CT visible markers are affixed on patient's skin allowing the CamC's optical camera to compute the C-arm's pose and its required displacement for acquiring a desired X-ray image. Dressel et al. [150] presented a work of C-arm artificial fluoroscopy. They register CT to the C-arm projection geometry and thus can generate simulated C-arm X-ray images from the CT for each known C-arm pose. In their implementation, the Camera Augmented Mobile C-arm system is also employed for performing C-arm motion estimation by using the optical camera with visual square markers. These simulated X-ray images can support C-arm positioning without real radiation exposure. In their work of optimizing and automating C-arm positioning procedures [130], Matthaeus et al. present a complete robotized mobile C-arm developed by equipping all the C-arm joints with motors and encoders and closed-form solutions for the inverse kinematics have been found for automated C-arm positioning. Grezda et al. [131] have used tilt sensing accelerometers for C-arm rotation encoding in order to track the C-arm angular and orbital rotations during the surgery. Lastly, several medical groups [132, 133, 134] have investigated the C-arm system equipped with laser aiming device for C-arm positioning and also for instrument placement. The aiming beam creates a crosshair on the patient's skin and thus allows the physicians to correctly position the C-arm without the need for X-ray imaging. However, standard mobile C-arms only have five joints (five DOF), three of which are rotational joints and two are translation joints. This restricts the X-ray source in terms of reaching an arbitrary position and orientation, which in turns creates difficulties for a precise positioning of the C-arm.

### 4.2.2 C-arm kinematic modeling

To our knowledge, only Matthaeus et al. [130] have presented the inverse kinematics for a general 5-DOF mobile C-arm. They found the closed-form, proving the existence of necessary joint parameters for imaging a given point from a given direction. They reduced the 3D Cartesian space to five DOF by considering a 2-DOF direction instead of a 3-DOF orientation, i.e. neglecting the rotation around the principal axis of the X-ray source. The desired projection X-ray image can be obtained by rotating the X-ray image around the principal point in order to compensate for the missing rotation around the principal axis. However, in spite of its extreme usefulness in practice, the limited DOF could impose some functional constraints on obstacle avoidance, physical limited joint range, and singularity avoidance. Obstacle collisions may happen for a specific C-arm

pose. The model of Matthaeus et al. [130] only has a unique solution for the C-arm joints satisfying the position and direction of the X-ray beam. This solution may not account for obstacle collision situations. Further, all joints have limited mechanical ranges that actually restrict the working space for acquiring desired X-ray images. Adding additional DOF can definitely increase the working space and the possibility of avoiding obstacles. As shown in our previous work [164], rotating the X-ray source around its center is sometimes impossible due to one missing DOF. Therefore, in order to enable the X-ray source to have a pure rotation relative to the patient¡¯s table, we proposed to move the table in order to compensate for the translational motion of the X-ray source. However, our preliminary work did not include this DOF into the formula.

### 4.2.3 Inverse kinematics

In this chapter, we present an original solution to model a kinematic chain having six DOFs for C-arm X-ray imaging by integrating a patient's table translation into the 5-DOF C-arm kinematics. This enables the 5-DOF C-arm to be positioned relative to the patient's table with 6-DOF. Note that, our modeling method has no constraint on the setup of the table position. Given a desired pose of the X-ray source relative to the table, computing the required values for the C-arm joint movements and table translation is an inverse kinematics problem. Many numerical solutions [209, 210, 211, 212, 213, 214, 215] have been proposed for the inverse kinematics problem. These numerical methods solve non-linear kinematic equations in an iterative way by successive linear interpolation of non-linear equations based on the manipulator Jacobian matrix. Wolovich and Elliott [209] use the transpose of the Jacobian instead of the inverse of the Jacobian for inverse kinematics. In order to solve inverse kinematics when the manipulator Jacobian matrix is not square or not full rank, e.g. at a kinematic singularity, the pseudoinverse Jacobian method has been widely used and discussed in the literature [210, 211, 212]. But it often performs poorly and oscillates badly near kinematic singularities. Wampler [213] and Nakamura and Hanafusa [214] have first applied a damped least squares method for inverse kinematics, which avoids many problems with singularities of the pseudoinverse method and can give a numerically stable method by selecting damping constants. There are many proposed methods for selecting damping constants dynamically based on the configuration of the articulated manipulator. The selectively damped least squares method has been developed by Buss and Kim [215], which can adjust the damping factor based on the difficulty of reaching the target positions. This method can converge in fewer iterations than the damped least squares method and does not require a constant damping factor. However, all of these numerical solutions are computationally expensive because they are iterative, may become unstable in the neighbourhood of kinematic singularities, and cannot always guarantee convergence. Therefore, a closed-form, i.e. analytic solution, is preferable. Moreover, the inverse kinematics generally can have multiple solutions. Having closed form solutions allows one to develop rules for choosing a particular solution among several. In our work, we derive closed-form solutions (i.e. analytic expressions for joint parameters) in an algebraic way for the inverse kinematics of the 6-DOF C-arm model.

## 4.3 Integrated Kinematic Modeling of Mobile C-arm and Operating Table

The standard mobile C-arm has five joints [208]: the vertical, which translates the C-arm up and down along the axis $Z_1$(see Figure 4.1); the wigwag (or swivel), which rotates the "C" around the axis $Z_2$; the horizontal, which changes the arm length along the axis $Z_3$; the angular, which rotates the "C" around its center axis $Z_4$; the orbital, which rotates the "C" in its own plane around the axis $Z_5$. These joint names are commonly used in the operating room by medical doctors [208]. Defining a unique pose in 3D Cartesian space requires six independent parameters, i.e. three rotation parameters for the orientation and three translation parameters for the position. It is impossible for mobile C-arms that have only five DOF to satisfy an arbitrary X-ray source pose having six DOF. Therefore, we propose to integrate a translational movement of the patient's table into the C-arm kinematics in order to enable the X-ray source to be positioned relative to the operating table with a full six DOFs.

### 4.3.1 Forward Kinematic Equation

The kinematic analysis of the 5-DOF C-arm is performed to model a kinematic chain for a general C-arm, which builds a relation between the five C-arm joint values and the pose of the X-ray source relative to the C-arm base. A kinematic chain model can be defined by a set of coordinate frames assigned to each link following the Denavit-Hartenberg (DH) rules [216]. The spatial relationship between these coordinate frames is expressed by link parameters. Thus, the transformations between the assigned coordinate frames can be derived from the link parameters, which define the kinematic chain. We assign a coordinate frame to each link of the C-arm according to Denavit-Hartenberg (DH) rules [216]. The origin of the coordinate frame 1 is chosen at the C-arm base. The coordinate frame 6 is defined at the last link of the C-arm kinematic chain, i.e. hereafter referred to the end-effector of the C-arm. Figure 4.1 shows the assigned coordinate frames and the table of corresponding link parameters for the 5-DOF C-arm model. Similar forward kinematic analysis for isocentric and non-isocentric 5-DOF C-arms have been studied in [165] and [130] respectively. In Figure 4.1, *length_offset* represents the distance between the X-ray beam and the rotational axis of the wigwag movement. *orbital_offset* denotes the distance between X-ray source center and the rotational axis of the angular movement. A general C-arm has two geometric offsets, denoted as $a_1$ and $a_2$. $a_1$ is the distance from the rotational axis of the angular movement to the rotational axis of the orbital movement. $a_2$ is the distance from the X-ray beam center to the rotational axis of the orbital movement. The C-arm becomes an isocentric C-arm when both $a_1$ and $a_2$ equal zero.

We define a vector $q_{5\text{dof}} = [d_1; \theta_2; d_3; \theta_4; \theta_5]$ representing the five C-arm joint variables, i.e. C-arm vertical translation, C-arm wigwag rotation, C-arm horizontal translation, C-arm angular rotation and C-arm orbital rotation. Let ${}^1T_6(q_{5\text{dof}}) \in \mathbb{R}^{4\times4}$ be a kinematic equation of the five joint variables for the 5-DOF C-arm model. ${}^1T_6(q_{5\text{dof}})$ represents the transformation from the end-effector to the C-arm base coordinate frame, which can be

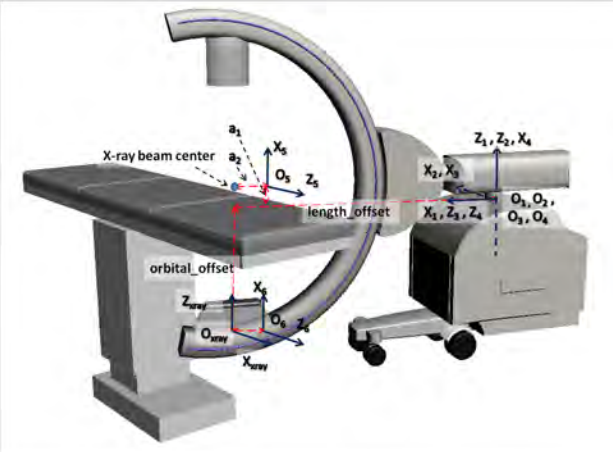


(a) Coordinate frames assignment

| | a (Tx) | d (Tz) | α (Rx) | θ(Rz) |
|---|---|---|---|---|
| 1 | 0 | $d_1$* | 0 | -pi/2 |
| 2 | 0 | 0 | -pi/2 | $\theta_2$* |
| 3 | 0 | $d_3$* | 0 | -pi/2 |
| 4 | $a_1$ | length_offset $-a_2$ | pi/2 | $\theta_4$* |
| 5 | $-a_1$ - orbital_offset | 0 | 0 | $\theta_5$* |

(b) Link parameters(*variable)

Figure 4.1: Kinematic chain of a general 5-DOF mobile C-arm. (a) coordinate frame assignments; (b) the corresponding link parameters.

established by,

$$ {}^{1}T_{6}(q_{5\text{dof}}) = {}^{1}A_{2} \cdot {}^{2}A_{3} \cdot {}^{3}A_{4} \cdot {}^{4}A_{5} \cdot {}^{5}A_{6} \tag{4.1} $$

where ${}^{i}A_{i+1} \in \mathbb{R}^{4\times4}$ is the transformation from the coordinate frame $i+1$ to $i$ and can be derived from the $i$-th row of the table of link parameters for the 5-DOF C-arm model (see Figure 4.1(b)) according to [217]. The coordinate system of the C-arm X-ray is usually expressed so that the origin is at the X-ray source center, the $Z_{\text{xray}}$ axis is the principal axis, $X_{\text{xray}}$ and $Y_{\text{xray}}$ axes are along the image width and height (see Figure 4.1(a)). Let ${}^{6}T_{\text{xray}} \in \mathbb{R}^{4\times4}$ represent a transformation from the X-ray source to the end-effector coordinate frame, which is a constant transformation defined as,

$$ {}^{6}T_{\text{xray}} = Tran_{y}(a_2) \cdot R_{x}(180^{\text{o}}) \cdot R_{y}(90^{\text{o}}) \tag{4.2} $$

where $R_x(\alpha_1)$, $R_y(\alpha_2)$ and $Tran_y(\alpha_3)$ are $4 \times 4$ matrices that represent rotations around $X$ and $Y$ axes and translation along $Y$ axis with value $\alpha_1$, $\alpha_2$, and $\alpha_3$ respectively. Finally, ${}^{1}T_{6} \cdot {}^{6}T_{\text{xray}}$ builds a relation between the five C-arm joint values and the pose of the X-ray source relative to the C-arm base.

We build a 6-DOF C-arm model by integrating the forward-backward translation of the table into the 5-DOF C-arm kinematics. Translating the table forward or backward is equivalent to moving the whole C-arm system in an opposite direction, therefore the table translation is modeled as the first joint and the table coordinate frame is defined as the base coordinate frame for 6-DOF C-arm model. We assign the coordinate frame 0 to the table, which is defined as the $Z_0$ axis parallel to the direction of the table forward-backward translation, the $X_0$ axis is chosen such that the $X_0$-$Z_0$ plane is parallel to the table surface (see Figure 4.2(a)), and the $Y_0$-axis follows the right hand rule.

Our modeling concept does not put any constraint on the setup of table position. However, in order to build a kinematic chain for the 6-DOF C-arm model satisfying the DH rules, we only need to re-assign the coordinate frame 1 of the 5-DOF C-arm model.

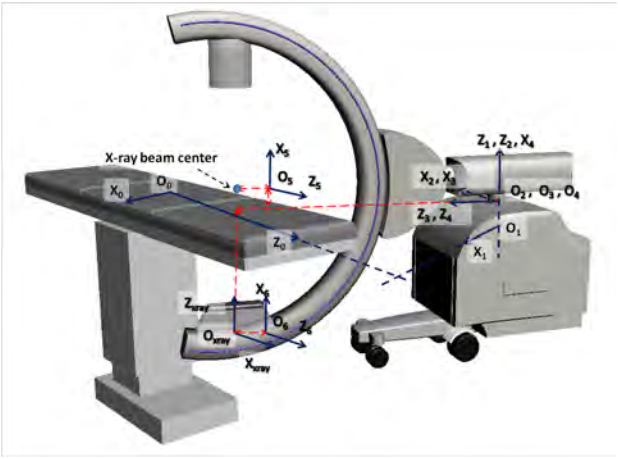


(a) Coordinate frames assignment

| | a (Tx) | d (Tz) | α (Rx) | θ(Rz) |
|---|---|---|---|---|
| 0 | Dist($Z_0$,$Z_1$) | $d_0^*$ + Dist($X_0$,$X_1$) | Ang($Z_0$,$Z_1$) | Ang($X_0$,$X_1$) |
| 1 | 0 | $d_1^*$ + Dist($X_1$,$X_2$) | 0 | Ang($X_1$,$X_2$) |
| 2 | 0 | 0 | -pi/2 | $\theta_2^*$ |
| 3 | 0 | $d_3^*$ | 0 | -pi/2 |
| 4 | $a_1$ | length_offset -$a_2$ | pi/2 | $\theta_4^*$ |
| 5 | -$a_1$ - orbital_offset | 0 | 0 | $\theta_5^*$ |

(b) Link parameters(*variable)

Figure 4.2: Kinematic chain of 6-DOF C-arm model for the general mobile C-arm. (a) coordinate frame assignments; (b) the corresponding link parameters.

The vertical movement axis $Z_1$ remains the same as in the 5-DOF model. According to the DH rules, the axis $X_1$ should be re-assigned such that it is orthogonal to and intersects with both axes $Z_0$ and $Z_1$. Having a known transformation ${}^{\text{xray}}T_0 \in \mathbb{R}^{4\times4}$ between X-ray source and the table, which can be obtained from various C-arm pose estimation methods [164, 207, 218], we can compute the transformation ${}^1T_0 \in \mathbb{R}^{4\times4}$ between the C-arm base (coordinate frame 1) and the table (coordinate frame 0) as,

$$ {}^1T_0 = {}^1T_6 \cdot {}^6T_{\text{xray}} \cdot {}^{\text{xray}}T_0. \tag{4.3} $$

Then, we can find two points on both axes $Z_0$ and $Z_1$, which define a minimum distance between these two axes. The axis $X_1$ for the 6-DOF C-arm model is defined by these two points. Figure 4.2(a) and 4.2(b) show the coordinate frames and the table of corresponding link parameters for the 6-DOF C-arm kinematic chain model.

Let a vector $q = [d_0; d_1; \theta_2; d_3; \theta_4; \theta_5]$ be the six joint variables, where $d_0$ represents the table translation. The kinematic equation ${}^0T_6(q) \in \mathbb{R}^{4\times4}$ for the 6-DOF C-arm model, which represents the pose of the end-effector with respect to the patient's table, can be derived as

$$ {}^0T_6(q) = {}^0\bar{A}_1 \cdot {}^1\bar{A}_2 \cdot {}^2\bar{A}_3 \cdot {}^3\bar{A}_4 \cdot {}^4\bar{A}_5 \cdot {}^5\bar{A}_6 \tag{4.4} $$

where ${}^i\bar{A}_{i+1} \in \mathbb{R}^{4\times4}$ is the transformation from the coordinate frame $i+1$ to $i$ and can be derived from the $i$-th row of the table of link parameters for the 6-DOF C-arm model (see Figure 4.2(b)) according to [217]. Thus, the pose of the X-ray source with respect to the patient's table, ${}^0T_{\text{xray}} \in \mathbb{R}^{4\times4}$, can be obtained as,

$$ {}^0T_{\text{xray}} = {}^0T_6 \cdot {}^6T_{\text{xray}}. \tag{4.5} $$

For the analysis of kinematic singularity and derivation of closed-form inverse kinematics, we denote the constant value *length_offset* and *orbital_offset* by $l_1$ and $l_2$. Ang($A$,$B$) (or Dist($A$,$B$)) represents the angle(or distance) between axes $A$ and $B$ in

Figure 4.2(a) and its sign is determined by the DH rules. We define $\gamma_1 = \text{Ang}(Z_0, Z_1)$, $\gamma_2 = \text{Ang}(X_0, X_1)$, $\gamma_3 = \text{Ang}(X_1, X_2)$, $D_1 = \text{Dist}(Z_0, Z_1)$, $D_2 = \text{Dist}(X_0, X_1)$, and $D_3 = \text{Dist}(X_1, X_2)$. Let $c_\alpha = \cos(\alpha)$ and $s_\alpha = \sin(\alpha)$.

### 4.3.2 Kinematic Singularity

Kinematic singularity is a kinematic configuration at which the mobility of the end-effector is reduced, i.e. losing one or more DOF of motion. A kinematic system has a singularity for a specific joint configuration when the rank of its manipulator Jacobian matrix is less than the number of required DOF. We derive the manipulator Jacobian matrix $J_{6\text{dof}}$ for the 6-DOF C-arm model from its kinematic equations according to the method proposed in [219]. $J_{6\text{dof}}$ is a function of vector $q$ and relates differential changes in the six joint positions to the X-ray source linear and angular velocity. The 6-DOF C-arm model consists of six joints, and thus $J_{6\text{dof}}$ is a $6 \times 6$ square matrix. Therefore, when the determinant of $J_{6\text{dof}}$ is zero, the rank of $J_{6\text{dof}}$ becomes less than six. We compute the determinant of $J_{6\text{dof}}$ as,

$$\det(J_{6\text{dof}}) \quad = \quad (s_{\gamma_3} c_{\theta_2} + c_{\gamma_3} s_{\theta_2}) \cdot s_{\gamma_1} \cdot c_{\theta_4}. \tag{4.7}$$

$\det(J_{6\text{dof}}) = 0$, when

a) $s_{\gamma_1} = 0$, the direction of the table translation is parallel to the C-arm vertical movement direction. This situation does not physically exist (see Figure 4.3(a)).

b) $c_{\theta_4} = 0$, the orbital rotation axis $Z_5$ is parallel to the wigwag rotation axis $Z_2$. Consequently, one DOF is missing (see Figure 4.3(b)).

c) $s_{\gamma_3} c_{\theta_2} + c_{\gamma_3} s_{\theta_2} = 0 \Rightarrow \theta_2 = -\gamma_3$, the direction of the table translation is parallel to the C-arm horizontal movement direction. Therefore, this configuration leads to losing one DOF (see Figure 4.3(c)).

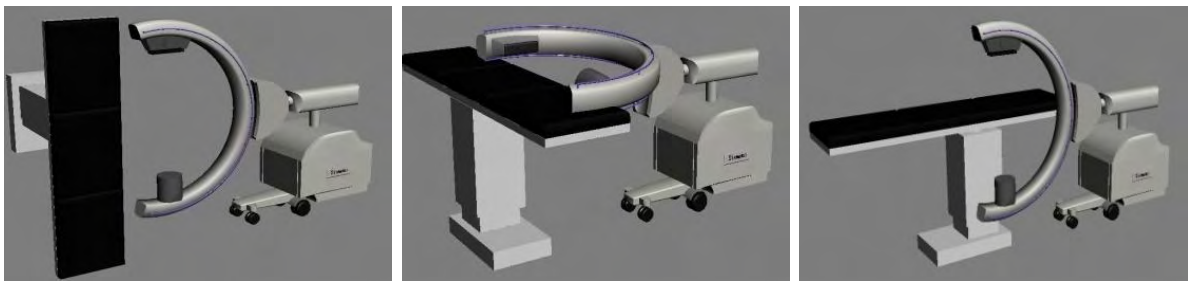

(a) (b) (c)

Figure 4.3: Example positions for the kinematic singularities of the 6-DOF C-arm model. (a) $s_{\gamma_1} = 0$; (b) $c_{\theta_4} = 0$; (c) $\theta_2 = -\gamma_3$.

$$
{}^0T_6(q) \;=\; \begin{bmatrix} r_{11} & r_{12} & r_{13} & p_x \\ r_{21} & r_{22} & r_{23} & p_y \\ r_{31} & r_{32} & r_{33} & p_z \\ 0 & 0 & 0 & 1 \end{bmatrix} \tag{4.6}
$$

where

$$
\begin{aligned}
r_{11} &= s_{\gamma_1}s_{\gamma_2}c_{\theta_4}\,c_{\theta_5} + (c_{\gamma_2}c_{\gamma_3} - c_{\gamma_1}s_{\gamma_2}s_{\gamma_3})\cdot(c_{\theta_2}\,s_{\theta_4}\,c_{\theta_5} - s_{\theta_2}\,s_{\theta_5}) \\
&\quad -(c_{\gamma_2}s_{\gamma_3} + c_{\gamma_1}s_{\gamma_2}c_{\gamma_3})\cdot(s_{\theta_2}\,s_{\theta_4}\,c_{\theta_5} + c_{\theta_2}\,s_{\theta_5}) \\
r_{12} &= -s_{\gamma_1}s_{\gamma_2}c_{\theta_4}\,s_{\theta_5} - (c_{\gamma_2}c_{\gamma_3} - c_{\gamma_1}s_{\gamma_2}s_{\gamma_3})\cdot(c_{\theta_2}\,s_{\theta_4}\,s_{\theta_5} + s_{\theta_2}\,c_{\theta_5}) \\
&\quad +(c_{\gamma_2}s_{\gamma_3} + c_{\gamma_1}s_{\gamma_2}c_{\gamma_3})\cdot(s_{\theta_2}\,s_{\theta_4}\,s_{\theta_5} - c_{\theta_2}\,c_{\theta_5}) \\
r_{13} &= s_{\gamma_1}s_{\gamma_2}s_{\theta_4} - (c_{\gamma_2}c_{\gamma_3} - c_{\gamma_1}s_{\gamma_2}s_{\gamma_3})\cdot c_{\theta_2}\,c_{\theta_4} + (c_{\gamma_2}s_{\gamma_3} + c_{\gamma_1}s_{\gamma_2}c_{\gamma_3})\cdot s_{\theta_2}\,c_{\theta_4} \\
r_{21} &= -s_{\gamma_1}c_{\gamma_2}c_{\theta_4}\,c_{\theta_5} + (s_{\gamma_2}c_{\gamma_3} + c_{\gamma_1}c_{\gamma_2}s_{\gamma_3})\cdot(c_{\theta_2}\,s_{\theta_4}\,c_{\theta_5} - s_{\theta_2}\,s_{\theta_5}) \\
&\quad -(s_{\gamma_2}s_{\gamma_3} - c_{\gamma_1}c_{\gamma_2}c_{\gamma_3})\cdot(s_{\theta_2}\,s_{\theta_4}\,c_{\theta_5} + c_{\theta_2}\,s_{\theta_5}) \\
r_{22} &= s_{\gamma_1}c_{\gamma_2}c_{\theta_4}\,s_{\theta_5} - (s_{\gamma_2}c_{\gamma_3} + c_{\gamma_1}c_{\gamma_2}s_{\gamma_3})\cdot(c_{\theta_2}\,s_{\theta_4}\,s_{\theta_5} + s_{\theta_2}\,c_{\theta_5}) \\
&\quad +(s_{\gamma_2}s_{\gamma_3} - c_{\gamma_1}c_{\gamma_2}c_{\gamma_3})\cdot(s_{\theta_2}\,s_{\theta_4}\,s_{\theta_5} - c_{\theta_2}\,c_{\theta_5}) \\
r_{23} &= -s_{\gamma_1}c_{\gamma_2}s_{\theta_4} - (s_{\gamma_2}c_{\gamma_3} + c_{\gamma_1}c_{\gamma_2}s_{\gamma_3})\cdot c_{\theta_2}\,c_{\theta_4} + (s_{\gamma_2}s_{\gamma_3} - c_{\gamma_1}c_{\gamma_2}c_{\gamma_3})\cdot s_{\theta_2}\,c_{\theta_4} \\
r_{31} &= c_{\gamma_1}c_{\theta_4}\,c_{\theta_5} + s_{\gamma_1}s_{\gamma_3}\cdot(c_{\theta_2}\,s_{\theta_4}\,c_{\theta_5} - s_{\theta_2}\,s_{\theta_5}) + s_{\gamma_1}c_{\gamma_3}\cdot(s_{\theta_2}\,s_{\theta_4}\,c_{\theta_5} + c_{\theta_2}\,s_{\theta_5}) \\
r_{32} &= -c_{\gamma_1}c_{\theta_4}\,s_{\theta_5} - s_{\gamma_1}s_{\gamma_3}\cdot(c_{\theta_2}\,s_{\theta_4}\,s_{\theta_5} + s_{\theta_2}\,c_{\theta_5}) - s_{\gamma_1}c_{\gamma_3}\cdot(s_{\theta_2}\,s_{\theta_4}\,s_{\theta_5} - c_{\theta_2}\,c_{\theta_5}) \\
r_{33} &= c_{\gamma_1}s_{\theta_4} - s_{\gamma_1}s_{\gamma_3}c_{\theta_2}\,c_{\theta_4} - s_{\gamma_1}c_{\gamma_3}s_{\theta_2}\,c_{\theta_4} \\
p_x &= c_{\gamma_2}D_1 + s_{\gamma_1}s_{\gamma_2}\cdot(d_1 + D_3 + a_1\cdot c_{\theta_4} - (l_2+a_1)\,c_{\theta_4}\,c_{\theta_5}) \\
&\quad +(c_{\gamma_2}c_{\gamma_3} - c_{\gamma_1}s_{\gamma_2}s_{\gamma_3})\cdot((l_2+a_1)\,s_{\theta_2}\,s_{\theta_5} - (l_1-a_2)\,s_{\theta_2} - s_{\theta_2}\,d_3 - (l_2+a_1)\,c_{\theta_2}\,s_{\theta_4}\,c_{\theta_5} \\
&\quad +a_1\cdot c_{\theta_2}\,s_{\theta_4}) + (c_{\gamma_2}s_{\gamma_3} + c_{\gamma_1}s_{\gamma_2}c_{\gamma_3})\cdot((l_2+a_1)\,s_{\theta_2}\,s_{\theta_4}\,c_{\theta_5} \\
&\quad +(l_2+a_1)\,c_{\theta_2}\,s_{\theta_5} - (l_1-a_2)\,c_{\theta_2} - c_{\theta_2}\,d_3 - a_1\cdot s_{\theta_2}\,s_{\theta_4}) \\
p_y &= s_{\gamma_2}D_1 - s_{\gamma_1}c_{\gamma_2}\cdot(d_1 + D_3 + a_1\cdot c_{\theta_4} - (l_2+a_1)\,c_{\theta_4}\,c_{\theta_5}) \\
&\quad +(s_{\gamma_2}c_{\gamma_3} + c_{\gamma_1}c_{\gamma_2}s_{\gamma_3})\cdot((l_2+a_1)\,s_{\theta_2}\,s_{\theta_5} - (l_1-a_2)\,s_{\theta_2} - s_{\theta_2}\,d_3 - (l_2+a_1)\,c_{\theta_2}\,s_{\theta_4}\,c_{\theta_5} \\
&\quad +a_1\cdot c_{\theta_2}\,s_{\theta_4}) + (s_{\gamma_2}s_{\gamma_3} - c_{\gamma_1}c_{\gamma_2}c_{\gamma_3})\cdot((l_2+a_1)\,s_{\theta_2}\,s_{\theta_4}\,c_{\theta_5} + (l_2+a_1)\,c_{\theta_2}\,s_{\theta_5} \\
&\quad -(l_1-a_2)\,c_{\theta_2} - c_{\theta_2}\,d_3 - a_1\cdot s_{\theta_2}\,s_{\theta_4}) \\
p_z &= D_2 + d_0 + c_{\gamma_1}\cdot(d_1 + D_3 + a_1\cdot c_{\theta_4} - (l_2+a_1)\,c_{\theta_4}\,c_{\theta_5}) \\
&\quad +s_{\gamma_1}s_{\gamma_3}\cdot((l_2+a_1)\,s_{\theta_2}\,s_{\theta_5} - (l_1-a_2)\,s_{\theta_2} - s_{\theta_2}\,d_3 - (l_2+a_1)\,c_{\theta_2}\,s_{\theta_4}\,c_{\theta_5} + a_1\,c_{\theta_2}\,s_{\theta_4}) \\
&\quad +s_{\gamma_1}c_{\gamma_3}\cdot(-(l_2+a_1)\,s_{\theta_2}\,s_{\theta_4}\,c_{\theta_5} - (l_2+a_1)\,c_{\theta_2}\,s_{\theta_5} + (l_1-a_2)\,c_{\theta_2} + c_{\theta_2}\,d_3 - a_1\,s_{\theta_2}\,s_{\theta_4})
\end{aligned}
$$

Table 4.1: The kinematic equation ${}^0T_6(q)$ for the 6-DOF C-arm model.

### 4.3.3 Closed-form Inverse Kinematics

The inverse kinematics problem for a manipulator deals with determining joint values given the position and orientation of the end-effector. Therefore, positioning the X-ray source at a desired pose relative to the operating table requires finding the six joint values by solving the inverse kinematics problem for the 6-DOF C-arm model. Given a pose of the X-ray source relative to the table ${}^0T_{\text{xray}}$, the end-effector pose relative to the table ${}^0T_6$ is obtained as,

$$ {}^0T_6 = {}^0\,T_{\text{xray}} \cdot ({}^6T_{\text{xray}})^{-1}. \tag{4.8} $$

Then, we solve kinematic equations of ${}^0T_6(q)$ in an algebraic way to find closed-form solutions, i.e. analytic expressions, for $d_0, d_1, \theta_2, d_3, \theta_4$, and $\theta_5$. Three rotational joints $\theta_2, \theta_4$, and $\theta_5$ are first solved by using the upper-left $3 \times 3$ matrix of ${}^0T_6$. Three translational joints $d_0, d_1$, and $d_3$ can be afterwards obtained by using the three equations from the upper-right 3-vector of ${}^0T_6$. It should be noted that the closed-form solutions are nonexistent for kinematic singular cases, and thus numerical solutions should be explored in these situations. Three kinematic singular cases for the 6-DOF C-arm model are (i) $s_{\gamma_1} = 0$, (ii) $c_{\theta_4} = 0$, and (iii) $\theta_2 = -\gamma_3$ as derived in Section 4.3.2. A common numerical solution using the pseudo-inverse Jacobian presented in [220] is employed to solve the inverse kinematics problem for the singular cases in our current implementation. The closed-form solutions for general cases are presented in Table 4.2. There are generally two solutions for $q$. Whether or not both mathematical solutions satisfy a given problem depends on specific applications and additional constraints, e.g. checking whether the solutions are within the physical range of joints.

When $c_{\theta_4} \neq 0$, $\theta_2$ can be first calculated by $\theta_2 = ATAN2(s_{\theta_2}, c_{\theta_2})$ where

$$s_{\theta_2} = \frac{(c_{\gamma_1} s_{\gamma_2} c_{\gamma_3} + c_{\gamma_2} s_{\gamma_3}) \cdot r_{13} + (s_{\gamma_2} s_{\gamma_3} - c_{\gamma_1} c_{\gamma_2} c_{\gamma_3}) \cdot r_{23} - s_{\gamma_1} c_{\gamma_3} \cdot r_{33}}{c_{\theta_4}} \quad (4.9)$$

$$c_{\theta_2} = \frac{(c_{\gamma_1} s_{\gamma_2} s_{\gamma_3} - c_{\gamma_2} c_{\gamma_3}) \cdot r_{13} - (s_{\gamma_2} c_{\gamma_3} + c_{\gamma_1} c_{\gamma_2} s_{\gamma_3}) \cdot r_{23} - s_{\gamma_1} s_{\gamma_3} \cdot r_{33}}{c_{\theta_4}} \quad (4.10)$$

Note that $\theta_2$ has two solutions in the interval of $[(-\pi, \pi]$, and one is calculated assuming $c_{\theta_4} < 0$ and the other is obtained assuming $c_{\theta_4} > 0$. Both solutions are theoretically correct.
Substituting $c_{\theta_2}$ (or $s_{\theta_2}$) into equation 4.10 (or 4.9), we obtain $c_{\theta_4}$. When $s_{\gamma_1} \neq 0$, $\theta_4$ is obtained by $\theta_4 = ATAN2(s_{\theta_4}, c_{\theta_4})$ where

$$s_{\theta_4} = \frac{r_{13} \cdot s_{\gamma_2} - r_{23} \cdot c_{\gamma_2} - (c_{\gamma_1} s_{\gamma_3} \cdot c_{\theta_2} c_{\theta_4} + c_{\gamma_1} c_{\gamma_3} \cdot s_{\theta_2} c_{\theta_4})}{s_{\gamma_1}} \quad (4.11)$$

When $c_{\theta_4} \neq 0$, $\theta_5$ can be solved by $\theta_5 = ATAN2(s_{\theta_5}, c_{\theta_5})$ where

$$c_{\theta_5} = \frac{r_{11} \cdot s_{\gamma_1} s_{\gamma_2} - r_{21} \cdot s_{\gamma_1} c_{\gamma_2} + c_{\gamma_1} \cdot r_{31}}{c_{\theta_4}} \quad (4.12)$$

$$s_{\theta_5} = \frac{-r_{12} \cdot s_{\gamma_1} s_{\gamma_2} + r_{22} \cdot s_{\gamma_1} c_{\gamma_2} - c_{\gamma_1} \cdot r_{32}}{c_{\theta_4}} \quad (4.13)$$

In the non-singular condition, $\theta_2 \neq -\gamma_3 \Rightarrow c_{\gamma_3} s_{\theta_2} + s_{\gamma_3} c_{\theta_2} \neq 0$. Thus $d_3$ can be expressed by $d_3 = \frac{Eq_0}{(c_{\gamma_3} s_{\theta_2} + s_{\gamma_3} c_{\theta_2})}$

$$\begin{aligned} Eq_0 = & -c_{\gamma_2} \cdot p_x - s_{\gamma_2} \cdot p_y + D_1 \\ & + c_{\gamma_3} \cdot ((l_2 + a_1)\, s_{\theta_2}\, s_{\theta_5} - (l_1 - a_2)\, s_{\theta_2} - (l_2 + a_1)\, c_{\theta_2}\, s_{\theta_4}\, c_{\theta_5} + a_1\, c_{\theta_2}\, s_{\theta_4}) \\ & + s_{\gamma_3} \cdot ((l_2 + a_1)\, s_{\theta_2}\, s_{\theta_4}\, c_{\theta_5} + (l_2 + a_1)\, c_{\theta_2}\, s_{\theta_5} - (l_1 - a_2)\, c_{\theta_2} - a_1\, s_{\theta_2}\, s_{\theta_4}) \end{aligned} \quad (4.14)$$

When $s_{\gamma_1} \neq 0$, $d_1$ can be expressed by $d_1 = \frac{Eq_1}{s_{\gamma_1}} + (l_2 + a_1)\, c_{\theta_4}\, c_{\theta_5} - D_3 - a_1 \cdot\ c_{\theta_4}$ where

$$\begin{aligned} Eq_1 = & s_{\gamma_2} p_x - c_{\gamma_2} p_y \\ & + c_{\gamma_1} s_{\gamma_3} ((l_2 + a_1)\, s_{\theta_2}\, s_{\theta_5} - (l_1 - a_2)\, s_{\theta_2} - s_{\theta_2}\, d_3 - (l_2 + a_1)\, c_{\theta_2}\, s_{\theta_4}\, c_{\theta_5} + a_1\, c_{\theta_2}\, s_{\theta_4}) \\ & - c_{\gamma_1} c_{\gamma_3} ((l_2 + a_1)\, s_{\theta_2}\, s_{\theta_4}\, c_{\theta_5} + (l_2 + a_1)\, c_{\theta_2}\, s_{\theta_5} - (l_1 - a_2)\, c_{\theta_2} - c_{\theta_2}\, d_3 - a_1 \cdot\ s_{\theta_2}\, s_{\theta_4}) \end{aligned} \quad (4.15)$$

$d_0$ has an analytic expression $d_0 = p_z - Eq_2$, where

$$\begin{aligned} Eq_2 = & D_2 + c_{\gamma_1} \cdot (d_1 + D_3 - (l_2 + a_1)\, c_{\theta_4}\, c_{\theta_5}) \\ & + s_{\gamma_1} s_{\gamma_3} ((l_2 + a_1)\, s_{\theta_2}\, s_{\theta_5} - (l_1 - a_2)\, s_{\theta_2} - s_{\theta_2}\, d_3 - (l_2 + a_1)\, c_{\theta_2}\, s_{\theta_4}\, c_{\theta_5} + a_1\, c_{\theta_2}\, s_{\theta_4}) \\ & + s_{\gamma_1} c_{\gamma_3} (-(l_2 + a_1)\, s_{\theta_2}\, s_{\theta_4}\, c_{\theta_5} - (l_2 + a_1)\, c_{\theta_2}\, s_{\theta_5} + (l_1 - a_2)\, c_{\theta_2} + c_{\theta_2}\, d_3 + a_1\, s_{\theta_2}\, s_{\theta_4}) \end{aligned} \quad (4.16)$$

Table 4.2: Closed-form solution for the inverse kinematics of the 6-DOF C-arm model, i.e. analytic expressions, for $d_0, d_1, \theta_2, d_3, \theta_4$, and $\theta_5$.

## 4.4 Inverse Kinematics for Parallax-free X-ray Image Stitching

Accurate intra-operative determination of mechanical axis alignment, joint orientation and leg length is crucial for the treatment of knee osteoarthritis, correction of deformities, and long bone shaft fractures [221, 126, 127, 164]. X-ray images acquired by mobile C-arms have a narrow field of view and cannot visualize the entire bone structure of a lower leg within a single X-ray image. Accurate evaluation of long bone geometry based on separated individual images remains challenging. Thus, surgeons require the visualization of a panoramic image comprising of several C-arm images stitched together showing all lower bones of interest. Stitching methods for combining multiple individual images into a panoramic X-ray image have been proposed for assisting intra-operative procedures of mechanical axis and extremity length [126, 127, 164]. However, methods [126, 127] suffer from parallax effects that can lead to perspective distortion, which introduces metric measurement errors on the panorama.

In order to generate a true parallax-free panoramic X-ray image, we have proposed a method of stitching multiple individual X-ray images acquired by rotating a C-arm around its X-ray source with respect to the patient's table [164]. This preliminary solution suffers from the complexity of the user interaction. Surgeons must first move the five C-arm joints and the table, and consequently the position of an additional X-ray image in the panorama frame is computed based on the C-arm motion. If the resulting location of the additional X-ray image is not optimal, the surgeons have to adjust the 5 C-arm joints and the table. After a series of adjusting the C-arm joints and table through trials and errors, they may get the desired location of the additional X-ray image in the panorama. Surgeons are interested only in the panoramic images, but do not know the C-arm and table movements. Therefore, it is preferable for surgeons to specify a target position of X-ray images in the panorama frame, and to be guided by the system on how to move the C-arm and the table. Furthermore, the previous solution also requires a strict protocol to acquire an X-ray image by first rotating the C-arm and then translating the table (or C-arm). The displacement of the X-ray source introduced by rotating the C-arm could result in a potential collision between the X-ray source and table. However, such collisions can actually be avoided by first translating the table (or C-arm), when required movements of the C-arm joints and the table for acquiring the desired X-ray image are pre-known.

In this work, we calculate C-arm joint movements and table translations needed for acquiring an optimal X-ray image defined by its image position in the panorama frame. Our method consists of two main steps. Given an X-ray image position within the panorama we first automatically compute the required C-arm pose, and then solve the necessary joint movements and table translations from the inverse kinematics to acquire the right X-ray image. The proposed algorithm for parallax-free X-ray image stitching is shown in Table 4.3.

### 4.4.1 C-arm Motion given an X-ray Image Position in Panorama

The key step of image stitching is the estimation of the homography for aligning images. A rotation $R \in \mathbb{R}^{3\times3}$ and a translation $t \in \mathbb{R}^3$ are from the coordinate system of the second camera view to the first camera view. In [126], the homography that aligns the second camera image to the first camera image is defined by,

$$H = KRK^{-1} + \frac{1}{d}Ktn^TK^{-1} \tag{4.17}$$

where $K \in \mathbb{R}^{3\times3}$ is the intrinsic matrix of the camera. $H$ is valid for all image points, for which corresponding space points are on the same plane defined by the normal vector $n \in \mathbb{R}^3$ and distance $d$ to the origin in the coordinate system of the second camera view. However, any structure that is not on this plane in 3D space will result in perspective distortion effects caused by parallax. In case that the camera motion only contains the rotation $R$ around its center, $\frac{1}{d}Ktn^TK^{-1}$ is equal to zero. Then the homography $H$ is independent of the plane parameters, and thus it is valid for all image points without the coplanar constraint on their corresponding space points. Therefore, a parallax-free panoramic X-ray image can be generated by aligning multiple individual X-ray images acquired by rotating C-arms around the X-ray source [164].

Without loss of generality, we define the first X-ray image as the reference panorama frame (see Figure 4.4). Any additional X-ray image can be registered to the reference frame with no parallax effects, when the image is acquired after the X-ray source undergoes a pure rotation $R$. Then, the position of the additional X-ray image in the panorama is defined by $H = KRK^{-1}$ according to equation 4.17. Homography $H$ can generally have eight parameters. Here, we present a practical and intuitive approach of specifying additional X-ray image positions by placing their principal points in the panorama frame assuming an unmoved X-ray source. Let $p \in \mathbb{R}^3$ be the 2D homogenous coordinate of the principal point in the panorama frame. Then, we need to compute the principal axis (denoted as a normal vector $V_p \in \mathbb{R}^3$) of acquiring an additional X-ray image in the coordinate system of the first X-ray view.

Let $P_{3d} \in \mathbb{R}^3$ be a 3D point in the coordinate system of the first X-ray view, whose image projection is $p$. The normalized vector $V_p$ from the X-ray source center to $P_{3d}$ in the coordinate system of the first X-ray viewing is

$$V_p = K^{-1}p. \tag{4.18}$$

The pure rotational motion $R$ can be computed as a rotation from the principal axis of acquiring the additional image to acquiring the first image, i.e. from $V_p$ to $[0; 0; 1]$. $K$ is obtained from an offline X-ray calibration. Then, the homography $H$ is computed for visualizing the area where the additional image will be projected in the panorama (see Figure 4.4). Therefore, we are able to obtain a C-arm motion $R$ for a given position of the X-ray image in the panorama frame by specifying its principal point.

### 4.4.2 Joint Parameters from the Inverse Kinematics

For obtaining the required C-arm joint parameters and table translations to position the C-arm at a given pose, we solve the closed-form inverse kinematics of the integrated kine-

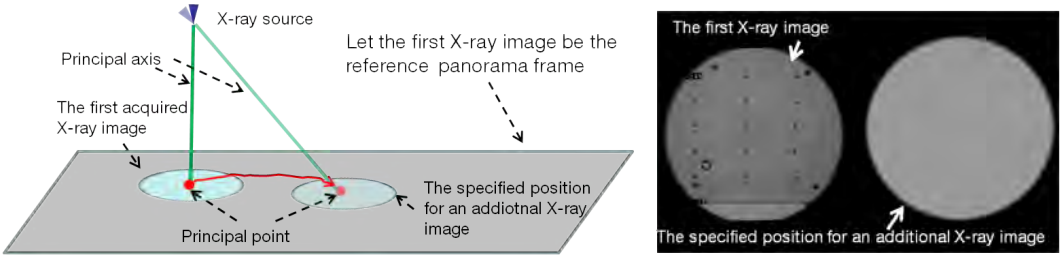


Figure 4.4: The reference panorama frame is defined by the first X-ray image. Any subsequent X-ray images can be registered to the reference frame in order to build the final panorama. The right image shows that the area of the X-ray image projected in the panorama is visualized as a grey circle in our implementation.

matic chain of the C-arm and the table. However, there are two mathematical solutions. For the particular problem of parallax-free X-ray stitching, we choose the solution based on the ordered constraints : (i) choose the one whose values are within possible limited mechanical ranges; (ii) choose the one who has a smaller sum of rotational joint movements; (iii) choose the one who has a smaller sum of translational joint movements. If none of two solutions satisfy constraint (i), we have the situation of invalid X-ray image position within the panorama frame, which is discussed in the next section.

### 4.4.3 Invalid X-ray image positions within the panorama frame

The limited mechanical range of each joint and invalid C-arm poses definitely put constraints on the position of the X-ray image in the reference panorama frame. Invalid C-arm pose occur because either: (i) an intersection between the table and the C-arm exists or (ii) the table is not within the X-ray cone beam of the C-arm. For detecting the invalid C-arm pose, we approximate the table by one oriented bounding box (OBB) and the C-arm machine by a set of OBBs. Separating axis theory for OBB interference detection [222] is employed for detecting the intersection between the table and the C-arm. The table is regarded as within the X-ray cone beam of the C-arm, when the principal axis of the X-ray source intersects the bounding box of the table. The X-ray image position in the panorama frame is not valid if one or more of the six joints exceed their mechanical ranges or the C-arm pose is invalid. Thanks to integrated kinematic modeling of the C-arm and the table, the joint parameters of the 6-DOF C-arm model and the C-arm pose relative to the table for acquiring an X-ray image can be obtained from its image position in the panorama. Therefore, for an arbitrary specified position of X-ray image in the panorama frame defined by the clinician for instance, we can compute its validity.

### 4.4.4 Clinical Protocol for Panoramic Imaging

The new proposed clinical protocol for parallax-free X-ray panoramic imaging is given as follows:

1. Position the C-arm to acquire the first X-ray image, which fixes the reference panorama frame. An integrated 6-DOF C-arm kinematic chain is built.

The pre-requistes are i) the first X-ray image is acquired, which defines the panorama frame. X-ray pose $P_{ref} \in \mathbb{R}^{4\times4}$ relative to the table for acquiring the first X-ray image is obtained from C-arm pose estimation. Our solution for C-arm pose estimation will be explained in Section 4.5; ii) the 6-DOF C-arm model is built with a known $P_{ref}$.
Algorithm for parallax-free X-ray image stitching by specifying the position of an additional X-ray image in panorama frame is as followings:

1. Specify the position of the principal point $p$ (expressed in the 2D homogeneous coordinate) in the panorama frame for the additional X-ray image.
2. Compute the principal axis of the X-ray geometry for acquiring the additional X-ray image as $K^{-1}p$.
3. Calculate the rotation $R$ from the X-ray acquisition of the additional X-ray image to the first image.
4. Obtain homography $H = K^{-1}RK$ that aligns the additional X-ray image to the panorama frame.
5. Visualize the area of the additional X-ray image in the panorama frame as a grey circle.
6. Compute the X-ray pose ${}^tP_x$ relative to the table for acquiring the additional X-ray image
$$ {}^tP_x = P_{ref} \cdot \begin{bmatrix} R & 0 \\ 0 & 1 \end{bmatrix} \tag{4.19} $$
7. Solve the inverse kinematics for the required joint values in order to position the C-arm at the desired pose ${}^tP_x$ using the closed-form solution presented in Section 4.3.3
8. Compute the validity of the position of the additional X-ray image according to Section 4.4.3.

Table 4.3: Algorithm for inverse kinematics based parallax-free X-ray image stitching.

2. Manually specify a position of the desired additional X-ray image in the panorama frame by dragging its principal point on the screen using a mouse. Consequently, the projection area of the additional X-ray image in the panorama is visualized and the required joint values for acquiring the right X-ray image are computed using the algorithm presented in Table 4.3. Note that, the surgeon, familiar with the bone geometries, knows roughly where they want the additional X-ray image to be in the panorama frame, as he or she will see the total area covered by the individual X-ray images, including the previously acquired images and the additional image.
3. Move each joint to its destination with continuous feedback.
4. Acquire an X-ray image and register it to the panorama.
5. Stop if the panoramic X-ray image is complete, else repeat steps 2-5.

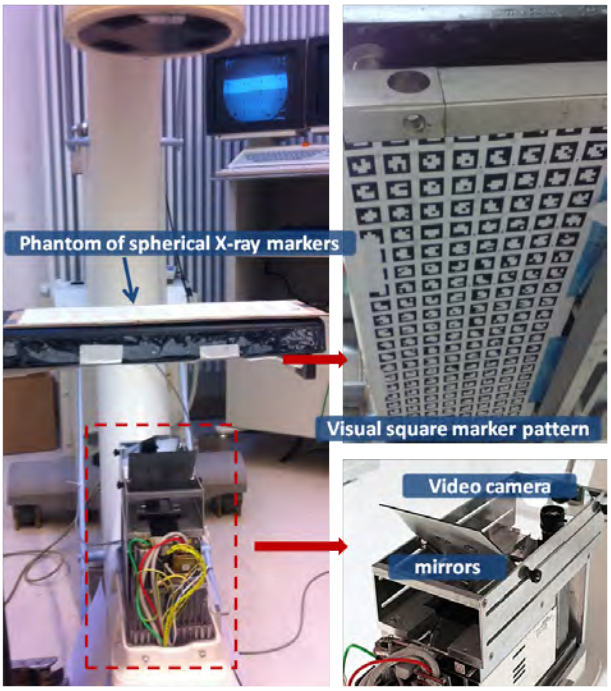


Figure 4.5: 6-DOF C-arm system implementation.

## 4.5 System Implementation

We perform C-arm pose estimation in order to obtain the transformation between the C-arm and the operating table. In our implementation, we attach a video camera and mirror construction to the X-ray gantry of a mobile C-arm and a visual planar marker pattern under the table (see Figure 4.5). The mobile C-arm is a Siremobile Iso-C 3D with the orbital offset of 625 mm and length offset of 1350 mm, from Siemens Healthcare. Table 4.4 shows the physical ranges of the joints of the Siremobile Iso-C 3D. The optical

- orbital offset: 625 mm
- length offset: 1350 mm
- vertical movement: 400 mm
- wigwag movement: $\pm 10^{o}$
- horizontal movement: 200 mm
- angular movement: $\pm 190^{o}$
- orbital movement: $\pm 95^{o}$

Table 4.4: Specification for Siremobile Iso-C 3D.

video camera is a Flea2, from Point Grey Research Inc. The camera is connected via a Firewire connection (IEEE-1394) to the computer with custom developed software. The computer is a standard PC extended by a frame grabber card, Falcon, from IDS Imaging Development System GmbH. The C-arm system and the video camera are calibrated by using the proposed method of [50]. This calibration enables the X-ray source and the video camera to have the same intrinsic and extrinsic parameters. Therefore, all of the poses and motions estimated using the video camera directly correspond to that of the X-ray projection geometry. The table and the marker coordinate systems are located at the same position, but may differ in orientation. We adapt the method presented in [164] to calibrate the table coordinate system. The calibration has to be performed only once after attaching the marker pattern to the table. Having the marker pattern with known geometry, we are able to estimate the pose of the X-ray source (camera) relative to the patient's table using the standard camera pose estimation method of [151]. Moreover, thanks to the visual marker based C-arm pose estimation, the joint values for each estimated C-arm pose can be computed by solving the inverse kinematics. Therefore, our system provides continuous guidance for the operator of the device on how much to move each joint (including the table translation) in order to position the C-arm at a desired 3D Cartesian location without the need for radiation.

## 4.6 Experiments and Results

A simulation experiment was first conducted to demonstrate that the 6-DOF C-arm model has a larger working space than the 5-DOF model in Section 4.6.1. Section 4.6.2 presents the C-arm repositioning experimentation that shows the practicality and accuracy of our developed 6-DOF C-arm system. The novel parallax-free X-ray stitching method was evaluated on phantom and dry bone, which is described in Section 4.6.3.

### 4.6.1 Simulation Experiments

Matthaeus et al. [130] presented the closed-form inverse kinematics for a general 5-DOF mobile C-arm model to acquire a desired X-ray image, which has a unique and existing solution. They reduced the 3D Cartesian space to five DOF by neglecting the rotation around the principal axis of the X-ray source. The desired projection X-ray image can be obtained by rotating the X-ray image around the principal point in order to compensate for the missing rotation around the principal axis. However, all joints of a manipulator have limited ranges that actually restrict the working space of reaching an arbitrary poses. Our simulation experiment was performed to show that the 6-DOF C-arm model has a larger working space than the 5-DOF C-arm model for acquiring desired X-ray images by taking the physical limited joint ranges into account. For comparison, closed-form solutions for the inverse kinematics of the 5-DOF C-arm model are obtained according to [130], which satisfy the 3-DOF position and 2-DOF direction of the X-ray principal axis. For building the 6-DOF C-arm model, a general setup between the table and the C-arm was chosen such that the origin of the table coordinate system is located at the X-ray beam center of the C-arm and the $Z_0$ axis has the same direction as the $X_{\text{xray}}$ axis, and the $X_0$ axis has the opposite direction as the $Y_{\text{xray}}$ axis (see Figure 4.2(a)).

In the simulation study, *orbital_offset*, *length_offset* and the physical ranges of the five C-arm joints were set according to the Siremobile Iso-C 3D (see Table 4.4) and the geometric offsets $a_1$ and $a_2$ are zeros for this isocentric C-arm model. Please note that, singular cases were excluded in all of the simulation experiments for the closed-form solutions of the inverse kinematics.

The forward kinematics of the 6-DOF C-arm model was used to create desired poses relative to the table. The values of the five C-arm joint were chosen within their physical ranges as follows:

- vertical joint: $d_1 = i \cdot 50$ mm where $i = 0, 1, ..., 8$
- wigwag joint: $\theta_2 = \pm i \cdot 10^{\text{o}}$ where $i = 0, 1$
- horizontal joint: $d_3 = i \cdot 50$ mm where $i = 0, 1, 2, 3, 4$
- angular joint: $\theta_4 = \pm i \cdot 30^{\text{o}}$ where $i = 0, 1, 2, 3$
- orbital joint: $\theta_5 = \pm i \cdot 30^{\text{o}}$ where $i = 0, 1, ..., 6$

With the above parameters and a fixed table translation value, one experiment yields a total of 12285 generated poses. We performed nine experiments with different table translations ranging from 0 mm to 400 mm and a step size of 50 mm to generate desired poses. With this protocol all of the generated desired poses are reachable by using our 6-DOF model in practice. For each desired pose, the required five C-arm joint values were solved from the closed-form inverse kinematic solutions of the 5-DOF C-arm model (see figure 4.6). If the required movement of one joint exceeds its physical range, the desired pose is actually unreachable in practice by using the 5-DOF C-arm model. For each C-arm joint, we counted the number of cases the joint movement exceeds its physical range, and the average, standard deviation, maximum and minimum of the excess part

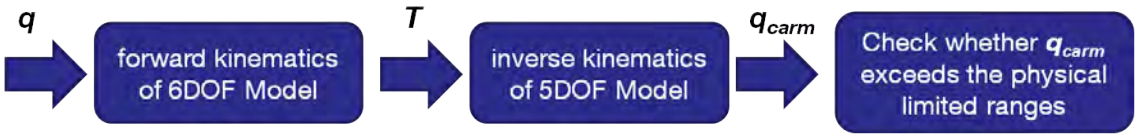


Figure 4.6: The workflow of the simulation experiment for the comparison of the 6-DOF C-arm model over the 5-DOF C-arm model. $q$ is a joint setting consisting of the six joint values. $T$ is a desired pose computed from $q$ using the 6-DOF C-arm model. $q_{carm}$ consisting of the five C-arm joint values are computed from the inverse kinematics of the 5-DOF C-arm model.

| | 0 | 50 | 100 | 150 | 200 | 250 | 300 | 350 | 400 |
|---|---|---|---|---|---|---|---|---|---|
| **wigwag (°)** | | | | | | | | | |
| mean ± std | 0 ± 0 | 1.94 ± 0.09 | 3.85 ± 0.16 | 5.73 ± 0.27 | 7.57 ± 0.35 | 6.79 ± 4.11 | 6.43 ± 4.75 | 8.24 ± 4.68 | 10.00 ± 4.61 |
| max, min | 0, 0 | 2.08, 1.81 | 4.12, 3.60 | 6.13, 5.35 | 8.10, 7.08 | 10.02, 0.12 | 11.90, 0.95 | 13.73, 2.72 | 15.51, 4.47 |
| $K$ | 0 | 4095 | 4095 | 4095 | 4095 | 5733 | 8190 | 8190 | 8190 |
| **horizontal (mm)** | | | | | | | | | |
| mean ± std | 0 ± 0 | 6.02 ± 3.75 | 12.5 ± 7.01 | 19.3 ± 10.6 | 26.6 ± 14.7 | 28.9 ± 19.5 | 39.2 ± 23.4 | 50.0 ± 29.8 | 44.7 ± 39.5 |
| max, min | 0, 0 | 9.46, 0.81 | 20.46, 3.22 | 32.96, 7.24 | 46.92, 12.85 | 62.32, 12.93 | 79.11, 18.90 | 97.24, 15.50 | 116.68, 2.42 |
| $K$ | 0 | 2457 | 2457 | 2457 | 2457 | 3276 | 3276 | 3276 | 4914 |

Table 4.5: The number of cases that joint value exceeds its physical range (denoted by $K$), and mean, standard deviation (std), maximum (max) and minimum (min) of the excess part of joint movements for each of C-arm wigwag and horizontal joints. The number of the test cases for each column (each table translation) is 12285.

of joint movements (the excess part is the difference between the required value and the closest boundary of the physical range) in each of the nine experiments. The experiment results show that all of the C-arm joint values obtained using the 5-DOF C-arm model are within the physical ranges when no table translation is involved in generating desired poses. The movements of vertical, angular and orbital joints required by the 5-DOF C-arm model do not exceed the physical ranges in all of the experiments. However, as we increase the table translation value, the number of cases that wigwag and horizontal joints exceed the physical ranges increases, and the maximum value of the excess part of wigwag and horizontal joint movements also increases (see Table 4.5). Therefore, we conclude that the 6-DOF C-arm model has a larger working space than the 5-DOF C-arm model for acquiring desired X-ray images. Interestingly, the 5-DOF C-arm kinematic model of Matthaeus et al. [130] finds a unique solution for the C-arm joints satisfying only the position (3-DOF) and direction (2-DOF) of the X-ray beam. However, this solution may result in a C-arm configuration having obstacle collision. In our C-arm model, we obtain the solution for the joints and table translation to satisfy the complete 6-DOF of the X-ray source pose. Therefore, our C-arm model produces multiple solutions and has a high probability to avoid collisions while satisfying the given position and direction of the X-ray beam.

### 4.6.2 C-arm Repositioning Experiments

Intra-operative repositioning of mobile C-arms is a common surgical task. During the intervention, the C-arm often has to be moved back to acquire the second X-ray image from the same viewing point as the first one, e.g. for the confirmation of surgical outcome. We evaluated the practicality and accuracy of our developed 6-DOF C-arm system by performing C-arm repositioning tasks.

For one repositioning experiment, the C-arm was first positioned to a random reference location in which the first X-ray image was acquired. Then, the operating table was translated randomly and the C-arm was moved to a starting position, which is a C-arm zero-joint configuration, i.e. all the five C-arm joints are set to zero. At the starting position, the 6-DOF C-arm kinematic model was built by using our proposed modeling method. After this, the required joint movements for repositioning were computed. Then, the second X-ray image was acquired after the C-arm was repositioned based on a continuous guidance on how to move each joint (including the table translation) in order to move the C-arm to the pre-defined reference position. In our experiment, the C-arm was considered to be repositioned if further required movements are below 2 mm for translational joints and 0.5° for rotational joints.

Four X-ray visible square markers that can be uniquely detected in X-ray images were randomly placed on the operating table. The four corners of each marker were extracted in X-ray images with subpixel accuracy and used to compute the image difference, which is the pixel distance between corresponding corners. Therefore, the pixel differences between the image acquired at the pre-defined position and the image acquired after repositioning are defined as errors. In addition, translational (mm) and rotational (°) errors are also calculated to quantify the accuracy of C-arm repositioning. Translational error is the Euclidean distance between reference pose and the repositioned pose. Rotational error is the average of rotational difference around the three axes. For our 6-DOF system implementation, all poses and motions estimated using the attached video camera directly corresponds to that of the C-arm X-ray projection geometry. In our experiment, the translational (mm) and rotational (°) errors of C-arm repositioning are computed based on the C-arm poses estimated from the integrated optical video camera. Alternatively, one could use an external optical tracking system to track the C-arm, similar to Mitschke's work in [223]. Here, the author shows comparable accuracy between the C-arm motions estimated using an external optical tracking system and an integrated optical camera.

We conducted ten C-arm repositioning tasks. The overall mean($\mu$) and standard deviation($\sigma$) image error is $5.2 \pm 2.6$ pixels for a total of 160 points. The maximum and minimum errors are 8.8 and 2.0 pixels. The resolution of C-arm X-ray is $800 \times 600$. As the four X-ray square markers were randomly positioned in each repositioning experiment, the image positions of the 160 points over the ten experiments were randomly chosen. Overall translational errors are: $\mu = 4.6$ mm, $\sigma = 1.5$ mm, max = 7.1 mm, and min = 2.8 mm. Overall rotational errors are $\mu = 0.37°$, $\sigma = 0.16°$, max = 0.58°, snd min = 0.20°.

In the experiment, errors were mainly due to calibration of the C-arm with the attached video camera, pose estimation, and manual movement of the C-arm. The calibration accuracy of aligning the video camera to the C-arm X-ray geometry was evaluated and quantified in the previous work [50]. The pose estimation error of using visual square

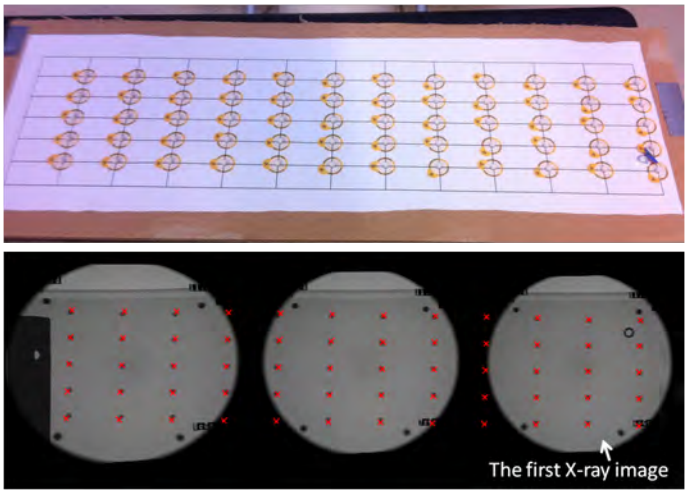


Figure 4.7: The top image shows the phantom composed of spherical X-ray markers and the bottom image is a parallax-free panorama generated by our method. The red crosses in the bottom image are the synthetic ground-truth positions of spherical X-ray markers in the panorama.

markers with the optical camera has been evaluated in [224, 225].

### 4.6.3 Parallax-free Stitching Experiments

In order to quantify the accuracy of parallax-free X-ray panoramas generated by our proposed method based on the inverse kinematics of the 6-DOF C-arm model, experiments were conducted to compute the image error of generated panoramas compared to synthetic ground-truth panoramas. Moreover, we performed metric measurements on the generated panoramas, since they are crucial for accurate determination of mechanical axis alignment and leg length. We constructed a planar phantom (440 mm long and 80 mm wide) composed of spherical X-ray markers with a known geometry (see Figure 4.7). This phantom was placed on the operating table, parallel to the marker pattern attached to the table. The physical distance between the phantom plane and the marker pattern plane was measured manually. This configuration allows metric measurements on generated panoramas [164].

In one procedure of parallax-free X-ray stitching, a parallax-free X-ray panorama of the phantom was created by combining three acquired X-ray images following the proposed protocol (see Section 4.4.4). The centroids of the spherical X-ray markers are extracted with subpixel accuracy as measured feature points in the generated panorama. A true parallax-free panorama can be treated as a single image acquired from a C-arm having an exceptional wide imaging field of view and it preserves the property of linear perspective projection. In our method, the first X-ray image defines the panorama frame. Therefore, having at least four measured feature points from the first X-ray image, the rotation $R$ and the translation $t$ from the phantom to the X-ray source can be estimated based on 2D-3D point correspondences. Having a known intrinsic parameter $K$ from the system calibration, a perspective projection matrix $P$ projecting 3D points of the phantom to 2D

| | #1 | #2 | #3 | #4 | #5 | overall |
|---|---|---|---|---|---|---|
| image errors | | | | | | |
| mean ± std (pixels) | 4.8 ± 2.7 | 3.6±2.8 | 4.9 ± 2.4 | 4.3 ± 2.1 | 3.8 ± 3.0 | 4.3 ± 2.6 |
| # X-ray markers | 33 | 32 | 35 | 35 | 33 | 168 |
| measurement errors for distances with actual value of 360 mm | | | | | | |
| mean ± std (mm) | 2.22 ± 0.74 | 1.98 ± 0.56 | 2.24 ± 0.76 | 1.96 ± 0.74 | 1.88 ± 0.70 | 2.06 ± 0.66 |
| measurement errors for angles with actual value of 90° | | | | | | |
| mean ± std (°) | 0.60 ± 0.42 | 0.60 ± 0.32 | 0.62 ± 0.35 | 0.54 ± 0.34 | 0.52 ± 0.37 | 0.58 ± 0.33 |

Table 4.6: The image errors (pixels) and the metric measurement errors (mm or °) on the five parallax-free panoramas generated by our method.

Figure 4.8: A parallax-free panoramic X-ray images of a dry femoral bone.

points in the panorama was computed as $P = K[R|t]$. Then, we project all spherical X-ray markers of the phantom from the 3D space onto the 2D panorama frame by $P$ in order to build a synthetic ground-truth panorama. We compute the image error of the generated panorama as image distances between the measured feature points and their corresponding ground-truth positions. The feature points within the first X-ray image were excluded from image error analysis, since they were used to create the synthetic ground-truth. Figure 4.7 shows one generated parallax-free panorama, in which the red crosses indicate the synthetic ground-truth positions of the X-ray markers in the panorama. Moreover, we conducted metric measurements. The distance is defined by two points in the image, three points for an angle. We measured the five different distances or angles with the actual value of 360 mm or 90° respectively on the generated panorama.

Parallax-free panorama imaging was performed 5 times and Table 4.6 shows the experiment results in terms of the image error and the metric measurement error for each experiment and for all the experiments. The overall image error is $4.3 \pm 2.6$ pixels based on a total of 168 markers. One individual C-arm X-ray image has the resolution of $800 \times 600$, so the relative image error is less than 1%. The overall metric measurement errors are $2.06 \pm 0.66$ mm for distances and $0.58 \pm 0.33°$ for angles. Thus, the relative error of metric measurements is also less than 1%. Once again for this system setup, errors were mainly due to calibration of the C-arm with the attached video camera, pose estimation, and manual movement of the C-arm.

Surgeons need to verify the alignment of the femoral mechanical axis and tibial mechanical axis in order to achieve a good weight-bearing load in long bone surgeries, e.g. high tibial osteotomy (HTO) [226] and total knee arthroplasty (TKA) [227]. The mechanical axis of the femur (or tibia) is determined by two geometrical points located at the two ends of the bone [228]. Figure 4.8 demonstrates a parallax-free panoramic X-ray image of a dry femoral bone generated by stitching two X-ray images using the proposed parallax-free stitching solution. The panoramic image shows the two ends of the bone in one common coordinate system, which can facilitate the determination of the mechanical axis of the long bone. This will reduce radiation exposure to both surgeons and patients for the intra-operative evaluation of the mechanical axis alignment, since no additional X-ray images showing the bone structure between the two ends of the bone are required. Note that, this example is an extreme case, in which the position of the additional X-ray image is located relatively far away from the first one. This situation could introduce a little difficulty in defining an exact optimal position of the additional X-ray image showing the condyle. If this second X-ray image does not show the complete condyle, the surgeon can easily find an optimal position of the 3rd X-ray image, as the bone structure of the second image is very close to the condyle. This is however more efficient than the previous proposed solution [164] of adjusting the movements of the five C-arm joints and table to see the position of an additional X-ray image in the panorama through a trial and error procedure. We have performed another two examples of parallax-free panoramic imaging for a plastic lumbar and sacrum and for the right half of a plastic pelvis. In these cases, our solution can efficiently facilitate the generation of a panoramic image showing the complete structure of the lumbar and sacrum (see Figure 4.9) or the right half of the pelvis (see Figure 4.10) with minimized overlapping area between the individual C-arm images.

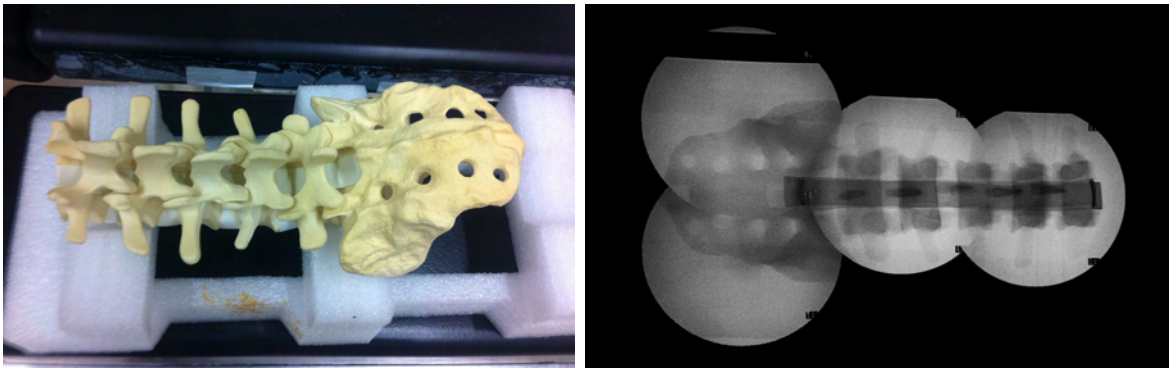

(a) (b)

Figure 4.9: (a) A plastic lumbar and sacrum; (b) A parallax-free panoramic X-ray image of the plastic lumbar and sacrum.

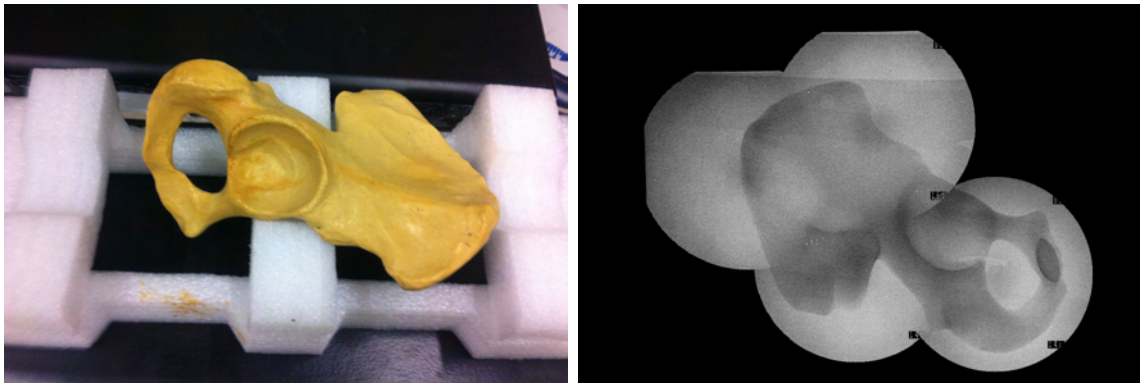

(a) (b)

Figure 4.10: (a) The right half of a plastic pelvis; (b) A parallax-free panoramic X-ray image of the right half of a plastic pelvis.

## 4.7 Discussion and Conclusion

Moving the mobile C-arm into a desired viewing position in regard to the anatomy is not only a common surgical task, but also an indispensable step for advanced X-ray imaging techniques. Standard mobile C-arms have only five DOF, which definitely restricts their motions that have six DOF in 3D Cartesian space. In this chapter, we proposed to build a 6-DOF C-arm X-ray imaging model by integrating a translational movement of the patient's table with the 5-DOF C-arm kinematics. We presented a method to develop the kinematic chain for the 6-DOF C-arm model without constraints on the initial setup of the table position. Positioning the X-ray source at a desired pose relative to the operating table with six DOF requires finding the six joint values, which is the inverse kinematics problem for the 6-DOF C-arm model. We have derived the closed-form solutions for the inverse kinematics problem. Our modeling method and the closed-form inverse kinematics solutions can be applied to general mobile C-arms, i.e. isocentric or non-isocentric.

Standard mobile C-arms have wheels and are moved in and out of the operating room frequently. In clinical practice, before the acquisition of an image the wheels are locked in order to fix the C-arm base. It is very rare to move the C-arm base because the C-arm machine is both bulky and heavy to adjust for, at numerous occasions, during the course of the surgery. Thus, the X-ray image is acquired by positioning the C-arm using the 5 available C-arm joints. Furthermore, only these 5 C-arm joints are motor controlled in commercial mobile motorized C-arms. All standard mobile C-arms are modeled with 5-DOF, as assumed in Matthaeus et al. [130], for their proposed inverse kinematic solution.

Typical motorized mobile C-arms only can be repositioned back relative to its own base. In clinical practice, the C-arm machine is often moved in and out of the surgical site, and thus repositioning relative to the C-arm base does not guarantee it is repositioned relative to the operating table. Integrated kinematic modeling of the C-arm and table enables the C-arm to be repositioned back relative to the table, as soon as the C-arm is next to the operating table, i.e. the computed table translation can compensate for the displacement of the C-arm base. This is one of the advantages of the 6-DOF C-arm

model.

Closed-form solutions usually do not exist for the inverse kinematics of the 5-DOF C-arm model, since it is an over-constrained system, i.e. computing five unknowns for six non-linear equations. However, if any of the six parameters for specifying an end-effector's pose is not maintained, then the desired pose of the end-effector is reduced to 5-DOF. Obviously, closed-form solutions for the inverse kinematics exist in this situation depending on which DOF is not satisfied. For solving the inverse kinematics of the 5-DOF C-arm, Matthaeus et al. [130] proposed to make the rotation around the principal axis of the X-ray source unconstrained, i.e. only satisfying the 2-DOF direction of the principal axis instead of a 3-DOF orientation. The desired projection X-ray image can be obtained by rotating the X-ray image around its principal point in order to compensate for the missing rotation. In this way, they reduce the 3D Cartesian space to five DOF and obtain the complete closed-form solutions of joint parameters for imaging a given point from a given direction. In this work, we build the 6-DOF C-arm model upon the 5-DOF C-arm model of Matthaeus et al. [130] by considering operating table translation and derive the complete closed-form solutions for the 6-DOF C-arm inverse kinematics. Our simulation experiment showed that the 6-DOF C-arm model has a larger working space than the 5-DOF C-arm model for acquiring desired X-ray images by taking the physical limited joint ranges into account. The larger working space also increases the possibility of avoiding obstacles.

Our experimental system provides continuous feedback on required movement of each joint (including the table translation) for moving the C-arm and table to a target position. For this, we attach a video camera to the C-arm for radiation-free pose estimation and solve the closed-form inverse kinematics for each estimated C-arm pose. We note that, X-ray marker based C-arm pose estimation methods or external tracking systems can also be employed for implementation of such systems. Since our C-arm and table system is manually controlled, our medical partners who performed the experiments have complained that it took a larger effort and additional time to move the joint within 1 mm or 0.3°, for example. Therefore, in our experimental setup, we choose the threshold of 2 mm and 0.5°, within which the C-arm is considered to be at the target position, and found that the results are acceptable. If a robotic system is available, the chosen thresholds would be equal to the minimum step of the C-arm and table joint movements depending on their mechanical and manufactured constraints.

The C-arm repositioning task was chosen to evaluate the practicality and accuracy of our developed 6-DOF C-arm system. The pixel difference between the image acquired at the pre-defined position and the image acquired after repositioning is $5.3 \pm 2.4$ pixels. The experimental results for the inverse kinematic based X-ray image stitching demonstrate that parallax-free panoramas generated by our method are within clinical tolerances for accurate evaluation of long bone geometry (i.e. image and metric measurement errors are less than 1% compared to ground-truth).

Currently, surgeons place additional efforts into manually moving the table and C-arm joints. However, motorized operating tables are available in most operating rooms and their forward-backward translation can be easily executed through a mechanical motor. An implementation of the robotized mobile C-arm system has been presented in [130].

Furthermore, one could easily apply our solution to an expensive robotic C-arm and table system for automated C-arm positioning.

Some modern motorized operating tables can have multiple DOFs, even rotational DOFs, e.g. tilting. The current work opens the path for researchers to further model an operating table having multiple DOFs and the mobile C-arm kinematics as a coupled multi-manipulator system. The closed-form solution for the inverse kinematics of such a coupled multi-manipulator system is challenging, since we need to find the complete solution to an underdetermined system of nonlinear equations.

We believe that the presented 6-DOF C-arm model with the closed-form solutions for its inverse kinematics paves the way for advanced applications in the fields of surgical navigation and advanced X-ray imaging that require C-arms to be precisely positioned or repositioned relative to the patient's table. Particularly in this work, we developed a novel and intuitive solution for parallax-free X-ray image stitching based on the inverse kinematics of 6-DOF C-arm model. This method does not require any overlap between X-ray images in the panorama, which reduces radiation. With the proposed solution, surgeons start by indicating where they want to see the additional interested anatomic structure in the panorama image. Our solution computes the position and orientation of the C-arm pose, and provides the required C-arm joints movements and table translation. For the surgeons who are quite familiar with anatomical structure, it is much easier to define the location of the imaging field in the panorama than the previous solution [164] of moving the bulky C-arm and guessing which movements of C-arm joints that could result in appropriate location of the viewing field. Having the robotic C-arm system, parallax-free X-ray image stitching only requires surgeons to specify the position of X-ray images in panorama. This definitely facilitates and speeds up interventional parallax-free panoramic X-ray imaging procedures. For future clinical applications, we will investigate integrating a 6-DOF C-arm kinematic model to enable the smooth transition of the CT-based pre-operative planning into the operating room, by accurately positioning the patient's table with regard to the X-ray C-arm.

This paragraph summarizes the contributions in the chapter. I have proposed the method to model both the mobile C-arm and patient's table as an integrated kinematic chain having six DOF. The forward kinematic formula of the 6DOF C-arm was developed according to the DH rule. The kinematic singularity of the 6-DOF C-arm was analyzed. The closed-form solution for its inverse kinematics was derived in order to obtain the required values for all C-arm joint and table movements to position the fluoroscope at a desired pose. The modeling method and the closed-form solutions can be applied to general isocentric or non-isocentric mobile C-arms. In addition, I have developed the inverse kinematics based method of parallax-free panoramic X-ray imaging and further proposed a clinical protocol for the panoramic imaging. The 6DOF C-arm system is implemented based on the CamC system. In contrast to the traditional optical tracking systems that could increase system complexity and introduce considerable investment, the developed 6-DOF C-arm system is low-cost, low-radiation and easy-setup thanks to the co-registered X-ray and video images of the CamC technology. Finally, the experiments were conducted in a close collaboration with our clinical partners to evaluate the developed 6-DOF C-arm system and the inverse kinematics based parallax-free panoramic X-ray

imaging.

CHAPTER

# FIVE

# DISCUSSION AND CONCLUSION

This chapter discusses the current challenges and potential impact of the video augmented X-ray imaging (i.e. CamC technology) on various advanced intra-operative imaging and surgical navigation applications. The chapter is concluded by the contributions and achievements made in the dissertation.

## 5.1 Impact of Video Augmented X-ray on IGOS: Outlook

Mobile C-arm is a primary imaging device used during orthopedic and trauma surgery to acquire X-ray images of bone structures. Optical tracking technology is commonly employed as an intra-operative navigation technique in order to align medical images, patient, implants and medical instruments. This facilitates the procedures and improves the quality of surgical outcomes. Many studies show the improved accuracy and reduced radiation exposure when using navigation systems for various orthopedic procedures. However, challenges arise when using these navigation technologies such as complex system set-ups. These include: on-site system calibration, additional devices inside an already crowded OR, cable spaghetti and the requirement of line of sight. Consequently, they impose radical changes to the surgical setup and overall procedure. Furthermore, a considerable financial investment is needed for these navigation systems, which makes them less accessible to clinics already experiencing limited budgets.

The CamC system that augments a standard C-arm by a video camera provides video augmented X-ray images to guide surgical procedures by aligning X-ray images, treated anatomy, implants and instruments in a common video image frame. It is important to understand that the CamC system can be operated as a standard C-arm device. No additional calibration, device, or even cable are required during the operation. For that reason, the CamC system can be smoothly integrated into the surgical workflow with much lower cost. This makes CamC the first medical AR technology consistently used in the OR worldwide. Over 40 patients have been successfully treated under CamC navigation between July 2009 and March 2010. Several clinical applications that can directly benefit

from AR imaging of the CamC system have been discovered, such as incision, entry point localization, instrument axis alignment, K-wire guidance, and surgery documentation.

IGOS solutions often consist of three components: imaging, information fusion, and user-system interaction. The inherent property of aligned X-ray and optical imaging enables the CamC system to be a low-cost platform technology for potential intra-operative advanced imaging, information fusion, and user-system interaction solutions.

The CamC system offers a video augmented X-ray imaging by combining two image modalities: X-ray images showing the internal bone structures or implants and optical (visible light) images displaying the external skin or medical instruments. In orthopedic surgeries, many X-ray images are acquired in order to guide surgeons with correct C-arm, implant and instrument placement. Having the CamC system, the optical video images can be used to guide such placements. However, sparing healthy tissue, nerves and different vasculatures that are invisible in both X-ray and optical (visible light) images are tricky components for interventional procedures. For example in spinal surgeries, injection via needle under C-arm X-ray fluoroscopy guidance is a common treatment for vertebroplasty. The risks for it could be: (i) needle insertion may encounter segmental vessels from deep or ascending cervical arteries, (ii) important vascular may be damaged to spinal cord if perforated, or even (iii) potential lung collapse and nerve injury. In vivo fluorescence imaging (see figure 5.1(a)) has the tremendous potential for: (i) early cancer diagnostics, (ii) identification of tumor boundaries, (iii) assessment of blood vessels, (iv) visualization of lymph vessels, and (v) treatment response assessments [229]. Several near-infrared (NIR) fluorescence imaging systems [230, 231] have been developed for real-time interventional imaging applications, improving tumor delineation, sentinel lymph node visualization, and vascular mapping to name a few.

Future work of CamC imaging: integrating fluorescence imaging into the system in order to provide co-registered X-ray, optical (visible) and fluorescence images for merging anatomical, functional or vascular contrast [232]. This superior imaging can enable orthopedic and trauma surgeons to minimize healthy tissue and vessel damage when using tools near areas of high vasculature and functional anatomy, as well as to facilitate and quicken surgery. Figure 5.1(b) shows a mimic overlay of X-ray, optical (visible light) and fluorescence image. Fluorescence imaging can be achieved by combining color CCD cameras and multiple-bandpass filters that transmit light in several different discrete narrow spectral bands, e.g. quadruplebandpass filters (QBPF) [233].

Fusion of surgical information is a critical component for modern IGOS. For this, computer based registration and tracking technologies are often applied to align medical images, treated anatomy and locations of instruments or implants in a common coordinate system. However, intra-operative registration or tracking solutions often require calibration and additional procedures and devices during intervention. The CamC technology inherently by construction relates internal bone structures, implants, skin and surgical tools in the common video image coordinate frame.

The CamC system can track the X-ray source without further calibration, tracking devices, or radiation exposure, when compared to other external tracking devices, thereby improving surgical workflow for orthopedic and trauma surgeries in the future. This is currently achieved using the video camera and a planar visual marker pattern. The two

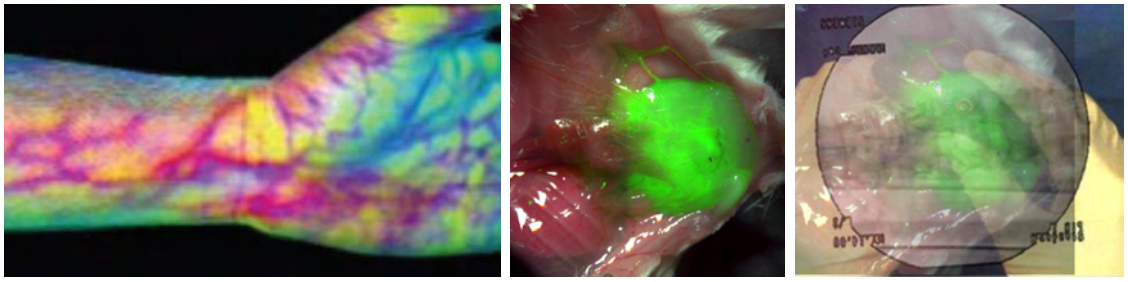

(a) (b)

Figure 5.1: (a) Multispectral fluorescence imaging would allow the augmentation of vessel structures or possible diseases (i.e. tumors). (b) A mimic sample image overlay (right) between VAX and a fluorescence image (left).

developed intra-operative X-ray imaging solutions in this dissertation, parallax-free X-ray stitching and inverse kinematics based C-arm positioning, are implemented based on C-arm pose estimation using the CamC system. However, using a planar visual marker pattern for pose estimation has several limitations. Placing the marker pattern above the patient is not practical and can occlude the surgeon's view onto the operation situs. Thus, the marker pattern is attached under the operating table and C-arm X-ray source is below the table for the implementation of parallax-free X-ray stitching. Consequently, the CamC system loses the ability for optical view on patients. Furthermore, a planar pattern restricts the viewing angle of the camera. A flexible setup of multiple randomly distributed markers that are not necessarily on the same plane, would be preferable for tracking. Unlike the marker pattern where relationships between all markers are exactly known and are expressed in a consistent coordinate frame, the markers must be calibrated for their relative poses in order to form a single coordinate system for all the markers. Our proposed method to estimate the relative poses between multiple randomly positioned square markers [234] can be adopted for it.

Furthermore, the attached video camera can act as an integrated sensor to detect or track tools, patient movements, and etc. The detected or tracked tools can be related to X-ray images without further registration procedures. This paves the way for building surgical navigation applications on the CamC technology. One potential application is integrating ultrasound images to the X-ray and video image overlay by tracking an ultrasound probe using the video camera. Another potential application is tracking the insertion of a linear tool using the video images. Thanks to the CamC system, the estimated linear tool can be directly visualized in the X-ray image. One idea is to use the property of cross ratio to estimate the tip from three collinear markers attached on the tool. This can definitely further improve the CamC guidance for placing linear tools such as K-wire insertion 5.2(a)and drill tip placement 5.2(b). A similar idea for tracking a linear tool has been proposed in [149]. In their implementation, the markers attached on one side of the tool thereby creating blind areas where the attached markers are not seen by the video camera. A smarter design for attaching markers such that no blind areas are created must be investigated.

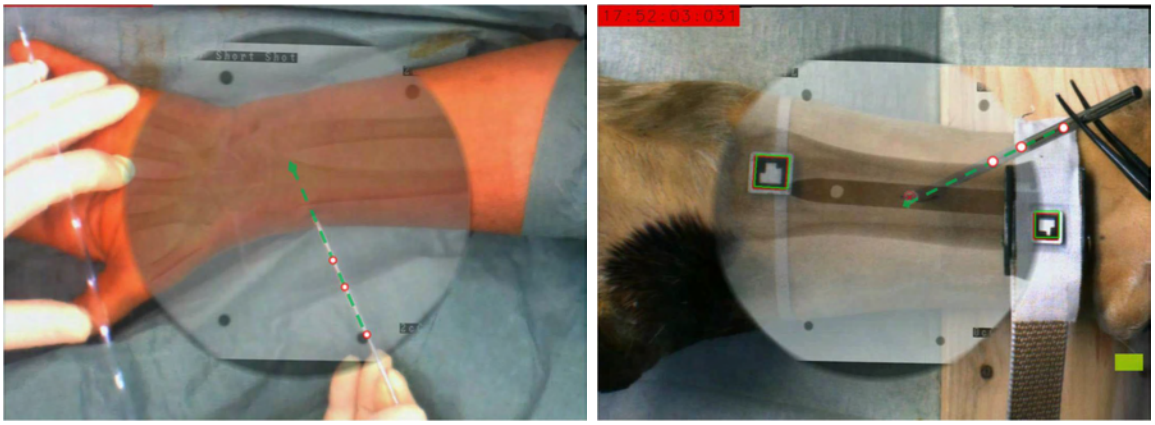

(a) (b)

Figure 5.2: The mimic examples of using the cross ratio to track the insertion of a linear tool into patients.

IGS systems often require user interactions to be fully advantageous. The traditional keyboard-mouse solution cannot be deployed in the OR for obvious reasons such as sterilization concerns and lack of space in an already crowded environment. Several strategies have been discussed in section 1.2.3.2 for the user interaction including touch screens, foot switches, tracked virtual keypads, speech recognition, visual marker detection, and gesture recognition. All these methods listed above would require additional sensors, and the attached video camera of the CamC system has the the potential to play this role for sensory recognition of user commands.

A possible idea for user interaction of the CamC system is hand gesture recognition using the video images. A hand gesture recognition based interaction is implemented for video see-through HMD based medical AR applications [91]. The video cameras of the HMD are used to detect hands and recognize gestures. However, it is difficult for surgeons to pose an appropriate hand gesture in stressful situations, which could lead to false-positive and positive-false recognition and thus reduces the robustness of gesture recognition. Another idea is employing visual fiducial markers. The visibility of the visual markers in the video images can be used as a binary input. Moreover, the visual markers' movements estimated by the video camera provide continuous parameters.

Online analysis of surgical workflow can support many promising applications, such as adaptive user interfaces, context-aware surgery rooms, better synchronization within the surgery department and automatic documentation. Padoy et al. [235] propose a method based on dynamic time warping and hidden markov models for the modeling, offline segmentation and online recognition of surgical phases. Real time signals or information of the conducted surgery are mandatory for analyzing surgical workflow intra-operatively. Blum et al. [236] use laparoscopic video as source information for modeling workflow and detecting surgical phases. Ahmadi et al. [237] introduce wearable accelerometers attached to surgeons to detect the surgical activities. Padoy et al. [238] employ 3D motion features reconstructed from multiple cameras mounted on the ceiling of the OR to

monitor workflow. The optical video camera of the CamC system could be an ideal sensor for workflow analysis, as it directly records the operation site and is seamlessly integrated into the C-arm system. This requires the analysis of human activities from videos. To achieve it, several works in the field of computer vision may be adapted as a starting point, such as recognition of human actions [239], recognizing complex and multitasked activities from video [240]; activities analysis [241].

For challenging medical procedures, the video image of the CamC system provides an ideal view for an expert surgeon to consult intra-operatively from a remote location.

## 5.2 Conclusion

The methods and techniques proposed in this dissertation offer great potential in shaping the operating room of the future specifically for orthopedic and trauma procedures. A workflow based methodology is proposed for assessing the clinical performance of novel IGS solutions. This methodology is applied to evaluate the clinical impact of the CamC system on animal cadavers. A novel method for intra-operative parallax-free panoramic X-ray imaging without requirements of a fronto-parallel setup or any overlap between the acquired X-ray images is developed. This is a promising technology to support various intra-operative clinical applications, e.g. determining the extremity length and mechanical axis of long bones online during surgeries. The developed inverse kinematics for the integrated C-arm and table setup paves the way for advanced applications in the fields of surgical navigation and advanced X-ray imaging that require C-arms to be precisely positioned or repositioned relative to the patient's table. Lastly, the current challenges and potential impact of the video augmented X-ray imaging on IGOS have been discussed.

APPENDIX

# A

# ABBREVATIONS

| | |
|---|---|
| IGS | Image Guided Surgery |
| CAS | Computer Assisted (or Aided) Surgery |
| IGOS | Image Guided Orthopedic Surgery |
| DRO | Dynamic Reference Object |
| ICP | Iterative Closest Point |
| CT | Computed Tomography |
| MRI | Magnetic Resonance Imaging |
| PET | Positron Emission Tomography |
| US | Ultrasonography |
| HMD | Head Mounted Display |
| LED | Light Emitting Diode |
| DVR | Direct Volume Rendering |
| MIP | Maximum Intensity Projection |
| TEE | Transesophageal Echocardiography |
| IXPV | Interactive X-ray Perceptual Visualization |
| AR | Augmented Reality |
| CamC | Camera Augmented Mobile C-arm |
| VAX | Video Augmented X-ray |
| DRR | Digitally Reconstructed Radiograph |
| DAP | Dose-Area Product |
| CF | Conventional Fluoroscopy |
| OR | Operating Room |
| HDR | High Dynamic Range |
| DLT | Direct Linear Transform |
| RMS | Residual Mean Square |
| STD | standard deviation |
| VDP | Virtual Detector Plane |
| DOF | Degree of Freedom |
| DH | Denavit-Hartenberg |
| SVD | Singular Value Decomposition |

| | |
|---|---|
| OBB | Oriented Bounding Box |
| HTO | High Tibial Osteotomy |
| TKA | Total Knee Arthroplasty |
| NIR | Near Infrared |
| QBPF | Quadruplebandpass Filters |

APPENDIX

# B

# AUTHORED AND CO-AUTHORED PUBLICATIONS


1. J. Wang, P. Fallavollita, L. Wang, M. Kreiser, and N. Navab, "Augmented reality during angiography: Integration of a virtual mirror for improved 2d/3d visualization," 2012. accepted at ISMAR 2012

2. A. Aichert, M. Wieczorek, J. Wang, L. Wang, M. Kreiser, P. Fallavollita, and N. Navab, "The colored x-rays," in *MICCAI 2012 Workshop on Augmented Environments for Computer-Assisted Interventions*, 2012

3. L. Wang, P. Fallavollita, A. Brand, O. Erat, S. Weidert, P.-H. Thaller, E. Euler, and N. Navab, "Intra-op measurement of the mechanical axis deviation: An evaluation study on 19 human cadaver legs," in *Medical Image Computing and Computer-Assisted Intervention – MICCAI 2012*, vol. 7511 of *LNCS*, pp. 609–616, 2012

4. B. Diotte, P. Fallavollita, L. Wang, S. Weidert, P.-H. Thaller, E. Euler, and N. Navab, "Radiation-free drill guidance in interlocking of intramedullary nails," in *Medical Image Computing and Computer-Assisted Intervention – MICCAI 2012*, vol. 7510 of *LNCS*, pp. 18–25, 2012

5. A. Brand, L. Wang, P. Fallavollita, P. Sandner, N. Navab, P. Thaller, E. Euler, and S. Weidert, "X-ray stitching for intra-operative mechanical axis determination of the lower extremity," in *the 12th Annual Meeting of the International Society for Computer Assisted Orthopaedic Surgery*, June 2012

6. N. Navab, T. Blum, L. Wang, A. Okur, and T. Wendler, "First deployments of augmented reality in operating rooms," *Computer*, vol. 45, pp. 48 –55, July 2012

7. S. Weidert, L. Wang, A. von der Heide, E. Euler, and N. Navab, "Intraoperative augmented-reality-visualisierung: Aktueller stand der entwicklung und erste erfahrungen mit dem camc," *Unfallchirurg*, vol. 115, Mar. 2012

8. L. Wang, P. Fallavollita, R. Zou, X. Chen, S. Weidert, and N. Navab, "Closed-form inverse kinematics for interventional c-arm x-ray imaging with six degrees of

freedom: modeling and application," *IEEE transactions on medical imaging*, vol. 31, pp. 1086–1099, May 2012

9. X. Chen, L. Wang, P. Fallavollita, and N. Navab, "Precise x-ray and video overlay for augmented reality fluoroscopy," *International journal of computer assisted radiology and surgery*, May 2012

10. X. Chen, L. Wang, P. Fallavollita, and N. Navab, "Error analysis of the x-ray projection geometry of camera-augmented mobile c-arm," in *SPIE Medical Imaging*, Feb. 2012

11. S. Demirci, A. Bigdelou, L. Wang, C. Wachinger, M. Baust, R. Tibrewal, R. Ghotbi, H. Eckstein, and N. Navab, "3d stent recovery from one x-ray projection," in *Medical Image Computing and Computer-Assisted Intervention – MICCAI 2011*, vol. 6891 of *LNCS*, pp. 178–185, 2011

12. M. Wieczorek, A. Aichert, P. Fallavollita, O. Kutter, A. Ahmadi, L. Wang, and N. Navab, "Interactive 3D visualization of a single-view X-Ray image," in *Medical Image Computing and Computer-Assisted Intervention – MICCAI 2011*, vol. 6891 of *LNCS*, pp. 73–80, 2011

13. L. Wang, R. Zou, S. Weidert, J. Landes, E. Euler, D. Burschka, and N. Navab, "Closed-form inverse kinematics for intra-operative mobile C-arm positioning with six degrees of freedom," in *Proceedings of SPIE*, vol. 7964, pp. 79641A–79641A–6, Mar. 2011

14. S. Weidert, L. Wang, P. Thaller, J. Landes, A. Brand, N. Navab, and E. Euler, "X-ray stitching for intra-operative mechanical axis determination of the lower extremity," in *the 11th Annual Meeting of the International Society for Computer Assisted Orthopaedic Surgery*, June 2011

15. L. Wang, M. Springer, T. H. Heibel, and N. Navab, "Floyd-warshall all-pair shortest path for accurate multi-marker calibration," in *ISMAR*, pp. 277–278, IEEE, 2010

16. L. Wang, J. Traub, S. Weidert, S. M. Heining, E. Euler, and N. Navab, "Parallax-free intra-operative X-ray image stitching," *Medical Image Analysis*, vol. 14, pp. 674–686, June 2010

17. L. Wang, J. Landes, S. Weidert, T. Blum, A. Von Der Heide, E. Euler, and N. Navab, "First animal cadaver study for interlocking of intramedullary nails under camera augmented mobile c-arm: a surgical workflow based preclinical evaluation," in *Proceedings of the First international conference on Information processing in computer-assisted interventions*, vol. 6135 of *LNCS*, pp. 56–66, Springer-Verlag, 2010

18. S. Weidert, L. Wang, J. Landes, A. von der Heide, N. Navab, and E. Euler, "Long bone x-ray image stitching using c-arm motion estimation," in *The 3rd Hamlyn Symposium for Medical Robotics*, May 2010

19. L. Wang, R. Zou, S. Weidert, J. Landes, E. Euler, D. Burschka, and N. Navab, "Modeling kinematics of mobile C-arm and operating table as an integrated six degrees of freedom imaging system," in *The 5th International Workshop on Medical Imaging and Augmented Reality – MIAR 2010*, vol. 6326 of *LNCS*, (Beijing, China), pp. 485–493, 2010

20. P. Dressel, L. Wang, O. Kutter, J. Traub, S. Heining, and N. Navab, "Intraoperative positioning of mobile C-arms using artificial fluoroscopy," in *Proceedings of SPIE*, vol. 7625, pp. 762506–762506–6, Mar. 2010

21. L. Wang, J. Traub, S. Weidert, S. M. Heining, E. Euler, and N. Navab, "Parallax-Free Long Bone X-ray Image Stitching," in *Medical Image Computing and Computer-Assisted Intervention – MICCAI 2009*, vol. 5761 of *LNCS*, (London, UK), pp. 173–180, 2009

22. L. Wang, J. Traub, S. M. Heining, S. Benhimane, E. Euler, R. Graumann, and N. Navab, "Long bone x-ray image stitching using c-arm motion estimation," in *Bildverarbeitung für die Medizin 2009* (H. Meinzer, T. M. Deserno, H. Handels, and T. Tolxdorff, eds.), pp. 202–206, Springer Berlin Heidelberg, 2009

23. L. Wang, S. Weidert, J. Traub, S. M. Heining, C. Riquarts, E. Euler, and N. Navab, "Camera augmented mobile c-arm," in *Bildverarbeitung für die Medizin 2009* (H. Meinzer, T. M. Deserno, H. Handels, and T. Tolxdorff, eds.), pp. 97–101, Springer Berlin Heidelberg, 2009

24. J. Traub, S.-A. Ahmadi, N. Padoy, L. Wang, S. M. Heining, E. Euler, P. Jannin, and N. Navab, "Workflow based assessment of the camera augmented mobile c-arm system," in *AMIARCS*, MICCAI Society, Sept. 2008

25. L. Wang, J. Traub, S. M. Heining, S. Benhimane, E. Euler, R. Graumann, and N. Navab, "Long bone x-ray image stitching using camera augmented mobile c-arm," in *Medical Image Computing and Computer-Assisted Intervention – MICCAI 2008*, vol. 5242 of *LNCS*, 2008

# LIST OF FIGURES

# REFERENCES


[1] I. V. Ponseti, "History of orthopaedic surgery," *The Iowa Orthopaedic Journal*, vol. 11, pp. 59–64, 1991.

[2] "Health grades inc.@ONLINE." http://www.wrongdiagnosis.com, Oct. 2011.

[3] "Becker's orthopedic & spine review @ONLINE." http://www.beckersorthopedicandspine.com/lists-and-statistics/, Oct. 2011.

[4] H. J. W. Dam, "The new marvel in photography," *McClure's Magazine*, vol. 6, pp. 403–414, 1986.

[5] S. Webb, *The Physics Of Medical Imaging*. Taylor & Francis Group, Jan. 1988.

[6] M. L. Apuzzo and J. K. Sabshin, "Computed tomographic guidance stereotaxis in the management of intracranial mass lesions," *Neurosurgery*, vol. 12, pp. 277–285, Mar. 1983.

[7] G. H. Barnett, D. W. Kormos, C. P. Steiner, and J. Weisenberger, "Use of a frameless, armless stereotactic wand for brain tumor localization with two-dimensional and three-dimensional neuroimaging," *Neurosurgery*, vol. 33, pp. 674–678, Oct. 1993.

[8] P. L. Gildenberg, H. H. Kaufman, and K. S. Murthy, "Calculation of stereotactic coordinates from the computed tomographic scan," *Neurosurgery*, vol. 10, pp. 580–586, May 1982.

[9] K. K. Tan, R. Grzeszczuk, D. N. Levin, C. A. Pelizzari, G. T. Chen, R. K. Erickson, D. Johnson, and G. J. Dohrmann, "A frameless stereotactic approach to neurosurgical planning based on retrospective patient-image registration. technical note," *Journal of Neurosurgery*, vol. 79, pp. 296–303, Aug. 1993.

[10] E. Watanabe, T. Watanabe, S. Manaka, Y. Mayanagi, and K. Takakura, "Three-dimensional digitizer (neuronavigator): new equipment for computed tomography-guided stereotaxic surgery," *Surgical Neurology*, vol. 27, pp. 543–547, June 1987.

[11] L. P. Nolte, L. J. Zamorano, Z. Jiang, Q. Wang, F. Langlotz, and U. Berlemann, "Image-guided insertion of transpedicular screws. a laboratory set-up," *Spine*, vol. 20, pp. 497–500, Feb. 1995.

[12] Z. Yaniv and K. Cleary, "Image-guided procedures: A review," tech. rep., Imaging Science and Information Systems Center, Georgetown University, 2007.

[13] J. Galloway, R L, "The process and development of image-guided procedures," *Annual Review of Biomedical Engineering*, vol. 3, pp. 83–108, 2001.

[14] T. M. Peters, "Image-guided surgery: from x-rays to virtual reality," *Computer Methods in Biomechanics and Biomedical Engineering*, vol. 4, no. 1, pp. 27–57, 2000.

[15] L. Joskowicz and R. Taylor, "Computers in imaging and guided surgery," *Computing in Science & Engineering*, vol. 3, no. 5, pp. 65–72, 2001.

[16] T. Peters and K. Cleary, *Image-Guided Interventions: Technology and Applications*. Springer, 1 ed., May 2008.

[17] M. D. Murphey, "Imaging aspects of new techniques in orthopedic surgery," *Radiologic Clinics of North America*, vol. 32, pp. 201–225, Mar. 1994.

[18] F. Langlotz, "State-of-the-art in orthopaedic surgical navigation with a focus on medical image modalities," *The Journal of Visualization and Computer Animation*, vol. 13, no. 1, pp. 77–83, 2002.

[19] J. B. Stiehl, W. H. Konermann, R. G. Haaker, and A. DiGioia, *Navigation and MIS in Orthopedic Surgery*. Springer, 1 ed., Dec. 2006.

[20] N. W. L. Schep, I. A. M. J. Broeders, and C. van der Werken, "Computer assisted orthopaedic and trauma surgery. state of the art and future perspectives," *Injury*, vol. 34, pp. 299–306, May 2003.

[21] F. Langlotz and L. Nolte, "Technical approaches to Computer-Assisted orthopedic surgery," *European Journal of Trauma*, vol. 30, no. 1, pp. 1–11, 2004.

[22] G. Zheng and L. Nolte, "Technical principles of computer assisted orthopaedic surgery," *Bone*, pp. 135–147, 2008.

[23] L. P. Nolte and T. Beutler, "Basic principles of CAOS," *Injury*, vol. 35 Suppl 1, pp. S–A6–16, June 2004.

[24] D. M. Kahler, "Image guidance: fluoroscopic navigation," *Clinical Orthopaedics and Related Research*, pp. 70–76, Apr. 2004.

[25] J. M. Sikorski and S. Chauhan, "Computer-assisted orthopaedic surgery: do we need CAOS?," *The Journal of Bone and Joint Surgery. British Volume*, vol. 85, pp. 319–323, Apr. 2003.

[26] A. B. Wolbarst and W. R. Hendee, "Evolving and experimental technologies in medical imaging," *Radiology*, vol. 238, pp. 16–39, Jan. 2006.

[27] National Radiological Protection Board, *Estimates of Radiation Detriment in a UK Population (NRPB Report 260)*, 1994.

[28] National Research Council, *Health Effects of Exposure to Low Levels of Ionizing Radiation: BEIR V*, 1990.

[29] International Commission on Radiological Protection, *Recommendations of the International Commission on Radiological Protection. ICRP Publication 60*, 1990.

[30] T. Stübig, D. Kendoff, M. Citak, J. Geerling, A. Khalafi, C. Krettek, and T. Hüfner, "Comparative study of different intraoperative 3-D image intensifiers in orthopedic trauma care," *The Journal of Trauma*, vol. 66, pp. 821–830, Mar. 2009.

[31] D. Kendoff, M. Citak, M. J. Gardner, T. Stübig, C. Krettek, and T. Hüfner, "Intraoperative 3D imaging: value and consequences in 248 cases," *The Journal of Trauma*, vol. 66, pp. 232–238, Jan. 2009.

[32] D. Kendoff, M. J. Gardner, M. Citak, J. Kfuri, M, B. Thumes, C. Krettek, and T. Hüfner, "Value of 3D fluoroscopic imaging of acetabular fractures comparison to 2D fluoroscopy and CT imaging," *Archives of Orthopaedic and Trauma Surgery*, vol. 128, pp. 599–605, June 2008.

[33] L. Lemieux, D. L. Bailey, and D. Bell, "Correcting for scanner errors in CT, MRI, spect, and 3D ultrasound." http://discovery.ucl.ac.uk/46565/, 2001.

[34] D. D. Robertson, P. J. Weiss, E. K. Fishman, D. Magid, and P. S. Walker, "Evaluation of CT techniques for reducing artifacts in the presence of metallic orthopedic implants," *Journal of Computer Assisted Tomography*, vol. 12, pp. 236–241, Apr. 1988.

[35] A. H. Mahnken, R. Raupach, J. E. Wildberger, B. Jung, N. Heussen, T. G. Flohr, R. W. Günther, and S. Schaller, "A new algorithm for metal artifact reduction in computed tomography: in vitro and in vivo evaluation after total hip replacement," *Investigative Radiology*, vol. 38, pp. 769–775, Dec. 2003.

[36] Rohlfing, D. Zerfowski, J. Beier, P. Wust, N. Hosten, R. Felix, and C. Virchow-Klinikum, "Reduction of metal artifacts in computed tomographies for the planning and simulation of radiation therapy," *Computer Assisted Radiology And Surgery*, pp. 1–6, 1998.

[37] M. Yazdi, L. Gingras, and L. Beaulieu, "An adaptive approach to metal artifact reduction in helical computed tomography for radiation therapy treatment planning: experimental and clinical studies," *International Journal of Radiation Oncology, Biology, Physics*, vol. 62, pp. 1224–1231, May 2005.

[38] L. Yu, H. Li, J. Mueller, J. M. Kofler, X. Liu, A. N. Primak, J. G. Fletcher, L. S. Guimaraes, T. Macedo, and C. H. McCollough, "Metal artifact reduction from reformatted projections for hip prostheses in multislice helical computed tomography: techniques and initial clinical results," *Investigative Radiology*, vol. 44, pp. 691–696, Nov. 2009.

[39] H. Li, L. Yu, X. Liu, J. G. Fletcher, and C. H. McCollough, "Metal artifact suppression from reformatted projections in multislice helical CT using dual-front active contours," *Medical Physics*, vol. 37, pp. 5155–5164, Sept. 2010.

[40] Y. Zhang, L. Zhang, X. R. Zhu, A. K. Lee, M. Chambers, and L. Dong, "Reducing metal artifacts in cone-beam CT images by preprocessing projection data," *International Journal of Radiation Oncology Biology Physics*, vol. 67, pp. 924–932, Mar. 2007.

[41] T. S. Sumanaweera, J. Adler, J R, S. Napel, and G. H. Glover, "Characterization of spatial distortion in magnetic resonance imaging and its implications for stereotactic surgery," *Neurosurgery*, vol. 35, pp. 696–704, Oct. 1994.

[42] S. J. Doran, L. Charles-Edwards, S. A. Reinsberg, and M. O. Leach, "A complete distortion correction for MR images: I. gradient warp correction," *Physics in Medicine and Biology*, vol. 50, pp. 1343–1361, Mar. 2005.

[43] S. A. Reinsberg, S. J. Doran, E. M. Charles-Edwards, and M. O. Leach, "A complete distortion correction for MR images: II. rectification of static-field inhomogeneities by similarity-based profile mapping," *Physics in Medicine and Biology*, vol. 50, pp. 2651–2661, June 2005.

[44] L. N. Baldwin, K. Wachowicz, S. D. Thomas, R. Rivest, and B. G. Fallone, "Characterization, prediction, and correction of geometric distortion in 3 t MR images," *Medical Physics*, vol. 34, pp. 388–399, Feb. 2007.

[45] Z. Hou, "A review on MR image intensity inhomogeneity correction," *International Journal of Biomedical Imaging*, vol. 2006, pp. 1–11, 2006.

[46] U. Vovk, F. Pernus, and B. Likar, "A review of methods for correction of intensity inhomogeneity in MRI," *IEEE Transactions on Medical Imaging*, vol. 26, pp. 405–421, Mar. 2007.

[47] G. Zheng, M. A. G. Ballester, M. Styner, and L. Nolte, "Reconstruction of patient-specific 3D bone surface from 2D calibrated fluoroscopic images and point distribution model," in *Medical Image Computing and Computer-Assisted Intervention – MICCAI 2006*, vol. 4190 of *LNCS*, pp. 25–32, 2006.

[48] H. Talib, K. Rajamani, J. Kowal, L. Nolte, M. Styner, and M. A. G. Ballester, "A comparison study assessing the feasibility of ultrasound-initialized deformable bone models.," *Computer aided surgery official journal of the International Society for Computer Aided Surgery*, vol. 10, no. 5-6, pp. 293–299, 2005.

[49] N. Navab, M. Mitschke, and A. Bani-Hashemi, "Merging visible and invisible: Two camera-augmented mobile C-arm (CAMC) applications," in *Proc. IEEE and ACM Int'l Workshop on Augmented Reality*, pp. 134–141, 1999.

[50] N. Navab, S. M. Heining, and J. Traub, "Camera augmented mobile C-arm (CAMC): Calibration, accuracy study and clinical applications," *IEEE Trans. Med. Imag.*, vol. 29, pp. 1412–1423, July 2010.

[51] S. L. Bacharach, "The new-generation positron emission tomography/computed tomography scanners: implications for cardiac imaging," *Journal of Nuclear Cardiology: Official Publication of the American Society of Nuclear Cardiology*, vol. 11, pp. 388–392, Aug. 2004.

[52] R. L. Bridges, "Software fusion: An option never fully explored," *Journal of Nuclear Medicine*, vol. 50, pp. 834 –836, May 2009.

[53] Y. Boykov, O. Veksler, and R. Zabih, "Fast approximate energy minimization via graph cuts," *IEEE Transactions on Pattern Analysis and Machine Intelligence*, vol. 23, pp. 1222–1239, Nov. 2001.

[54] D. Zeng, Z. Zhou, and S. Xie, "Image segmentation based on poincar map method," *IEEE Transactions on Image Processing: A Publication of the IEEE Signal Processing Society*, Sept. 2011.

[55] O. Gloger, K. D. Tonnies, V. Liebscher, B. Kugelmann, R. Laqua, and H. Voelzke, "Prior shape level set segmentation on Multi-Step generated probability maps of MR datasets for fully automatic kidney parenchyma volumetry," *IEEE Transactions on Medical Imaging*, Sept. 2011.

[56] C. Li, C. Xu, C. Gui, and M. D. Fox, "Distance regularized level set evolution and its application to image segmentation," *IEEE Transactions on Image Processing: A Publication of the IEEE Signal Processing Society*, vol. 19, pp. 3243–3254, Dec. 2010.

[57] F. van der Lijn, M. de Bruijne, S. Klein, T. den Heijer, Y. Hoogendam, A. van der Lugt, M. Breteler, and W. Niessen, "Automated brain structure segmentation based on atlas registration and appearance models," *IEEE Transactions on Medical Imaging*, Sept. 2011.

[58] A. A. Goshtasby, *2-D and 3-D Image Registration: for Medical, Remote Sensing, and Industrial Applications*. Wiley, Apr. 2005.

[59] J. V. Hajnal, *Medical image registration*. CRC Press, 2001.

[60] W. Crum, L. Griffin, D. Hill, and D. Hawkes, "Zen and the art of medical image registration: correspondence, homology, and quality," *NeuroImage*, vol. 20, pp. 1425–1437, Nov. 2003.

[61] R. H. Taylor, *Computer-integrated surgery: technology and clinical applications*, ch. Registration for computer-integrated surgery: Methodology, state of the art, pp. 77–97. MIT Press, 1996.

[62] J. Maintz and M. Viergever, "A survey of medical image registration.," *Medical Image Analysis*, vol. 2, pp. 1–36, Mar. 1998.

[63] B. Zitová and J. Flusser, "Image registration methods: a survey," *Image and Vision Computing*, vol. 21, pp. 977—1000, Oct. 2003.

[64] S. Kaneko, T. Kondo, and A. Miyamoto, "Robust matching of 3D contours using iterative closest point algorithm improved by m-estimation," *Pattern Recognition*, vol. 36, pp. 2041–2047, Sept. 2003.

[65] D. Chetverikov, D. Stepanov, and P. Krsek, "Robust euclidean alignment of 3D point sets: the trimmed iterative closest point algorithm," *Image and Vision Computing*, vol. 23, pp. 299–309, Mar. 2005.

[66] Y. Liu, "Improving ICP with easy implementation for free-form surface matching," *Pattern Recognition*, vol. 37, pp. 211–226, Feb. 2004.

[67] Z. Zhang, "Iterative point matching for registration of free-form curves and surfaces," *International Journal of Computer Vision*, vol. 13, pp. 119–152, Oct. 1994.

[68] P. J. Besl and H. D. McKay, "A method for registration of 3-D shapes," *IEEE Transactions on Pattern Analysis and Machine Intelligence*, vol. 14, pp. 239–256, Feb. 1992.

[69] Y. Tamura, N. Sugano, T. Sasama, Y. Sato, S. Tamura, K. Yonenobu, H. Yoshikawa, and T. Ochi, "Surface-based registration accuracy of CT-based image-guided spine surgery," *European Spine Journal: Official Publication of the European Spine Society, the European Spinal Deformity Society, and the European Section of the Cervical Spine Research Society*, vol. 14, pp. 291–297, Apr. 2005.

[70] J. L. Herring, B. M. Dawant, J. Maurer, C R, D. M. Muratore, R. L. Galloway, and J. M. Fitzpatrick, "Surface-based registration of CT images to physical space for image-guided surgery of the spine: a sensitivity study," *IEEE Transactions on Medical Imaging*, vol. 17, pp. 743–752, Oct. 1998.

[71] P. L. Docquier, L. Paul, O. Cartiaux, and X. Banse, "Registration accuracy in computer-assisted pelvic surgery," *Computer Aided Surgery: Official Journal of the International Society for Computer Aided Surgery*, vol. 14, no. 1-3, pp. 37–44, 2009.

[72] N. Sugano, T. Sasama, Y. Sato, Y. Nakajima, T. Nishii, K. Yonenobu, S. Tamura, and T. Ochi, "Accuracy evaluation of surface-based registration methods in a computer navigation system for hip surgery performed through a posterolateral approach," *Computer Aided Surgery: Official Journal of the International Society for Computer Aided Surgery*, vol. 6, no. 4, pp. 195–203, 2001.

[73] S. Nishihara, N. Sugano, M. Ikai, T. Sasama, Y. Tamura, S. Tamura, H. Yoshikawa, and T. Ochi, "Accuracy evaluation of a shape-based registration method for a computer navigation system for total knee arthroplasty," *The Journal of Knee Surgery*, vol. 16, pp. 98–105, Apr. 2003.

[74] A. Guéziec, P. Kazanzides, B. Williamson, and R. H. Taylor, "Anatomy-based registration of CT-scan and intraoperative x-ray images for guiding a surgical robot," *IEEE Transactions on Medical Imaging*, vol. 17, pp. 715–728, Oct. 1998.

[75] Knaan and L. Joskowicz, "Effective Intensity-Based 2D/3D rigid registration between fluoroscopic X-Ray and CT," in *Medical Image Computing and Computer-Assisted Intervention - MICCAI 2003*, vol. 2878 of *LNCS*, pp. 351–358, 2003.

[76] A. Khamene, P. Bloch, W. Wein, M. Svatos, and F. Sauer, "Automatic registration of portal images and volumetric CT for patient positioning in radiation therapy," *Medical Image Analysis*, vol. 10, pp. 96–112, Feb. 2006.

[77] H. Livyatan, Z. Yaniv, and L. Joskowicz, "Gradient-based 2-D/3-D rigid registration of fluoroscopic x-ray to CT," *IEEE Transactions on Medical Imaging*, vol. 22, pp. 1395–1406, Nov. 2003.

[78] D. Tomazevic, B. Likar, T. Slivnik, and F. Pernus, "3-D/2-D registration of CT and MR to x-ray images," *IEEE Transactions on Medical Imaging*, vol. 22, pp. 1407–1416, Nov. 2003.

[79] G. Welch and E. Foxlin, "Motion tracking: no silver bullet, but a respectable arsenal," *IEEE Computer Graphics and Applications*, vol. 22, pp. 24–38, Dec. 2002.

[80] J. B. Stiehl and D. A. Heck, "Six sigma analysis of computer-assisted surgery tracking protocols in TKA," *Clinical Orthopaedics and Related Research*, vol. 464, pp. 105–110, Nov. 2007.

[81] R. Khadem, C. C. Yeh, M. Sadeghi Tehrani, M. R. Bax, J. A. Johnson, J. N. Welch, E. P. Wilkinson, and R. Shahidi, "Comparative tracking error analysis of five different optical tracking systems," *Computer Aided Surgery*, vol. 5, pp. 98–107, Jan. 2000.

[82] J. V. Clarke, A. H. Deakin, A. C. Nicol, and F. Picard, "Measuring the positional accuracy of computer assisted surgical tracking systems," *Computer Aided Surgery: Official Journal of the International Society for Computer Aided Surgery*, vol. 15, no. 1-3, pp. 13–18, 2010.

[83] T. Rudolph, L. Ebert, and J. Kowal, "Comparison of three optical tracking systems in a complex navigation scenario," *Computer Aided Surgery: Official Journal of the International Society for Computer Aided Surgery*, vol. 15, no. 4-6, pp. 104–109, 2010.

[84] R. Elfring, M. de la Fuente, and K. Radermacher, "Assessment of optical localizer accuracy for computer aided surgery systems," *Computer Aided Surgery: Official Journal of the International Society for Computer Aided Surgery*, vol. 15, no. 1-3, pp. 1–12, 2010.

[85] O. Kutter, *Visual Computing for Computer Assisted Interventions.* PhD thesis, Technischen Universitüt München, 2010.

[86] Y. Nakayama, M. Imuta, Y. Funama, M. Kadota, D. Utsunomiya, S. Shiraishi, Y. Hayashida, and Y. Yamashita, "CT portography by multidetector helical CT: comparison of three rendering models," *Radiation Medicine*, vol. 20, pp. 273–279, Dec. 2002.

[87] D. G. Heath, P. A. Soyer, B. S. Kuszyk, D. F. Bliss, P. S. Calhoun, D. A. Bluemke, M. A. Choti, and E. K. Fishman, "Three-dimensional spiral CT during arterial portography: comparison of three rendering techniques," *Radiographics: A Review Publication of the Radiological Society of North America, Inc*, vol. 15, pp. 1001–1011, July 1995.

[88] B. S. Kuszyk, D. G. Heath, D. F. Bliss, and E. K. Fishman, "Skeletal 3-D CT: advantages of volume rendering over surface rendering," *Skeletal Radiology*, vol. 25, pp. 207–214, Apr. 1996.

[89] G. Gao, G. Penney, N. Gogin, P. Cathier, A. Arujuna, M. Wright, D. Caulfield, A. Rinaldi, R. Razavi, and K. Rhode, "Rapid image registration of three-dimensional transesophageal echocardiography and x-ray fluoroscopy for the guidance of cardiac interventions," in *Proceedings of the First international conference on Information processing in computer-assisted interventions*, LNCS, pp. 124–134, Springer-Verlag, 2010.

[90] M. Wieczorek, A. Aichert, P. Fallavollita, O. Kutter, A. Ahmadi, L. Wang, and N. Navab, "Interactive 3D visualization of a single-view X-Ray image," in *Medical Image Computing and Computer-Assisted Intervention – MICCAI 2011*, vol. 6891 of *LNCS*, pp. 73–80, 2011.

[91] C. P. Bichlmeier, *Immersive, Interactive and Contextual In-Situ Visualization for Medical Applications.* PhD thesis, Technischen Universitüt München, 2010.

[92] M. Bajura, H. Fuchs, and R. Ohbuchi, "Merging virtual objects with the real world," in *The 19th annual conference on Computer graphics and interactive techniques – SIGGRAPH 92*, pp. 203–210, 1992.

[93] H. Fuchs, M. A. Livingston, R. Raskar, D. Colucci, K. Keller, A. State, J. R. Crawford, P. Rademacher, S. H. Drake, and A. A. Meyer, "Augmented reality visualization for laparoscopic surgery," *Medical Image Computing and ComputerAssisted InterventionMICCAI*, vol. 01, no. 1496, pp. 934–943, 1998.

[94] F. Saucer, A. Khamene, B. Bascle, and G. J. Rubino, "A Head-Mounted display system for augmented reality image guidance: Towards clinical evaluation for iMRI-guided nuerosurgery," in *Medical Image Computing and Computer-Assisted Intervention – MICCAI 2001*, vol. 2208 of *LNCS*, pp. 707–716, 2001.

[95] J. Traub, P. Stefan, S. M. Heining, T. Sielhorst, C. Riquarts, E. Euler, and N. Navab, "Hybrid navigation interface for orthopedic and trauma surgery," in *Medical Image Computing and Computer-Assisted Intervention – MICCAI 2006*, vol. 4190 of *LNCS*, pp. 373–380, 2006.

[96] C. Bichlmeier, S. M. Heining, M. Rustaee, and N. Navab, "Virtually extended surgical drilling device: virtual mirror for navigated spine surgery," in *Medical Image Computing and Computer-Assisted Intervention – MICCAI 2007*, vol. 4791 of *LNCS*, pp. 434–441, 2007.

[97] C. Bichlmeier, S. M. Heining, M. Rustaee, and N. Navab, "Laparoscopic virtual mirror for understanding vessel structure evaluation study by twelve surgeons," in *IEEE International Symposium on Mixed and Augmented Reality (ISMAR'07)*, pp. 1–4, Nov. 2007.

[98] Bichlmeier, "Evaluation of the virtual mirror as a navigational aid for augmented reality driven minimally invasive procedures," *arintumde*, pp. 91–97, 2010.

[99] C. Bichlmeier, F. Wimmer, S. M. Heining, and N. Navab, "Contextual anatomic mimesis hybrid In-Situ visualization method for improving Multi-Sensory depth perception in medical augmented reality," in *IEEE International Symposium on Mixed and Augmented Reality (ISMAR'07)*, pp. 1–10, Nov. 2007.

[100] M. Blackwell, C. Nikou, A. M. DiGioia, and T. Kanade, "An image overlay system for medical data visualization," *Medical Image Analysis*, vol. 4, pp. 67–72, Mar. 2000.

[101] G. Fichtinger, A. Deguet, K. Masamune, E. Balogh, G. S. Fischer, H. Mathieu, R. H. Taylor, S. J. Zinreich, and L. M. Fayad, "Image overlay guidance for needle insertion in CT scanner," *IEEE Transactions on Bio-Medical Engineering*, vol. 52, pp. 1415–1424, Aug. 2005.

[102] G. S. Fischer, A. Deguet, C. Csoma, R. H. Taylor, L. Fayad, J. A. Carrino, S. J. Zinreich, and G. Fichtinger, "MRI image overlay: application to arthrography needle insertion," *Computer Aided Surgery: Official Journal of the International Society for Computer Aided Surgery*, vol. 12, pp. 2–14, Jan. 2007.

[103] H. Visarius, J. Gong, C. Scheer, S. Haralamb, and L. P. Nolte, "Man-machine interfaces in computer assisted surgery," *Computer Aided Surgery: Official Journal of the International Society for Computer Aided Surgery*, vol. 2, no. 2, pp. 102–107, 1997.

[104] C. Grätzel, T. Fong, S. Grange, and C. Baur, "A non-contact mouse for surgeon-computer interaction," *Technology and Health Care: Official Journal of the European Society for Engineering and Medicine*, vol. 12, no. 3, pp. 245–257, 2004.

[105] E. Samset, E. Gjesteland, and M. Sæ ter, "3D graphical user interface for computer-assisted surgery," *International Congress Series*, vol. 1256, pp. 414–418, June 2003.

[106] L. Schwarz, A. Bigdelou, and N. Navab, "Learning gestures for customizable human-computer interaction in the operating room," in *Medical Image Computing and Computer-Assisted Intervention – MICCAI 2011*, vol. 6891 of *LNCS*, 2011.

[107] I. I. O. for Standardization and I. I. O. for Standardization, "ISO - international organization for standardization." http://www.iso.org/iso/catalogue_detail?csnumber=42180.

[108] D. G. Fryback and J. R. Thornbury, "The efficacy of diagnostic imaging," *Medical Decision Making*, vol. 11, pp. 88 –94, June 1991.

[109] R. Verbeeck, J. Michiels, B. Nuttin, M. Knauth, D. Vandermeulen, P. Suetens, G. Marchal, and J. Gybels, "Protocol for the clinical functionality assessment of a workstation for stereotactic neurosurgery," *IEEE Transactions on Medical Imaging*, vol. 14, pp. 577–586, Sept. 1995.

[110] "HTA 101: Introduction to health technology assessment, table of contents." http://www.nlm.nih.gov/nichsr/hta101/ta101_c1.html, Aug. 2004.

[111] P. Jannin and W. Korb, *Image-Guided Interventions - Technology and Applications*, vol. chapter 18. Springer, May 2008.

[112] D. Simon, R. O'Toole, M. Blackwell, F. Morgan, A. Di Gioia, and T. Kanade, "Accuracy validation in image-guided orthopaedic surgery," in *Proceedings of the Second International Symposium on Medical Robotics and Computer Assisted Surgery*, pp. 185–192, 1995.

[113] C. Lavernia, V. Hernández, and J. Hommen, *Navigation and MIS in Orthopedic Surgery*, vol. chapter 8. Springer, 1 ed., Dec. 2006.

[114] P. Jannin, J. M. Fitzpatrick, D. J. Hawkes, X. Pennec, R. Shahidi, and M. W. Vannier, "Validation of medical image processing in image-guided therapy," *IEEE Transactions on Medical Imaging*, vol. 21, pp. 1445–1449, Dec. 2002.

[115] M. Breeuwer, J. P. Wadley, H. L. de Bliek, J. Buurman, P. A. Desmedt, P. Gieles, F. A. Gerritsen, N. L. Dorward, N. D. Kitchen, B. Velani, D. G. Thomas, O. Wink, J. D. Blankensteijn, B. C. Eikelboom, W. P. Mali, M. A. Viergever, G. P. Penney, R. Gaston, D. L. Hill, C. R. Maurer, D. J. Hawkes, F. Maes, D. Vandermeulen, R. Verbeeck, and M. H. Kuhn, "The EASI project–improving the effectiveness and quality of image-guided surgery," *IEEE Transactions on Information Technology in Biomedicine: A Publication of the IEEE Engineering in Medicine and Biology Society*, vol. 2, pp. 156–168, Sept. 1998.

[116] Z. Jiang, "Technology and human errors in image-guided surgeries," in *SPIE*, vol. 3262, pp. 78–84, 1998.

[117] J. Traub, S.-A. Ahmadi, N. Padoy, L. Wang, S. M. Heining, E. Euler, P. Jannin, and N. Navab, "Workflow based assessment of the camera augmented mobile c-arm system," in *AMIARCS*, MICCAI Society, Sept. 2008.

[118] F. A. Jolesz, J. Kettenbach, and W. S. Grundfest, "Cost-effectiveness of image-guided surgery," *Academic Radiology*, vol. 5 Suppl 2, pp. S428–431, Sept. 1998.

[119] R. G. Watkins, A. Gupta, and R. G. Watkins, "Cost-effectiveness of image-guided spine surgery," *The Open Orthopaedics Journal*, vol. 4, pp. 228–233, 2010.

[120] F. Langlotz, "Potential pitfalls of computer aided orthopedic surgery," *Injury*, vol. 35 Suppl 1, pp. S–A17–23, June 2004.

[121] r. DiGioia, Anthony M and L. Nolte, "The challenges for CAOS: what is the role of CAOS in orthopaedics?," *Computer Aided Surgery: Official Journal of the International Society for Computer Aided Surgery*, vol. 7, no. 3, pp. 127–128, 2002.

[122] G. Zheng, X. Dong, and P. A. Gruetzner, "Reality-augmented virtual fluoroscopy for computer-assisted diaphyseal long bone fracture osteosynthesis: A novel technique and feasibility study results," *Proceedings of the Institution of Mechanical Engineers, Part H: Journal of Engineering in Medicine*, vol. 222, pp. 101 –115, Jan. 2008.

[123] T. Leloup, W. El Kazzi, F. Schuind, and N. Warzee, "A novel technique for distal locking of intramedullary nail based on two non-constrained fluoroscopic images and navigation," *IEEE Transactions on Medical Imaging*, vol. 27, pp. 1202–1212, 2008.

[124] K. Foley, D. Simon, and Y. Rampersaud, "Virtual fluoroscopy: computer-assisted fluoroscopic navigation," *Spine*, vol. 26, no. 4, p. 347, 2001.

[125] N. Suhm, P. Messmer, I. Zuna, L. A. Jacob, and P. Regazzoni, "Fluoroscopic guidance versus surgical navigation for distal locking of intramedullary implants: A prospective, controlled clinical study," *Injury*, vol. 35, pp. 567–574, June 2004.

[126] Z. Yaniv and L. Joskowicz, "Long bone panoramas from fluoroscopic X-Ray images," *IEEE Trans. Med. Imag.*, vol. 23, pp. 26–35, Jan. 2004.

[127] P. Messmer, F. Matthews, C. Wullschleger, R. Hügli, P. Regazzoni, and A. L. Jacob, "Image fusion for intraoperative control of axis in long bone fracture treatment," *European Journal of Trauma*, vol. 32, pp. 555–561, Dec. 2006.

[128] L. Wang, J. Traub, S. M. Heining, S. Benhimane, E. Euler, R. Graumann, and N. Navab, "Long bone x-ray image stitching using camera augmented mobile c-arm," in *Medical Image Computing and Computer-Assisted Intervention – MICCAI 2008*, vol. 5242 of *LNCS*, 2008.

[129] F. Matthews, D. J. Hoigne, M. Weiser, G. A. Wanner, P. Regazzoni, N. Suhm, and P. Messmer, "Navigating the fluoroscope's C-arm back into position: an accurate and practicable solution to cut radiation and optimize intraoperative workflow," *Journal of Orthopaedic Trauma*, vol. 21, pp. 687–692, Dec. 2007.

[130] L. Matthaeus, N. Binder, C. Bodensteiner, and A. Schweikard, "Closed-form inverse kinematic solution for fluoroscopic C-arms," *Advanced Robotics*, vol. 21, no. 8, pp. 869–886, 2007.

[131] V. Grzeda and G. Fichtinger, "Rotational encoding of C-arm fluoroscope with tilt sensing accelerometer," in *Medical Image Computing and Computer-Assisted Intervention - MICCAI 2010*, vol. 6363 of *LNCS*, pp. 424–431, 2010.

[132] R. M. Schwend, P. J. Dewire, and T. M. Kowalski, "Accuracy of fluoroscopically assisted laser targeting of the cadaveric thoracic and lumbar spine to place transpedicular screws," *Journal of Spinal Disorders*, vol. 13, pp. 412–418, Oct. 2000.

[133] I. Harris, P. M. Walker, and L. Trieu, "Radiation exposure using laser aiming guide in orthopaedic procedures," *ANZ Journal of Surgery*, vol. 72, pp. 349–351, May 2002.

[134] R. Ko and H. Razvi, "C-arm laser positioning device to facilitate percutaneous renal access," *Urology*, vol. 70, pp. 360–361, Aug. 2007.

[135] R. T. Azuma *et al.*, "A survey of augmented reality," *Presence-Teleoperators and Virtual Environments*, vol. 6, no. 4, pp. 355–385, 1997.

[136] C. Nikou, A. M. Digioia, M. Blackwell, B. Jaramaz, and T. Kanade, "Augmented reality imaging technology for orthopaedic surgery," *Operative Techniques in Orthopaedics*, vol. 10, no. 1, pp. 82–86, 2000.

[137] J. H. Shuhaiber, "Augmented reality in surgery," *Arch Surg*, vol. 139, pp. 170–174, Feb. 2004.

[138] G. Stetten, A. Cois, W. Chang, D. Shelton, R. Tamburo, J. Castellucci, and O. von Ramm, "C-mode real-time tomographic reflection for a matrix array ultrasound sonic flashlight," *Academic Radiology*, vol. 12, pp. 535–543, May 2005.

[139] M. Feuerstein, T. Mussack, S. M. Heining, and N. Navab, "Intraoperative laparoscope augmentation for port placement and resection planning in minimally invasive liver resection," *IEEE Transactions on Medical Imaging*, vol. 27, pp. 355–369, Mar. 2008.

[140] T. Wendler, M. Feuerstein, J. Traub, T. Lasser, J. Vogel, F. Daghighian, S. I. Ziegler, and N. Navab, "Real-time fusion of ultrasound and gamma probe for navigated localization of liver metastases," *Medical Image Computing and Computer-Assisted Intervention – MICCAI 2007*, vol. 4792, pp. 252–260, 2007.

[141] T. Wendler, A. Hartl, T. Lasser, J. Traub, F. Daghighian, S. Ziegler, and N. Navab, "Towards intra-operative 3d nuclear imaging: reconstruction of 3d radioactive distributions using tracked gamma probes," in *Medical Image Computing and Computer-Assisted Intervention – MICCAI 2007*, vol. 4792 of *LNCS*, pp. 909–917, 2007.

[142] A. Okur, S.-A. Ahmadi, A. Bigdelou, T. Wendler, and N. Navab, "MR in OR: First analysis of AR/VR visualization in 100 intra-operative Freehand SPECT acquisitions," in *Proceedings of the 10th International Symposium on Mixed and Augmented Reality (ISMAR)*, pp. 211–218, Oct. 2011.

[143] N. Navab, M. Mitschke, and O. Schütz, "Camera-Augmented mobile c-arm (CAMC) application: 3D reconstruction using a Low-Cost mobile c-arm," in *Medical Image Computing and Computer-Assisted Intervention – MICCAI 1999*, vol. 1679 of *LNCS*, pp. 688–697, Springer Berlin Heidelberg, 1999.

[144] J. Traub, *New Concepts for Design and Workflow Driven Evaluation of Computer Assisted Surgery Solutions*. PhD thesis, Technischen Universitüt München, 2008.

[145] M. Mitschke, A. Bani-Hashemi, and N. Navab, "Interventions under Video-Augmented X-Ray guidance: Application to needle placement," in *Medical Image Computing and Computer-Assisted Intervention – MICCAI 2000*, vol. 1935 of *LNCS*, pp. 858–868, 2000.

[146] S.-M. M. Heining, S. Wiesner, E. Euler, W. Mutschler, and N. Navab, "Locking of intramedullary nails under video-augmented flouroscopic control: first clinical application in a cadaver study," in *Proceedings of The 6th Computer Assisted Orthopaedic Surgery (CAOS 2006)*, June 2006.

[147] S. M. Heining, S. Wiesner, E. Euler, and N. Navab, "Pedicle screw placement under video-augmented fluoroscopic control. first clinical application in a cadaver study," *International Journal of Computer Assisted Radiology and Surgery*, vol. 1, pp. 189–190, June 2006.

[148] N. Navab, S. Wiesner, S. Benhimane, E. Euler, and S. M. Heining, "Visual servoing for intraoperative positioning and repositioning of mobile c-arms," in *Medical Image Computing and Computer-Assisted Intervention – MICCAI 2006*, vol. 4190 of *LNCS*, pp. 551–560, 2006.

[149] J. Traub, T. H. Heibel, P. Dressel, S. M. Heining, R. Graumann, and N. Navab, "A multi-view Opto-Xray imaging system: development and first application in trauma surgery," in *Medical Image Computing and Computer-Assisted Intervention – MICCAI 2007*, vol. 4792 of *LNCS*, pp. 18–25, 2007.

[150] P. Dressel, L. Wang, O. Kutter, J. Traub, S. Heining, and N. Navab, "Intraoperative positioning of mobile C-arms using artificial fluoroscopy," in *Proceedings of SPIE*, vol. 7625, pp. 762506–762506–6, Mar. 2010.

[151] Z. Zhang, "A flexible new technique for camera calibration," tech. rep., Microsoft Research, 1998 (last updated in 2008).

[152] M. Groher, "Development of a planning and navigation tool for endoscopic treatment of aortic aneurysms-computer supported implantation of a stent graft," 2003.

[153] Z. Yaniv, L. Joskowicz, A. Simkin, M. Garza-Jinich, and C. Milgrom, "Fluoroscopic image processing for computer-aided orthopaedic surgery," in *Medical Image Computing and Computer-Assisted Interventation – MICCAI 1998*, vol. 1496 of *LNCS*, pp. 325–334, 1999.

[154] R. Tsai, "A versatile camera calibration technique for high-accuracy 3D machine vision metrology using off-the-shelf TV cameras and lenses," *IEEE Journal of Robotics and Automation*, vol. 3, pp. 323–344, Aug. 1987.

[155] H. Livyatan, Z. Yaniv, and L. Joskowicz, "Robust automatic C-Arm calibration for Fluoroscopy-Based navigation: A practical approach," in *Medical Image Computing and Computer-Assisted Intervention – MICCAI 2002*, vol. 2489 of *LNCS*, pp. 60–68, 2002.

[156] R. Hofstetter, M. Slomczykowski, M. Sati, and L. P. Nolte, "Fluoroscopy as an imaging means for computer-assisted surgical navigation," *Computer Aided Surgery: Official Journal of the International Society for Computer Aided Surgery*, vol. 4, no. 2, pp. 65–76, 1999.

[157] R. Fahrig, M. Moreau, and D. W. Holdsworth, "Three-dimensional computed tomographic reconstruction using a c-arm mounted XRII: correction of image intensifier distortion," *Medical Physics*, vol. 24, pp. 1097–1106, July 1997.

[158] G. Shechter, *Respiratory Motion of the Heart: Implications for Magnetic Resonance Coronary Angiography*. PhD thesis, Johns Hopkins University, 2004.

[159] D. A. Forsyth and J. Ponce, *Computer Vision: A Modern Approach*. Prentice Hall, 1 ed., Aug. 2002.

[160] X. Zhang, "Projection matrix decomposition in AR - a study with Access3D," in *Third IEEE and ACM International Symposium on Mixed and Augmented Reality, 2004. ISMAR 2004*, pp. 258– 259, IEEE, Nov. 2004.

[161] X. Chen, L. Wang, P. Fallavollita, and N. Navab, "Error analysis of the x-ray projection geometry of camera-augmented mobile c-arm," in *SPIE Medical Imaging*, Feb. 2012.

[162] L. Wang, J. Landes, S. Weidert, T. Blum, A. Von Der Heide, E. Euler, and N. Navab, "First animal cadaver study for interlocking of intramedullary nails under camera augmented mobile c-arm: a surgical workflow based preclinical evaluation," in *Proceedings of the First international conference on Information processing in computer-assisted interventions*, vol. 6135 of *LNCS*, pp. 56–66, Springer-Verlag, 2010.

[163] L. Wang, J. Traub, S. Weidert, S. M. Heining, E. Euler, and N. Navab, "Parallax-Free Long Bone X-ray Image Stitching," in *Medical Image Computing and Computer-Assisted Intervention – MICCAI 2009*, vol. 5761 of *LNCS*, (London, UK), pp. 173–180, 2009.

[164] L. Wang, J. Traub, S. Weidert, S. M. Heining, E. Euler, and N. Navab, "Parallax-free intra-operative X-ray image stitching," *Medical Image Analysis*, vol. 14, pp. 674–686, June 2010.

[165] N. Navab, S. Wiesner, S. Benhimane, E. Euler, and S. M. Heining, "Visual servoing for intraoperative positioning and repositioning of mobile C-arms," in *Medical Image Computing and Computer-Assisted Intervention – MICCAI 2006*, vol. 4190 of *LNCS*, (Copenhagen, Denmark), pp. 551–560, 2006.

[166] N. Navab and M. Mitschke, "Method and apparatus using a virtual detector for three-dimensional reconstruction form x-ray images," 2001. Patent US 6236704; Filing date: Jun 30, 1999; Issue date: May 22,.

[167] "The 2007 recommendations of the international commission on radiological protection. ICRP publication 103," *Annals of the ICRP*, vol. 37, no. 2-4, pp. 1–332, 2007.

[168] H. P. Agency, "NRPB - w4 radiation exposure of the UK population from medical and dental X-Ray examinations." http://www.hpa.org.uk/web/HPAweb&HPAwebStandard/HPAweb_C/1247816602523. Approval date: August 2001.

[169] F. W. Schultz and J. Zoetelief, "Dose conversion coefficients for interventional procedures," *Radiation Protection Dosimetry*, vol. 117, no. 1-3, pp. 225–230, 2005.

[170] K. Perisinakis, N. Theocharopoulos, J. Damilakis, P. Katonis, G. Papadokostakis, A. Hadjipavlou, and N. Gourtsoyiannis, "Estimation of patient dose and associated radiogenic risks from fluoroscopically guided pedicle screw insertion," *Spine*, vol. 29, pp. 1555–1560, July 2004.

[171] K. Perisinakis, J. Damilakis, N. Theocharopoulos, G. Papadokostakis, A. Hadjipavlou, and N. Gourtsoyiannis, "Patient effective dose and radiogenic risks from fluoroscopically assisted surgical reconstruction of femoral fractures," *Radiation Protection Dosimetry*, vol. 108, no. 1, pp. 65–72, 2004.

[172] L. Wang, S. Weidert, J. Traub, S. M. Heining, C. Riquarts, E. Euler, and N. Navab, "Camera augmented mobile c-arm," in *Bildverarbeitung für die Medizin 2009* (H. Meinzer, T. M. Deserno, H. Handels, and T. Tolxdorff, eds.), pp. 97–101, Springer Berlin Heidelberg, 2009.

[173] X. Zhang, S. Fronz, and N. Navab, "Visual marker detection and decoding in ar systems: A comparative study," in *IEEE International Symposium on Mixed and Augmented Reality (ISMAR'02), October 2002*, 2002.

[174] T. Sielhorst, M. Feuerstein, J. Traub, O. Kutter, and N. Navab, "Campar: A software framework guaranteeing quality for medical augmented reality," *International Journal of Computer Assisted Radiology and Surgery*, vol. 1, pp. 29–30, June 2006.

[175] T. Neumuth, N. Durstewitz, M. Fischer, G. Strauss, A. Dietz, J. Meixensberger, P. Jannin, K. Cleary, H. Lemke, and O. Burgert, "Structured recording of intraoperative surgical workflows," in *SPIE Medical Imaging 2006*, 2006.

[176] T. Neumuth, P. Jannin, G. Strauss, J. Meixensberger, and O. Burgert, "Validation of Knowledge Acquisition for Surgical Process Models," *Journal of the American Medical Informatics Association*, vol. 16, no. 1, pp. 72–80, 2009.

[177] G. M. Whatling and L. D. M. Nokes, "Literature review of current techniques for the insertion of distal screws into intramedullary locking nails," *Injury*, vol. 37, pp. 109–119, Feb. 2006.

[178] T. R. Blattert, U. A. Fill, E. Kunz, W. Panzer, A. Weckbach, and D. F. Regulla, "Skill dependence of radiation exposure for the orthopaedic surgeon during interlocking nailing of long-bone shaft fractures: a clinical study," *Archives of Orthopaedic and Trauma Surgery*, vol. 124, pp. 659–664, Dec. 2004.

[179] P. Levin, R. Schoen, and B. Browner, "Radiation exposure to the surgeon during closed interlocking intramedullary nailing," *The Journal of Bone and Joint Surgery (American)*, vol. 69, pp. 761–766, June 1987.

[180] S. Skjeldal and S. Backe, "Interlocking medullary nails–radiation doses in distal targeting," *Archives of Orthopaedic and Traumatic Surgery. Archiv Für Orthopädische Und Unfall-Chirurgie*, vol. 106, no. 3, pp. 179–181, 1987.

[181] L. P. Müller, J. Suffner, K. Wenda, W. Mohr, and P. M. Rommens, "Radiation exposure to the hands and the thyroid of the surgeon during intramedullary nailing," *Injury*, vol. 29, pp. 461–468, July 1998.

[182] Z. Yaniv and L. Joskowicz, "Precise robot-assisted guide positioning for distal locking of intramedullary nails," *IEEE Transactions on Medical Imaging*, vol. 24, pp. 624–635, 2005.

[183] M. Fuchs, H. Modler, A. Schmid, and K. M. Stürmer, "Strahlenschutz im operationssaal," *Operative Orthopädie und Traumatologie*, vol. 11, pp. 328–333, Dec. 1999.

[184] G. Van Staden, K. Farrant, R. Richards, and T. Bunker, "Image intensifier position for hand and wrist fractures," *Injury*, vol. 31, pp. 351–352, June 2000.

[185] C. Bichlmeier, F. Wimmer, S. Heining, and N. Navab, "Contextual Anatomic Mimesis: Hybrid In-Situ Visualization Method for Improving Multi-Sensory Depth Perception in Medical Augmented Reality," in *Proceedings of the 6th International Symposium on Mixed and Augmented Reality (ISMAR)*, pp. 129–138, Nov. 2007.

[186] W. M. Ricci, C. Bellabarba, R. Lewis, B. Evanoff, D. Herscovici, T. DiPasquale, and R. Sanders, "Angular malalignment after intramedullary nailing of femoral shaft fractures," *Journal of Orthopaedic Trauma*, vol. 15, pp. 90–95, Feb. 2001.

[187] W. M. Ricci, M. O'Boyle, J. Borrelli, C. Bellabarba, and R. Sanders, "Fractures of the proximal third of the tibial shaft treated with intramedullary nails and blocking screws," *Journal of Orthopaedic Trauma*, vol. 15, pp. 264–270, May 2001.

[188] W. T. Obremskey and M. Medina, "Comparison of intramedullary nailing of distal third tibial shaft fractures: before and after traumatologists," *Orthopedics*, vol. 27, Nov. 2004.

[189] R. L. Jaarsma, D. F. M. Pakvis, N. Verdonschot, J. Biert, and A. van Kampen, "Rotational malalignment after intramedullary nailing of femoral fractures," *Journal of Orthopaedic Trauma*, vol. 18, pp. 403–409, Aug. 2004.

[190] M. Boewer, H. Arndt, P. A. W. Ostermann, J. Petersein, and S. Mutze, "Length and angle measurements of the lower extremity in digital composite overview images," *European Radiology*, vol. 15, pp. 158–164, January 2005.

[191] O. W. Hamer, M. Strotzer, N. Zorger, C. Paetzel, K. Lerch, S. Feuerbach, and M. Völk, "Amorphous silicon, flat-panel, x-ray detector: Reliability of digital image fusion regarding angle and distance measurements in long-leg radiography," *Investigative radiology*, vol. 39, pp. 271–276, 2004.

[192] A. H. W. van Eeuwijk, S. Lobregt, and F. A. Gerritsen, "A novel method for digital x-ray imaging of the complete spine," in *CVRMed-MRCAS '97: Proceedings of the First Joint Conference on Computer Vision, Virtual Reality and Robotics in Medicine and Medial Robotics and Computer-Assisted Surgery*, pp. 521–530, Springer-Verlag, 1997.

[193] H. Geijer, K.-W. Beckman, B. Jonsson, T. Andersson, and J. Persliden, "Digital radiography of scoliosis with a scanning method: initial evaluation," *Radiology*, vol. 218, no. 2, pp. 402–410, 2001.

[194] R. Szeliski, "Image alignment and stitching: A tutorial," tech. rep., Microsoft Research, 2006.

[195] I. Zoghlami, O. Faugeras, and R. Deriche, "Using geometric corners to build a 2d mosaic from a set of image," in *CVPR '97: Proceedings of the 1997 Conference on Computer Vision and Pattern Recognition (CVPR '97)*, p. 420, IEEE Computer Society, 1997.

[196] S. Peleg, B. Rousso, A. Rav-Acha, and A. Zomet, "Mosaicing on adaptive manifolds," *IEEE Trans. Pattern Anal. Mach. Intell.*, vol. 22, no. 10, pp. 1144–1154, 2000.

[197] Z. Qi and J. R. Cooperstock, "Overcoming parallax and sampling density issues in image mosaicing of non-planar scenes," in *British Machine Vision Conference (BMVC)*, September 2007.

[198] S. B. Kang, R. Szeliski, and M. Uyttendaele, "Seamless stitching using multi-perspective plane sweep," tech. rep., Microsoft Research, June 2004.

[199] B. Kainz, M. Grabner, and M. Rüther, "Fast marker based c-arm pose estimation," in *Medical Image Computing and Computer-Assisted Intervention – MICCAI 2008* (D. Metaxas, L. Axel, G. Fichtinger, and G. Székely, eds.), vol. 5242 of *LNCS*, pp. 652–659, Springer, 2008.

[200] R. Hartley and A. Zisserman, *Multiple View Geometry in Computer Vision*. Cambridge University Press, 2003.

[201] S. Umeyama, "Least-squares estimation of transformation parameters between two point patterns," *IEEE transactions on pattern analysis and machine intelligence*, vol. 13, no. 4, pp. 376–380, 1991.

[202] K. Kanatani, "Analysis of 3-d rotation fitting," *IEEE Trans. Pattern Anal. Mach. Intell.*, vol. 16, no. 5, pp. 543–549, 1994.

[203] L. Wang, P. Fallavollita, R. Zou, X. Chen, S. Weidert, and N. Navab, "Closed-form inverse kinematics for interventional c-arm x-ray imaging with six degrees of freedom: modeling and application," *IEEE transactions on medical imaging*, vol. 31, pp. 1086–1099, May 2012.

[204] L. D. M. Nokes, "Literature review of current techniques for the insertion of distal screws into intramedullary locking nails," *Injury*, vol. 37, pp. 109–119, Feb. 2006.

[205] R. Hart, B. Hansen, M. Shea, F. Hsu, and G. Anderson, "Pedicle screw placement in the thoracic spine: A comparison of image-guided and manual techniques in cadavers," *Spine.*, vol. 30, pp. 326–331, June 2005.

[206] S. M. Heining, S. Wiesner, E. Euler, and N. Navab, "Pedicle screw placement under video-augmented fluoroscopic control: First clinical application in a cadaver study," *International Journal of Computer Assisted Radiology and Surgery*, vol. 1, pp. 189–190, June 2006.

[207] C. Schaller, C. Rohkohl, J. Penne, M. Stürmer, and J. Hornegger, "Inverse C-arm positioning for interventional procedures using real-time body part detection," in *Medical Image Computing and Computer-Assisted Intervention – MICCAI 2009*, vol. 5761 of *LNCS*, (London, UK), pp. 549–556, 2009.

[208] S. Chaganti, D. Kumar, S. Patil, and P. Alderman, "A language for effective communication between surgeons and radiographers in trauma theatre," *Annals of The Royal College of Surgeons of England*, vol. 91, pp. 509–512, Sept. 2009.

[209] W. Wolovich and H. Elliott, "A computational technique for inverse kinematics," in *The 23rd IEEE Conference on Decision and Control*, pp. 1359–1363, IEEE, Dec. 1984.

[210] A. A. Maciejewski and C. A. Klein, "Obstacle avoidance for kinematically redundant manipulators in dynamically varying environments," *The International Journal of Robotics Research*, vol. 4, no. 3, pp. 109–117, 1985.

[211] T. Yoshikawa, "Dynamic manipulability of robot manipulators," in *1985 IEEE International Conference on Robotics and Automation*, pp. 1033–1038, Mar. 1985.

[212] T. Yoshikawa, "Manipulability of robotic mechanisms," *The International Journal of Robotics Research*, vol. 4, pp. 3–9, June 1985.

[213] C. W. Wampler, II, "Manipulator inverse kinematic solutions based on vector formulations and damped least-squares methods," *IEEE Trans. Syst. Man Cybern.*, vol. 16, pp. 93–101, Jan. 1986.

[214] Y. Nakamura and H. Hanafusa, "Inverse kinematic solutions with singularity robustness for robot manipulator control," *Journal of Dynamic Systems, Measurement, and Control*, vol. 108, no. 3, pp. 163–171, 1986.

[215] S. R. Buss and J.-S. Kim, "Selectively damped least squares for inverse kinematics," *Journal of Graphics, GPU, and Game Tools*, vol. 10, no. 3, pp. 37–49, 2005.

[216] J. Denavit and R. S. Hartenberg, "A kinematic notation for lower-pair mechanisms based on matrices," *Trans ASME J. Appl. Mech*, vol. 23, pp. 215–221, 1955.

[217] M. W. Spong, S. Hutchinson, and M. Vidyasagar, *Robot Modeling and Control*. Wiley, Nov. 2005.

[218] B. Kainz, M. Grabner, and M. Rüther, "Fast marker based C-arm pose estimation," in *Medical Image Computing and Computer-Assisted Intervention – MICCAI 2008*, vol. 5242 of *LNCS*, pp. 652–659, 2008.

[219] R. P. Paul, B. Shimano, and G. E. Mayer, "Differential kinematic control equations for simple manipulators," *IEEE Transactions on Systems, Man and Cybernetics*, vol. 11, pp. 456–460, June 1981.

[220] P. Corke, "A robotics toolbox for MATLAB," *IEEE Robotics and Automation Magazine*, vol. 3, pp. 24–32, Mar. 1996.

[221] S. Hankemeier, T. Gosling, M. Richter, T. Hufner, C. Hochhausen, and C. Krettek, "Computer-assisted analysis of lower limb geometry: higher intraobserver reliability compared to conventional method," *Comput Aided Surg*, vol. 11, no. 2, pp. 81–6, 2006.

[222] S. Gottschalk, M. C. Lin, and D. Manocha, "OBBTree: a hierarchical structure for rapid interference detection," in *SIGGRAPH*, pp. 171–180, 1996.

[223] M. M. Mischke and N. Navab, "Recovering projection geometry: how a cheap camera can outperform an expensive stereo system," in *IEEE Conference on Computer Vision and Pattern Recognition*, vol. 1, (South Carolina, USA), pp. 193–200, IEEE, 2000.

[224] K. Pentenrieder, P. Meier, and G. Klinker, "Analysis of tracking accuracy for single-camera square-marker-based tracking," in *Third Workshop on Virtual and Augmented Reality of the GI-Fachgruppe VR/AR*, Sept. 2006.

[225] D. F. Abawi, J. Bienwald, and R. Dorner, "Accuracy in optical tracking with fiducial markers: an accuracy function for ARToolKit," in *Third IEEE and ACM International Symposium on Mixed and Augmented Reality*, (Arlington, VA, USA), pp. 260–261, Nov. 2004.

[226] S. Kim, Y. Koh, Y. Chun, Y. Kim, Y. Park, and C. Sung, "Medial opening wedge high-tibial osteotomy using a kinematic navigation system versus a conventional method: a 1-year retrospective, comparative study," *Knee Surgery, Sports Traumatology, Arthroscopy*, vol. 17, pp. 128–134, Oct. 2008.

[227] H. Baethis, L. Perlick, M. Tingart, C. Luering, D. Zurakowski, and J. Grifka, "Alignment in total knee arthroplasty. a comparison of computer-assisted surgery with the conventional technique," *The Journal of Bone and Joint Surgery. British Volume*, vol. 86, pp. 682–687, Jul. 2004.

[228] T. D. V. Cooke, E. A. Sled, and R. A. Scudamore, "Frontal plane knee alignment: a call for standardized measurement," *The Journal of Rheumatology*, vol. 34, pp. 1796–1801, Sept. 2007.

[229] "The official website of the nobel prize@ONLINE." http://nobelprize.org/nobel_prizes/chemistry/laureates/2008/press.html, June 2011.

[230] A. M. De Grand and J. V. Frangioni, "An operational near-infrared fluorescence imaging system prototype for large animal surgery," *Technology in Cancer Research & Treatment*, vol. 2, pp. 553–562, Dec. 2003.

[231] G. Themelis, J. S. Yoo, K. Soh, R. Schulz, and V. Ntziachristos, "Real-time intraoperative fluorescence imaging system using light-absorption correction," *Journal of Biomedical Optics*, vol. 14, p. 064012, Dec. 2009.

[232] N. Navab and J. P. Williams, "Real-time acquisition of co-registered x-ray and optical images," 2001. Patent US 7198404; Filing date: Mar 30, 2004; Issue date: Apr 03 2007.

[233] G. Themelis, J. S. Yoo, and V. Ntziachristos, "Multispectral imaging using multiple-bandpass filters," *Opt. Lett.*, vol. 33, pp. 1023–1025, May 2008.

[234] L. Wang, M. Springer, H. Heibel, and N. Navab, "Floyd-Warshall All-Pair Shortest Path for Accurate Multi-Marker Calibration," in *Proceedings of the 9th International Symposium on Mixed and Augmented Reality (ISMAR)*, Oct. 2010.

[235] N. Padoy, T. Blum, S.-A. Ahmadi, H. Feussner, M.-O. Berger, and N. Navab, "Statistical modeling and recognition of surgical workflow," *Medical Image Analysis*, pp. 131–138, 2010. In press.

[236] T. Blum, N. Padoy, H. Feussner, and N. Navab, "Modeling and online recognition of surgical phases using hidden markov models," in *Medical Image Computing and Computer-Assisted Intervention – MICCAI 2008*, vol. 5242 of *LNCS*, pp. 627–635, 2008.

[237] S.-A. Ahmadi, N. Padoy, S. M. Heining, H. Feussner, M. Daumer, and N. Navab, "Introducing wearable accelerometers in the surgery room for activity detection," in *7. Jahrestagung der Deutschen Gesellschaft fuer Computer-und Roboter-Assistierte Chirurgie (CURAC 2008)*, Sept. 2008.

[238] N. Padoy, D. Mateus, D. Weinland, M.-O. Berger, and N. Navab, "Workflow monitoring based on 3d motion features," in *Proceedings of the International Conference on Computer Vision Workshops, IEEE Workshop on Video-oriented Object and Event Classification*, 2009.

[239] J. K. Aggarwal and Q. Cai, "Human motion analysis: a review," in *Nonrigid and Articulated Motion Workshop*, pp. 90–102, IEEE, June 1997.

[240] D. Moore and I. Essa, "Recognizing multitasked activities from video using stochastic context-free grammar," in *Eighteenth national conference on Artificial intelligence*, pp. 770–776, American Association for Artificial Intelligence, 2002.

[241] R. Hamid, S. Maddi, A. Bobick, and M. Essa, "Structure from statistics - unsupervised activity analysis using suffix trees," in *IEEE 11th International Conference on Computer Vision, 2007. ICCV 2007*, pp. 1–8, IEEE, Oct. 2007.

[242] J. Wang, P. Fallavollita, L. Wang, M. Kreiser, and N. Navab, "Augmented reality during angiography: Integration of a virtual mirror for improved 2d/3d visualization," 2012. accepted at ISMAR 2012.

[243] A. Aichert, M. Wieczorek, J. Wang, L. Wang, M. Kreiser, P. Fallavollita, and N. Navab, "The colored x-rays," in *MICCAI 2012 Workshop on Augmented Environments for Computer-Assisted Interventions*, 2012.

[244] L. Wang, P. Fallavollita, A. Brand, O. Erat, S. Weidert, P.-H. Thaller, E. Euler, and N. Navab, "Intra-op measurement of the mechanical axis deviation: An evaluation study on 19 human cadaver legs," in *Medical Image Computing and Computer-Assisted Intervention – MICCAI 2012*, vol. 7511 of *LNCS*, pp. 609–616, 2012.

[245] B. Diotte, P. Fallavollita, L. Wang, S. Weidert, P.-H. Thaller, E. Euler, and N. Navab, "Radiation-free drill guidance in interlocking of intramedullary nails," in *Medical Image Computing and Computer-Assisted Intervention – MICCAI 2012*, vol. 7510 of *LNCS*, pp. 18–25, 2012.

[246] A. Brand, L. Wang, P. Fallavollita, P. Sandner, N. Navab, P. Thaller, E. Euler, and S. Weidert, "X-ray stitching for intra-operative mechanical axis determination of the lower extremity," in *the 12th Annual Meeting of the International Society for Computer Assisted Orthopaedic Surgery*, June 2012.

[247] N. Navab, T. Blum, L. Wang, A. Okur, and T. Wendler, "First deployments of augmented reality in operating rooms," *Computer*, vol. 45, pp. 48 –55, July 2012.

[248] S. Weidert, L. Wang, A. von der Heide, E. Euler, and N. Navab, "Intraoperative augmented-reality-visualisierung: Aktueller stand der entwicklung und erste erfahrungen mit dem camc," *Unfallchirurg*, vol. 115, Mar. 2012.

[249] X. Chen, L. Wang, P. Fallavollita, and N. Navab, "Precise x-ray and video overlay for augmented reality fluoroscopy," *International journal of computer assisted radiology and surgery*, May 2012.

[250] S. Demirci, A. Bigdelou, L. Wang, C. Wachinger, M. Baust, R. Tibrewal, R. Ghotbi, H. Eckstein, and N. Navab, "3d stent recovery from one x-ray projection," in *Medical Image Computing and Computer-Assisted Intervention – MICCAI 2011*, vol. 6891 of *LNCS*, pp. 178–185, 2011.

[251] L. Wang, R. Zou, S. Weidert, J. Landes, E. Euler, D. Burschka, and N. Navab, "Closed-form inverse kinematics for intra-operative mobile C-arm positioning with six degrees of freedom," in *Proceedings of SPIE*, vol. 7964, pp. 79641A–79641A–6, Mar. 2011.

[252] S. Weidert, L. Wang, P. Thaller, J. Landes, A. Brand, N. Navab, and E. Euler, "X-ray stitching for intra-operative mechanical axis determination of the lower extremity," in *the 11th Annual Meeting of the International Society for Computer Assisted Orthopaedic Surgery*, June 2011.

[253] L. Wang, M. Springer, T. H. Heibel, and N. Navab, "Floyd-warshall all-pair shortest path for accurate multi-marker calibration," in *ISMAR*, pp. 277–278, IEEE, 2010.

[254] S. Weidert, L. Wang, J. Landes, A. von der Heide, N. Navab, and E. Euler, "Long bone x-ray image stitching using c-arm motion estimation," in *The 3rd Hamlyn Symposium for Medical Robotics*, May 2010.

[255] L. Wang, R. Zou, S. Weidert, J. Landes, E. Euler, D. Burschka, and N. Navab, "Modeling kinematics of mobile C-arm and operating table as an integrated six degrees of freedom imaging system," in *The 5th International Workshop on Medical Imaging and Augmented Reality – MIAR 2010*, vol. 6326 of *LNCS*, (Beijing, China), pp. 485–493, 2010.

[256] L. Wang, J. Traub, S. M. Heining, S. Benhimane, E. Euler, R. Graumann, and N. Navab, "Long bone x-ray image stitching using c-arm motion estimation," in *Bildverarbeitung für die Medizin 2009* (H. Meinzer, T. M. Deserno, H. Handels, and T. Tolxdorff, eds.), pp. 202–206, Springer Berlin Heidelberg, 2009.